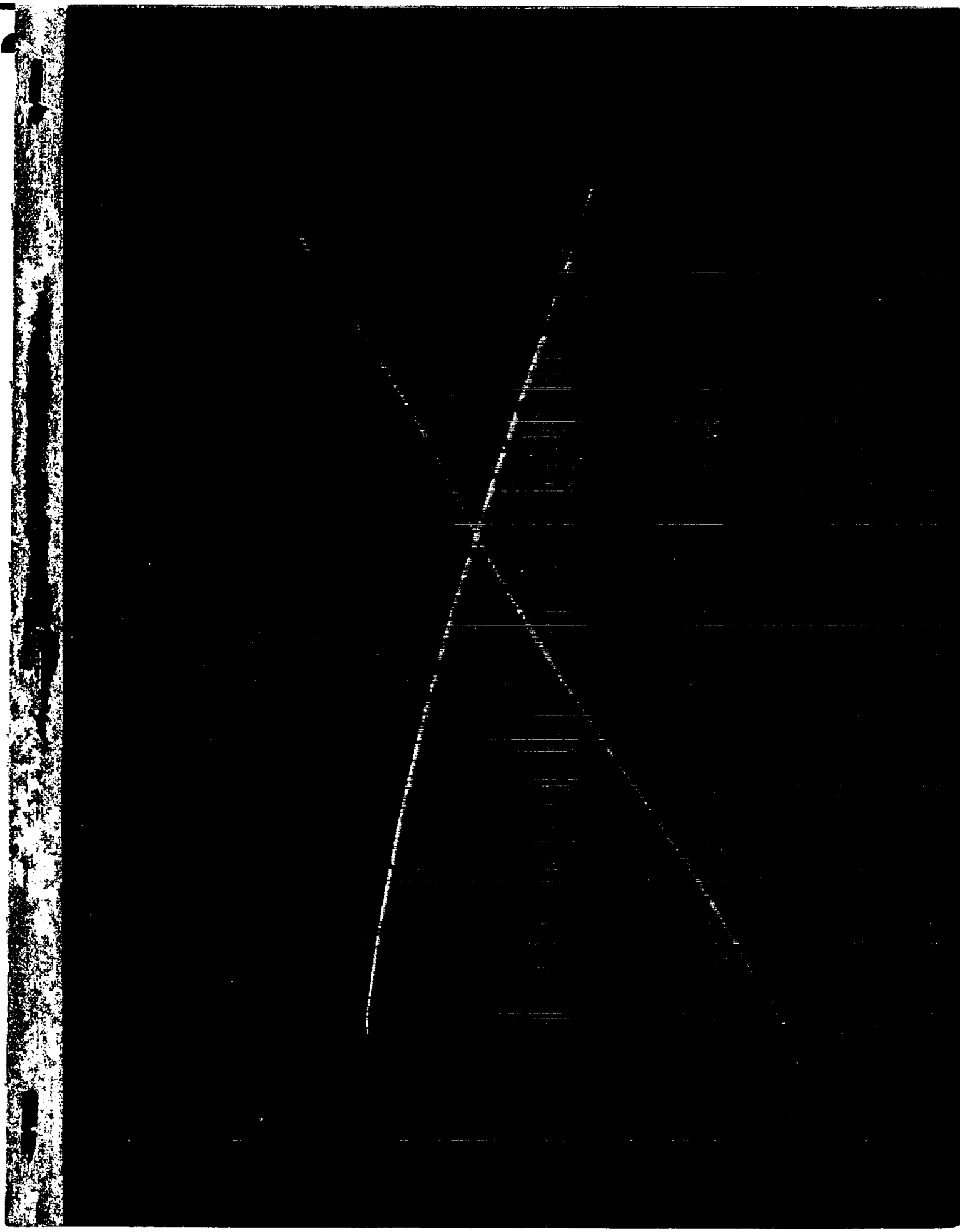

NASA CR-72301
Aerotherm Report No.67-15
Aerotherm Copy No. _____

FINAL REPORT

EXPERIMENTAL AND THEORETICAL ANALYSIS OF ABLATIVE MATERIAL RESPONSE IN A LIQUID-PROPELLANT ROCKET ENGINE

by

Roald A. Rindal
Kimble J. Clark
Carl B. Moyer
Donald T. Flood

prepared for

NATIONAL AERONAUTICS AND SPACE ADMINISTRATION

September 1, 1967

CONTRACT NAS3-7945

Technical Management
NASA Lewis Research Center
Cleveland, Ohio
Liquid Rocket Technology Branch
Erwin A. Edelman

AEROTHERM CORPORATION

460 California Avenue, Palo Alto, California 94306 • Teletype (TWX): 415-492-9243

ABSTRACT

Ablative material performance in a nitrogen tetroxide-Aerozine rocket engine is investigated experimentally and theoretically. Ablation simulation experiments are conducted in an arc-plasma device designed to duplicate the primary aerothermochemical parameters. Computerized computational techniques are developed for mathematically modeling material degradation phenomena giving consideration to equilibrium and kinetically controlled chemical reactions at the char surface, and to liquid-layer removal from silica-reinforced materials. These techniques are employed to correlate the ablation simulation data and to predict ablative material performance in a liquid-propellant rocket engine. Predicted surface recession for the rocket engine throat was significantly greater than measured for each of six ablative materials considered. Local oxidizer-to-fuel mixture ratio variations can have a significant effect upon predicted ablation and represent a logical explanation for lack of agreement between predicted and measured surface recession. An approach for investigating the effect of local mixture ratio variation on surface recession is recommended.

SUMMARY

A combined experimental-theoretical program has been conducted for the purpose of analyzing ablative material degradation phenomena in a liquid-propellant rocket engine environment. The following tasks were performed.

1. Simulation requirements for modeling ablative material degradation phenomena in a subscale test were established. The requisite parameters are:
   - o Elemental composition of the boundary layer edge gas ($\tilde{K}_{ke}$)
   - o Boundary layer heat transfer coefficient ($\rho_e U_e C_H$)
   - o The variation of nozzle area ratio in the streamwise direction at the test section ($A/A^* = f(x)$)
   - o An additional requirement is that the local pressure should be within a factor of 2 of that in the rocket engine.
2. Ablation data were acquired for six materials in a simulated nitrogen tetroxide-Aerozine environment utilizing an arc-plasma generator as the simulation device. The following list depicts the boundary conditions to which ablative materials were exposed.
   - o Total pressure - initially 100 psia decaying to 50 psia with increasing throat erosion
   - o Total temperature - after an 8 second starting transient the total temperature varied between 5,600 and 6,000°R. The corresponding total temperature for the rocket engine is 5,540°R.
   - o Gas stream chemical composition - the elemental composition was within two percent of that for a N_2O_4 - N_2H_4/UDMH rocket engine with an oxidizer-to-fuel mass ratio of 2.0.
   - o Heat transfer coefficient - the ratio of measured heat transfer coefficient to that predicted with the simplified Bartz equation ranged from 0.326 with a transient calorimeter to 0.454 with a steady state calorimeter.
3. Existing computational schemes, based upon the assumptions of chemical equilibrium at the ablating surface and no mechanical removal, were modified to include (1) a more realistic model for representing the thermal conductivity of partially degraded organic reinforced materials, (2) provision for considering kinetically controlled oxidation of a carbonaceous char by H_2O, CO_2, and O_2, and for considering kinetics of the homogeneous water-gas shift reaction, and (3) a mathematical model for considering kinetically controlled reactions between carbon and silica reinforcement fibers

in the char layer. The mathematical treatment includes consideration of all associated energy and mass-transfer events and enables considering liquid-layer removal phenomena within the framework of a simplified phenomenological model.

4. An extensive data correlation effort was conducted in order to verify the applicability of the modified computational schemes. The correlations consisted of utilizing the theoretical techniques and the data to establish the most probable values of several undefined coefficients required for theoretical evaluation. The undefined coefficients relate to, (1) thermal conductivity of the virgin, char, and partially degraded material, (2) kinetic coefficients which control the rate of surface (char) oxidation, and (3) specific criteria included in the semi-empirical liquid-layer removal model. No attempt was made to construct a phenomenological model to represent char spallation. Surface recession for 2 of the 6 materials considered (nylon-phenolic and asbestos-phenolic) is believed to be controlled by mechanical failure of the char layer, and, as such, a major part of the correlation effort was directed toward the other four materials (silica-phenolic, graphite-phenolic, carbon-phenolic, and silica-phenyl silane + Buna "N").

   The correlation effort was conducted in two phases. Phase 1 consisted of specifying measured surface temperature and recession histories as boundary conditions in the CMA (Charring Material Ablation) program in order to establish an acceptable thermal conductivity model for the subsurface solutions. Thermal conductivity coefficients were varied in an iterative manner until agreement between predicted and measured subsurface thermocouple histories was achieved. It is encouraging to note that the final subsurface correlation also resulted in good agreement between measured and predicted degradation depths. Phase 2 of the data correlation effort consisted of a series of predictions of the overall ablative material performance utilizing the subsurface solution demonstrated as adequate in Phase 1. The Phase 2 correlations consisted of predicting the surface temperature and recession histories and varying surface interaction coefficients in an iterative manner until reasonable agreement was achieved between prediction and data.

5. Predictions of the ablative material performance in a rocket nozzle for each of the six materials were performed and compared to measured ablation data from rocket engine firings. The predicted surface recession rate is generally from 2 to 3 times greater than that measured. Probable causes of the discrepancy are considered

and it is concluded that either one, or a combination of two effects are primarily responsible, (1) an ill-defined heat transfer coefficient, and (2) a poorly defined boundary layer edge thermodynamic state resulting from a local off-optimum mixture ratio.

6. Recommendations are offered for investigating the effect of local mixture ratio variations upon ablative material performance in a liquid propellant rocket engine.

TABLE OF CONTENTS

TABLE OF CONTENTS (concluded)

LIST OF FIGURES

LIST OF FIGURES (continued)

LIST OF FIGURES (concluded)

LIST OF TABLES

LIST OF SYMBOLS

A	cross-sectional area, also, pre-exponential constant for silica carbon reactions
B'	$B'_c + B'_g = (\rho_v)_w/(\rho_e U_e C_M)$, the normalized blowing rate parameter
B'_c	$\dot{m}_c/\rho_e U_e C_M$, normalized char mass recession rate
B'_g	$\dot{m}_g/\rho_e U_e C_M$, normalized pyrolysis gas blowing rate
C_{ki}	number of atoms of element k in species i
$\overline{C}_p$	average specific heat
C_N	nozzle discharge coefficient
C_H	Stanton number for heat transfer
C_M	Stanton number for mass transfer
D	nozzle diameter
$\overline{D}$	a mixture property which depends upon composition, pressure, and temperature
$\mathcal{D}_{ij}$	binary coefficient for diffusion of species i into j
ΔE	activation energy
F_i	diffusion factor for species i defined by empirical relation for correlating binary diffusion coefficient data, $\mathcal{D}_{ij} = \overline{D}/F_i F_j$
H_o	total enthalpy, chemical + thermal
H_r	recovery enthalpy, taken equal to total enthalpy for low Mach number flow considered herein
H_{inj}	total enthalpy of gases injected to simulator
H_{prop}	total enthalpy of propellant
ΔH_{arc}	net energy added to gases in arc-plasma generator
h	heat transfer coefficient based on temperature driving potential
h_i	total enthalpy (thermal + chemical) of component i
I	total number of i species
$\tilde{j}_{kw}$	the normal diffusional mass flux of element k at the wall
K	total number of k elements

LIST OF SYMBOLS (continued)

K_i	gas phase mass fraction of species i
$\tilde{K}_k$	gas phase mass fraction of element k independent of molecular configuration
$\tilde{K}_{kg}, \tilde{K}_{kc}$	mass of element k per unit mass of pyrolysis gas and char, respectively
$K_{p,n}$	equilibrium constant for n^{th} reaction
k	thermal conductivity
$k_{f,n}$	forward rate coefficient for n^{th} chemical reaction (Eq. (15))
k_n	pre-exponential constant for n^{th} reaction (Eq. (15))
Le	Lewis number
M_i	molecular weight of species i
M_k	atomic weight of element k
m_i	mass of component i
$\dot{m}$	total surface mass recession rate per unit area
$\dot{m}_i$	mass consumption rate of species i per unit area
$\dot{m}_c, \dot{m}_g, \dot{m}_r$,	mass removal rate of char, pyrolysis gas, and condensed phase (liquid or solid), respectively
$\dot{m}_{thermo-chemical}$, $\dot{m}_{liquid}$, $\dot{m}_{spallation}$	that portion of mass loss rate resulting from surface thermo-chemical erosion, liquid layer removal, and char spallation respectively
n_n	reaction order of n^{th} reaction
P	pressure
P_{iw}	partial pressure of species i adjacent to the wall
q_w	surface energy flux per unit area
R	gas constant
$\dot{S}$	linear surface recession rate
T	temperature
X	mass fraction of undecomposed material, X = 1 for virgin material, X = 0 for pure char

x	streamwise coordinate, or normal coordinate fixed to receding surface (Fig. 37)
y	coordinate normal to the surface
$\tilde{Z}^*_{ke}$	driving potential for mass transfer in the multicomponent boundary layer defined by $\tilde{J}_{kw} = \rho_e U_e C_M (\tilde{Z}^*_{kw} - \tilde{Z}^*_{ke})$

GREEK

δ	eroded depth
γ	a fractional weighting factor representing the relative mass transfer by diffusional and convective processes
θ	time
ρ	density
$\rho_e U_e$	boundary layer edge mass velocity
$(\rho v)_w$	gas phase mass velocity normal to the heated (char) surface
τ	total firing time
τ_w	aerodynamic shear stress at the surface

SUBSCRIPTS

A	pertaining to arc-plasma generator simulation device
c	pertaining to char
e	evaluated at boundary layer edge
g	pertaining to pyrolysis gas
i	pertaining to species i
k	pertaining to element k
p	pertaining to virgin material (plastic)
R	pertaining to rocket engine
w	evaluated at heated surface

SUPERSCRIPT

*	evaluated at nozzle throat, also signifies a condensed phase

EXPERIMENTAL AND THEORETICAL ANALYSIS OF ABLATIVE MATERIAL RESPONSE IN A LIQUID-PROPELLANT ROCKET ENGINE

SECTION 1

INTRODUCTION

Ablative materials provide a low cost, reliable means of insulating rocket engine components from high temperature, corrosive combustion product environments. Specification of ablative material composition and thickness for adequate thermal protection with minimum weight requires that consideration be given to a number of high temperature thermal, chemical, and mechanical interactions between the ablative material and the environment to which it is exposed. The phenomena requiring quantitative specification include 1) boundary layer transfer rates of energy and chemical species to and from the ablating surface, 2) the rates of reactions between the combustion products, the char surface, and organic polymer degradation products, 3) the rate at which inorganic reinforcement fibers melt and are removed from the surface, 4) fragmentation and departure of portions of the char layer from the surface, and 5) energy, mass transfer, and chemical degradation events below the ablating surface. Sufficient quantitative information to specify the magnitude of these events does not presently exist for the numerous materials and propellant environments of interest.

An investigation has been conducted to develop experimental and analytical procedures for characterizing ablative material response in liquid-propellant-rocket nozzles and is described herein. Ablation data were acquired for six materials in a simulated nitrogen tetroxide-Aerozine environment utilizing the arc-plasma rocket-environment simulation technique described in Reference 1. Existing computational schemes (Ref. 1), based upon the assumption of chemical equilibrium at the ablating surface and no mechanical removal, were modified to include consideration of certain kinetically controlled heterogeneous reactions and a phenomenological model for representing removal of liquid silica from the ablating surface. The modified computational schemes were employed to correlate the arc-plasma data and to predict the ablative material response in a rocket engine. The experimental investigations and ablation data are presented first, in Section 2, and are followed, in Section 3, by a description of the modified computational schemes for predicting ablative material behavior. Section 4 presents comparisons between measured ablation data from the arc-plasma simulator and that predicted by the computational schemes both before and after modification. Comparisons between predicted and measured ablation data for a series of rocket engine firings are presented in Section 5, and are followed, in Section 6, by a summary of conclusions and recommendations.

SECTION 2

EXPERIMENTAL SIMULATION OF ROCKET-ENGINE ABLATIVE MATERIAL PHENOMENA

An experimental program was conducted to test six ablative materials in a simulated nitrogen tetroxide-aerozine rocket engine environment. Ablative material testing was preceded by a calibration phase which included accurate measurement of the primary simulation parameters. The ablative material tests were accompanied by measurement of the primary material response parameters of interest. The basic experimental approach is described first, in Section 2.1, and is followed, in Section 2.2 by a presentation of test results.

2.1 EXPERIMENTAL APPROACH

The basic experimental approach consists of introducing appropriate gas mixtures to an arc-plasma generator where they are heated and subsequently expanded out through an ablative test nozzle. The requirements of simulating ablative material degradation phenomena are presented and discussed first, in Section 2.1.1. The specific technique employed to duplicate the appropriate simulation parameters is described next, in Section 2.1.2, and is followed by a description of the test apparatus and test procedure in Sections 2.1.3 and 2.1.4 respectively.

2.1.1 Simulation Requirements

The list of parameters required to simulate ablative material degradation phenomena is obtained by considering previous analysis directed toward mathematical characterization of thermochemical ablation, liquid layer removal, and char spallation. A more detailed investigation of certain of these phenomena as relates to analysis of the ablation data is presented subsequently, in Section 3. At this point it is desired to consider the analysis only to the extent required to identify the parameters which control each material removal mechanism.

The analyses of thermochemical surface recession in the chemical equilibrium and kinetically controlled regimes are considered in References 2 and 3 respectively. From the analyses presented in the references it is possible to formulate a list of parameters which must be duplicated in order to simulate surface thermochemical erosion:

1. Chemical elemental composition of the free stream gas ($\tilde{K}_{ke}$)
2. Total enthalpy of the free stream gas (H_o).
3. Boundary layer heat and mass transfer coefficients ($\rho_e U_e C_H$ and $\rho_e U_e C_M$)
4. Surface temperature (T_w)
5. Local pressure (P_e)

The first three parameters govern the reactivity of the chemical species approaching the surface, the rate at which chemically reactive species are transported to the surface, and the heat-transfer rate. It is reasonable to expect that duplication of the first three parameters will result in duplication of the fourth parameter (surface temperature) provided we ignore transient effects[1], so we need not include surface temperature as a required simulation parameter provided the first three parameters are duplicated. The fifth parameter (pressure) is included in the above list because of its effect upon boundary-layer transport phenomena, chemical equilibrium composition, and heterogeneous chemical kinetics at the ablating surface. As long as the boundary-layer transfer coefficients are duplicated, only the effect of pressure upon chemical equilibrium and chemical kinetics need be considered to establish its importance as a simulation parameter. If chemical equilibrium is achieved, the chemical ablation rate will not change substantially for a chamber pressure change of a factor of 2 or 3, provided the first three items above are held fixed. When chemical kinetics are controlling the primary surface erosion reactions, the effect of pressure on the ablation rate depends on the reaction order of the primary reactions. For high-temperature, heterogeneous reactions, the reaction order is normally between zero and unity. Perhaps the most thoroughly documented reaction of this nature is for the oxidation of graphite by molecular oxygen. Chemical kinetic data for this reaction are best correlated by a reaction order of one half, (Ref. 3) and, as such, the chemical erosion rate will depend on the square root of pressure when this is the primary reaction. It is concluded that duplication of pressure is not required provided it does not differ by more than a factor of 2 between rocket engine and simulation test. It is noted that in a subscale simulation test it is not possible to duplicate both the pressure and heat-transfer coefficient ($\rho_e U_e C_H$) since:

$$\rho_e U_e C_H \propto \frac{P^{.8}}{D^{.2}}$$

As a result, a reduced nozzle diameter (D) must be accompanied by a reduced pressure (P) if the heat transfer coefficient is to be duplicated. The heat transfer coefficient is usually more important in controlling ablation than pressure, and for this reason it is believed appropriate to sacrifice duplication of pressure (as long as it is within a factor of 2 or so) in order to retain duplication of heat transfer coefficient. Based upon the above

[1] Transient effects may be important for a significant part of the total test time, and must be considered in subsequent analysis of ablation data. These effects are ignored here only for the purpose of constructing a list of simulation parameters.

arguments the primary list of simulation parameters for investigating thermochemical events is taken to be represented by the first three parameters on the above list, composition ($\tilde{K}_{ke}$), enthalpy (H_o), and transfer coefficient ($\rho_e U_e C_H$). Functionally, we may express the thermochemical ablation rate as:

$$\dot{m}_{thermochem} = f\ (\tilde{K}_{ke},\ H_o, \rho_e U_e C_H) \qquad (1)$$

The removal of a liquid melt layer from the surface may be an important, if not dominant, mechanism for the ablative performance of certain inorganic reinforced composite materials. Organic materials reinforced with fiberglas or quartz cloth may or may not have their surface characterized by a flowing liquid layer, depending upon the relative amount of silica in the composite material. When the silica content is low, there is more than sufficient carbon to reduce all of the silica; for high silica-content materials, however, all of the carbon can be oxidized, before the silica is consumed, resulting in excess silica at the surface in the form of a liquid layer. It has been demonstrated experimentally that silica-reinforced organic materials having less than approximately 50-percent glass are not characterized by a liquid-melt layer (e.g., the air-arc experimental data by McAllister, et al., Ref. 4). This has also been predicted theoretically (Ref. 1) for a number of liquid-propellant rocket-engine environments.

Solution of the equations governing heat and mass transfer in a melting material has been the subject of numerous investigations (Refs. 5 through 10 e.g.). The differential equations containing the terms appropriate to ablating entry vehicles having a liquid layer are well established, solutions have been generated, and, in fact, correlations with test results have generally been satisfactory. Very little work has been done with respect to characterizing liquid-layer flow in rocket nozzles and, as such, analyses directed toward the reentry problem are relied upon here to provide the theoretical basis of liquid-layer flow phenomena. Almost all of the liquid-layer analyses for the case of reentry are based on the assumption that the liquid layer is thin and continuous, which results in a great simplification in the governing equations. The thin-liquid-layer assumption allows the momentum equation in the direction normal to the surface to be neglected. Removal of the thin-liquid-layer assumption from the analysis of the liquid layer requires that consideration be given to the onset of surface instability and subsequent droplet formation and removal. Two analyses do give some consideration to this phenomenon. Anliker and Beam (Ref. 6) present results of an inviscid solution which indicate the onset of liquid-layer instabilities on the surface of cylinders and spheres. An analysis presented by Feldman (Ref.7), which includes viscous effects in the liquid layer, results in the conclusion that the liquid surface on an entering vehicle may form instabilities

resulting in longitudinal liquid rivulets along the surface. From photographic observation of silica-phenolic degradation during a rocket-engine firing it appears that a thin liquid layer does exist, but that droplets form and flow at a greater velocity than the liquid layer. Based upon this observation one may conclude that parameters governing droplet size, velocity, and shape should be included in constructing a proper list of simulation parameters. Indeed such a requirement rapidly leads to the conclusion that simulation of liquid removal may be accomplished only in a full scale rocket test. Because of the current lack of even semi-rigorous theories to characterize droplet formation and removal under liquid rocket conditions, it is believed most expedient to retain the thin-liquid-layer approximation in establishing a list of parameters appropriate to simulating this surface removal mechanism. Considering the analysis of reference 5, for example, it may be shown that the primary parameters affecting liquid removal at a point are:

1. The streamwise derivative of aerodynamic surface shear stress, $d\tau_w/dx$.
2. The second derivative of pressure in the streamwise direction, dP^2/dx^2.
3. The temperature distribution through the liquid layer, i.e. T_w and $T(y)$.

As rationalized earlier, for thermochemical simulation, it would seem that duplication of free stream gas composition, heat transfer coefficient, and stagnation enthalpy would result in reasonable duplication of surface temperature. It would seem that duplication of temperature distribution through the liquid layer would also be approximately achieved. For simulation purposes, it appears reasonable to replace temperature and temperature distribution in the above list with parameters appropriate to simulating thermochemical ablation (Relation 1). Simulation of liquid layer removal phenomena may then be expressed as follows:

$$\dot{m}_{liquid} = f\left(\frac{d\tau_w}{dx}, \frac{dP^2}{dx^2}, \tilde{K}_{ke}, H_o, \rho_e U_e C_H\right) \qquad (2)$$

The analysis of char layer fragmentation presented in Reference 11 is considered appropriate for establishing the primary parameters affecting char spallation. Although the analysis presented in the reference is directed toward a particular material (carbon-phenolic) in a particular environment (earth-entry of a high performance vehicle) it is expected that the primary contributors to char spallation identified therein are appropriate to rocket nozzle performance as well. The predominant mechanisms may be simply stated to depend upon the following parameters.

1. Size and shape
2. Temperature level and distribution
3. Pressure gradient along the surface, dp/dx
4. Pressure gradient through the char layer, dp/dy
5. Aerodynamic Shear Stress, τ_w

The first two parameters establish the state of thermal stress in the char layer. As indicated in the reference the function of the last three parameters is primarily to cause the failed pieces to be removed from the char matrix. For char layers that are less permeable to pyrolysis gas flow than the carbon-phenolic char considered in Reference 11, however, the pressure gradient normal to the surface $\frac{dp}{dy}$ can give rise to significant stress levels relative to thermal stress (see the e.g. Ref.12). As such, it is believed that the normal pressure gradient, dp/dy (or more precisely, pressure distribution through the char layer) should be duplicated if char spallation phenomena are to be simulated. The necessity of duplicating aerodynamic shear stress, τ_w , and streamwise pressure gradient dp/dx, may not be stated in general. Their effects are believed to be minor relative to thermal stress and normal pressure gradient; however, as will be shown subsequently, they will be nearly duplicated in the tests under consideration, and as such, it is not necessary to evaluate their importance at this point.

Based upon the above discussion the functional dependence of char layer mechanical failure may be written as follows:

$$\dot{m}_{spallation} = f\ (\text{size, shape, } \tilde{K}_{ke}, H_o, \rho_e U_e C_H, dP/dy, dp/dx, \tau_w) \qquad (3)$$

Simulation of the ablation process in general would require duplication of the parameters appropriate to simulating mass removal resulting from thermochemical action, liquid layer removal, and char spallation, that is:

$$\dot{m} = \dot{m}_{thermochem} + \dot{m}_{liquid} + \dot{m}_{spallation}$$

The parameters appropriate to modeling each of these mechanisms are embodied in Relations 1 through 3. Considering the above in conjunction with Relations 1 through 3 results in a list of parameters which should be duplicated to simulate ablative material degradation.

$$\dot{m} = f\ (\text{size, shape, } \tilde{K}_{ke}, H_o, \rho_e U_e C_H, dp/dy, dp/dx, d^2P/dx^2, \tau_w, d\tau_w / d\,x) \qquad (4)$$

It is apparent from the above list of requisite simulation parameters that further compromises must be made to rationalize the existence of a meaningful sub scale ablative material test. The compromises to be made and appropriate comments are given here.

Size and Shape Will Not be Duplicated - Failure to duplicate size and shape will result in failure to simulate char spallation phenomena completely, however, because char thickness and temperature distribution will be approximately duplicated it would seem that the results of a subscale test should provide a relative indicator of the char's ability to remain intact. As indicated earlier, liquid layer removal phenomena will also not be duplicated in a subscale test, however, liquid layer removal can be modeled at a point from one-dimensional considerations provided the derivatives of pressure gradient and aerodynamic shear are duplicated. Duplication of size and shape is not required to model thermochemical events provided the other parameters in Relation (1) are duplicated.

Boundary Layer Edge Gas Elemental Composition - $\tilde{K}_{ke}$ - Boundary layer gas composition will be duplicated. The specific approach to achieve duplication is presented subsequently, in Section 2.1.2

Total Enthalpy (H_o) - Total enthalpy will be duplicated

Heat transfer Coefficient ($\rho_e U_e C_H$) - Boundary layer heat transfer coefficient will be duplicated.

Normal Pressure Gradient (dP/dy) - The pressure distribution through the char layer results primarily from viscous losses as the pyrolysis gases percolate through the char layer. Duplication of $\tilde{K}_{ke}$, H_o and $\rho_e U_e C_H$ should result in approximate duplication of the pyrolysis gas flow rate, char structure, char temperature distribution, and char layer thickness. Transient effects and different heat conduction geometries will cause some difference between normal pressure distributions in the subscale and full scale test, but these differences are believed of secondary importance. It is concluded that the normal pressure distribution (dP/dy) need not be listed as a required simulation parameter provided that $\tilde{K}_{ke}$, H_o, and $\rho_e U_e C_H$ are duplicated.

Flow Field Quantities (dP/dx, τ_w, d^2P/dx^2, and $d\tau_w/dx$) - As evidenced by Relations (2) and (3) the first two quantities may be active in controlling char spallation whereas the second two influence liquid layer removal. It is recognized that for complete simulation of liquid layer removal at a point it would be necessary to duplicate the streamwise integrals of these quantities upstream of the point, however duplication of the streamwise integrals may be accomplished only by duplicating the complete nozzle geometry and this cannot be done in a subscale test. It is possible to rationalize approximate duplication of the above quantities in the throat region of a convergent-divergent

nozzle in a subscale test as follows. Assuming one dimensional isentropic flow in the nozzle, and requiring that gas composition, total enthalpy, and chamber pressure be approximately the same in subscale and full scale tests, it is noted that full-scale throat pressure and aerodynamic shear stress will be approximately duplicated in the subscale nozzle throat. Also, for both full and subscale nozzles the pressure and shear stress in the vicinity of the throat may be expressed as a function of local area ratio alone:

$$P = f_1 \ (A^*/A) \qquad \text{and} \qquad \tau_w = f_2 \ (A^*/A)$$

Since the pressure and shear stress may both be expressed as functions of (A^*/A) alone, it is rationalized that their streamwise derivatives will be the same in full- and subscale tests if A^*/A is the same function of x for each nozzle. This rationalization is admittedly crude, but believed appropriate in the light of earlier mentioned compromises which must be made in a subscale test. It is therefore believed reasonable to replace the quantities dP/dx, τ_w, d^2P/dx^2, and $d\tau_w/dx$, in the simulation Relation (4) with the requirement that $(A/A^*) = f\ (x)$ be duplicated in the nozzle throat region.

A reduced set of requisite simulation parameters results from substituting the conclusions of the above arguments into Relation (4)

$$\dot{m} = f\ (\tilde{K}_{ke},\ H_o,\ \rho_e U_e C_H,\ A/A^*\ (x)) \qquad (5)$$

The above list of parameters may be considered adequate provided the simulation test pressure does not differ by more than a factor of 2 or so from the pressure in the rocket engine.

Because of the rather numerous compromises required to rationalize Relation (5) as adequate for simulating ablative material response it is apparent that some means of interpreting the experimental results and relating them to anticipated performance in the rocket engine is necessary. Relation (5) is believed to contain the most important parameters controlling ablative material response in a liquid propellant rocket engine, and, as such, experimental data acquired while maintaining these parameters near their levels in the rocket engine should provide quantitative information on the fundamental mechanisms controlling ablative material response.

The experimental approach for duplicating the parameters in Relation 5 and the ablation data acquired with this approach are presented in the remainder of this section and are followed, in subsequent sections, by a description of improved theoretical models for representing various material degration mechanisms, and by comparisons of predictions to the measured data.

2.1.2 Simulation Technique

The parameters to be duplicated for a meaningful ablative material test have been identified. In this section, a specific technique is described for achieving duplication of the requisite simulation parameters for a rocket engine operating on N_2O_4 - N_2H_4/UDMH rocket propellant with an oxidizer - to - fuel (O/F) ratio of 2.0 a nominal chamber pressure of 100 psia, and having a throat diameter of 1.2 inch. Duplication of these parameters is achieved by introducing a specially tailored gas mixture to an arc-plasma generator, dissipating the appropriate amount of arc-energy to increase the gas total enthalpy to correspond to that in the rocket engine, and then expanding this high temperature gas mixture through an ablative material test nozzle. Each of the parameters is listed and the means of achieving duplication are given here.

Simulation gas elemental composition ($\tilde{K}_{ke}$)

The simulation gases selected for a particular propellant environment are established by considering the chemical composition of the propellant. The quantity of each chemical element in the simulation gas mixture is required to equal that in the propellant. For N_2O_4 - N_2H_4/UDMH propellant with an oxidizer-to-fuel mass ratio (O/F) of 2.0, the following chemical balance may be written between the propellant and the simulation gases:

$$0.725\ N_2O_4 + 0.520\ N_2H_4 + 0.277\ C_2N_2H_8 \rightarrow$$

$$\underbrace{1.522\ N_2 + 1.212\ H_2}_{\text{Mixture F}} + \underbrace{0.554\ CO_2 + 0.430\ O_2}_{\text{Mixture G}} + \underbrace{0.933\ H_2O}_{\text{Steam}}$$

The following mass fractions represent the simulation gas mixture

$$\left.\begin{aligned} K_{N_2} &= 0.4261 \\ K_{H_2} &= 0.0244 \end{aligned}\right\} \quad K_{\text{Mix F}} = 0.4504$$

$$\left.\begin{aligned} K_{CO_2} &= 0.2438 \\ K_{O_2} &= 0.1377 \end{aligned}\right\} \quad K_{\text{Mix G}} = 0.3815$$

$$K_{H_2O} = 0.168 \qquad K_{\text{Steam}} = 0.168$$

Mixtures F and G are premixed gas mixtures. Mixture F is employed as the arc-heated gas with mixture G and steam injected into the mixing plenum chamber downstream of the arc zone. Utilization of the above gas mixtures in the indicated proportions will yield duplication of the chemical elemental composition ($\tilde{K}_{ke}$) . Duplication of the molecular composition will also

result if the total enthalpy and pressure match those of the rocket engine being simulated.

Total Enthalpy (H_o)

The total enthalpy of the simulation gas mixture is obtained by arc heating the gas with the appropriate amount of electic energy. The amount of arc heating required is determined by considering the enthalpy of the propellant and the enthalpy of the simulation gas mixture. For the above gas mixture, and considering the temperatures at which the gases are injected, the sum of thermal and chemical enthalpy is

$$H_{inj} = -1895 \text{ Btu/lb}$$

Assuming that the propellant in the rocket engine is injected at room temperature ($298^{\circ}K$) its enthalpy is

$$H_{prop} = +105 \text{ Btu/lb}$$

The required arc-energy addition then becomes

$$\Delta H_{arc} = H_{prop} - H_{inj} = 2000 \text{ Btu/lb}$$

Utilization of the above simulation gas mixture with the indicated amount of arc heating results in complete duplication of the first two requisite simulation parameters, $\tilde{K}_{ke}$, and H_o.

Heat transfer coefficient ($\rho_e U_e C_H$)

The relationship between the heat-transfer coefficient in the simulation test and the rocket engine may be evaluated approximately by referring to the simplified Bartz Equation (Ref. 13). This equation is approximate, but it does give a relatively accurate indication of the change in heat-transfer coefficient with chamber pressure and throat diameter. Utilizing the simplified Bartz Equation and forming the ratio of heat-transfer coefficients in the arc (sub A) and rocket (sub R) yields:

$$\frac{(\rho_e U_e C_H)_A}{(\rho_e U_e C_H)_R} = \left(\frac{P_A}{P_R}\right)^{0.8} \left(\frac{D_R^*}{D_A^*}\right)^{0.2} \qquad (6)$$

where C_H is the Stanton number defined by:

$$q_w = \rho_e U_e C_H (H_r - H_w)$$

In order to duplicate the heat-transfer coefficient ($\rho_e U_e C_H$), the ratio in Equation (6) must equal unity. It is apparent that if the pressure is to be duplicated ($P_A = P_R$), then the throat diameter in the simulation test must equal that in the rocket as well ($D_A^* = D_R^*$). In an arc plasma generator, for a given pressure and enthalpy ($\triangle H_{arc}$), the throat diameter is limited by the available electrical power. Giving consideration to chamber pressures in the vicinity of 100 psia with typical propellants, the present Aerotherm constrictor arc unit is limited to throat diameters in the range of 0.3 to 0.5 inch. With this restriction on throat diameter, or for any subscale test, the simulation test pressure must be less than the actual case in order to duplicate the heat-transfer coefficient.

As discussed above in Section 2.1.1, duplication of the heat-and mass-transfer coefficients is of prime importance, while pressure duplication is of secondary importance. Based on this premise, it is reasonable to sacrifice pressure duplication in order to achieve heat-transfer-coefficient duplication. Duplication of the mass-transfer coefficient (C_M) will result directly if the heat-transfer coefficient is duplicated since

$$C_M = C_H \, Le^{2/3}$$

and the boundary-layer Lewis number will be the same in the simulation test and rocket engine.

Employing Equation (6), rocket-nozzle heat transfer coefficient simulation capabilities for the N_2O_4-N_2H_4/UDMH environment are shown in Figure 1. Shown in the figure are established operating points and lines of constant heat-transfer coefficient. The shaded region between the lines represents the range of rocket engine operation conditions for which duplication of throat heat transfer coefficient may be achieved in the simulation device. The operating points shown in Figure 1 are based on a throat diameter of 0.3 inch. It is noted that as ablation of the throat occurs the throat diameter will increase which will result in a drop in chamber pressure and heat transfer coefficient. The heat transfer coefficient decay in the simulation test is shown in Figure 2 where the ratio of arc-to-rocket heat transfer coefficient is shown as a function of simulation test throat diameter corresponding to a chamber pressure decay from 100 psia to 50 psia. The rocket heat transfer coefficient is based upon a 100 psia chamber pressure and 1.2 inch throat diameter. It is noted from the figure that the simulation test will initially have a heat transfer coefficient 30 percent greater than the rocket and it will be 40 percent less than the rocket heat transfer coefficient at test termination, so the average simulation test heat transfer coefficient is near that in the rocket engine to be simulated.

Area Ratio Variation $A/A^* = f(x)$

The last parameter to be simulated is nozzle area ratio variation in the throat region.

A variety of rocket-arc nozzle combinations was considered which will result in duplication of $A/A^* = f(x)$ in the nozzle throat region. Several of these are shown in Figure 3. In Figure 3c is shown a rocket nozzle contour previously employed for ablative material tests at NASA Lewis Research Center along with two arc-plasma test nozzle contours which would have the same $A^*/A = f(x)$ in Figures 3a and 3b. It is noted that the arc-nozzle configurations have very nearly tubular throats, and, as such, these contours are not particularly desirable for ablative material tests because of the uncertainty associated with a knowledge of the actual throat location during the test. On Figure 3g is shown an arc-nozzle having a 2 inch radius throat curvature and two corresponding rocket nozzles in Figures 3h and 3i. The rocket nozzles shown in Figure 3h and 3i have a relatively sharp curvature at the throat, and, as such, two dimensional heat conduction effects could produce difficulties in interpreting the ablation data. The nozzle configurations shown in Figures 3d through 3f represent a realistic compromise between those having a quite tubular throat for the arc-nozzle (Figs. 3a, 3b) and those having a very small radius of curvature for the rocket nozzle (Figs. 3h, 3i). A detailed drawing of the rocket and simulation test nozzles employed for the ablative material tests is shown in Figure 4 where it is noted that the area ratio is duplicated for a distance of 1/4 inch up and downstream of the nozzle throat.

2.1.3 Test Apparatus

The experimental device consists primarily of the arc-plasma generator to add energy to the gas stream; a plenum chamber in which the arc-heated and other simulation gases are introduced for mixing to achieve mechanical, thermal, and chemical equilibrium; a nozzle test section designed to provide well defined and repeatable boundary layer heat and mass-transfer coefficients; and a gas metering and control system. A schematic view of the simulation apparatus is shown in Figure 5. The plasma generator is a conventional air arc-heater modified to operate on special mixtures of gases including nitrogen, hydrogen, carbon dioxide, water (steam) and oxygen. The plasma generator is attached to a plenum chamber which has provisions for gas injection and is thermally controlled by high temperature ($275^{\circ}F$), high pressure (200 psig) cooling water. Temperature control of the plenum chamber wall is required to prevent condensation of the steam in the test gas. The cooling system employed is similar to that shown in Reference 1, with the exception of the addition of a heat exchanger to the closed loop cooling circuit. Previously the high temperature water was returned to the main cooling water storage tank causing an additional heat load on the system which eventually limited the daily operating cycle. A tube-and-shell/heat-

exchanger was added, reducing the temperature of the plenum chamber water before it was returned to the system. A schematic of the modified cooling loop is shown in Figure 6.

The gas metering and control system was the only portion of the apparatus to undergo major alteration relative to that described in Reference 1. Basically the system was changed to incorporate (1) faster response, (2) more accurate metering and recording of all gases including the inert gases for purging, (3) simplified operator control, and (4) increased system reliability and repeatability. The gas system is required to control and meter three separate sources: Mixture F, Mixture G, and steam. This is accomplished with remotely actuated solenoid valves and air operated throttling valves. A schematic of the system is shown in Figure 7. The air operated throttling valves control the mass rate of flow of both the arc heated and secondary gases. The solenoid valves are automatically sequenced to cease the N_2 purging flow and start the flow of the test gases. Likewise on shutdown the combustible gases are shut off and followed with an inert purge.

The test apparatus instrumentation for measuring heat transfer coefficient and ablative material response is described subsequently along with a presentation of the test data.

2.1.4 Test Procedure

The test procedure generally follows that employed in earlier simulation tests (Reference 1). The use of hydrogen containing gas mixtures in the arc chamber required special gas handling systems and pre- and post-test purging procedures to avoid combustible gas concentrations before and after the test. The test procedure is as follows (refer to Figure 7 for identification of valves):

1. The steam lines are preheated by circulation of steam through the bypass solenoid valves SV3 and operation of strip heaters between the valves and injection ports on the arc.
2. The plenum chamber is preheated with hot water.
3. A purge gas flow (N_2) is initiated through SV4F into the Mixture F injection systems and through SV4G through the Mixture G injection system. The purge flow rate is measured at the orifice meter M4 and balanced between the two systems by the hand valves downstream of SV4F and SV4G, respectively.
4. The Mix F and Mix G lines are pressurized to SV1 and SV2, respectively. The lines are bled of inert fill gases by the hand-operated vent valves for a prescribed time to insure the appropriate gases fill the lines up to a point very close to the arc heater.
5. With the purge flow at a prescribed rate, voltage is applied to the arc and it is ignited by a radio-frequency spark.
6. At arc ignition SV4F is closed and SV1 opened allowing Mix F to flow. The flow rate is manually increased to the proper setting by adjusting LV11.
7. After a 2-second delay, SV4G is closed and SV2 opened admitting Mix G to the system. Mix G is brought to full flow manually by LV22.

8. After a 3-second delay from arc ignition, steam is introduced by actuation of SV3A and B. No flow rate adjustment is made since the venting flow is set at prescribed test conditions.
9. With the introduction of all gases the power to the arc is set at a prescribed level by adjusting arc current.

The test is terminated by interrupting the electrical current to the arc which in turn returns all of the gas systems to their off and purge functions. Both the Mix F and Mix G systems are completely vented to the atmosphere and filled with N_2 prior to the next test.

The modified piping system provided simpler and more accurate control than had been used in the previous efforts. It was found necessary, however, to start the arc on N_2 at reduced flow to insure RF ignition. Attempts were made to start the arc at actual test flow rates on N_2 with immediate transfer to the hydrogen containing Mix F. In doing this it was found that the power supply had to be set for a very high voltage condition to sustain the arc when the Mix F flow started, yet the high voltage setting caused excessively high instantaneous current, often resulting in damage to the electrodes. More moderate power supply settings were unable to sustain the arc when the flow was transferred to Mix F. A compromise solution was achieved by starting at reduced flow and power conditions and rapidly increasing both to prescribed test settings after arc ignition. It was found that the mass flow rates could be brought to about 85 percent of the desired setting within 5 seconds and to full flow within about 7 to 8 seconds by this method.

2.2 TEST RESULTS

A number of tests were run to establish the test conditions and verify the means of measuring ablative material surface temperature histories. This was followed by testing six ablative material nozzles in the arc-plasma rocket environment simulator. A list of calibration and ablative material tests performed is shown in Table I where the test number, type of test, and test duration is given. The test conditions are presented first, in Section 2.2.1, and are followed, in Section 2.2.2, by a description of ablative material test results.

2.2.1 Test Conditions

The test conditions are established by considering (1) gas composition, (2) chamber pressure, (3) total enthalpy, and (4) heat transfer coefficient. The values of each of these parameters achieved during the test series are presented in the following 4 subsections.

2.2.1.1 Simulation Gas Composition

The elemental composition of the simulation gas is established by considering the flow rate of each gas mixture. Table II shows the flow rate of

each test gas and compares the resulting gas composition to the desired composition.

The maximum error in the composition of any one test gas is 2.5 percent. This is believed quite acceptable since it is noted that the actual rather than the desired gas composition will be employed in subsequent data correlation with the theoretical technique. As indicated above the actual flow rate of each gas mixture was pre-set at a fixed value for all tests, and, as such, the above table is representative of all simulation tests conducted.

2.2.1.2 Chamber Pressure

A nominal maximum chamber pressure of 100 psia was achieved during all tests. Chamber pressure decay resulted during all ablative material tests due to a gradually increasing throat flow area with time. Ablative material test durations were specified to correspond to that time when the chamber pressure had decayed to half its initial value, or about 50 psia. The chamber pressure history for each ablative material test is shown in Figures 8a through 8f. These pressure histories are employed subsequently, in Section 2.2.2.1, to infer the surface recession rate for each ablative material tested.

2.2.1.3 Enthalpy

The total arc-energy added to the test stream for all simulation tests was somewhat greater than required. The amount of arc-energy to be added to the simulation gas would ideally be 2000 Btu/lb. Actual arc-energy additions varied from 2200 to 2500 Btu/lb. This extra energy addition corresponds to total temperatures ranging from 200°F to 500°F greater than in the rocket engine. The histories of recovery enthalpy and temperature for the six ablative material tests are shown and compared to the corresponding values for the rocket engine in Figures 9a through 9f.

2.2.1.4 Heat Transfer Coefficient

The heat transfer coefficient at the throat of the ablative material test nozzles is evaluated by measuring the heat transfer rate to the throat section of each of two calorimeter nozzles having the same throat diameter as the ablative material nozzles. The two calorimeter nozzles, a steady state water cooled, and transient heat-sink type calorimeter are described in detail in Reference 1 and are shown schematically in Figures 10 and 11 respectively. Test results reported herein were obtained employing only one of the three water cooled throat segments shown in Figure 10, in order that the nozzle profiles for the steady state and transient calorimeters would be the same. The water-cooled calorimeter operates with a surface temperature somewhat below the steam saturation temperature at the H_2O partial pressure in the test gas stream, and, as such, some condensation of steam upon the calorimeter surface would be expected. Condensation upstream of the throat will produce a film cooling effect in the area of the throat which would tend to decrease

the measured heat transfer rate at the throat. On the other hand, condensation at the throat will increase heating to the throat region. It is not apparent a priori which of these two effects will dominate. The transient calorimeter should therefore yield results which are more representative of conditions experienced during ablative material tests.

The boundary layer heat transfer coefficient is determined by dividing the measured heat flux, q_w, by the enthalpy driving potential $(H_r - H_w)$, where H_r and H_w represent the enthalpy of the free-stream gas at recovery and wall temperature respectively.

$$\rho_e U_e C_H = \frac{q_w}{(H_r - H_w)}$$

The test results indicate that heat transfer coefficients measured with the steady state calorimeter are 42 percent of that predicted by the simplified Bartz equation (Ref. 13) and those measured with the transient calorimeter are 30 percent of that predicted by the simplified Bartz equation. Detailed results for each calorimeter are presented in the next two subsections.

2.2.1.4.1 Transient calorimeter

The transient (hot wall) calorimeter consists of a solid copper body with a short tubular throat section comprised of a thermally insulated copper segment. The calorimeter is essentially the same as that reported in Reference 1 except for the method of attaching thermocouples to the calorimeter segment. Previously (Reference 1) the thermocouples were spring loaded against the side of the calorimeter segment but an adequate thermal junction was not achieved. The technique employed for the present test series consists of peening the thermocouple junction into the calorimeter segment as shown in Figure 11.

The surface heat flux to the calorimeter throat section is backed out from the measured subsurface temperature histories utilizing a transient, axisymmetric conduction solution computer program. The program enables specification of the surface temperature history and solves for the surface heat flux as a function of time. Since the present technique results in subsurface rather than surface temperature histories, a certain amount of iteration must be done in order to prescribe a surface temperature history which results in predicted subsurface temperature histories corresponding to the measured data. Approximately 5 such iterations were required to match the temperature data for each of the four transient calorimeter tests performed (test numbers 423, 424, 432, 433, see Table I). The predicted temperature histories for the last iteration are shown and compared to measured subsurface temperature histories in Figures 12a through 12d. Measurement of the surface heat flux by this technique is remarkably accurate. A good feeling for its accuracy

was gained during the iteration process where it was found that predicted internal temperature histories which bracketed the measured data corresponded to surface heat flux variations of only 2 to 5 percent. It is thus concluded that the surface heat flux measurement by this technique is accurate to within 5 percent. The surface heat fluxes corresponding to the temperature histories shown in Figure 12 are shown in Figure 13.

Evaluation of the boundary layer heat transfer coefficient from the measured heat fluxes results from consideration of the free stream total pressure and total enthalpy histories. The measured total pressure histories for each of the four transient calorimeter tests are shown in Figure 14 and the corresponding recovery (total) enthalpies are shown in Figure 15. Nozzle flow coefficients, C_N, were also evaluated for each calorimeter test by performing equilibrium isentropic flow calculations corresponding to the measured gas flow rate, total pressure, total enthalpy, and known gas elemental composition. The calculated nozzle flow coefficient histories are shown in Figure 16 for each of the four transient calorimeter tests. These nozzle flow coefficients are utilized subsequently to represent the flow coefficients of the ablative nozzles when inferring the ablative material throat diameter history from the measured chamber pressure history. This is described subsequently in Section 2.2.2.1.

The heat transfer coefficient histories for each of the transient calorimeter tests were calculated from the following equation.

$$\rho_e U_e C_H = \frac{q_w}{H_r - H_w}$$

The heat flux, q_w, is taken from Figure 13, the recovery enthalpy, H_r is taken from Figure 15, and the wall enthalpy is taken as the gas equilibrium enthalpy at the wall temperature. The resulting heat transfer coefficients are shown in Figure 17. The measured heat transfer coefficients with the steady state calorimeter are presented in the following subsection, 2.2.1.4.2, which is followed, in Section 2.2.1.4.3, by a brief description of comparisons between the measured heat transfer coefficients with both calorimeters and those predicted by the simplified Bartz equation.

2.2.1.4.2 Steady state calorimeter

The steady state (cold wall) calorimeter shown in Figure 10 is a water-cooled copper nozzle composed of several water cooled seqments insulated from each other for measuring average local heat flux. Employing only one of the three throat segments shown in the Figure, the nozzle has the same contour as the transient calorimeter shown in Figure 11. Three cold wall calorimeter tests were performed and measurements were taken at one time during each test. Data was taken at a time represented by reasonably steady boundary

conditions which were, in turn, utilized to compute the boundary layer heat transfer coefficient from the measured throat heat flux. The results of the measurements are presented in Table III where the recovery enthalpy, total pressure, measured heat flux, and calculated heat transfer coefficient are shown for each of the three steady state calorimeter tests.

2.2.1.4.3 Comparison of measured to theoretical heat transfer coefficient

Calculations of the boundary layer heat transfer coefficient were performed for free stream conditions corresponding to those of the calorimeter tests described above. The calculations were performed with a boundary layer integration technique and according to the modified interpretation of the simplified Bartz equation as described in Appendix A of Reference 1. The measurements are compared to the Bartz values in Table IV for all seven calorimeter tests. It is noted that the average ratio of measured heat transfer coefficient to that predicted by the Bartz equation is 0.454 $\pm$ 0.7 percent and 0.326 $\pm$ 8 percent for the steady state and transient calorimeter tests respectively. The measurements are shown for a typical test in Figure 18 and are compared to the heat transfer coefficients predicted by each of two analytical techniques, the simplified Bartz equation as interpreted in Appendix A of Reference 1, and a numerical boundary layer integration technique described in Reference 14. The boundary layer integration technique is based upon the assumptions that the flat plate relation between surface heat flux and boundary layer energy thickness is valid for the turbulent boundary layer with pressure gradient as well. As shown in Figure 18, two boundary layer integration solutions were performed to evaluate the effect of boundary layer transition on nozzle throat heat flux. One integration was performed assuming the boundary layer is turbulent over the entire nozzle surface and the other integration includes a laminar boundary layer solution until a momentum thickness Reynolds number (Re_θ) of 250 is reached, at which point the boundary layer is assumed to undergo transition to fully turbulent flow. Based upon the results shown in Figure 18 it may be concluded that the point at which transition occurs has virtually no effect upon the nozzle throat heat transfer coefficient. It is interesting to note the rather wide disparity between the various predictions and data in Figure 18. The difference in predicted heat transfer coefficient between the Bartz equation and the boundary layer integration technique may be attributed primarily to the large difference between nozzle geometries considered in the two solutions. As such, the boundary layer integration result ($C_H = 0.546\ C_{H_{Bartz}}$) is believed more representative of the two predictions for the particular nozzle geometry of interest here. It is not too apparent, however, which of the two experimental measurements is more realistic relative to the intended utilization of the data. The calorimeter data is to be used for establishing

the boundary layer heat and mass transfer coefficients in the ablative material tests. As mentioned earlier, the coldwall calorimeter measurements may be accompanied by water condensation on the surface which could significantly affect the results obtained with this calorimeter. Water condensation will not occur during ablative material testing because of the high wall temperatures. On the other hand, the transient calorimeter results are accompanied by a significant surface temperature variation in the streamwise direction. Because the heat transfer rate increases in the streamwise direction to a maximum at the throat, it is reasonable to expect that the surface temperature will vary in a like manner. This surface temperature variation could result in a low throat heat flux relative to what would result if no surface temperature variation existed. The effects described have not been investigated quantatively herein, but, because of the better agreement between the steady state calorimeter results and the boundary layer integration results shown in Figure 18, the heat transfer coefficients specified for subsequent ablation calculations will be based upon the heat transfer coefficients measured with the cold wall calorimeter. It is assumed that $\rho_e U_e C_H = 0.454\ (\rho_e U_e C_H)_{Bartz}$.

Two values of the heat transfer coefficient are shown in Figure 18. One is based upon an enthalpy driving potential and the other upon a temperature driving potential. They are defined by the following equations.

$$\rho_e U_e C_H = \frac{q_w}{H_r - H_w} \qquad lb/ft^2\text{-sec}$$

$$h = \frac{q_w}{T_r - T_w} \qquad Btu/ft^2\text{-sec-}^\circ F$$

From the above the two heat transfer coefficients may be related as follows.

$$h = \rho_e U_e C_H \frac{H_r - H_w}{T_r - T_w} = \rho_e U_e C_H (\bar{C}_p)$$

In the reacting gas mixture $\bar{C}_p \neq$ constant so it is necessary to select a particular wall temperature in order to compare the two values numerically. The numerical values shown for the heat transfer coefficient, h, in Figure 18 are for a wall temperature of about 1000°F (800°K) for which $\bar{C}_p = 0.671$. The enthalpy-temperature relation corresponding to this specific heat is compared to the actual enthalpy-temperature relation in Figure 19. Examination of the figure and the above equation reveals that significant errors in the calculated heat flux will result if a constant heat transfer coefficient, h, is employed when there are significant wall temperature variations.

2.2.2 Ablation Data

In the previous section, those measurements which establish the environmental conditions were presented. In this section the measured material response resulting from subjecting each of six ablative material test nozzles

to these conditions is presented. The six materials tested are identified in Table I by test number, nozzle number, nozzle material and test duration. The primary material response measurements performed for each nozzle are the histories of surface recession, surface temperature, and subsurface temperature. These measurements are reported for all six nozzles in the following three subsections.

2.2.2.1 Surface Recession Rate

Evaluation of the surface recession rate is often accomplished by simply dividing the total eroded depth by the total test time. This is strictly correct only when most of the test is characterized by steady state ablation. As pointed out in Reference 1, the steady state assumption is often a poor one, and gross errors may be incurred when determining surface recession rate histories simply from pre- and post-test measurements. In the present test program an attempt has been made to assess the time variation of surface recession for each ablative material test by utilizing the following information: (1) the measured chamber pressure history, (2) the nozzle coefficient for the calorimeter tests to represent the nozzle coefficient of the ablative nozzle at the onset of ablation, and (3) the nozzle coefficient from the ablative material test at test termination as evaluated from the final measured flow area and the test conditions existing just prior to test termination. Pre-test throat diameters were accurately measured with a bore micrometer, and post-test average throat diameters were measured by integration of enlarged post-test throat shadowgraphs. The shadowgraphs were made by passing a beam of collimated light through the nozzle and out through a focusing lens in such a manner as to achieve a 10 to 1 amplification of the throat contour. The shadowgraphs (reduced size) for each of the six nozzles are shown in Figures 20a through 20f. Also shown in the figures is the circumferential location of the radial line along which the thermocouple probes were placed, and the measured distance below the final surface of the first thermocouple probe. It is important that this dimension be recorded because circumferential variations in erosion may result in local erosion adjacent to the thermocouple sensor which is significantly different from the average. Subsequent attempts to correlate measured subsurface temperature histories are therefore based upon the surface recession history at the thermocouple rather than upon the average recession history.

The distance of the thermocouple probes below the post-test surface was established by measurement after sawing the nozzle in half. The pre-test thermocouple depths were established by X-ray photography of each instrumented nozzle prior to testing. The X-ray photographs are presented subsequently in Section 2.2.2.3 (Subsurface temperature histories).

The measured surface recession histories (average and local at the

thermocouple location) for each of the six nozzles are shown in Figures 21a through 21f. Also shown in the figures are various predicted surface recession histories to be discussed subsequently in Section 4.3. For each test the following information is given.

1. Final average surface recession
2. Final surface recession at thermocouple location
3. Surface recession history based on final nozzle coefficient
4. Surface recession history based on linearly varying nozzle coefficient from final value to 0.925 taken as representative of the initial nozzle coefficient based upon the measured nozzle flow coefficients for the calorimeter nozzles (Fig. 16)

The average recession histories are based upon equilibrium isentropic flow calculations corresponding to the measured chamber conditions (P_o from Figures 8, and H_o from Figures 9), and the recession history at the thermocouple location is simply taken as the average recession times the ratio of local final to average final erosion.

$$\delta(\theta)_{\text{at thermocouple}} = \delta(\theta)_{\text{average}} \left(\frac{\delta_{\text{at thermocouple}}}{\delta_{\text{average}}} \right)_{\text{final}}$$

where $\delta(\theta)$ represents the surface erosion at any instant.

The relatively large departure of the measured nozzle coefficients from unity ($0.7 < C_N < 0.9$) is, at first sight, bothersome, however it is believed to result from the significant contribution to the total flow of the ablation products. Utilization of the low nozzle coefficients in calculating the surface recession is believed appropriate since the nozzle coefficient, in effect, will then account for not only irreversibilities in the flow, but the contribution of ablation material products as well.

2.2.2.2 Surface Temperature Measurement

Two methods of measuring ablative material surface temperature were considered, surface thermocouples, and an optical pyrometer. After performing several check-out tests to assess the relative accuracy of each method the optical pyrometer was selected as the most promising. The check-out tests for each measurement technique are described first and are followed by a presentation of measured surface temperature histories for the ablative material test nozzle.

2.2.2.2.1 Surface thermocouple

Consideration was given to the utility of instrumenting the ablative material test nozzles with NANMAC[2] surface temperature sensors. In particular, concern was exhibited with respect to the possibility that excessive erosion may occur in the vicinity of the surface temperature sensor and thereby

[2] The NANMAC Corporation, Needham Heights, Massachusetts

result in an irregular flow field in the nozzle throat test section. In order to establish the validity of this concern an ablative material test nozzle was sent to the NANMAC Corporation, instrumented with a surface temperature sensor, and tested in the arc-plasma facility in a high temperature, oxidizing environment. The purpose of the test was to establish the effect of the sensing element on the erosion profile and to ascertain the utility of this instrumentation technique for subsequent rocket environment simulation ablative material tests in the arc-plasma facility. A Schematic view of the thermocouple instrumentation is shown in Figure 22. Details of the test conditions and pre- and post-test nozzle throat contours are shown in Figure 23. Post test examination of the nozzle revealed uniform erosion of the nozzle throat at the sensing element; however a 1/8 inch-deep gouge appeared immediately downstream of the sensing element. Two views of the post-test, sectioned nozzle are shown in Figure 24 where the relative location and depth of the gouge may be clearly seen. Surface temperatures measured with the surface thermocouple and with an optical pyrometer[3] differed by more than 1000°R. The pyrometer indicated temperatures from 4800 to 5100°R whereas the surface temperature sensor registered temperatures ranging from 3400°R to 3800°R. The significant discrepancies between surface temperatures measured with the optical pyrometer and with the surface thermocouple were tentatively assigned to either or both of two phenomena, (1) oxidation of the tungsten-rhenium thermocouple junction could cause contamination which altered the voltage-temperature relation, and (2) conduction down the thermocouple ribbon (0.002 inch x 0.062 inch) could cause a local temperature depression.

On the basis of the test results it was concluded that the surface temperature sensors are of questionable utility for the particular tests being considered here and effects detrimental to the overall test objectives could result if they were employed.

2.2.2.2.2 Optical pyrometer

Consideration was given to the accuracy of the optical pyrometer surface temperature measurement technique. Two factors were considered, (1) the effect of radiation from ablation products and simulation gas products in the boundary layer, and (2) the error incurred in the optical measurement resulting from not knowing the ablating surface emittance. The effect of simulation gas and ablation product radiation on the optical temperature measurement was established by performing two tests. The optical pyrometer was focused on a calibrated, tungsten filament lamp in such a manner that it "looked through" the simulation gas test stream. The test set-up is shown in Figure 25. One test was run utilizing a water cooled nozzle so that only simulation gas products flowed between the pyrometer and the lamp filament,

[3] Infrared Industries "Thermodot"

and a second test was run with a graphite phenolic nozzle so that the gas stream between the lamp and pyrometer contained a mixture of simulation gas and ablation products. The results of the two tests are shown in Figure 26 where the observed lamp temperature is plotted as a function of actual lamp temperature. It is noted that the optically measured lamp temperature is not substantially affected by the presence of either gas mixture. A maximum error of about 6 percent results over the calibrated lamp temperature range ($2400^{\circ}R$ to $3600^{\circ}R$).

The accuracy with which the surface temperature may be measured considering surface emittance uncertainty was evaluated by considering the measurement instrument dependence on emittance and simply plotting temperature measurement error as a function of actual surface emittance with assumed surface emittance as a parameter for each of two indicated temperatures. The results are shown in Figures 27a for $T_w = 5000^{\circ}R$ and 27b for $T_w = 2000^{\circ}R$. These two temperatures bracket the range of interest here and errors for intermediate temperatures lie in between those for the extremes considered. The measuring instrument being considered here (Infrared Industries, Thermodot) senses thermal radiation at a wavelength of 0.8 microns so the emittance shown in Figure 27 should be taken as the emittance at 0.8 microns. Based upon measured surface emittances reported in Reference 15 for carbon, graphite, and zirconia, it appears that a value, $\epsilon = 0.9$ at 0.8 microns, is reasonable for both the carbonaceous and metal oxide surfaces of interest here. Referring to Figures 27, it is noted that if a value $\epsilon = 0.9$ is assumed, then the maximum temperature measurement error is 4.2 percent for $0.7 \leq \epsilon_{actual} \leq 1.0$, and 1.7 percent for $0.8 \leq \epsilon_{actual} \leq 1.0$. Based upon the measurements reported in Reference 15, and the results shown in Figures 26 and 27, it is concluded that the surface temperature measurement technique is accurate to within 8 percent for the range of surface temperatures and surface material compositions of interest here.

2.2.2.3 Measured Surface Temperature Histories

Surface temperature histories measured with the optical pyrometer for each of the ablative material rocket-engine simulation tests are shown in Figures 28a through 28F. Also shown in the figures are the measured and predicted subsurface temperatures which are discussed subsequently. The surface temperature histories in most all cases rise rapidly immediately after arc-ignition, pause briefly while the various gas mixtures are introduced, and rise again to a relatively steady value after steady flow conditions are achieved. Two anomalies exist in the data. The first is for nozzle NL-2 (Figure 28b) where the first subsurface thermocouple indicates a temperature in excess of the surface temperature. This resulted because the surface intercepted the thermocouple, exposing the thermocouple junction to the boundary layer gases. The second, somewhat anamalous result is noted in Figure 28e

for the nylon phenolic nozzle where the surface temperature is noted to oscillate continually throughout the test duration. This oscillalation is attributed to char spallation of a cyclic nature where the temperature oscillation corresponds to heat-up, and char fracture, exposing lower temperature material, followed by another heat-up. This conclusion is somewhat substantiated by post-test examination of the nozzle (Figure 32e) which reveals a very irregular surface characterized by large areas where the char layer has been broken away from the substrate.

Considering the rationalization offered above to be reasonable explanations of the apparent anomalies it is concluded that the measured surface temperature histories shown in Figures 28a through 28f are realistic.

2.2.2.4 Measured Subsurface Temperature Histories

Subsurface temperature histories were measured with fine wire thermocouple probes. A number of different thermocouple instrumentation techniques have been considered for obtaining internal temperature histories. The prime requirement in selecting a technique is that the sensor does not disturb the heat flow at the point of measurement. To satisfy this, the sensor should be as small as practicable and the thermocouple leads in the vicinity of the junction should be placed along an isotherm. This last consideration is particularly important in low-conductivity materials and is impressively illustrated in Reference 16. Also, the thermocouple junction must be in intimate contact with the material in order to minimize errors due to contact resistance. Another obvious requirement is that the location of the junction be precisely known.

Considering these requirements and the practical aspects of fabrication, the thermocouple installation scheme shown in Figure 29 was selected. A photograph of one of the thermocouple probes is presented in Figure 30. Three thermocouple ports 0.040-inch-diameter were drilled into the ablation nozzles at nominal depths of 0.15, 0.25, and 0.40 inch. The thermocouple probes employed are similar to those described in Reference 1 except the probe diameter was reduced to 0.03 inch with 0.003-inch thermocouple wire. Each nozzle was instrumented with two Chromel-Alumel probes and one tungsten-5 percent rhenium/tungsten-26 percent rhenium probe. The probes are inserted into the test nozzle so that they are tangent to an isotherm at their junction. The thermocouples are spring-loaded against the bottom of the thermocouple-probe hole to insure good contact of the thermocouple junction with the ablation material. Thermocouple locations are X-ray verified prior to testing. A photograph of an instrumented nozzle prepared for X-ray is shown in Figure 31. Pre-test X-ray photographs of all 6 test nozzles are shown in Figures 32a through 32f. Also shown in Figures 32 are the thermocouple depths measured

from the X-ray photographs.

A photograph taken of a typical simulation test is presented in Figure 33, and post-test sectioned views of all six ablative nozzles are shown in Figures 34a through 34f. Measured subsurface temperature histories for the six ablative nozzles are shown in Figures 28a through 28f. The data all appear reasonable except for thermocouple no. 1 in nozzle NL-2 (Fig. 28b) which was discussed previously. The actual location of the thermocouple junction after test termination may be noted by referring to the post-test sectioned view shown in Figure 34b. Careful examination reveals that the receding surface did not pass the thermocouple junction but it did reach the hole in which the thermocouple was inserted. This resulted in exposure of the thermocouple junction to the gas stream and thereby caused the excessive temperature rise shown in Figure 28b. Comparison of the size of two thermocouple ports that may be seen in the figure reveals that the partially consumed hole is larger which suggests that it has been slightly enlarged due to erosion by the gas stream.

No other apparent anomalies exist in the measured subsurface temperature data. It is concluded that the temperature histories shown in Figures 28a through 28f are reasonable with the one noted exception.

2.3 SUMMARY OF EXPERIMENTAL PROGRAM

The primary ablative material degradation mechanisms have been identified and the parameters which must be duplicated in order to simulate ablative material response in a liquid-propellant rocket engine were established. They are:

1. Elemental composition of the boundary layer edge gas ($\tilde{K}_{ke}$)
2. Total enthalpy (H_o)
3. Boundary layer heat transfer coefficient ($\rho_e U_e C_H$)
4. The variation of nozzle area ratio in the streamwise direction at the test Section ($A/A^* = f(x)$)
5. An additional requirement is that the local pressure should be within a factor of 2 of that in the rocket engine.

An experimental technique was described which enables satisfying the above simulation requirements in a sub-scale test utilizing an arc-plasma generator as the primary source of energy addition. This is accomplished by adding special gas mixtures to the arc-heater and controlling the electric power input to achieve duplication of gas total enthalpy.

A number of rocket-engine simulation tests have been performed utilizing an arc-plasma generator for the purpose of evaluating the performance of six different ablative materials in an N_2O_4 - N_2H_4/UDMH exhaust product environment. The ablative material tests were accompanied by a number of tests directed toward establishing quantitative definition of the pertinent boundary

conditions. The following list depicts the boundary conditions to which the ablative materials were exposed.

- Total pressure - initially 100 psia decaying to 50 psia with increasing throat erosion
- Total temperature - after an 8 second starting transient the total temperature varied between 5600 and 6000°R. The corresponding total temperature for the rocket engine is 5540°R.
- Gas stream chemical composition - the elemental composition was within two percent of that for a N_2O_4 - N_2H_4/UDMH rocket engine with an oxidizer-to-fuel mass ratio of 2.0.
- Heat transfer coefficient - the ratio of measured heat transfer coefficient to that predicted with the simplified Bartz equation ranged from 0.326 with a transient calorimeter to 0.454 with a steady state calorimeter.

The response of each of six ablative materials to the above boundary conditions was measured and presented. Measurements of surface recession, surface temperature, and internal temperature are presented as a function of time. The following table summarizes the ablative material test results.

Nozzle No.	Material	Test No.	Test Time (sec)	Ablated Depth (in)	Average Recession Rate (Mils/sec)	Comments
NL-1	Silica-Phenolic	427	35.4	0.0690	1.95	Liquid flow uniform erosion
NL-2	Graphite-Phenolic	426	48.2	0.0775	1.61	Uniform erosion
NL-3	Asbestos-Phenolic	430	15.2	0.0775	5.10	Some irregularities. Trace of liquid
NL-4	Carbon-Phenolic	431	29.0	0.0775	2.67	Uniform erosion
NL-5	Nylon-Phenolic	429	21.5	0.1300	6.05	Char fracture irregular erosion
NL-6	Silica-Phenyl Silane	428	25.8	0.0705	2.73	Some liquid flow, uniform erosion

The accuracy of measuring surface and subsurface temperature histories is believed adequate and the measured temperature histories are believed reasonable. Evaluation of the surface recession history, however, is subject to some question. Pre- and post-test measurements establish the total ablated depth but evaluation of the recession history which produced the observed total recession requires the use of nozzle flow coefficients which are not precisely known. In particular, it is difficult to establish precisely when

ablation begins. The reported recession results are based on linearly varying nozzle flow coefficients which are consistent with measurements corresponding to the pre- and post-test nozzle contour.

SECTION 3

IMPROVED COMPUTATIONAL SCHEMES

The utility of experimental ablation data such as presented in the previous section may be significantly enhanced if computational schemes are available for extrapolating the observed results to anticipated ablative material performance in a full scale rocket engine. Such an extrapolation may be accomplished by, (1) identifying the pertinent independent variables, (2) presuming theoretical relations between these variables and the ablative material response parameters of interest, (3) utilizing the presumed theoretical model to predict subscale test results, (4) modifying the theoretical model as necessary to make the predictions realistic in the light of the ablation data, and (5) after having established confidence in the theoretical model, to predict ablative material performance in the full scale rocket engine. Clearly, the success of such an approach is dependent upon how nearly the simulation parameters are duplicated in the sub-scale test and how realistic the theoretical model is. Efforts directed toward identifying and duplicating the pertinent simulation parameters were presented in the previous section. This section describes efforts directed toward the modification of computational schemes to include consideration of specific phenomena believed to be important in controlling the response of certain classes of ablation materials.

Two computer programs were modified. The CMA (Charring Material Ablation) program provides the in-depth response of a charring type material, and the EST (Equilibrium Surface Thermochemistry) program provides generalized boundary conditions for the CMA program within the constraints of chemical equilibrium at the ablating surface. Theoretical justification for the mathematical models embodied in these two programs is presented in References 1 and 2, details pertaining to program operation are presented in References 17, and 18, and a brief description of input-output options for the CMA program is presented herein as Appendix A.

Utilization of the CMA and EST programs to predict the ablative material response (recession rate and temperature histories) of the nozzles tested in the simulated rocket exhaust environment served to illustrate the inadequacy of certain assumptions in the programs for modeling the physical events associated with particular types of materials. Comparisons between data and predictions both with the modified and unmodified computer programs, are presented subsequently, in Section 4. Poor agreement between data and predictions with the unmodified programs in some cases provided motivation for re-examining the mathematical treatment of certain physical phenomena and postulating new models believed more consistant with the observed results. Specific restrictions embodied in the CMA and EST programs which required modification are listed here.

1. The thermal conductivity of partially degraded ablative materials is taken to be represented by a weighted average of the char and virgin material conductivity, whereas the thermal conductivity of the partially degraded material may, in some cases, be significantly less than that of either the char or virgin material. A phenomenological model for more realistically representing the thermal conductivity of of partially degraded materials has been built into the CMA program and is described in Section 3.1.

2. The EST program, which provides the generalized chemistry boundary condition for the CMA program, requires that chemical equilibrium be achieved between the surface and the gases adjacent to it, whereas, in some cases, it appears that equilibrium is not achieved. Specific reactions which may be kinetically controlled and which may significantly effect the ablation rate have been identified and modifications to the computer program to account for these kinetics have been performed. Details are presented in Section 3.2.

3. The CMA program represents subsurface ablative material degradation by a single overall reaction.

   Virgin Material $\rightarrow$ Char + Gas

   In the case of organic materials reinforced with inorganic oxides such as silica-phenolic, the char would consist of a mixture of silica fibers and a carbonaceous residue from polymer degradation. A certain amount of evidence exists to support the opinion that reactions between these fibers and the carbon in the char have a profound effect upon the ablative material response. The CMA program has been modified to include evaluation of reaction rates between silica fibers and carbon. The extent to which the reaction has proceeded provides information employed to evaluate the rate at which liquid silica is removed from the surface. The modified program is described in Section 3.3.

4. The CMA program does not include provision for realistic evaluation of char spallation phenomena. Char spallation is believed to be the primary surface recession mechanism for the nylon-phenolic and asbestos-phenolic materials tested and reported in Section 2. No modifications have been made to the program to account for char spallation.

3.1 THERMAL CONDUCTIVITY MODEL FOR PARTIALLY DEGRADED ORGANIC MATERIALS

An improved model for evaluating the thermal conductivity of partially degraded organic materials has been formulated and incorporated in the CMA program. This improvement consists of the introduction of a new equation to represent thermal conductivity of the composite material, i.e., the virgin

material which is partially degraded and not yet fully charred.

Previously, thermal conductivities for the virgin and fully-charred materials as a function of temperature were input in table form into the CMA program, and the thermal conductivity of the partially-degraded material at a particular temperature was calculated using the following equation.

$$k = X\, k_p + (1 - X)\, k_c$$

where X is the mass fraction of undecomposed material, k is the thermal conductivity, and the subscript p referes to plastic or virgin material, c refers to the fully-charred material, and the unsubscripted variables indicate the composite material. This equation has worked adequately in the past, and it has a certain degree of physical appeal in that it seems reasonable to define a thermal conductivity for the composite material as a weighted average of the plastic and char thermal conductivities. However, data that has been published for some materials indicates that the thermal conductivity of the partially-decomposed material can not be adequately represented by such an averaged combination of the char and plastic conductivities. In Reference 19 a plot of thermal conductivity of partially-degraded nylon phenolic as a function of residual weight fraction indicates that the thermal conductivity obtains a value considerably lower than the virgin material conductivity for intermediate weight fractions. If the virgin material conductivity is less than or equal to the char thermal conductivity for all temperatures, as most published data indicate, it is impossible to obtain the conductivity variation just described by using the mass-averaging equation for composite conductivity. Nylon phenolic is a particularly outstanding example of a material whose thermal conductivity decreases with decreasing plastic mass fraction until a carbonaceous char begins to form, because about 75 percent of the material is lost as pyrolysis off-gas, resulting in a partially-degraded material density much lower than the plastic density. For other materials this effect would be expected, buy not to as great an extent, because the density decrease is not as great.

To provide a physical model which would account for a decrease in composite conductivity from the virgin material value while still using only the char and plastic thermal conductivities to make the calculation, the following equation was introduced:

$$k = f_1(X)\, k_p + f_2(X)\, k_c$$

where f_1 and f_2 are functions of the plastic mass fraction X. An examination of typical experimental data on k_p and k_c (references 19 and 20) indicates that these two quantities are approximately constant for the range of temperatures for which a partially-degraded material exists. Thus the only limits on

the two functions are

$$f_1(X) = 1 \ , \ f_2(X) = 0 \ , \ \text{for } X = 1$$

$$f_1(X) = 0 \ , \ f_2(X) = 1 \ , \ \text{for } X = 0$$

It is noted that this new equation for composite material thermal conductivity is considerably more flexible than the previous equation used. The following sketch indicates the capabilities of both the new and old conductivity equations in comparison to experimental data (e.g. nylon phenolic, Reference 19):

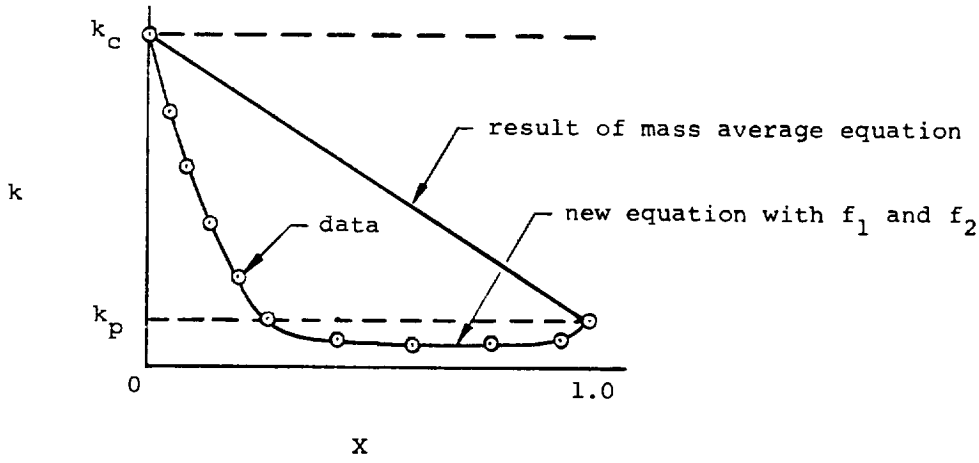

A further indication of the desirability of the new conductivity equation over the previous one is shown in Figure 35 where the in-depth temperature response of silica phenolic is predicted using the two different conductivity models in the CMA program. Initially, the old equation was used with a particular table of k_p and k_c versus temperature. Prediction number 1 is the resulting set of three curves which predict the temperature response of the three in-depth thermocouples. The prediction is especially poor for the first thermocouple, and it was found that not even drastic changes in the k_p and k_c tables input into the program would improve the situation significantly. Then the new equation was added to the CMA program, and provision was made to input a table of $f_1(X)$ and $f_2(X)$. After three iterations (predictions 2, 3, and 4) on the functions $f_1(X)$ and $f_2(X)$, using the same k_p and k_c tables as before, a quite satisfactory prediction of the thermocouple temperature response was obtained.

By allowing the composite thermal conductivity to take on values lower than that of the virgin material, the predicted temperature response curve for the first thermocouple could attain an inflection point and thus match very closely the experimental data for the first thermocouple. This inflection point in the temperature response curve was unattainable when the old equation

for thermal conductivity was used. The composite thermal conductivity curves which resulted from the iterations on $f_1(X)$ and $f_2(X)$, assuming k_p and k_c to be approximately constant at 0.0001 and 0.000355 Btu/ft-sec $^\circ$R for silica phenolic at temperatures less than 2000°R, are shown on an inset in Figure 35. These curves are labeled corresponding to the second, third, and fourth thermocouple temperature predictions. The magnitude of the shift in the temperature response predictions for a particular change in the composite conductivity curve is readily apparent. It can be noted that the iterations on $f_1(X)$ and $f_2(X)$, while keeping the k_p and k_c versus temperature curves constant, change significantly only the first thermocouple temperature response predictions in the time interval from ten seconds to twenty-five seconds. The apparent reason for this behavior is that the chemical transition of the material from plastic to char at the depth of the first thermocouple occurs over the ten to twenty-five second interval. It follows that this transition did not occur during the firing interval at the lower depths of the second and third thermocouples.

The conductivity model introduced here is admittedly based upon a certain amount of conjecture. It is believed, however, to be based upon a reasonable approach both with respect to better representing the conductivity data for partially degraded materials, and because one would expect the thermal conductivity to decrease during initial decomposition prior to carbonization. The model represents a powerful tool for forcing agreement between data and prediction while operating under the constraints of utilizing measured conductivities to represent pure plastic and pure char (when they are available). The results obtained have been encouraging and the model is utilized for subsequent data interpretation presented in Section 4.

3.2 KINETICALLY CONTROLLED HETEROGENEOUS CHAR SURFACE REACTIONS

The calculated surface recession for the graphite-phenolic nozzle (NL-2) utilizing the EST - CMA program combination resulted in about 50 percent more recession than was actually measured (Fig. 21b). Because the prediction is based on the assumption of chemical equilibrium at the ablating surface it is reasonable to expect that certain kinetically controlled chemical reactions may be the cause of the discrepancy. This observation is somewhat substantiated by noting the good agreement between equilibrium prediction and measurement for graphite-phenolic reported in Reference 21 where observed surface temperatures were in excess of 4000°R. In the present results, however, observed surface temperatures were substantially less for graphite-phenolic (3400°R, see Figure 28b) in which case chemical kinetics would be expected to play a more significant role. Additonally, predicted equilibrium surface recession for carbon-phenolic is rather close to that measured (Figure 21d), and for this nozzle the measured surface temperature is about 3900°R (Figure 28d) where it is expected that chemical kinetics would be faster.

Consideration has been given to establishing which chemical reactions at the ablating surface are likely to be most important when considering chemical kinetics. The results of this effort are described first, in Section 3.2.1, and are followed, in Section 3.2.2, by a brief description of the mathematical treatment of the surface boundary condition in the presence of kinetically controlled heterogeneous chemical reactions.

3.2.1 Kinetic Reaction Importance

As part of the effort toward defining the significant aspects of chemical kinetics for the materials and boundary conditions of interest, the Aerotherm Kinetic Reaction Importance Program was used to study a typical graphite phenolic erosion case. Since Reference 1 gives a rather complete description of this program, the present discussion is limited to a brief description of the program and a presentation of the results.

In general, the Aerotherm EST and CMA programs produce ablation predictions under the assumption of surface chemical equilibrium. These general equilibrium calculations do not require that the user specify any particular reaction events.

In the present instance, however, it is desired to specify a number of reactions through which the ablation might have been accomplished. We have available, from the EST program, the chemical composition of the gases adjacent to the ablating surface. These may be regarded as "products". We can generate, with an additional pass through the EST program, the"reactants" from which these products were formed, as indicated in the sketch:

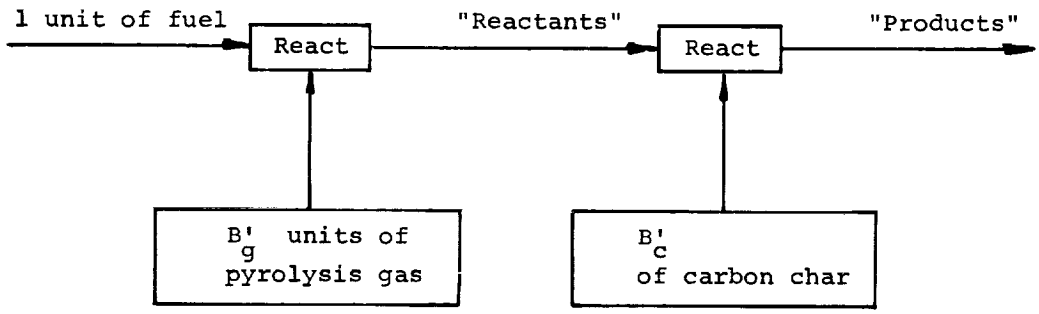

With the reactants and products thus defined, the Reaction Importance Program accepts the specification of a number of chemical reactions and then balances as best as possible the relative amounts of each reaction so as to obtain the correct amount of products from the reactants.

For a typical graphite phenolic ablation case in N_2O_4-N_2H_4/UDMH with a surface temperature of 1897°K (3410°R), a B'_c of 0.225, and a B'_g of 0.15, the reaction importance program produced the following assessment of the relative amounts of four reactions:

Reaction	Percent of Equilbrium Ablation Resulting from the Reaction
$C + H_2O \rightarrow CO + H_2$	83.5
$C + CO_2 \rightarrow 2\ CO$	14.7
$2C + H_2 + N_2 \rightarrow 2HCN$	1.5
$2C + H_2 \rightarrow C_2H_2$	0.3

Thus for the conditions considered it may be concluded that if chemical kinetics are important, only the kinetics of the first two reactions need be considered, and that of these two reactions, the first (the water gas reaction) is by far the most important.

It is of interest to compare these results with the chemical composition of the "reactants". Without presenting the detailed results here, it may be stated that essentially all of the H_2O in the reactants is consumed by the water gas reaction, and that also essentially all of the CO_2 in the reactants is consumed in Reaction 2. Extending this observation, it may be concluded that a fairly good idea of the relative importance of the two reactions may be obtained by a simple comparison of the relative amounts of H_2O and CO_2 in the reactants. Figure 36 shows the ratio of the moles of CO_2 to the moles of H_2O in the "reactants" (1 unit of edge material plus B'_g units of pyrolysis gases, at equilibrium) for B'_g values of 0.1 and 0.2 over a range of temperatures. The H_2O is generally dominant for surface temperatures above 3000°R.

In addition to establishing the potential importance of each chemical reaction, it is necessary to determine kinetic coefficients for each reaction as well. This matter is given attention subsequently, in Section 4.3.2. The next section describes the basic modifications to the EST program which enable consideration of specific kinetically controlled chemical reactions at the ablating surface.

3.2.2 The Mathematical Model

This section presents the basic equations that have been selected to represent the rate at which kinetically controlled reactions may proceed, and briefly describes the resulting set of equations in the modified computer program for representing char recession in the mixed equilibrium-nonequilibrium system.

The basic objective is to allow the majority of possible chemical reactions to proceed according to the dictates of chemical equilibrium, but to impose constraints upon the rate at which particular pre-selected reactions may proceed. The reason for this objective is best illustrated by considering an example. Consider the ablation of a carbonaceous surface in the presence of several oxidizing species such that the following reactions are of interest:

$C^* + H_2O \rightarrow CO + H_2$		Water gas reaction
$C^* + CO_2 \rightarrow 2\ CO$		
$C^* \rightarrow C$		Carbon sublimation
$H_2O + CO \rightarrow CO_2 + H_2$		Water-gas shift

where the asterisk signifies a condensed phase (eg. C* is solid carbon) and unsuperscripted species are gaseous. The first two reactions are recognized as being major contributors to the surface recession of graphite-phenolic as discussed in the previous section, and it is desired that they be constrained to proceed at some rate governed by a chemical kinetic relation. The fourth reaction represents one of many possible carbon sublimation reactions and, although not important for the immediate problem, is a reaction which would normally proceed fast such that equilibrium would be achieved. It is therefore desired to preserve the generality of allowing some reactions to equilibrate while restraining others to obey kinetic laws. Caution must be execised when treating such a mixed equilibrium - nonequilibrium system as illustrated by considering the above reactions for example. If at some surface temperature the second reaction approaches equilibrium but the first reaction (water-gas) does not, and the last reaction (water-gas shift) is assumed to occur infinitely fast (gas phase equilibrium), then more CO_2 will be produced which will in turn react with carbon to equilibrium via the second reaction. The net effect is that the water-gas reaction proceeds infinitely fast via the intermediate water-gas shift reaction.

The basic approach utilized herein for treating the mixed equilibrium - nonequilibrium system was introduced in Reference 22. The method was employed in Reference 14 for reactions pertinent to the ablation of graphite in a solid propellant environment with assumed equal diffusion coefficients in the boundary layer. Details relating to the generalized mathematical treatment for the mixed equilibrium - non equilibrium system are presented most completely in Reference 23. The fundamental solution procedure has been coded in a new computer program termed GNAT (Generalized Nonequilibrium Ablation Thermochemistry). The GNAT program represents a rather extensive rewriting of the EST program discussed previously and is coded such that modifications to incorporate specific kinetic reactions may be accomplished in a relatively straightforward manner.

Under the present contract effort the program has been modified to include consideration of 4 specific kinetically controlled reactions.

$$C^* + H_2O \rightarrow CO + H_2 \qquad (7)$$

$$C^* + CO_2 \rightarrow 2CO \qquad (8)$$

$$2C^* + O_2 \rightleftarrows 2\,CO \tag{9}$$

$$CO + H_2O \rightleftarrows CO_2 + H_2 \tag{10}$$

The first three reactions are heterogeneous (gas solid) and the last is homogeneous, but presumed to be surface catalyzed, that is, the forward rate coefficient is prescribed on the basis of a unit surface area. The following equations have been adopted to represent the direction and rate at which the reactions may proceed

$$\dot{m}_{c,7} = \pm k_{f,7} \left| P_{H_2O} - \frac{P_{CO}\, P_{H_2}}{K_{p,7}} \right|^{n_7} \tag{11}$$

$$\dot{m}_{c,8} = \pm k_{f,8} \left| P_{CO_2} - \frac{P_{CO}^2}{K_{p,8}} \right|^{n_8} \tag{12}$$

$$\dot{m}_{c,9} = \pm k_{f,9} \left| P_{O_2} - \frac{P_{CO}^2}{K_{p,9}} \right|^{n_9} \tag{13}$$

$$\dot{m}_{H_2O,10} = \pm k_{f,10} \left| P_{H_2O} P_{CO} - \frac{P_{CO_2} P_{H_2}}{K_{P,10}} \right|^{n_{10}} \tag{14}$$

In the above rate equations, $K_{P,n}$ is the equilibrium constant for the n^{th} reaction, and as such the net reaction rate, $\dot{m}$, will approach zero as the equilibrium composition is reached. The sign used is the same as that of the difference within the absolute bars.

Thus, the equilibrium composition will be reached from either side of equilibrium. The reaction rate, $\dot{m}_{i,n}$, represents the mass rate at which species i is consumed in the n^{th} reaction. The forward rate coefficient is expressed in Arrhenius form.

$$k_{f,n} = k_n e^{-\frac{\Delta E_n}{RT}} \tag{15}$$

and n_n represents the reaction order for the n^{th} reaction.

The method by which the kinetic reactions are included in the computational scheme is best illustrated by first considering the treatment of the chemical equilibrium case presented in Reference 2, and then considering the modifications appropriate to including chemical kinetics.

3.2.2.1 Evaluation of the Surface State for Chemical Equilibrium

A rather complete description and development of the equations for evaluating the state of the gas in equilibrium with an ablating surface is presented in Reference 2. The resulting relations are summarized here because they provide a convenient point of departure for analyzing the surface state in the presence of chemical kinetics. The conservation equation for chemical elements at the ablating surface is written in terms of the species concentrations adjacent to the surface (Eq. 36, Ref. 2)

$$B' \frac{\sum_i C_{ki} P_{iw}}{\sum_i M_i P_{iw}} + \frac{\sum_i C_{ki} P_{iw}/F_i^{\gamma}}{\sum_i M_i P_{iw}/F_i^{\gamma}} = \frac{1}{M_k} \left(\tilde{Z}^*_{ke} + B'_g \tilde{K}_{kg} + B'_c \tilde{K}_{kc} - \frac{\dot{m}_r}{\rho_e U_e C_M} \tilde{K}_{kr} \right) \quad (16)$$

where

$B' = B'_c + B'_g = (\rho v)_w / \rho_e U_e C_M$, the normalized blowing rate parameter

$B'_c = \dot{m}_c / \rho_e U_e C_M$, normalized char mass recession rate

$B'_g = \dot{m}_g / \rho_e U_e C_M$, normalized pyrolysis gas blowing rate

$\dot{m}_c$, $\dot{m}_g$, $\dot{m}_r$, mass removal rate of char, pyrolysis gas, and liquid, respectively

$(\rho v)_w$ = gas phase mass velocity normal to the heated (char) surface

$\rho_e U_e$ = boundary layer edge mass velocity

C_M = Stanton number for mass transfer

C_{ki} = number of k elements in species i

P_{iw} = partial pressure of species i adjacent to the wall

M_i = molecular weight of species i

M_k = atomic weight of element k

F_i = diffusion factor for species i defined by empirical relation for correlating binary diffusion coefficient data

$$\mathcal{B}_{ij} = \overline{D}/F_i F_j$$

$\mathcal{B}_{ij}$ = binary coefficient for diffusion of species i into j

$\overline{D}$ = a mixture property which depends upon composition, pressure, and temperature

γ = a fractional weighting factor representing the relative mass transfer by diffusional and convective processes

$\tilde{Z}^*_{ke}$ = driving potential for mass transfer in the multicomponent boundary layer defined by

$$\tilde{j}_{kw} = \rho_e U_e C_M \left(\tilde{Z}^*_{kw} - \tilde{Z}^*_{ke}\right)$$

$\tilde{j}_{kw}$ = the normal diffusional mass flux of element k at the wall

$\tilde{K}_{kg}, \tilde{K}_{kc}$ = mass of element k per unit mass of pyrolysis gas and char, respectively

There is one equation like Equation 16 for each chemical element in the system, but only (K-1) of these are unique where K is the total number of k elements. The K^{th} relation requires that the sum of the partial pressures equals the system pressure

$$\sum_i P_i = P \tag{17}$$

The chemical equilibrium relations provide additional equations. If there are I species and K elements, (I-K) reactions may be written forming each gaseous species i from the gaseous elements, k.

$$\sum_k C_{ki} N_k \rightarrow N_i \tag{18}$$

for which the following equilibrium relations apply.

$$\ell n\ P_i - \sum_k C_{ki}\ell nP_k = \ell n\ K_{pi} \qquad (19)$$

Similarly, for formation of condensed phase species (the char surface) from the gaseous elements, the following reaction may be written.

$$\sum_k C_{k\ell}N_k \rightarrow N_\ell \qquad (20)$$

where subscript ℓ signifies a condensed phase (e.g., solid carbon) and the following equilibrium relation applies.

$$\sum_k C_{k\ell}\ \ell n\ P_k = \ell n\ K_{p\ell} \qquad (21)$$

In Equations 19 and 21 the equilibrium constant, K_p, is for Reactions 18 and 20 respectively. Equations 16, 17, 19, and 21 represent a set of I + 1 equations with as many unknowns provided the normalized ablation rates, B'_c, B'_g, $\frac{\dot{m}_r}{\rho_e U_e C_M}$, surface pressure, and composition of the boundary layer edge gas, char, and pyrolysis gas are specified. Solution of the equations yields the chemical equilibrium composition (P_i and P_k for all i and k) and the surface temperature for the case of chemical equilibrium between all gaseous species and the char surface. The situation relating to the number of equations and unknowns is most clearly illustrated as follows:

Unknown	Number of such unknowns
P_i	I - K
P_k	K
T_w	1
Total	I + 1

Equation	Number of such equations
(16)	K - 1
(17)	1
(19)	I - K
(20)	1
Total	I + 1

Although the surface temperature, T_w, does not explicitly appear in the equations, the equilibrium constants, K_{pk} do appear, and they are uniquely related to temperature. Solution of the above set of equations is accomplished

with the EST program discussed previously. The modified set of equations to include certain kinetically controlled reactions is presented in the following section.

3.2.2.2 Evaluation of the Surface State for Mixed Equilibrium-Nonequilibrium

The inclusion of kinetically controlled chemical reactions in the equilibrium solution described above is accomplished by removing equilibrium relations from the set of equations for certain species participating in kinetically controlled reactions, and replacing these equations by the kinetic rate equation for each kinetically controlled reaction. This is accomplished by first identifying the primary reactive species in the reactions which are to be kinetically controlled, and second, by allowing these species to be created or destroyed only via the kinetic rate equations. This approach requires a relabeling of species to be considered in the kinetically controlled reactions. These species are called pseudo elements since they behave like elements in the boundary layer, but differ from elements in that they may be created or destroyed at the ablating surface. This concept is best illustrated by considering the specific reactions of interest as examples.

$$C^* + (H_2O) \rightleftarrows CO + H_2 \qquad (7)$$

$$C^* + (CO_2) \rightleftarrows 2CO \qquad (8)$$

$$2C^* + (O_2) \rightleftarrows 2\,CO \qquad (9)$$

$$CO + (H_2O) \rightleftarrows (CO_2) + H_2 \qquad (10)$$

The species in brackets are pseudo elements, and are not allowed to react in the boundary layer until they reach the surface. At the surface, as the indicated reactions proceed to the right, pseudo elements will be destroyed and either elements or other pseudo elements will be created. In Reaction (7) the pseudo element (H_2O) is destroyed and real elements C, O, and H are created, whereas in Reaction (10) pseudo element (H_2O) is converted to pseudo element (CO_2). Because elements and pseudo elements are both being created and/or destroyed at the surface, it is necessary to add a rate of creation term to the surface conservation equation for chemical elements (Eq. 16)

$$B'\frac{\sum_i C_{ki}P_{iw}}{\sum_i M_iP_{iw}} + \frac{\sum_i C_{ki}P_{iw}/F_i^{\gamma}}{\sum_i M_iP_{iw}/F_i^{\gamma}} = \frac{1}{M_k}\left(\tilde{Z}^*_{ke} + B'_g\tilde{K}_{kg} + B'_c\tilde{K}_{kc}\right) + \frac{\dot{m}_k}{\rho_e U_e C_M M_k} \qquad (22)$$

The last term represents the rate of creation of element k at the surface. It is noted that the mechanical removal term, $\dot{m}_r$, has been eliminated so Equation (22) represents only thermochemical events. The subscript k in Equation (22) pertains to both elements and pseudo elements. The last term is evaluated from the kinetic rate Equations (11-14) by considering the stoichiometry of the corresponding reaction. For example, $\dot{m}_{(H_2O)} = -\dot{m}_{c,7}\left(\frac{M_{H_2O}}{M_C}\right) - \dot{m}_{H_2O,10}$ where $\dot{m}_{c,7}$ is given by Equation (11) and represents the carbon char mass recession rate from oxidation by H_2O (Reaction 7), and $\dot{m}_{H_2O,10}$ is given by Equation (14).

The system of equations and unknowns for the mixed equilibrium-nonequilibrium system is as follows.

Unknown	Number of Such Unknowns
P_i	I - K
P_k	K
$P_{(k)}$	(K)
T_w	1
Total	I + (K) + 1

Equation	Number of Such Equations
22	K + (K) - 1
17	1
19	I - K
20	1
Total	I + (K) + 1

In the above tables, I represents the total number of species not counting those species which are bound elements, K is the number of real chemical elements, and (K) is the number of pseudo elements.

Solution of the above set of equations is obtained with the GNAT (Generalized Nonequilibrium Ablation Thermochemistry) program. In addition to the input required for the equilibrium case, it is also necessary to specify, 1) the concentrations of pseudo elements at the boundary layer edge, in the pyrolysis gas, and/or in the char, and 2) the forward rate coefficients (K_f), reaction order (n), and activation energy (ΔE) for each kinetically controlled reaction being considered.

3.3 A MATHEMATICAL TREATMENT FOR THE RESPONSE OF SILICA REINFORCED ABLATIVE MATERIALS

The present section describes the development of a computer program suitable for predicting the in-depth response of silica containing charring ablators. First, a description of the complex physical problem is given and is followed by a description of the mathematical details of the program analysis. The final subsection describes the resulting program itself.

3.3.1 Physical Problem

The present subsection presents a description of the physical problems of interest in silica-reinforced charring ablators. These problems have complex interrelationships, and the importance of certain aspects has been debated in the literature over the years. Thus, the description necessarily contains some historical orientation as well.

3.3.1.1 General Remarks

It has been known for a long time that there are important differences between the thermal response of such refractory ablators as carbon phenolic on the one hand and silica-reinforced materials such as Refrasil and silica phenolic on the other hand. One important difference is that the silica reinforcement softens and flows away as a liquid layer under some conditions. Another important factor is the possibility of in-depth chemical reactions between the silica reinforcement and the carbonaceous organic residue. These reactions, where they occur, have profound effects on the char density and strength and involve significant amounts of energy.

Existing charring ablator computer programs do not incorporate adequate treatments of the liquid layer removal problem and of in-depth char-reinforcement reactions. A certain part of the present technical effort was, therefore, devoted to computational experimentation with computer programs modified to include these physical aspects of silica phenolic material response.

Before presenting the details of the mathematical treatment of these physical events, it will be of some use to offer the following general remarks about predictive techniques.

The first observation concerns the circumstances under which it is necessary to consider the details of the in-depth response of the material. It is well known, for example, that if there are no liquid layers to consider, then a prediction of the ablating material surface temperature and surface recession rate in the steady state does not require any consideration of in-depth details. The heated surface boundary condition, plus certain details about the virgin material and the surface thermochemistry, is entirely sufficient to define these quantities. The same observation holds true if liquid layer run-off is occurring, provided that the liquid layer is infinitely thin (as would occur, for instance, with a vanishingly small viscosity) and covers the entire surface. For this case, the liquid layer removal rate could be computed as part of the surface thermochemistry solution without reference to complicated mechanical details, provided some appropriate "flow temperature" could be defined. The surface thermochemistry solution could readily accommodate the restriction that the surface material could not exist at temperatures above its flow temperature. Employment of this

restriction would produce the liquid flow rate as an additional unknown.

On the other hand, it is necessary to consider the details of the in-depth response when

a. in-depth quantities, such as isotherm penetration, are of interest, or

b. the problem is transient, so that the in-depth energy absorption rate is important, or

c. thick liquid layer run-off is occuring in such a way that either the rate of run-off or the thickness is determined by the in-depth response.

It happens that the rocket-nozzle problems of interest in the present work definitely fall in classes a and b, and usually into c as well. Therefore, the computational details of interest concern mainly the in-depth solution. These will be discussed in Section 3.3.2 below. Before that, however, it is of interest to present some historical background.

3.3.1.2 Historical Background

While it is not the purpose of the present report to survey in detail the history of analytical studies of silica-reinforced ablative materials, it will be of some utility to cite a few literature references in chronological order in order to provide some perspective for the present analytical effort. The survey paper of Adams (Ref. 24) indicates that in 1959 any analysis of silica-reinforced materials was in a very rudimentary state. Beecher and Rosensweig presented in 1961 a survey of the various physical processes involved which indicated that a truly satisfactory performance prediction scheme would probably need to be very complex, accounting for boundary-layer transport, surface thermochemistry, liquid layer physics, subsurface carbon-silica reactions, and pyrolysis kinetics (Ref. 25). Shortly thereafter, the same authors offered a tentative analysis of the ablation problem incorporating a thick continuous layer model with a kinetic controlled in-depth carbon-silica reaction model for steady-state problems (Ref. 26). The published work presented only a single comparison to one recession rate, however, so the general adequacy of the analysis cannot be verified. It seems unlikely to be of very general utility for a number of reasons, principally a very rudimentary surface thermochemistry model. Richman (Ref. 27) has recently described a highly simplified analysis which does not allow for subsurface reactions other than pyrolysis, and Romie (Ref. 28) has presented a simplified steady-state account of the subsurface events during silica-carbon reactions, but his analysis is not coupled to a surface boundary condition.

The general complexity of the ablation mechanisms in silica-reinforced plastics, coupled with the lack of extensive experimental confirmation of the proposed mechanisms, appears to have discouraged any other extensive analysis work. A great number of experimental studies have, of course, been conducted. The published results are far too numerous to be cited here, but three accessible examples are References 29, 30, and 31. The experimental work which these publications exemplify raised some basic questions about the ablation mechanisms proposed by Beecher and Rosensweig. In particular, debate and controversy arose over whether or not in-depth silica-carbon reactions actually occurred, and if so, to what extent. Ladacki gives a good summary of this debate, including a bibliography (Ref. 32). Gutman offers some additional remarks in Reference 33. In addition, Blumenthal, Santy, and Burns have recently shown experimentally that carbon and silica will react rapidly under some conditions, and have measured the kinetic coefficients involved for particular char samples (Ref. 34). Appendix B gives an outline of the experimental work. Additional work was reported in Reference 35.

3.3.1.3 Summary of Physical Problem

To summarize the state of knowledge about the physical events occurring during the ablation of silica-reinforced charring materials, the present section presents brief descriptions of the physical events, starting from the virgin material and proceeding toward the heated surface. Following a particle of material as it traverses the distance from the virgin material to the heated surface, the first event to occur is the pyrolysis of the resinous constituents, which for phenolic begins at about 1500^{o}R and is essentially complete at about 2500^{o}R, leaving a carbon residue matrix imbedded in the original silica reinforcement. The pyrolysis gas given off in this degradation passes immediately through the char layer and enters the boundary layer.

A very important and, as yet, unanswered question concerns the chemical history of these gases as they pass through the char layer. Equilibrium calculations indicate that these gases should condense out carbon. If this carbon deposits on the char structure, then it should play a very important role in the carbon-silica condensed phase reactions which may be occurring. This aspect will be discussed below. For the moment, it may be observed that the appearance of silica phenolic chars seems to indicate that carbon deposition does not take place, presumably due to chemical kinetic limitation on the rate of formation of condensed phase carbon.

Proceeding closer to the surface, the carbon and silica char material remains unchanged until about 3000^{o}R, when a condensed phase reaction between carbon and silica begins. Despite the controversy which has in the past

surrounded this reaction, there is now abundant experimental evidence that some reaction of this kind takes place. A number of specific candidate reactions have been proposed, but surprisingly little analysis work has been devoted to identifying dominant reactions. A useful approach in this case would be to consider equilibrium compositions. Some work along this line was reported in References 22 and 30, but in these cases only the virgin material composition was considered. Probably a more realistic procedure for evaluating silica-carbon reaction in the char is to consider the char composition alone. Although Beecher and Rosensweig (Ref. 25) attempted this evaluation by comparing the equilibrium constants of several individual reactions, evidently no complete equilibrium calculations have ever been reported in detail. Romie (Ref. 28) asserts, however, that the results of such calculations for pressures of 25, 50, and 100 psia indicate the dominating reaction

$$SiO_2^* + C^* \rightarrow CO + SiO$$

Furthermore, there is abundant experimental evidence to indicate that this reaction dominates but is kinetically controlled. The kinetic coefficients have been experimentally defined.

Depending on the ratio of carbon to silica in the char this reaction results in either a porous carbon or porous silica residue structure. For the silica phenolic of interest in the present work (nozzle NL-1) the computed residue is a silica of 9 lb/ft^3 density (if dimensional stability is assumed).

Before the reaction has a chance to go to completion, however, the remaining silica structure softens drastically at about 3350^oR (Ref. 36). Over a certain range of the residual carbon density, the carbon residue may retain enough structure to support the "molten" silica but close to the heated surface the remaining carbon structure becomes discontinous and no longer supports the silica, which then begins to flow off the surface under the influence of external stresses.

The pyrolysis gases and the CO + SiO reaction gas generated in-depth are injected into the gaseous boundary layer adjacent to the heated surface. Some analyses presume for simplicity that these gases do not react chemically in the boundary layer. There is some evidence, however, (to be presented in Section 4.3.1 below) that the SiO reaction gas combines with oxygen in the boundary layer to yield SiO_2^* as a precipitate. This reaction is approximately as exothermic as the in-depth silica-carbon reaction is endothermic; thus, the net energy effect of SiO production in-depth is not large.

In summary, the behavior of a silica-reinforced charring material differs from that of simpler charring materials due to additional complications of surface thermochemistry, subsurface char-reinforcement reactions, and liquid layer removal. The subsurface carbon-silica reaction, strongly endothermic, causes SiO gas to be injected into the boundary layer. In the usual case of an oxidizing boundary layer, the SiO is oxidized and condensed out again as SiO_2* in a sharply exothermic reaction. Thus the net effect of the silica-carbon reaction is CO production, not a strongly energetic event. The true importance of the silica-carbon reaction is structural: the weak silica layer left behind is readily removed by external stresses.

3.3.2 Description of Modifications to CMA Program Accounting for Silica-Reactions and Thick Liquid Layer Removal

Section 3.3.1 above presents some of the background information which indicated that it would be highly desirable, in any computation scheme for the in-depth thermal response of silica containing charring materials, to have some provision for treating the reaction.

$$C^* + SiO_2^* \rightarrow CO + SiO$$

as it occurs in-depth. Since this reaction appears to be kinetically controlled, to incorporate this computation in a general way would involve very complex bookkeeping operations throughout the entire decomposition area of the material. This in turn would require the development of a substantial computer program. For the present study, it has seemed more expedient to account for the subsurface reactions by modifying the existing CMA (Charring Material Ablation) computer program. This program accounts for the in-depth pyrolysis events; in modifying the program it was necessary to add the carbon-silica reaction events. To accomplish this in an expedient manner certain assumptions were made. In order to describe the effect and utility of these assumptions, Appendix A describes, in general terms, the workings of the CMA program. The present section describes details of the modifications. The treatment of silica-carbon reactions is given first in Section 3.3.2.1, and is followed by a description of the treatment given liquid layer removal and thermochemical surface recession in Sections 3.3.2.2 and 3.3.2.3 respectively.

3.3.2.1 Silica-Carbon Reactions

Basic Assumptions

The basic pyrolysis calculation of the CMA program produces only density change rates. It is not necessary in this computation actually to identify the chemical nature or identity of any of the material components. Any

carbon-silica reaction scheme, however, necessarily involves the definite identification of the amount of carbon present in each location. Obviously, the required computational bookkeeping is much simplified if the carbon-silica reactions do not start until the resins have been completely carbonized. Fortunately complete carbonization of organic constituents develops at temperatures around 2400°R, well below the temperatures at which the silica-carbon reactions begin to proceed appreciably (3000°R) and far below the temperatures of rapid reaction (3500°R).

With this in mind, the basic assumptions for the in-depth carbon-silica calculations may be summarized as follows

1. Silica-carbon reactions do not begin until the resinous components of the virgin material are fully charred and carbonized. Hence, the material can be divided into a distinct zone of decomposing (charring) material and another distinct zone of silica and carbon where silica-carbon reactions take place and from which liquid silica may be removed. The thickness of this zone may increase or decrease with time.

2. For any control volume the rate of consumption of carbon by silica-carbon reactions is given by $\partial m_C/\partial\theta = m_C A\, e^{-E/RT}$ where the constants A and E may be obtained from Reference 34 for the overall reaction:

$$SiO_2^* + C^* \rightarrow SiO + CO$$

3. The pyrolysis gas passing through the char does not contribute carbon for this reaction. All the carbon supply is provided by the original carbon residue of pyrolysis.

4. The SiO + CO gas generated by this reaction differs sufficiently in its thermal and chemical properties from the pyrolysis gas originating from the decomposition of the resinous constituents of the virgin material that it is necessary to account for the amounts of each gas in calculating the in-depth response (and hence it is necessary in the construction of the surface thermochemistry tables to have two gas-rate parameters, rather than one, in the CMA program, as noted below).

5. In the zone where silica-carbon reactions may take place, the occurrence of these reactions will not affect the dimensional stability of the material. There is no shrinking or swelling effect. (The experimental evidence available suggests that any shrinking or swelling which might exist is very slight. Since it is much more convenient, within the CMA program framework, to ignore swelling and shrinking than to account for such effects, they will be ignored.)

Computational Aspects

As noted above, the interior of the ablating material is divided into a deep zone where charring is occuring and an upper zone where silica-carbon

reactions are taking place. The mathematical treatment of the charring zone will remain unchanged from that presently incorporated in the CMA program.

The upper zone will be handled independently and, for convenience, somewhat differently. In particular, it will be most convenient to write the mass balance equations for the "nodes" in this zone in terms of masses of constituents (carbon and silica) rather than the densities of these components. The differential equation for the rate of change of mass of carbon for example is (refer to the control volume shown in Figure 37)

$$\left.\frac{\partial m_C}{\partial \theta}\right|_x = \left.\frac{\partial m_C}{\partial \theta}\right|_y + \dot{S} \left.\frac{\partial m_C}{\partial x}\right|_\theta \tag{23}$$

where the x-coordinate is tied to the receding surface (this system is chosen for finite-differencing convenience) and the y-coordinate is fixed in space (relative to the back wall). The term $\partial m_C/\partial\theta)_y$ represents the chemical consumption rate and is given by Equation (B-5) of Appendix B.

$$\dot{m}_C = m_C A e^{-E/RT} \tag{24}$$

The corresponding mass balance differential equation for the silica is

$$\left.\frac{\partial m_{SiO_2}}{\partial \theta}\right|_x = (R-1) \left.\frac{\partial m_C}{\partial \theta}\right|_y + \dot{S} \left.\frac{\partial m_{SiO_2}}{\partial x}\right|_\theta \tag{25}$$

where R is the mass of silica and carbon reacting per mass of carbon and is given by

$$R = \frac{M_{SiO_2} + M_C}{M_C} = 7.32$$

The conservation of energy equation corresponding to these mass equations is

$$\sum_i \frac{\partial}{\partial \theta} (m_i h_i)_x = \Delta_x \; kA \left.\frac{\partial T}{\partial x}\right|_\theta + \Delta_x (\dot{m}_g h_g)_\theta + \dot{S} \sum_i \frac{\partial}{\partial x} (m_i h_i)_\theta \tag{26}$$

where the index i extends over the two components carbon and silica. The energy equation is self explanatory except for one aspect: a crucial test of the problem formulation requires consistency between the mass and energy equations in both their difference and differential forms. For example, the differential energy equation (26) above reduces to an overall mass balance involving Equations (23) and (25) above for uniform T and h_i values.

A final aspect of the in-depth response computation involves the "bridge" necessary between the top silica-carbon zone and the deeper charring zone.

It would be possible to devise some elaborate, self-consistent schemes for making this bridge, but the task is far from simple. In the interests of speed and economy, a more blunt approach is employed. The two computational zones are separated by a distinct line. As soon as a node becomes fully charred, this "mix line" is set at the bottom of that node. Thereafter, the "competition" between surface recession convection effects and the local charring rate will determine whether the mix line migrates upward toward the surface or moves deeper into the material.

3.3.2.2 Liquid Layer Removal

Basic Assumptions

The actual specification of the liquid layer removal rate would appear to be a highly complex matter involving pressure and shear stress gradients, surface tension and stability phenomena, viscosity, and the role of the carbon residue matrix in supporting and retaining the silica layer. Since the present effort is of an exploratory nature the following simple assumptions were employed to obtain a reliable, rudimentary computation scheme which still appeared to model observed physical events with reasonable fidelity. (These assumptions are in addition to the assumptions regarding silica-carbon reactions described above; the numbering is continued):

6. A " liquid layer thickness" can be defined as the distance between the heated surface and the area where the density of carbon has been reduced, through the carbon silica reaction, to some specific value.

7. Liquid layer run off occurs so as to maintain a constant liquid layer thickness.

8. Any carbon particles in the liquid layer do not float off with any liquid layer flow.

9. The temperature drop across the liquid layer is small enough such that the removed liquid layer may be presumed isothermal and at the surface temperature.

Assumption 8 will be discussed in more detail in Section 3.3.2.3.

Computational Aspects

The only computational aspect of interest concerns the calculation of the surface recession rate due to run-off. If the liquid-layer thickness is less than the maximum, the run-off recession rate is zero. If the thickness is momentarily greater than that allowed, the run-off recession rate may be set equal to some value sufficient to reduce the liquid-layer thickness to the maximum allowed within the next few time steps in the computation.

3.3.2.3 Surface Thermochemistry and Thermochemical Recession

Experience shows that economy of computation time and core storage limits the number of parameters in the surface thermochemistry tables to three. One must obviously be the usual thermochemical erosion rate B_c' . Another is as usual,

the pyrolysis gas injection rate B'_g. The third must be the injection rate of SiO + CO gas resulting from carbon-silica reactions in depth.

The chemical composition of the "char" must be unique in order to avoid a fourth parameter, and in the absence of any definitive information to be contrary, the composition of the chemically eroded char will be assumed to be pure silica. At first glance this assumption may appear to be questionable if carbon particles exist at the surface, since the assumption implies that carbon cannot be consumed by the boundary layer gases. Actually however this assumption is quite appropriate, since at the surface temperatures of interest, very little carbon appears near the surface for the high silica content materials studied here, as verified by calculations and by visual inspection of the arc plasma test specimen and actual rocket nozzles after testing. (Furthermore, the results of numerous calculations indicate that for the problems of interest the SiO reaction gas injected with the boundary layer combines with oxygen here and precipitates out as SiO_2^*. Thus SiO_2^* condensate most probably covers any carbon particles at the surface and screens them from direct attack by boundary layer gases.)

3.3.3. The SCRIMP Program

The standard Aerotherm charring material ablation program (CMA) described in Appendix A was modified to account for the in-depth silica-carbon mechanisms and the liquid layer removal mechanism described above. Most of the interesting computational aspects of the modifications have already been described in that section. The present section gives a brief supplementary description of the program as a whole.

The resulting modified program has been denoted the SCRIMP program (after "Silica-Carbon Reactions Including Melting Phenomena"). The program is a coded computational procedure based upon a finite difference formulation of in-depth energy and mass transfer. The program allows for the usual pyrolysis of resin constituents and the subsequent condensed phase reaction

$$C^* + SiO_2^* \rightarrow SiO + CO$$

between the carbon residue of pyrolysis and the char. The flows of pyrolysis gas and of the reaction gas are accounted for separately.

The in-depth computation may be coupled to a film-coefficient boundary layer model in the same general manner as the CMA program described in Appendix A. This coupling is effected through "surface tables" which contain tabulated values of the information necessary to conduct a surface energy balance, for an array of thermochemical erosion rates and gas injection rates. These tables are most easily prepared with special purpose chemistry programs: The Equilibrium Surface Thermochemistry Program (EST) or the Generalized Non-Equilibrium Ablation Thermochemistry Program (GNAT).

Physically, the SCRIMP program is a Fortran IV program of about 2900 lines. The program requires about 25,000 words of machine storage for both instructions and data. Highly transient rocket nozzle computations appear to consume about five times real time for machines of IBM 7094 speed, but, since the program is implicit in its energy equation formulation, computing economy increases markedly as steady state is approached.

The SCRIMP program has been developed as a special purpose program for high silica content charring materials. The program has been operated successfully for two different materials, and,as will be discussed in Section 4.3 below, has given some encouraging results. However, it should be noted that the program is an "unseasoned" program which has not yet received the benefit of extensive computing experience. (Some recommendations for future development of the program appear in Section 6.) Furthermore, the program was developed quickly as a badly needed working tool, and has not yet received any documentation other than the present report.

3.4 SUMMARY OF PREDICTION TECHNIQUES

The Aerotherm computer programs for analyzing ablative material performance have been modified to include consideration of certain additional phenomena believed to play a significant role in controlling the response of several classes of ablative materials. These modifications include (1) a more realistic model for representing the thermal conductivity of partially degraded organic reinforced materials, (2) provision for considering kinetically controlled oxidation of a carbonaceous char by H_2O, CO_2, and O_2, and for considering kinetics of the homogeneous water-gas shift reaction, and (3) a mathematical model for considering kinetically controlled reactions between carbon and silica reinforcement fibers in the char layer. The mathematical treatment includes consideration of all associated energy and mass-transfer events and enables considering liquid-layer removal phenomena within the framework of a simplified phenomenological model.

Motivation for performing the modifications was provided by comparisons between measured ablation data and predictions using the "old" (unmodified) computer programs. The following section includes these comparisons and also compares predictions with the modified computer programs to measured ablation data.

SECTION 4

CORRELATION OF ABLATION DATA

Ablation data have been acquired for each of six ablative materials in a simulated N_2O_4-N_2H_4/UDMH rocket-engine environment. The data includes a rather comprehensive documentation of all pertinent independent and dependent variables. Computational schemes have been modified to enable consideration of certain phenomena believed to be important in controlling ablative material degradation. This section describes efforts directed toward correlating the ablation data with the improved computational schemes.

The term "data correlation" is subject to interpretation, and it is believed expedient, in the interest of clarity, to present the intended meaning of the term as it relates to the efforts described in this section. Data correlation is a process which begins with a collection of data and a postulated theoretical relationship between independent and dependent variables, and ends with the demonstration of a predictable relation between measured dependent and independent variables. The probability of successfully correlating data clearly depends upon a number of factors.

1. The pertinent independent variables must be identified and their values known.
2. The postulated theoretical relations between dependent and independent variables must include provision for considering all significant phenomena in a realistic manner.
3. The multitude of coefficients employed to characterize all state properties and rate-controlling events must be known.

When considering the ablation of composite organic reinforced materials in a high-temperature, chemically active stream, the accuracy to which many of the pertinent variables and coefficients are known often leaves something to be desired and the postulated theoretical dependence relating many of the pertinate variables must necessarily often be based upon a certain amount of conjecture.

The specific approach for correlating the subject ablation data is presented first in Section 4.1. This is followed, in Section 4.2, by a presentation of all material property data and coefficients employed for the correlations, and is followed, in Section 4.3, by comparisons of measured ablation data to predictions.

4.1 APPROACH

The approach for achieving correlation of the ablation data consists of first correlating the subsurface data and then, having an adequate representation of subsurface events, proceeding to correlation of surface data. The motivation for proceeding in this manner is illustrated by considering a typical example. If an attempt is made to predict the over-all response of a material, the predicted surface temperature may be too low and the predicted recession and internal temperature histories may be too high. It might be speculated that utilization of a somewhat lower thermal conductivity for the char would force agreement between measured and predicted temperature histories, and imposition of a particular kinetic rate law for oxidation would have decreased surface recession to the observed value. It is likely that several combinations of surface kinetic coefficients and char thermal conductivity would enable correlation of the data and, as such, it would be difficult to demonstrate any uniqueness in the coefficients derived in this manner. Thermal conductivity and kinetic coefficients represent only two of many coefficients which lack accurate definition and, as illustrated by the above example, it would be desirable to isolate the effects of each variable in the correlation process. This may be accomplished in a rather gross sense, by splitting the problem at the ablating surface and first correlating the subsurface data by specifying measured surface recession and temperature histories as boundary conditions. After successful correlation of measured subsurface temperature histories and post-test density distributions, efforts are directed toward correlating surface data by attempting to predict surface recession and temperature histories. Any lack of agreement between measured and predicted surface phenomena may then be attributed to unrealistic treatment of surface phenomena rather than subsurface phenomena.

Prior to delving into the many particular aspects associated with the data correlation process, it is appropriate to place the analysis in perspective by summarizing the primary variables of interest and by briefly reviewing the proposed theoretical model for accomplishing data correlation.

Variables of Interest

The primary independent variables and the means of evaluating them are as follows.

1. Boundary-layer edge pressure

   Calculated from measured chamber pressure (Figures 8a-8f) by equilibrium isentropic flow calculation. Other state properties required for the calculation are given below.

2. Boundary-layer edge chemical composition

   Obtained from isentropic flow calculation employing measured quantity of each chemical element from Table II.

3. Boundary-layer edge total enthalpy

   Measured as described in Section 2 and shown in Figures 9a-9f.

4. Boundary-layer heat-transfer coefficient

   Taken as 0.454 of that predicted by the Bartz equation. This represents an average of the data shown in Table IV.

5. Ablation material composition

   Prescribed by the manufacturer. The material properties are given extensive consideration in the following Section (4.2).

6. Ablation material geometry

   See Figure 4.

The primary dependent variables and their values are:

1. Temperature history at the surface and at discrete locations below the surface (at thermocouple locations)

   Measured as described in Section 2 and shown in Figures 28a-28f.

2. Surface recession history

   Measured as described in Section 2 and shown in Figures 21a-21f.

3. Subsurface material density distribution after the test

   Obtained from visual observation of post test, sectioned nozzles shown photographically in Figures 34a-34f.

The Theoretical Model

The theoretical model to be employed for achieving data correlation is embodied in each of several computer programs which were described above and are summarized here. The GNAT program is employed to generate generalized boundary conditions at the ablating surface considering boundary-layer transport phenomena and chemical reactions which may proceed to equilibrium or be kinetically controlled. The CMA program models the subsurface solution utilizing the GNAT output for boundary condition evaluation. Decomposition of organic materials may be treated with a three-component Arrhenius type equation. The gaseous pyrolysis products may continue to react and absorb energy as they pass through the char layer. The surface temperature and recession rate are evaluated by performing a surface energy and mass balance with imposed constraints of chemical equilibrium or mixed equilibrium-nonequilibrium. The SCRIMP program performs the same functions as the CMA program, but also includes a model for representing liquid-layer removal in silica-reinforced materials.

The many coefficients and property data which represent various aspects of each material are presented in the following section.

4.2 MATERIAL PROPERTIES

Characterization of the subsurface response requires specification of a large number of coefficients which control various energy transport and absorption phenomena. Of primary importance on this list are the heats of formation of the various virgin material constituents, the chemical elemental composition and quantity of each constituent, the heat of formation and density of the char residue, organic constituent decomposition kinetic coefficients, the enthalpy-temperature relation for the organic constituent pyrolysis products, and the thermal conductivity of the virgin, partially degraded, and fully degraded material. A number of the properties listed above may be obtained from direct or secondary measurement, or they may be estimated to a fair degree of accuracy. Other properties on the above list, however, are not well characterized. For example, the temperature-enthalpy dependence of the pyrolysis products is not well defined because it depends critically upon the molecular configuration assumed by the high molecular weight hydrocarbon fragments as they pass through the high-temperature char layer. Even though techniques do exist for measuring thermal conductivity of pure plastic and pure char, data are often lacking when one wishes to investigate a particular material, and, even when conductivity data are available for the two extremes, it is not clear how the very significant partially degraded zone should be treated.

In order to characterize the in-depth response for each of the six ablative materials considered here, the following approach is being taken. The Charring Material Ablation (CMA) program is employed to represent the mathematical model for all subsurface energy transfer and absorption mechanisms. All requisite coefficients and material property data except thermal conductivity and pyrolysis-gas temperature-enthalpy are taken directly from or estimated on the basis of results reported in the literature. The pyrolysis-gas temperature-enthalpy dependence is calculated assuming chemical equilibrium in the gas phase. The thermal conductivity of the material is established by a successive approximation procedure which consists of predicting the test nozzle internal temperature histories utilizing the CMA program with the measured surface temperature and recession rate histories as boundary conditions. The thermal conductivity is varied within reasonable bounds until agreement between prediction and data is achieved.

The above procedure may be looked upon in the following manner. We have data which represent the combined effect of a large number of simultaneous events. Some of these events may be quantitatively characterized with a fair degree of accuracy while others may not. We presume we may prescribe the coefficients which characterize all but one event and then determine the coefficients for this event by varying them until agreement with the data is achieved. The success of such an approach is clearly dependent upon the

adequacy of the mathematical model and the accuracy with which the various coefficients may be estimated. Another requirement for success is that the one event which is characterized in the final iteration process must be of major significance in controlling the observed data. It is believed that thermal conductivity is a proper choice.

The material property data for all six ablative materials except pyrolysis gas enthalpy, material specific heat, and thermal conductivity are given detailed evaluation in Appendix C and are summarized in Table V. A brief description of these properties is given first, and is followed by a presentation of pyrolysis gas enthalpy, thermal conductivity and specific heat.

Density Information

Density data are required for both the virgin material and the fully decomposed char. The material may be composed of as many as three basic constituents (A, B, and C). The density of each constituent prior to, and after decomposition, are required (e.g. ρ_{A_1} and ρ_{A_2} respectively). The virgin material and char densities may be evaluated directly from these densities and a knowledge of the resin mass or volume fraction.

Resin Mass Fraction

The resin is presumed to consist of one or two constituents (A and/or B), and the third constituent (component C) represents the reinforcement fiber and/or filler. The resin mass fraction K_r (lb resin/lb virgin plastic), or the resin volume fraction Γ (ft^3 resin/ft^3 virgin material) is required. Either one or the other may be specified as either one may be evaluated from the other and the density information above.

Chemical Elemental Composition

The mass fraction of each chemical element in the char $\tilde{K}_{k_c}$, and pyrolysis products, $\tilde{K}_{k_g}$, is required.

Heat of Formation

The heat of formation of the virgin plastic and char (ΔH_{fv} and ΔH_{fc}) at 298^{o}K are specified relative to the JANAF thermochemical base state (Ref. 37).

Decomposition Kinetic Coefficients

Each of as many as three basic material constituents may decompose according to a decomposition rate equation of the Arrhenius form. The pre-exponential constant, (k), activation energy, (E), and reaction order, (n), for each of the three parallel decomposition reactions (A, B, and C) must be specified.

The values of the above coefficients for each of six ablation materials are presented in Table V. The six materials correspond to those tested in the

simulated rocket engine environment. The property values listed in Table V should be considered as approximate; they are based upon a combination of measurements and estimates so constrained as to yield an internally consistent set of values. A detailed description of all fundamental relations, property measurements, and estimation procedures is presented in Appendix C.

Pyrolysis Gas Enthalpy

If the subsurface composition is computed on the basis of chemical equilibrium considerations, a far more dense char is predicted to occur than is observed from char density measurements (Ref. 19). It may be concluded either that condensed phase carbon is formed from the pyrolysis gas but does not stick to the char, or that the high molecular weight hydrocarbons in the pyrolysis gas do not decompose according to the dictates of chemical equilibrium. The latter possibility seems more probable but conclusive experimental evidence on this matter is lacking. The pyrolysis gas enthalpy ($H_g = f(T,P)$) is presumed to be represented by the equilibrium molecular composition with the imposed constraint that no carbon may precipitate out. The resulting pyrolysis gas enthalpy for each of the six ablative materials is shown in Figure 38. The gas elemental composition is taken from Table V, the pressure is taken as an average at the throat during ablative material tests and the temperature is prescribed over the anticipated range of interest.

Specific Heat

Specific heat of the virgin material and char are taken from reported measurements when available and estimated based upon similarities to other materials when data are not available. Specific heat values for the six ablative materials are shown in Figures 39a through 39f along with the thermal conductivity data discussed next.

Thermal Conductivity

Thermal conductivity for 4 of the 6 materials (all except carbon- and graphite-phenolic) was evaluated directly from the ablation data utilizing the CMA program and the other material properties presented above. Evaluation is performed by specifying measured values of surface temperature and recession rate, and iterating on the thermal conductivity model until agreement is achieved between measured and predicted subsurface temperature histories as described above in Section 3.1. The conductivity for two of the other materials, graphite-phenolic and carbon-phenolic, had been established previously in a similar manner on a different program (Ref. 21). The previously evaluated conductivities are based upon the old conductivity model (no f(X) functions), but it is believed reasonable to utilize them here anyway for the following reasons: (1) the conductivity difference between virgin plastic and char for carbon and graphite reinforced materials at low temperatures is very slight so the averaging procedure employed to characterize the partially

degraded material is not too critical and (2) the test data employed to back-out these conductivities was obtained with an arc-heated inert gas stream so no surface recession occurred. This enabled a more accurate specification of the surface recession history ($\dot{S} = 0$). Because the surface recession history specified strongly affects the predicted internal temperature history, it is felt that the conductivities reported in Reference 21 are more accurate than could be obtained utilizing the data reported herein because of the possible uncertainties in the measured surface recession histories.

The thermal conductivity model for all six materials is shown in Figures 39a-39f. As was described above, in Section 3.1, the thermal conductivity is evaluated within the program from an equation of the following form.

$$k = f_1(X)k_p(T) + f_2(X)k_c(T)$$

where $k_p(T)$ and $k_c(T)$ are the temperature-dependent conductivities of pure plastic and pure char materials respectively. The quantity X is the undegraded plastic mass fraction ($X = 1$ for virgin plastic and $X = 0$ for pure char). The functions $f_1(X)$ and $f_2(X)$ are input to enable a more realistic evaluation of the conductivity of partially degraded materials. During the course of evaluating the thermal conductivity data, an attempt was made to standardize the general behavior of the functions f_1 and f_2. The sketch below illustrates the general form of the function utilized for characterizing the thermal conductivity of each material considered.

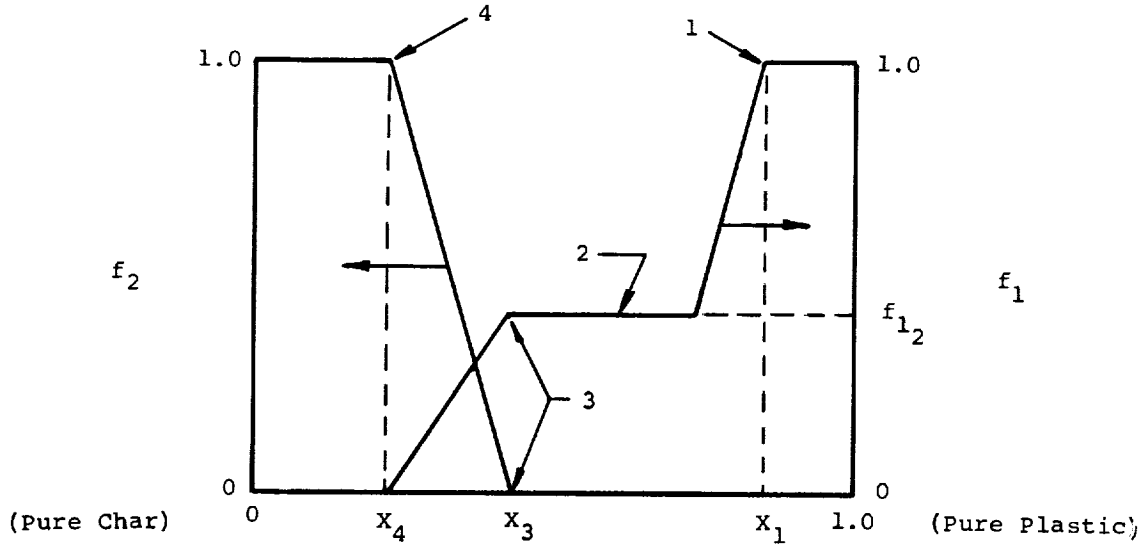

1. Consideration of the sketch and the above equation reveals that for $1.0 \geq X \geq X_1$, $k = k_p$. The point 1 on the sketch represents that mass fraction for which the thermal conductivity departs significantly from that of the virgin plastic.

2. This plateau represents the thermal conductivity minimum for the partially degraded material, i.e., $k = f_{1_2} k_p$. This plateau will continue until $X = X_3$.

3. This point signifies the state of degradation which represents the transformation from a basically organic structure to a carbonaceous char.

4. For $X \geq X_4$ the material behaves as the pure char, i.e., $k = k_c$.

The derived functions, f_1 and f_2, are shown along with the plastic and char conductivities and specific heats in Figures 39a through 39f for each of the six ablative materials.

The following section describes the results of the data correlation process employing the properties presented in this section and the previously described computer programs.

4.3 COMPARISON OF MEASURED AND PREDICTED ABLATION DATA

Two sets of ablation material response calculations were performed for the six materials tested in the experimental program. The first set of calculations was employed to "back out" thermal conductivity and establish the accuracy of the numerical technique for characterizing subsurface thermal response. As indicated above, these calculations were performed by specifying the measured surface temperature and recession histories. Sequential runs were accompanied by varying the thermal conductivity model in order to bring about agreement between predicted and measured subsurface temperature histories. After having established an acceptable model to represent the subsurface solution, a second series of calculations was performed in an effort to predict measured surface recession and temperature histories. This sequence of calculations was accompanied by perturbing coefficients which influence the surface energy and mass balances such as kinetic coefficients for char oxidation and allowable liquid-layer thickness for silica-reinforced materials.

Results from the subsurface solution are presented first in Section 4.3.1 and are followed, in Section 4.3.2, by a description of results for predicting the surface response.

4.3.1 Subsurface Response

The final predicted subsurface response for the six nozzles is represented by comparisons of calculated and measured thermocouple histories in Figures 28a through 28f, and by comparisons of calculated and measured char depth in Figures 40a through 40f. The calculations were performed employing the material properties shown in Table V, the pyrolysis gas enthalpies shown in Figure 38, and the thermal conductivity models presented in Figures 39a through 39f. The boundary conditions for the solutions consisted of specifying the measured surface temperature histories shown in Figures 28a through 28f and the measured surface recession histories shown in Figures 21a through 21f. It is noted that 2 sets of surface recession data are presented in Figure 21 for each nozzle. The average recession is based on the average post-test throat area (see shadowgraphs in Figures 20a-20f) and the other recession is that immediately above the location of the subsurface thermocouples. The two measurements differ somewhat because of irregularities in the throat erosion pattern as shown in the post-test shadowgraphs (Figs. 20a-20f). The measured surface recession above the thermocouple was believed to be a more appropriate boundary condition for comparing predicted and measured thermocouple histories.

It is not surprising that agreement between predicted and measured subsurface temperatures is pretty good since the temperature data were employed to establish the thermal conductivity utilized in the prediction with the exception of graphite phenolic (NL-2) and carbon-phenolic (NL-4), Figures 28b and 28d, respectively. The thermal conductivity model for these two materials was not established in the same manner as the rest, but was rather taken directly from Reference 21. Except for the prediction for graphite-phenolic (Fig. 28b), where there is reason to suspect thermocouple malfunction, it is felt that the internal temperature response predictions are adequate.

Comparisons of predicted and measured char depth penetration were also made and are shown in Figures 40a through 40f for nozzle numbers NL-1 through NL-6, respectively. The measured surface recession history was specified as a boundary condition, and the predicted char depth history is shown and compared to the post-test measured char depth. The measurement was taken from the nozzle section after sawing in half. Photographs of the sectioned nozzles are shown as Figures 34a through 34f. The limits on the predicted char depth and decomposition zone thickness shown in Figures 40a through 40f are somewhat arbitrary. The bottom side of the decomposition zone is taken as that point in the material where enough decomposition has occurred to cause a density decrease equal to 2 percent of the density decrease which the material will experience prior to complete decomposition.

$$\rho = \rho_c + 0.98\ (\rho_p - \rho_c)$$

The measured value shown in the figure for this boundary is taken as that point in the material where some discoloration in the material is noted. The top side of the decomposition zone is arbitrarily defined as that point in the material which has experienced 1/2 of its potential density loss.

$$\rho = \rho_c + 0.5\ (\rho_p - \rho_c)$$

This point is located in the material as the point midway between the beginning of the discolored zone and the edge of what appears to be a fully developed char layer.

It is encouraging to note the good agreement between measured and predicted material degradation depths shown in the figures since, unlike thermal conductivity, information pertaining to organic decomposition processes was not derived from the test data presented herein. Based upon the agreement achieved between measured and predicted subsurface response, it is concluded that the theoretical model and material properties are adequate for characterizing energy and mass-transfer events below the heated surface for all six ablative materials. This model is employed in the following section for predicting over-all material performance where any disagreement between predicted and actual material response may be logically attributed to a mistreatment of phenomena at or near the ablating surface.

4.3.2 Surface Response

Three different types of predictions are reported in this section. The ablative material performance of all six nozzles was first predicted utilizing the EST-CMA program combination described above in Section 3. These predictions consider chemical equilibrium at the ablating surface and do not include provision for any mechanical erosion such as liquid-layer run-off or char spallation. Subsequent predictions were performed to consider heterogeneous chemical kinetics or liquid-layer removal phenomena utilizing the GNAT and SCRIMP programs as described in Sections 3.2 and 3.3, respectively. No attempt has been made to construct a realistic mathematical model for representing char spallation phenomena.

The results of these calculations are summarized in Table VI where total predicted surface recession and nominal predicted surface temperature are shown for each of the several predictions for all six nozzles. It may be noted in Table VI that predicted surface recession for the silica-reinforced nozzles (NL-1 and NL-6) is negligible considering only chemical erosion. As a result, a number of subsequent calculations were performed with the SCRIMP program (see Section 3.3) in an attempt to devise a realistic liquid-layer removal model. These efforts were directed primarily toward the silica-phenolic nozzle (NL-1) and are described in detail below in Section 4.3.2.1.

Section 4.3.2.2 gives a description of efforts directed toward evaluating heterogeneous kinetic coefficients for the graphite-phenolic nozzle (NL-2). Particular comments relating to predictions for the remaining 4 nozzles (NL-3 through NL-6) are given in Sections 4.3.2.3 through 4.3.2.6, respectively.

Prior to delving into the details regarding each prediction, however, it is appropriate to summarize the boundary conditions employed for each prediction. All predictions were initiated by specifying the surface temperature history during the starting transient of the arc-plasma simulation device (a period of about 8 seconds). This was done because it is difficult to estimate the actual free-stream gas composition and enthalpy during the start-up period. After steady conditions were achieved in the simulation device, the prediction of surface temperature and recession was initiated. The heat-transfer coefficient ($\rho_e U_e C_H$) for each test is taken as 0.454 times the heat-transfer coefficient calculated with the simplified Bartz equation. This approach resulted from comparisons of the Bartz prediction to measured heat flux data and was described previously (Section 2.2.1.4.3). The recovery enthalpy, H_r , heat-transfer coefficient, $\rho_e U_e C_H$, and cold wall heat flux, q_{cw} , is shown as a function of time for each ablative material test in Figures 41a through 41f. The cold wall heat flux is defined here as the energy transfer rate which would occur to a nonablating surface at room temperature (this includes energy transfer resulting from chemical reactions in the boundary layer). Another set of results which is of general interest, but will be discussed in detail in the sections devoted to each nozzle, is shown in Figures 42a through 42f. These figures display a variety of energy and mass flux terms which are of interest for each prediction and are based upon the first set of predictions employing the EST-CMA program combination. The mass flux terms are represented in the top half of the figures where the normalized pyrolysis gas injection rate, $B'_g = \dot{m}_g / \rho_e U_e C_M$, and char rate, $B'_c = \dot{m}_c / \rho_e U_e C_M$, are shown as a function of time. Surface energy flux terms and subsurface energy absorption terms are shown in the lower half of each figure. These terms include the following:

- $q_{\text{cold wall}}$ - cold wall heat flux
- $q_{\text{hot wall}}$ - heat flux to a nonablating wall at the same temperature as the ablating surface
- q_{cond} - $k\frac{\partial T}{\partial X}\Big|_w$, the energy-transfer rate into the char layer by conduction
- q_{sen} - sensible energy-transfer rate: this is the energy-transfer rate to the hot wall if no chemical reactions occurred in the boundary layer or at the surface

q_{chem} - chemical energy-transfer rate: this energy flux includes a number of terms which represent the net energy-transfer rate to the wall resulting from all chemical reactions in the boundary layer and at the surface between boundary-layer edge species,pyrolysis products and the char surface material

storage - this term represents the rate at which energy is absorbed due to a temperature increase of the virgin material and the char layer

pyrol pickup - this term represents the rate at which energy is absorbed by the pyrolysis gas due to temperature increase and further decomposition as the gas passes through the char layer.

decomp absorption - this terms represents the rate at which energy is absorbed by organic decomposition reactions, i.e., plastic → char + gas.

The mathematical significance of the above terms is described in detail in Reference 39.

Examination of the relative magnitudes of the above terms for the six tests shown in Figures 42a through 42f reveals that the energy transferred to the surface is split about equally between chemical and sensible energy for the two silica-reinforced and the asbestos-reinforced materials all of which have metal oxide surfaces (Figs. 42a, c, and f). The chemical energy transfer rate is much lower than the sensible rate for carbon and graphite-reinforced materials (Figs. 42b and 42d). These materials each have carbonaceous surfaces. For all five of the above materials the net energy-transfer rate into the material, q_{cond}, is on the order of 150 to 200 Btu/ft^2-sec. Referring to Figure 42c, it is noted that the above generalities do not hold for nylon-phenolic. For this material the chemical energy-transfer rate to the surface is negative which means the reactions occurring in the boundary layer and at the surface are predicted to have a rather significant endothermic effect. These energy absorbing reactions reduce the energy-transfer rate into the material (q_{cond}) to about 50 Btu/ft^2-sec, lower by a factor of 3 than for the other materials. This factor is primarily responsible for the low predicted surface temperature for nylon-phenolic (see Figure 28e). At first thought, it is not too apparent why the nylon phenolic-boundary layer reactions should be endothermic while the reactions for the other materials are exothermic. Examination of Table V reveals that the elemental composition of the nylon-phenolic pyrolysis gas products is not vastly different from the rest so one would not expect vastly different reactions to occur with the boundary layer gases. The pyrolysis gases consist primarily of hydrocarbon species and we may consider a typical reaction with the boundary-layer gas to be of the following general form.

$$\underbrace{C_nH_m}_{\text{pyrolysis gas}} + \underbrace{H_2O + CO_2}_{\text{boundary layer gas}} \rightarrow CO + H_2$$

The above general reaction is typically endothermic and reactions of this type are occurring to some extent for all of the ablation materials considered. These reactions are, however, competing with numerous other reactions occurring in the boundary layer which are exothermic, e.g., $2H \rightarrow H_2$. Referring to Figure 42f it is noted that the pyrolysis gas injection rate B'_g is about a factor of 3 larger for nylon phenolic than for the other materials. This results in a proportionately larger quantity of endothermic reactions to the extent that the over-all effect is very significantly endothermic.

Another interesting factor in Figures 42a through 42f is the division of energy transferred into the material. In all cases this energy is roughly equally divided between sensible energy rise of the material (plastic and char) and energy absorbed by the pyrolysis gas in depth. In all but one case (asbestos-phenolic) the energy absorbed in char formation reactions is not very significant. For asbestos phenolic, however, about 20 percent of the energy conducted in is absorbed in the char formation reaction. This is a direct result of the water vaporization energy which is presumed to be absorbed during dehydration of the asbestos fibers (see Appendix C). In the following sections the ablation response predictions are considered in the light of the measurements, and subsequent attempts to bring about better agreement between predictions and measurements are described.

4.3.2.1 Silica Phenolic (NL-1)

The response of the silica-phenolic nozzle was predicted first with the EST-CMA program which does not consider liquid-layer removal. This was followed by a series of numerical experiments utilizing the EST-SCRIMP program combination in an effort to better understand the parameters of primary importance in modeling liquid-layer removal phenomena. The primary objective of these efforts was to devise a reasonable and acceptable method for predicting the response of silica-reinforced ablative materials. The CMA-EST program predictions are described first and are followed by a description of predictions with the SCRIMP program.

4.3.2.1.1 EST-CMA program prediction

The assumptions embodied in the EST-CMA program combination were described in Section 3. The results of the equilibrium ablation solution with no liquid-layer removal are shown in Figures 21a and 28a where the predicted surface recession and temperature histories are compared to the measured data. The predicted surface temperature is very good, but the predicted recession

is practically nil; whereas, the actual recession is 68 mils. Evidently, the discrepancy is due to liquid-layer flow, since post-test examination of the actual nozzle shows a lumpy,glassy layer of SiO_2*covering the surface. The EST-CMA combination correctly predicts a SiO_2* surface, but accounts only for thermochemical erosion of SiO_2* , which proceeds very slowly in the environment being considered. The fundamental motivation behind constructing the SCRIMP program was to provide a realistic scheme for evaluating the response of materials which are characterized by a liquid silica surface. Results achieved with the SCRIMP program are described next.

4.3.2.1.2 SCRIMP program prediction

The SCRIMP program was used to generate a large number of predictions for parametric variations of the adjustable parameters of this program. The fundamental principles embodied in the SCRIMP program were described above in Section 3.3. Before discussing the various parameters of interest, however, it might be well to point out that all the calculations employed certain important physical models: (1) The pyrolysis gases are always in equilibrium as they pass through the char, except that condensed phase products are not allowed to form; (2) the same model applies to the SiO + CO reaction gas, and (3) the surface thermochemical calculations presume equilibrium.

The adjustable parameters may be listed as follows:

1. liquid-layer edge carbon density[4]
2. maximum liquid-layer thickness allowed
3. silica-carbon reaction kinetic parameters
4. thermal conductivity model for the reaction area

The significance of each of the first three parameters is obvious. A variety of plausible values can be tried for the liquid-layer edge carbon density and the maximum allowed liquid-layer thickness. Nominal values for the silica-carbon reaction kinetic parameters may be obtained from Reference 34, but since such data are inherently not very accurate, it is of interest to explore the effects of different kinetic values.[5]

The choice of a model for thermal conductivity involves more complex considerations which are described next.

[4] The liquid-layer edge carbon density represents the quantity of carbon residue present in the silica-carbon matrix which divides the char layer and the liquid layer. For higher carbon contents in the mixture the carbon acts as a structural matrix and prevents the silica from flowing. When the carbon content is below this value, the mixture acts more like a liquid layer, i.e., a sea of silica containing lumps of carbon.

[5] The "nominal values" for the kinetic parameters are $A = 9 \times 10^7$ sec^{-1} and $B = 80{,}000$ cal/mole as cited in Appendix B. These values were used in calculations 1 - 6 reported below and illustrated in Figure 43.

Thermal Conductivity Model for Silica-Carbon Reaction Zone

It is not very obvious what should be done for a thermal conductivity model in the zone where silica-carbon reactions are occurring. This is the case because as silica-carbon reactions proceed, a "frothy like" silica foam is generated with varying amounts of carbon particles present depending on the extent to which the reaction has proceeded. Presumably, a literature search could provide some guidance for evaluating conductivity of porous, composite materials. Alternatively, a "recalibration" of the in-depth thermal conductivity model using the SCRIMP program, as was done for the CMA program and described in Section 4.1 above, might be sufficient.

The first mentioned possibility was excluded due to time pressure and the second would have to be done for each variation of the other parameters, obviously an expensive and time-consuming task. For the present study, a much simpler but not unreasonable procedure was adopted as described below.

It is suggested that it will be adequate to give conductivity data for the carbon-silica reacting mixture as a function of density,[6] temperature, and some factor to account for the geometrical appearance of the porosity of the material. With this general objective in mind, a fairly plausible thermal conductivity model can be constructed for the silica-carbon reaction zone. The details of the model are somewhat complicated and, therefore, are relegated to Appendix D. The present section gives only a sketch of the model and an overview of the important implications:

The conductivity model will be "tied to" a number of easily identifiable composition points for which the conductivity (as a function of temperature) is well known. For densities below the char density, some density dependence must be postulated. In addition, some allowance for the effect of the porosity arrangement (an effect independent of the density dependence) must be included. This factor is both very strong and largely unknown and is left as an adjustable parameter. Thus, given the density model (as described in Appendix D), the thermal conductivity in the reaction zone has only one adjustable parameter.

The proposed density and porosity model offered in Appendix D undoubtedly has numerous deficiencies. It has the virtues of being plausible and of having

[6] Since it is presumed that silica-carbon reactions do not begin until after the virgin material has been completely pyrolyzed to pure char, then density uniquely fixes the carbon-silica ratio for all nodes (except the surface node, where carbon can accumulate due to the restriction that carbon does not flow away with the silica, but since experience shows that for problems of current interest carbon rarely accumulates, the exception is not significant). Thus, density alone accounts for all the composition information needed for the proposed conductivity model.

one important adjustable parameter. Unfortunately, the calculations described below indicate that the conductivity in the reaction zone is a key parameter influencing the predicted response; hence, either a truly well founded model or some experimental data will be required for future work. Since the present work is chiefly devoted to discovering and exploring the important aspects of the prediction problem, the present model, with its one dominating adjustable parameter, is suitable as a first step.

Typical SCRIMP Predictions

Figure 43 shows a number of SCRIMP predictions made for various values of important parameters such as maximum allowed liquid-layer thickness, indicating both the predicted surface temperature history and the predicted surface location history. It will be noted that the surface temperature predictions oscillate; these oscillations are unimportant and are due to

1. the assigned-temperature computation start for the first 8 seconds (for reasons discussed in Section 4.3.2). At the switch to a surface equilibrium procedure at 8 seconds, the solution usually finds itself at a slightly inappropriate temperature and has trouble seeking its own level, and
2. a too large nodal size, chosen for reasons of economy during the parametric study.

Perhaps the most striking feature of the predictions viewed as a group is the general accuracy of the temperature predictions combined with generally low recession predictions. This suggests that the surface thermochemistry treatment is probably correct but that the treatment of subsurface thermal conductivity and of liquid-layer flow needs improvement.

Detailed comparison of the series of predictions shown in Figure 43 indicates that of the four parameters involved, minor importance may probably be attached to the kinetic constants of the silica-carbon reaction and to the maximum allowed liquid-layer thickness. The liquid-layer carbon density (the quantity of carbon below which the material is presumed to behave like a liquid layer) and the reaction zone conductivity, on the other hand, appear to have a dominating influence on the predictions, primarily because they have a major influence on the "rate of creation of liquid layer" available for runoff.

None of the predictions shown in Figure 43 does an outstanding job of predicting the observed total recession although prediction 4 is respectable, showing 52 mils, compared with the measured 68 mils. No doubt, some further juggling of the primary parameters would produce a "better" prediction. However, no additional calculations were performed since the existing array of predicted results had served its intended purposes of yielding at least one "close" prediction and of revealing the dominating aspects of the problem.

The relative accuracy of the predicted surface temperature is encouraging in that it tends to give confidence in the relatively complex, generalized chemistry boundary conditions employed in the solution. Clearly, some further efforts are required to obtain an entirely satisfactory prediction scheme, but it is believed that the significant parameters identified in the study represent the key to obtaining a satisfactory prediction technique.

4.3.2.2 Graphite Phenolic (NL-2)

The equilibrium prediction (EST-CMA) for graphite-phenolic resulted in a surface temperature that was too low (about 500°R, see Figure 28b) and a surface recession that was too high (about 50 percent, see Figure 21b). It is noted that the measured surface temperature for this material is below the others by from 400°R to 900°R, and, as such, if heterogeneous chemical kinetics are controlling in any of the tests, this is the most likely candidate. Efforts directed toward evaluating the appropriate kinetic coefficients are described in this section.

Generation of the GNAT computer program was motivated by past experiences in predicting too much surface recession for carbonaceous surfaces in the presence of certain oxidizing environments. The predicted equilibrium recession and surface temperature, shown in Figures 21b and 28b for the graphite-phenolic nozzle is a prime example of such an experience. The primary reactions likely to control surface recession for carbonaceous surfaces in the N_2O_4-N_2H_4/UDMH environment were identified above in Section 3.2.1 where it was shown that oxidation of carbon by H_2O and CO_2 represented the primary potential for surface recession. The GNAT computer program enables consideration of heterogeneous chemical kinetics for these reactions plus two others. The reactions constrained to obey kinetic laws in the GNAT program were given in Section 3.2.2 and are repeated here for convenience.

$$C^* + H_2O \rightleftarrows CO + H_2 \qquad (7)$$

$$C^* + CO_2 \rightleftarrows 2CO \qquad (8)$$

$$2C^* + O_2 \rightleftarrows 2CO \qquad (9)$$

$$CO + H_2O \rightleftarrows CO_2 + H_2 \qquad (10)$$

The kinetic rate laws of the first 3 (heterogeneous) reactions are given in terms of the carbon mass consumption rate per unit area.

$$\dot{m}_{C,7} = \pm k_{f,7} \left| P_{H_2O} - \frac{P_{CO}P_{H_2}}{K_{P,7}} \right|^{n_7} \tag{11}$$

$$\dot{m}_{C,8} = \pm k_{f,8} \left| P_{CO_2} - \frac{P_{CO}^2}{K_{P,8}} \right|^{n_8} \tag{12}$$

$$\dot{m}_{C,9} = \pm k_{f,9} \left| P_{O_2} - \frac{P_{CO}^2}{K_{P,9}} \right|^{n_9} \tag{13}$$

The kinetic rate for the water-gas shift reaction is given in terms of the water consumption rate per unit surface area. Expressing the rate coefficient in this manner, rather than per unit volume, implies that the reaction is surface catalized.

$$\dot{m}_{H_2O,10} = \pm k_{f,10} \left| P_{H_2O}P_{CO} - \frac{P_{CO_2}P_{H_2}}{K_{p,10}} \right|^{n_{10}} \tag{14}$$

In each equation, the sign out front takes on the sign of the difference within the absolute brackets, and the rate coefficient is given in Arrhenius form

$$k_{f,n} = k_n \; e^{\frac{-\Delta E_n}{RT}} \tag{15}$$

Table VII displays the variety of rate coefficients, activation energies, and reaction orders employed in the sequence of calculations performed to predict the proper total surface recession for the graphite-phenolic nozzle. Some rough estimates of rate coefficients were first taken from the literature (Refs. 3 and 14) in order to establish the need for giving detailed consideration to any particular set of rate coefficients. It is apparent from the coefficients in Table VII, and the above equations, that the CO_2 and O_2 oxidation reactions will essentially go to equilibrium at the temperature and pressure of interest so no further consideration was given to detailed evaluation of the coefficients for Reactions 8, and 9. Kinetic coefficients for the water-gas-shift reaction (10) are not included in Table VII because this reaction was "turned-off" in the calculations ($K_f = 0$) in order that the "shift" reaction did not consume the water and generate CO_2 which would in turn, react essentially to equilibrium.

The literature value for the water gas rate coefficient shown in Table VII

would be such as to produce very little ablation so no prediction was performed with that rate coefficient. Instead, a series of three calculations was performed with the rate coefficients designated in the table as 1st, 2nd, and 3rd iteration . Each successive prediction was followed by an upward adjustment in the rate coefficient in order that the subsequent prediction would result in a predicted recession equal to that measured. This goal was accomplished with the third iteration . The results of this last prediction are shown in Figures 21b and 28b along with the corresponding predictions assuming chemical equilibrium. It is encouraging to note that for the final prediction, the surface temperature also agrees with the measurement, but no constraint was imposed to force agreement with the measured surface temperature. The agreement suggests that surface energy transfer events are being treated properly.

In order to better illustrate the role played by the kinetic coefficients in the ablation prediction, some results from the EST and GNAT programs are shown in Figures 44 through 46. Figure 44 displays a generalized surface ablation rate map for graphite-phenolic in the simulated rocket environment when chemical equilibrium is assumed. This map, generated with the EST program, shows the normalized char ablation rate, B'_c, as a function of surface temperature with normalized pyrolysis off-gas rate, B'_g, as a parameter. The map represents a part of the generalized ablating surface boundary condition for the CMA program prediction for the equilibrium case. A corresponding set of results for a single pyrolysis gas rate ($B'_g = .225$) is shown in Figure 45 where the equilibrium char rate (B'_c) is compared to that for each of the three sets of kinetically controlled predictions performed with the GNAT program. It may be noted that the char rate for the kinetically controlled calculations is substantially lower than for the equilibrium case. The generalized ablation rate for the 3rd (last) iteration is shown in Figure 46 for all three pressures and pyrolysis gas rates of interest for the NL-2 nozzle. This figure represents a part of the generalized boundary conditions for the CMA prediction with kinetics shown in Figures 21b and 28b.

In conclusion it may be stated that a reasonable technique has been devised for predicting the response of graphite-phenolic in an oxidizing environment. The kinetic coefficients have been backed out from the data, and if the proper reactions have been selected in the mathematical model, then the technique should be relatively general. It is believed that a fair amount of evidence has been presented to support the opinion that the water-gas reaction is the dominating surface eroding reaction, and furthermore, that it is most likely kinetically controlled at the temperature experienced with graphite-phenolic in the experimental program.

4.3.2.3 Asbestos-Phenolic (NL-3)

The predicted equilibrium surface temperature agrees well with the measurement (Fig. 28c), but no surface recession is predicted and the measured ablation rate for this material is very high (Fig. 21c). Chemical equilibrium dictates that the surface material will be MgO which has originated from the asbestos fibers. The measured surface temperature of about 3600°R is well below the melt temperature of MgO so if it is removed mechanically the fibers must be breaking and being swept away. Visual examination of the char layer reveals only slight traces of "metal oxide-appearing species" with the surface material being predominantly carbonaceous in appearance. The surface recession for this material is substantially greater than could be rationalized from equilibrium considerations even if the MgO fibers are assumed to be removed from the matrix, and, as such it is concluded that mechanical removal of the char plays a dominant role in the recession of this material. Because of the poor performance of this material in the rocket engine environment, no efforts were expended to construct a phenomenological surface recession law for this material.

4.3.2.4 Carbon-Phenolic (NL-4)

The predicted surface recession and temperature histories for the equilibrium case are shown in Figures 21d and 28d, respectively. The predicted surface recession agrees well with the measurements, but the predicted surface temperature is from 500°R to 800°R too low. A subsequent prediction was performed considering chemical kinetics in order to assess how much higher the surface temperature would get if the water-gas reaction was slowed down. The kinetic rate coefficients derived from the graphite-phenolic nozzle (Table VII) were employed and the results for this calculation are also shown in Figures 21d and 28d. It is noted that a slight increase in surface temperature did result, but not near enough to agree with the measurement. As expected, the prediction also resulted in a substantial reduction in predicted surface recession.

It must be concluded that the techniques are not adequate to predict the response of this material. It would be helpful to have more data of the type generated herein in order to insure that the single test considered does not contain any anomalies. The equilibrium prediction does give a good indication of the measured surface recession, and, as such, the EST-CMA program combination is perhaps the most reasonable technique for predicting the response of this material.

4.3.2.5 Nylon-Phenolic (NL-5)

The equilibrium prediction of surface temperature and recession shown in Figures 21e and 28e reveal that both predictions are substantially below the

measurements. The predicted surface recession is too low primarly because the char layer experienced substantial spallation which was not included in the prediction. A subsequent prediction was made considering chemical kinetics in order to see if the predicted surface temperature could be brought into agreement with the data. An increase in predicted surface temperature did occur, but not enough to agree with the measurement. No further effort was expended to correlate these data, because nylon-phenolic is not a good performer in the simulated rocket-engine environment.

4.3.2.6 Silica-Phenyl Silane + Buna "N"

The equilibrium prediction for this material was quite similar to the equilibrium prediction for the silica-phenolic nozzle in that the surface temperature and composition are correctly predicted, but the predicted surface recession is nil (Figs. 21f and 28f). Poor agreement with predicted and measured surface recession is attributed to liquid-layer removal phenomena which are not included in the straight equilibrium (EST-CMA) prediction.

One prediction for this nozzle was performed with the SCRIMP program and these results are also shown in Figures 21f and 28f. The predicted surface recession is low by about a factor of 2, but the predicted surface temperature is not bad. The primary difference between the char structure for this material and the silica-phenolic material (NL-1) is that the carbon residue fraction in the char is substantially lower (0.1 vs 0.15, see Table V). It is expected that this difference has a significant effect upon the various parameters that must be specified for the SCRIMP solution such as carbon content at the char-liquid-layer interface and possibly, maximum liquid-layer thickness allowed. The predictions shown in the figure were based upon a carbon density at the char-liquid interface at 6 lb carbon/ft^3, (rather than 7 for silica phenolic) and a liquid-layer thickness of 0.015 inch.

It is believed that additional efforts directed toward correlating these data with the SCRIMP program would result in a far more acceptable prediction than is shown in the figures.

4.4 DATA CORRELATION SUMMARY

The modified theoretical techniques described in Section 3 have been put to the test of correlating the experimental ablation data presented in Section 2. The correlations consisted of utilizing the theoretical techniques and the data to establish the most probable values of several undefined coefficients required for theoretical evaluation. The undefined coefficients relate to, (1) thermal conductivity of the virgin, char, and partially degraded material, (2) kinetic coefficients which control the rate of surface (char) oxidation, and (3) specific criteria included in the semi-empirical

liquid layer removal model. No attempt was made to construct a phenomenological model to represent char spallation. Surface recession for 2 of the 6 materials considered (nylon-phenolic and asbestos-phenolic) is believed to be controlled by mechanical failure of the char layer, and, as such, a major part of the correlation effort was directed toward the other four materials (silica-phenolic, graphite-phenolic, carbon-phenolic, and silica-phenyl silane + Buna "N").

The correlation effort was conducted in two phases. Phase 1 consisted of specifying measured surface temperature and recession histories as boundary conditions in the CMA program in order to establish an acceptable thermal conductivity model for the subsurface solutions. Thermal conductivity coefficients were varied in an iterative manner until agreement between predicted and measured subsurface thermocouple histories was achieved. It is encouraging to note that the final subsurface correlation resulted in good agreement between measured and predicted degradation depths as well. Phase 2 of the data correlation effort consisted of a series of predictions of the overall ablative material performance utilizing the subsurface solution demonstrated as adequate in Phase 1. The Phase 2 correlations consisted of predicting the surface temperature and recession histories and varying surface interaction coefficients in an iterative manner until reasonable agreement was achieved between prediction and data. Surface interaction coefficients that were varied consisted of heterogeneous kinetic coefficients for surface (char) oxidation and liquid layer removal parameters such as maximum allowed liquid layer thickness and carbon content at the edge of the liquid layer.

Results of the data correlations are summarized in Table VI where it is noted that reasonable agreement between predicted and measured surface recession is achieved with silica-phenolic, graphite-phenolic, and carbon-phenolic. Relatively poor agreement was achieved with the silica-phenyl silane + Buna "N" nozzle but it is believed that good agreement could be achieved with more effort directed toward better establishing the empirical liquid layer removal coefficients. As noted above, significant surface recession resulting from mechanical char failure is evident for the remaining two nozzles (asbestos-phenolic and nylon-phenolic) so no effort was directed toward achieving correlation for these two materials.

In the following section the theoretical techniques believed to be most realistic are employed to predict the response of the six materials in a rocket engine firing.

SECTION 5

PREDICTION OF ABLATIVE MATERIAL RESPONSE FOR ROCKET ENGINE FIRINGS

The careful reader of this report will have detected in the analysis the utilization of more than a few assumptions which lack rigorous justification. These assumptions relate to the basic treatment given certain fundamental phenomena (e.g., liquid layer removal), the nature of the boundary layer edge conditions (e.g., is the boundary layer edge gas in a rocket engine representative of the nominal O/F ratio?), and the many coefficients which relate to material properties (e.g., thermal conductivity). The assumptions that have been made are the result of careful consideration for numerous factors and are believed reasonable in the light of available information. The results presented in this section demonstrate the collective effect of all assumptions upon the accuracy of the analysis. These analyses include the experimental simulation technique described in Section 2, the theoretical techniques presented in Section 3, and the empirically derived coefficients presented above in Section 4. The accuracy and applicability of these analysis techniques for ablative material performance prediction in liquid propellant rocket engines is established in this section by comparing predicted and measured performance for each of six materials fired in rocket engine tests.

Rocket engine firing conditions are presented first, in Section 5.1. Next, in Section 5.2, particulars relating to the predictions are described, and last, in Section 5.3, comparisons of predicted and measured ablative material performance are presented.

5.1 ROCKET ENGINE FIRING CONDITIONS

Six rocket engine firings were conducted by the Chemical Rocket Evaluation Branch at the NASA Lewis Research Center. The primary purpose of the firings was to evaluate ablative material performance in a liquid propellant rocket engine. The six materials tested were taken from the same lot as those tested in the rocket simulation tests described above, in Section 2, so the materials tested by both techniques should be identical and any differences in performance of a given material must be related to inadequate simulation rather than differences in material make up. Certain rocket engine operating conditions were forwarded to Aerotherm prior to making the predictions in order that the input boundary conditions for the predictions would be as realistic as possible. The rocket engine operating conditions are presented in this section.

Actual rocket engine operating conditions for each test are summarized in Table VIII. The propellant was N_2O_4 - 50 percent N_2H_4 + 50 percent UDMH

with a nominal oxidizer to fuel mass ratio (O/F) of 2.0. The nominal chamber pressure at test initiation was 100 psi and test termination occurred at a chamber pressure of 90 psia. The nozzle throat diameter was 1.2 inches and the nozzle contour is shown in Figure 4b. Rather than predict the throat erosion for a given firing time, the predictions consisted of predicting the firing time that would produce sufficient throat erosion to cause the observed chamber pressure decay. Particulars relating to the predictions are presented next.

5.2 ROCKET PREDICTIONS

The basic approach taken to predict the response of the six ablative materials tested in the rocket engine is described here. Two primary questions need be answered to make the predictions: (1) what is the heat transfer coefficient in the throat of the rocket engine, and (2) how should mechanical erosion be treated for those materials which are expected to experience char fragmentation. Heat transfer coefficient evaluation is discussed first and is followed by a brief description of the prediction technique employed for each nozzle.

Heat Transfer Coefficient

Calorimeter data such as obtained for the simulation tests are not available for the rocket engine firings so it was not possible to establish values of the throat heat and mass transfer coefficients with confidence. The value of the heat transfer coefficient employed for the predictions was estimated from data presented in Reference 1. The data consists of subsurface temperature measurements in a molybdenum nozzle having a 1.2 inch diameter throat. The data were taken for a hydrogen-oxygen rocket engine operating at a chamber pressure of 100 psia. In Reference 1, the throat heat transfer coefficient for these firings was rationalized as 60 percent of that predicted by the simplified Bartz equation (Ref. 13). Based upon the similarity of the rocket conditions considered in Reference 1 and those of interest here, (i.e., P_c = 100 psia, D* = 1.2 inch) the heat transfer coefficient is taken as 60 percent of that predicted by the simplified Bartz equation as interpreted in Appendix A of Reference 1. This interpretation simply converts the heat transfer coefficient to an enthalpy driving potential rather than a temperature driving potential in order to more correctly consider real gas effects in the chemically reacting boundary layer. Heat transfer coefficients evaluated in this manner for each of the six rocket engine firings are shown in Table VIII along with the rocket engine operating conditions. The coefficients shown are those for the initial conditions also shown in the table. The reduction in heat transfer coefficient resulting from chamber pressure decay

and increased throat area are accounted for automatically in the predictions based upon the computed surface recession.

Silica-Phenolic

The response of the silica-phenolic nozzle in the rocket engine firing was predicted employing the EST-SCRIMP computer program combination as described above, in Sections 3.3.3 and 4.3.2.1. Based upon the relative agreement between measured and predicted response for the arc-plasma simulation tests shown in Figure 43, the empirical coefficients utilized in prediction Number 4 were employed for the rocket nozzle prediction. These coefficients are as follows:

1. Silica-carbon reaction rate coefficients are the nominal values of ΔE = 80,000 cal/mole and A = 9 x 10^7 sec^{-1}.
2. Carbon content which establishes the point in the char where the char behaves as a liquid layer is 7 lb/ft^3, i.e., where there is more than 7 lb/ft^3 carbon it behaves as a pure char, and when there is less than 7 lb/ft^3 carbon it is treated as a liquid layer.
3. The maximum allowed liquid layer thickness is 2 mils (0.002 inch).
4. The silica foam thermal conductivity parameter is 0.5 (see Appendix D).

Graphite-Phenolic

The graphite-phenolic nozzle response in the rocket engine was predicted with the GNAT-CMA program combination utilizing the heterogeneous char oxidation kinetic coefficients shown in Table VII (third iteration).

Asbestos-Phenolic

As discussed in Section 4.3.2.3, mechanical erosion of the char layer is suspected as the dominant surface recession mechanism for this material. Since no phenomenological model was developed for representing this mechanism, an empirical approach, based upon the simulation test results, was taken for predicting the performance of this material. The prediction was accomplished by two passes with the computer programs. First, the EST-CMA program combination was employed for a standard prediction. Because of the good agreement between predicted and measured surface temperature for this material previously, (Fig. 28c) the resulting predicted temperature was taken as correct. A second prediction was then made specifying the surface temperature history from the first prediction and specifying the surface recession rate in the following manner.

$$\dot{S}_{rocket} = \dot{S}_{arc} \frac{\int_0^{\tau_{rocket}} (\rho_e U_e C_H)_{rocket} d\theta}{\int_0^{\tau_{arc}} (\rho_e U_e C_H)_{arc} d\theta} \left(\frac{\tau_{arc}}{\tau_{rocket}} \right)$$

where τ represents the total firing time. Utilization of the above equation simply implies that whatever mechanism is controlling surface recession will depend in a linear manner upon the heat transfer coefficient. It is recalled that the rocket firing time, τ_{rocket}, is not known a priori, but the relation may be evaluated quite accurately a priori by noting that the variation of heat transfer coefficient with time for the rocket is fairly linear (since there is such a small chamber pressure decay). Evaluating the integral in the numerator assuming a linear variation of heat transfer coefficient with time results in the following expression for the surface recession rate in the rocket.

$$\dot{S}_{rocket} = \dot{S}_{arc} \frac{\tfrac{1}{2}\left[(\rho_e U_e C_H)_{initial} + (\rho_e U_e C_H)_{final} \right]_{rocket}}{\int_0^{\tau_{arc}} (\rho_e U_e C_H)_{arc} d\theta / \tau_{arc}} \qquad (27)$$

where $\dot{S}_{arc}$ is taken as the average recession during the measured period of active ablation and the integral in the denominator is evaluated by referring to Figure 41c. The prediction for the asbestos-phenolic nozzle corresponds to utilizing the surface temperature history from the prediction with no surface recession and a constant recession rate obtained from the above equation.

Carbon-Phenolic

The predicted equilibrium surface recession for the carbon-phenolic nozzle compared rather well to that measured in the simulation tests (see Table VI). Because of this, the response of carbon-phenolic in the rocket engine environment was predicted employing the standard EST-CMA program combination.

Nylon-Phenolic

The previous prediction for the nylon-phenolic surface temperature (Fig. 28e) was about 1,000°R below the measured surface temperature so the surface

temperature for the rocket prediction was set equal to that measured in the simulation test (3,600°R). Because the previously predicted equilibrium surface recession (Fig. 21e) for this material was in the same range as the data, the surface recession for nylon-phenolic in the rocket environment was computed from chemical equilibrium considerations utilizing the EST-CMA program combination.

Silica-Phenyl Silane + Buna "N"

Insufficient experience was gained with the SCRIMP program to predict the performance of this material. As pointed out previously, (Section 4.3.2.6) this material differs substantially from silica-phenolic and significant adjustment of the input coefficients would appear to be in order. The performance of this material in the rocket engine environment was predicted in the same manner as asbestos-phenolic (see above). The surface temperature history was predicted from equilibrium considerations with the EST-CMA program combination and the surface recession rate was specified as equal to the measured recession during the period of active ablation in the arc test times the ratio of average heat transfer coefficient in the rocket to that in the arc (Eq. (27)).

5.3 COMPARISON OF PREDICTION AND DATA FOR ROCKET ENGINE FIRINGS

The predicted and measured ablative material performance for each of the six rocket engine tests are presented in Figures 47(a) through 47(1). The lack of agreement between data and prediction is discouraging. Because of the many complex interactions that govern the ablative material performance it is rather difficult to identify the specific phenomena responsible for the rather wide disparity between predicted and measured surface recession rates. Because surface temperature histories were not measured in the rocket engine tests, no direct comparisons can be made between predicted and measured surface temperature histories, however, it is possible to gain an approximate feeling for discrepancies between predicted and actual surface temperature histories by comparing predicted and measured subsurface temperature histories while considering the effect of differences between predicted and measured surface recession histories. Surface recession results presented in Figure 47 for the six nozzles are summarized in Table IX along with comparisons to predicted recession rates, and measured recession rates in the arc-plasma simulation tests. No effort was expended to offer extensive rationalization of the poor predictions for the rocket engine tests. It is believed, however, that brief consideration of some of the fundamental assumptions in the light of these results will be informative. Some general comments regarding the comparisons are given first, in Section 5.3.1, and are followed, in

Section 5.3.2, by conclusions regarding the most probable causes of poor agreement between prediction and data.

5.3.1 General Comments on Comparisons

Some generalizations regarding trends between predicted and measured ablative material performance in the rocket engine environment may be made and are listed here.

1. The predicted recession rates are between 2 and 3 times greater than the measurements.
2. The predicted initiation of ablation is substantially before ablation actually begins.
3. The actual surface temperature is, in most cases, higher than that predicted.
4. The relative rating of measured material performance is about the same as that predicted.

Material	Relative Rating*	
	Actual	Predicted
Silica-phenolic	1	1
Graphite-phenolic	2	2
Asbestos-phenolic**	5	6
Carbon-phenolic	4	3
Nylon-phenolic**	6	5
Silica-phenyl silane + Buna "N"**	3	4

*1 - lowest average recession rate
6 - highest average recession rate

**Predictions based upon pure empiricism, i.e., surface energy and mass balance not satisfied.

5.3.2 The Most Probable Causes of Discrepancy

It is interesting to note that all predictions are in error in the same direction and by roughly the same amount. This fact is encouraging for the following reason. The predictions incorporate a number of assumptions regarding a rather wide variety of different phenomena which control the response of each material. It is unlikely that some error has been made in the mathematical representation of each phenomena (e.g., thermal conduction,

liquid layer removal, and kinetic coefficients) in such a manner that the net effect for each different material is about the same. Indeed, such an occurrance is possible, but a more probable cause of a constant source of error would be in the evaluation of the boundary conditions. It is believed that the boundary conditions at the throat of the rocket engine are relatively repeatable from test to test, and, as such, a shift in the boundary conditions relative to the assumed boundary conditions would be expected to produce a shift in material performance of a relatively constant nature. A comment is offered here relative to 2 boundary conditions believed to be of primary importance.

1. The heat transfer coefficient employed for the rocket predictions is questionable. The value of 60 percent of the Bartz heat transfer coefficient is believed reasonable, but certainly not beyond reproach. It is noted that the surface recession for a given material is related in a near linear manner to the heat transfer coefficient.

2. All experimental simulations and theoretical predictions performed during this effort are based upon the assumption that the rocket engine products are well mixed and that the boundary layer edge thermodynamic state is representative of the average oxidizer-fuel ratio. It is well known that injectors for liquid propellant rocket engines are most usually designed to provide a fuel rich film near the chamber and nozzle walls in order to reduce surface recession. No specific data are available upon which to evaluate the local mixture ratios for the rocket engine tests being considered here, so the local mixture ratio was taken equal to the average. This assumption is believed reasonable in the absence of contradictory data, but it is believed to represent a potential source of large error in predicted ablation rate.

The two above items are offered as the most probable cause of discrepancy between prediction and data. This is not to say that other assumptions in the analysis are not subject to question. They certainly are, but errors resulting from them are not believed sufficient to produce discrepancies as large as those experienced. The effect of the heat transfer on ablation rate is relatively straightforward to comprehend, but the effect of local oxidizer-to-fuel ratio variations is more difficult to appreciate physically. Oxidizer-fuel variations cause two important effects, (1) the quantity of chemical constituents which are hostile to a particular material is changed, and (2) the energy level, or local recovery enthalpy may be substantially changed. In order to provide some insight into the possible quantitative effects of

local oxidizer-fuel variations, a series of steady state ablation calculations was performed assuming chemical equilibrium. Input for the solutions was generated with the EST program and the steady state surface energy balance presented in Reference 1 was solved for a series of oxidizer-to-fuel ratios considering N_2O_4-N_2H_4/UDMH propellant and each of two ablation materials, silica-phenolic and graphite-phenolic. For these calculations the recovery enthalpy was taken to be that corresponding to adiabatic combustion of oxidizer and fuel at the local mixture ratio being considered. The results are presented in Figure 48 where normalized surface recession rate is shown as a function of local oxidizer-to-fuel ratio. It is noted that a local oxidizer-to-fuel ratio of 1.2 results in half the thermochemical surface recession predicted for a ratio of 2.0.

5.4 SUMMARY

The results of rocket engine tests for six ablative materials are presented and compared to predictions utilizing the techniques described in previous sections. The predicted surface recession rate is generally from 2 to 3 times greater than that measured. Probable causes of the discrepancy are considered and it is concluded that either one of, or a combination of, two effects are primarily responsible, (1) an ill-defined heat transfer coefficient, and (2) a poorly defined boundary layer edge thermodynamic state resulting from a local off-optimum mixture ratio.

In the following section recommendations are offered for quantitative investigation of these effects and the relation of these effects to ablative material performance in a rocket engine.

SECTION 6

CONCLUSIONS AND RECOMMENDATIONS

Major conclusions reached during the course of the study are summarized first and are followed by a list of recommendations believed appropriate for improved analysis of ablative material performance in liquid-propellant rocket engine environments.

6.1 CONCLUSIONS

1. A valid subscale simulation test of ablative material performance phenomena should include duplication of the following parameters.
   a) Elemental composition of the boundary layer edge gas ($\tilde{K}_{ke}$)
   b) Total enthalpy (H_o)
   c) Boundary layer heat transfer coefficient ($\rho_e U_e C_H$)
   d) The variation of nozzle area ratio in the streamwise direction at the test section ($A/A^* = f(x)$)
   e) An additional requirement is that the local pressure should be within a factor of 2 of that in the rocket engine.
2. It is possible to duplicate the parameters in the above list for a wide range of rocket engine conditions (see Figure 1) utilizing an arc-plasma generator in the 500 kw range which operates on mixtures of commercially available gases.
3. Chemical kinetics of the water-gas reaction play a significant role in governing the ablative material performance of carbonaceous chars in the N_2O_4 - N_2H_4/UDMH environment. Inclusion of a kinetic rate law in a computational scheme (GNAT program) enabled correlating graphite-phenolic ablation data acquired in the simulation tests.
4. The recession rate of carbon-phenolic is substantially greater than the recession rate of graphite-phenolic because of chemical kinetic effects. Although the two materials are identical chemically, the lower carbon-phenolic thermal conductivity results in a higher surface temperature and thereby faster reactions rates.
5. Both asbestos- and nylon-phenolic experience rather severe mechanical erosion in the form of char failure in the simulated rocket engine environment.
6. High silica content reinforced materials are consumed primarily as a result of liquid layer removal from the surface.
7. A computer program (SCRIMP) written to model the primary phenomena governing the response of silica-reinforced materials enables relatively realistic mathematical modeling of material response. The following conclusions relate specifically to experience with the SCRIMP program during data correlation efforts.
   a) SiO gas products formed in depth from reactions between silica and carbon is re-oxidized at the surface resulting in SiO_2

precipitation at the surface. The energy associated with this precipitation cancels the energy absorbed in depth so the net energy effect of silica-carbon reactions is small.

b) The maximum allowed liquid layer thickness in the solution has minor influence in predicted recession rate and hence the rudimentary treatment of liquid layer removal phenomena appears justified.

c) The most important parameters governing liquid layer removal are thermal conductivity of the liquid layer, and the criteria for defining the location of the interface between the char and liquid layer.

8. The local oxidizer-to-fuel mixture ratio at the boundary layer edge is very important in controlling ablative material performance, and predicted ablation rates assuming complete mixing in the combustion chamber may differ by factors of 2 or 3 from reality.

6.2 RECOMMENDATIONS

The investigations performed on this program have provided insight into basic ablative material degradation mechanisms and have resulted in the generation of experimental and mathematical analogs which model the primary phenomena that control ablative material performance in a liquid propellant rocket engine. Certain additional efforts are required however, to relate boundary conditions in the simulation device to those in a rocket engine, and additional simulations (both experimental and numerical) should be performed to investigate the effect of variation of primary variables over their anticipated range of variation in a rocket engine. Specific recommendations directed toward accomplishing the necessary investigations are listed here.

1. A series of experiments should be conducted in the arc-plasma rocket simulator for a wide range of oxidizer-to-fuel ratios while holding boundary layer edge gas temperature, pressure, and heat transfer coefficient constant; and for a wide range of chamber temperatures while holding oxidizer-to-fuel ratio, pressure, and heat transfer coefficient constant. Such a series of tests could be performed on several materials of interest (e.g. silica-phenolic and graphite-phenolic) in order to derive fundamental material response data resulting from the variation of only one pertinent parameter at a time. Both the boundary layer edge gas chemical composition and enthalpy (temperature) are key parameters in affecting material performance and and experimental data acquired while varying them independently will provide valuable information for subsequent numerical correlations that may be employed to establish confidence in the theoretical ablative material prediction techniques.

2. Consideration should be given to eliminating the starting transient in the simulation tests. The boundary conditions to which the test specimen is exposed during this period are ill defined and subsequent data correlation becomes more complicated and uncertain as the starting

period becomes significant relative to the total test time. It is also recommended that duplicate tests be run for each test condition in order that any anamolous data be identified prior to investing significant effort in rationalizing such results.

3. The computational techniques for predicting ablative material performance, GNAT, CMA, and SCRIMP, should be put to the test of correlating a rather wide variety of ablation data. Only data for which the boundary conditions are well defined should be considered for this exercise since failure to predict performance may often be a direct result of failure to accurately estimate boundary conditions, and when this happens, nothing of a quantitative nature is learned. It is recommended that data derived in the manner described above (1) be employed for this purpose. Lack of agreement between prediction and data will then suggest modifications to particular coefficients or the treatment given certain specific phenomena. At present, neither the GNAT nor the SCRIMP program has been put to the test of correlating much ablation data, and, as such, it would be presumptuous to expect that the coefficients derived to date are of general utility. Numerous comparisons between data and predictions with these programs over a wide range of boundary conditions should result in proven techniques that may be employed to predict ablative material performance with confidence.
4. The above recommended efforts will result in techniques for predicting ablative material performance subjected to known boundary conditions (i.e. heat transfer coefficient, local O/F ratio, and enthalpy). It is recommended that efforts be directed toward establishing these quantities in a rocket engine in terms of measurable injector, chamber, and nozzle parameters in addition to engine performance parameters. For example the injector cold flow tests and heat transfer distribution measurements reported in Reference 40 may be coupled with such combustion chamber mixing analysis as described in Reference 41 to provide a rudimentary basis for estimating mixture ratio distribution around and along the thrust chamber and nozzle walls. Experimental techniques such as described in Reference 42 should be employed to verify these estimates. The estimated mixture ratio distributions would, in turn, provide boundary layer edge thermodynamic state properties and information necessary to perform boundary layer integrations along the chamber and nozzle walls to establish boundary layer transfer coefficients. Such an approach would result in reasonable boundary condition specification for ablative material analysis.

Closure to Recommendations

The first three recommendations may be accomplished in a relatively straightforward manner and will most probably result in a substantial improvement in the understanding of and the ability to analyze ablative material

response subjected to known boundary conditions. It is recognized that the fourth recommendation is relatively ambitious and the probability of success is more remote. It is believed, however, that the heat transfer coefficient and local mixture ratio are of paramount importance in governing ablative material behavior and any attempts to predict ablation performance without the knowledge of these parameters should be subject to question.

REFERENCES

1. Rindal, R. A., Flood, D. T., and Kendall, R. M.: Analytical and Experimental Study of Ablation Material for Rocket-Engine Application. Contract NAS 7-218, Vidya Report No. 201, NASA CR-54757, May 15, 1966.

2. Kendall, R. M., Rindal, R. A., and Bartlett, E. P.: A Multicomponent Boundary Layer Chemically Coupled to an Ablating Surface.AIAA Jour., Vol. 5, no. 6, June 1967.

3. Scala, S. M.: The Ablation of Graphite in Dissociated Air, Part I, Theory, IAS Paper No. 62-154, Presented June 1962.

4. McAllister, L., et al.: Ablation of Pure and Reinforced Materials Under Hypervelocity Reentry Conditions. AVCO RAD. Presented at 46th National Meeting of the AIChE, Los Angeles, Calif., Feb. 5, 1962.

5. Georgiev, S.: Unsteady Ablation. AVCO Research Report No. 94, Sept. 1959.

6. Anliker, M. and Beam, R. M.: On the Stability of Liquid Layers Spread over Simple Curved Bodies. Jour. Aero. Sci., vol. 20, Oct. 1962.

7. Feldman, S.: On the Instability Theory of the Soft or Melted Surface of an Ablating Body When Entering the Atmosphere. AVCO Research Report No. 34, Aug. 1958.

8. Sutton G. W.: The Hydrodynamics and Heat Conduction of a Melting Surface. Jour. of Aero. Sci., Jan. 1958.

9. Bethe, H. A. and Adams, M. C.: A Theory for the Ablation of Glassy Materials. AVCO Research Report No. 38, Nov. 1958.

10. Hidalgo, H.: A Theory of Ablation of Glassy Materials for Laminar and Turbulent Heating. AVCO Research Report No. 62, June 1959.

11. Schneider, P. J., Dolton, T. A., and Reed, G. W.: Char-Layer Structural Response in High-Performance Ballistic Reentry, AIAA Paper No. 66-424. Presented at 4th Aerospace Sciences Meeting. June 27-29, 1966.

12. Mathieu, R. D.: Mechanical Spallation of Charring Ablators in Hyperthermal Environments. AIAA Jour., Vol. 2, no. 9, Sept. 1964.

13. Bartz, D. R.: A Simple Equation for Rapid Estimation of Rocket Nozzle Convective Heat-Transfer Coefficients. Jet Prop., Jan. 1957, p. 49.

14. McCuen, P. A., Schaefer, J. W., Lundberg, R. E., and Kendall, R. M.: A Study of Solid-Propellant Rocket Motor Exposed Materials Behavior. Vidya Report No. 149, Contract No. AF 04(611)-9073, AFRPL-TR-65-33, Feb. 1965.

15. Wilson, G. G.: Hemispherical Spectral Emittance of Ablation Chars, Carbon, and Zirconia (to 6,000°F). Thermal Radiation of Solids, NASA SP-55, 1965.

16. Dow, M. B.: Comparisons of Measurements of Internal Temperatures in Ablation Materials by Various Thermocouple Configurations. NASA TN-D-2165, Nov. 1964.

17. User's Manual, Aerotherm Equilibrium Surface Thermochemistry Program (EST) Version 2. Aerotherm Corporation, June 1966.

18. User's Manual, Charring Material Ablation Program (CMA), Version 2. Aerotherm Corporation, January 1966.

19. Kratsch, K. M., Hearne, L. F., and McChesney, H. R.: Thermal Performance of Heat Shield Composites During Planetary Entry. Presented at AIAA-NASA National Meeting, Palo Alto, Calif., Sept. 30, 1963.

20. Wilson, R. G.: Thermophysical Properties of Six Charring Ablators from 140° to 700°K and Two Chars from 800° to 3000°K. NASA TN-D-2991, October 1965.

21. Schaefer, J. W. and Dahm, T. J.: Studies of Nozzle Ablative Material Performance for Large Solid Boosters. Aerotherm Report No. 66-2, NASA CR-72080, Dec. 15, 1966.

22. Kendall, R. M., and Rindal, R. A.: "Analytical Evaluation of Rocket Nozzle Ablation", American Institute of Aeronautics and Astronautics, Solid Propellant Rocket Conference, Palo Alto, Calif., Jan. 29-31, 1964.

23. Kendall, R. M.: A General Approach to the Thermochemical Solution of Mixed Equilibrium-Nonequilibrium, Homogeneous or Heterogeneous Systems. Aerotherm Report No. 66-7, Part IV, March 14, 1967.

24. Adams, Mac C.: Recent Advances in Ablation. ARS Journal, Vol. 29, No. 9, Sept. 1959, pp. 625-632.

25. Beecher, N., and Rosensweig, R. E.: Ablation Mechanisms in Plastics with Inorganic Reinforcement. ARS Journal, vol. 31, No. 4, April, 1961, pp. 532-539.

26. Rosensweig, R. E., and Beecher, N.: Theory for the Ablation of Fiberglas-Reinforced Phenolic Resins. AIAA Journal. Vol. 1, No. 8, August 1963, pp. 1802-1809.

27. Richman, J. W.: Theoretical and Experimental Results Using Fiberglass as an Ablative Material on the Black Brant III Nose Cone. AIAA Sounding Rocket Vehicle Technology Specialist Conference. Williamsburg, Va., Feb. 27 - March 1, 1967 (American Institute of Aeronautics and Astronautics, New York), pp. 384-388.

28. Romie, F. E.: Carbon-Silica Reaction in Silica-Phenolic Composites. AIAA Journal. Vol. 5, No. 8, August 1967, pp. 1511-1513.

29. Batchelor, J. D., Simmons, J. A., and West, W. E.: Chemical Reactions between Plastic Composite Materials and Propellant Exhaust Products. Atlantic Research Corporation, Alexandria, Va., ASD-TDR-63-737 (AD 422 955), August 1963.

30. Wilhelm, J. R.: Ablation of Refrasil-Phenolic Nozzle Inserts in Solid Propellant Exhausts. Journal of Spacecraft and Rockets. Vol. 2, No. 3, May - June 1965, pp. 337-344.

31. Blaes, H. M., Hale, J. K., Hale, R. M., et al., Application of Materials to Advanced Nozzle and Hot Gas Control Systems. Aeronutronic Division, Philco Corporation, Newport Beach, Calif., AFML-TR-65-125 (AD 494717), April 1965.

32. Ladacki, M.: Silicon Carbide in Ablative Chars. AIAA Journal, Vol. 4, No. 8, August 1966, pp. 1445-1447.

33. Gutman, V. R.: Comment on Silicon Carbide in Ablative Chars. AIAA Journal, Vol. 5, No. 5, May 1967, pp. 1053-1054.

34. Blumenthal, J. L., Santy, M. J. and Burns, E. A.: Kinetic Studies of High-Temperature Carbon-Silica Reactions in Charred Silica-Reinforced Phenolic Resins. Western States Section, The Combustion Institute, Fall Meeting, Santa Barbara, Calif., October 25-26, 1965. Paper No. WSCI 65-25; also AIAA Journal. Vol. 4, No. 6, June 1966, pp. 1053-1057.

35. Blumenthal, J. L., Larsen, R. D., and Nordberg, R. C.: Determination of Thermophysical Properties of Ablative Materials, Phase I - Laboratory Determinations. TRW Systems, Redondo Beach, Calif. NASA CR 65486, July 1, 1966, pp. 52-54.

36. Corning Glass Works, Corning, N.Y.: Properties of Selected Commercial Glasses. 1957.

37. JANAF Thermochemical Tables. The Dow Company, Midland, Michigan, including quarterly supplements through 1966.

38. Pears, C. D., Engelke, W. T., and Thornburgh, J. D.: The Thermophysical Properties of Plastic Materials from -50°F to over 700°F. Air Force Materials Laboratory Report ML-TDR-64-87, Part I, August 1964.

39. Moyer, C. B. and Rindal, R. A.: Finite Difference Solution for the In-Depth Response of Charring Materials Considering Surface Chemical and Energy Balances. Aerotherm Corporation Final Report 66-7, Part II, March 14, 1967.

40. Rowley, R. W., Tyler, W. H. : The Effect of Injector Design on Thrust-Chamber Erosion. Jet Propulsion Laboratory, California Institute of Technology, Pasadena, California, March 1, 1966.

41. Hersch, Martin: A Mixing Model for Rocket Engine Combustion. National Aeronautics and Space Administration. Lewis Research Center, NASA TN D-2881, June 1965.

42. Tobey, Aubrey C.: Combustion Instability Studies. WSS/CI Paper 64-10-1964, Spring Meeting Western States Section, The Combustion Institute, Stanford University, April, 1964.

TABLE I

LIST OF CALIBRATION AND ABLATIVE MATERIAL SIMULATION TESTS

Test Number	Test Type	Nozzle	Test Duration (sec)
416	Pyrometer check-out	0.3 inch throat water cooled	40.6
425	Pyrometer check-out	0.3 inch throat graphite phenolic	33.9
416	Heat flux calibration	0.3 inch throat water cooled	40.6
420	Heat flux calibration	0.3 inch throat water cooled	31.4
421	Heat flux calibration	0.3 inch throat water cooled	33.6
423	Heat flux calibration	0.3 inch transient calorimeter	15.3
424	Heat flux calibration	0.3 inch transient calorimeter	15.4
426	Ablative Material test	0.299 inch throat NL-2, Graphite Phenolic, MX4500	48.2
427	Ablative Material test	0.298 inch throat NL-1, Silica Phenolic, MXS-89	35.4
428	Ablative Material test	0.299 inch throat NL-6, Silica- Phenyl Silane + Buna N, XR2015	25.8
429	Ablative Material test	0.300 inch throat NL-5, Nylon Phenolic, FM5051	21.5
430	Ablative Material test	0.299 inch throat NL-3, Asbestos Phenolic, MXA-11	15.2
431	Ablative Material test	0.299 in ch throat NL-4, Carbon Phenolic, MX4926	29.0
432	Heat flux calibration	0.3 inch throat transient calorimeter	30.6
433	Heat flux calibration	0.3 inch throat transient calorimeter	30.5

TABLE II

SIMULATION GAS COMPOSITION

Gas	Mass Flow Rate (lb/sec)	Mass Fraction Actual	Mass Fraction Desired	Error (Percent)
N_2 } Mix F	0.0171	0.430	0.4261	+1.0
H_2 } Mix F		0.025	0.0244	+2.5
CO_2 } Mix G	0.0141	0.239	0.2438	-2.0
O_2 } Mix G		0.136	0.1377	-1.2
H_2O Steam	0.0064	0.170	0.1680	+1.2

TABLE III

STEADY STATE CALORIMETER RESULTS

Test No.	Test Time (sec)	H_r (Btu/lb)	P_o (psia)	C_N	q_w (Btu/ft^2-sec)
416	36.2	480.	102.5	0.935	599.3
420	26.8	506.	98.9	0.945	585.8
421	22.1	480.	97.5	0.966	574.4

TABLE IV

COMPARISON OF MEASURED AND PREDICTED HEAT TRANSFER COEFFICIENTS

Test No.	Calorimeter	Test Time (sec)	$\rho_e U_e C_H$ (lb/ft^2-sec)		$\frac{\rho_e U_e C_H \text{ Meas.}}{\rho_e U_e C_H \text{ Bartz}}$
			Measured	Bartz	
416	Steady State	36.2	0.182	.390	.466
420	Steady State	26.8	0.177	.388	.456
421	Steady State	22.1	0.175	.390	.449
423	Transient	14.5	0.119	.361	.330
424	Transient	14.0	0.118	.372	.317
432	Transient	21.3	0.126	.369	.341
432	Transient	29.3	0.120	.370	.324
433	Transient	21.4	0.113	.363	.312
433	Transient	29.4	0.123	.361	.341

TABLE V

ABLATION MATERIAL CHEMICAL PROPERTIES

Nozzle Number		NL-1	NL-2	NL-3	NL-4	NL-5	NL-6
Material		Silica Phenolic (MXS 89)	Graphite-Phenolic (MX 4500)	Asbestos-Phenolic (MXA 11)	Carbon-Phenolic (MX 4926)	Nylon-Phenolic (FM 5051)	Silica-Phenyl Silane + Buna N (XR-2015)
ρ_{virgin}	Lb virgin/ft^3 virgin	104.8	87.9	102.3	91.3	75.3	98.8
ρ_{char}	Lb char/ft^3 char	85.6	70.7	68.1	73.2	15.1	70.8
Effective resin molecule		C_6H_6O	C_6H_6O	C_6H_6O	C_6H_6O	C_6H_6O	$C_6H_{8.14}O_{.955}N_{.366}$
Effective reinforcement molecule		SiO_2	C	$(M_gO)_3 \cdot (SiO_2)_2 \cdot (H_2O)_2$	C	$C_6H_{11}ON$	SiO_2
ρ_{A1}	Lb initial A/ft^3 resin	60.75	60.75	60.75	60.75	60.75	57.8
ρ_{A2}	Lb final A/ft^3 resin	32.4	32.4	32.4	32.4	32.4	15.4
ρ_{B1}	Lb initial B/ft^3 resin	20.24	20.25	20.25	20.25	20.25	19.1
ρ_{B2}	Lb final B/ft^3 resin	0	0	0	0	0	0
ρ_{C1}	Lb initial C/ft^3 resin	120.3	91.7	128.3	97.4	70.4	117.0
ρ_{C2}	Lb final C/ft	120.3	91.7	111.7	97.4	0	117.0
K_r	Lb resin/lb virgin	0.305	0.326	0.435	0.330	0.500	0.354
Γ	ft^3 resin/ft^3 virgin	0.395	0.354	0.549	0.372	0.465	0.455
k_A	Sec^{-1}	4.48×10^9	4.48×10^9	4.48×10^9	4.48×10^9	4.48×10^9	4.48×10^9
k_B	Sec^{-1}	1.40×10^4	1.40×10^4	1.4×10^4	1.4×10^4	1.4×10^4	1.4×10^4
k_C	Sec^{-1}	--	--	5.27×10^6	--	1.85×10^{13}	--
$-E_A/R$	(^oR)	3.68×10^4	3.68×10^4	3.68×10^4	3.68×10^4	3.68×10^4	3.68×10^4
$-E_B/R$	(^oR)	1.54×10^4	1.54×10^4	1.54×10^4	1.54×10^4	1.54×10^4	1.54×10^4
$-E_C/R$	(^oR)	--	--	5.8×10^4	--	4.71×10^4	-
n_A		3	3	3	3	3	3
n_B		3	3	3	3	3	3
n_C		--	--	1	--	1	--
$\tilde{K}$	Lb Hydrogen/Lb gas	0.107	0.107	0.108	0.107	0.102	0.103
$\tilde{K}_{Cg}$	Lb Carbon/Lb gas	0.609	0.609	0.476	0.609	0.626	0.646
$\tilde{K}_{Ng}$	Lb Nigrogen/Lb gas	0	0	0	0	0.077	0.064
$\tilde{K}_{Og}$	Lb Oxygen/Lb gas	0.284	0.284	0.416	0.284	0.195	0.187
$\tilde{K}_{Cc}$	Lb Carbon/Lb char	0.149	1.000	0.262	1.000	1.000	0.101
$\tilde{K}_{Oc}$	Lb Oxygen/Lb char	0.453	0	0.343	0	0	0.479
$\tilde{K}_{Mgc}$	Lb Magnesium/Lb char	0	0	0.223	0	0	0
$\tilde{K}_{Sic}$	Lb Silicon/Lb char	0.398	0	0.172	0	0	0.420
ΔH_{fv}	Btu/Lb virgin Matl.	-4856	-358.6	-4151	-363.0	-1311	-4590
ΔH_{fc}	Btu/Lb char	-5540	0	-4780	0	0	-5850

TABLE VI

SUMMARY OF PREDICTED SURFACE RECESSION AND TEMPERATURE FOR ABLATION SIMULATION TESTS

Nozzle	Nominal Surface Temperature (R^o) (Fig.28)				Surface Recession(in)(Fig. 21)				Surface Composition		Comments
	Measured	Predicted			Measured	Predicted			Observed	Predicted	
		EST-CMA	GNAT	SCRIMP		EST-CMA	GNAT	SCRIMP			
NL - 1 Silica Phenolic	4100	4000	——	3800	0.068	0.004	——	.051	SiO_2	SiO_2	Based upon post test nozzle examination it appears that removal of liquid silica is the dominant surface recession mechanism.
NL - 2 Graphite - Phenolic	3400	3100	3400	——	.077	0.115	0.077	——	C	C	Heterogeneous kinetic coefficients defined to force agreement with data. Encouraging to note agreement with surface temperature as well.
NL - 3 Asbestos - Phenolic	3700	3600	——	——	.077	.000	——	——	C	MgO	Gross failure of char layer suspected as dominant surface recession mechanism.
NL - 4 Carbon - Phenolic	3900	3300	3400	——	.077	.071	.047	——	C	C	Best recession prediction with chemical equilibrium but temperature is too low.
NL - 5 Nylon - Phenolic	3600	2500	3000	——	.130	.068	.016	——	C	C	Gross failure of char layer suspected as dominant surface recession mechanism.
NL - 6 Silica - Phenyl Silane and Buna "N"	4100	4000	——	3700	.070	.001	——	.025	SiO_2	SiO_2	Based upon post test nozzle examination it appears that removal of liquid silica is the dominant surface recession mechanism.

TABLE VII

SEQUENCE OF KINETIC COEFFICIENTS EMPLOYED FOR CORRELATING GRAPHITE PHENOLIC ABLATION DATA

Reaction	$C^* + H_2O \rightleftarrows CO + H_2$			$C^* + CO_2 \rightleftarrows 2CO$			$2C^* + O_2 \rightleftarrows 2CO$		
Rate Coefficients	k	$-\Delta E$	n	k	$-\Delta E$	n	k	$-\Delta E$	n
Literature Values	$(0.666)^1$	$(3.55\times10^4)^1$	$(1.0)^1$	$(3.77\times10^7)^1$	$(8.34\times10^4)^1$	$(1.0)^1$	$(5.05\times10^8)^2$	$(4.40\times10^4)^2$	$(1/2)^2$
First Iteration	2.09×10^2	3.55×10^4	1.	3.77×10^7	8.34×10^4	1.	"	"	"
Second Iteration	1.11×10^3	"	"	2.01×10^8	"	"	"	"	"
Third (Final) Iteration	1.43×10^3	"	"	2.59×10^8	"	"	"	"	"

Units on Coefficients

k Lb carbon/ft^2-sec-$(atm)^n$

ΔE Cal / mole

[1] Reference 14

[2] Reference 3 (fast-reactions)

TABLE VIII

SUMMARY OF ROCKET ENGINE FIRING CONDITIONS

Nozzle	Initial Chamber Pressure* (psia)	Propellant Flow Rate* (lb/sec)		O/F**	Initial Throat Heat Transfer Coefficient $\rho_e U_e C_H$ (lb/ft^2-sec)**
		Oxidizer	Fuel		
Silica-Phenolic	101	0.447	0.218	2.05	0.1737
Graphite-Phenolic	99.7	.445	.215	2.17	.1725
Asbestos-Phenolic	98.0	.446	.211	2.12	.1691
Carbon-Phenolic	101.7	.450	.217	2.08	.1730
Nylon-Phenolic	97.7	.437	.210	2.08	.1690
Silica-Phenyl Silane + Buna "N"	100.5	.451	.216	2.09	.1742

Characteristic velocity (c*) for all firings $\cong$ 94.5 percent of theoretical.*

Thrust termination for all firings when $P_{chamber}$ = 90 psia.*

Throat diameter of all nozzles - 1.2 inch.*

Oxidizer - N_2O_4, Fuel - N_2H_4/UDMH 50/50.*

*Data supplied by NASA-Lewis Research Center

**Computed

TABLE IX

COMPARISON OF MEASURED AND PREDICTED ROCKET FIRING ABLATION RESULTS

Nozzle	Firing Time (sec)		Initiation of Ablation (sec)		Total Surface Recession (mils)		Average Recession Rate (mils/sec)			Average Recession During Period of Active Ablation (mils/sec)		
	Actual	Predicted	Actual	Predicted	Actual	Presumed for Predictions	Actual	Predicted	Measured in Arc-Simulator**	Actual	Predicted	Measured in Arc-Simulator**
Silica-Phenolic	37.6	18.0	12.0	8.0	34.0	36.0	0.9	2.0	1.91	1.3	3.6	2.38
Graphite-Phenolic	24.0	15.6	9.0	3.0	27.5	31.3	1.1	2.0	1.60	1.8	2.5	2.48
Asbestos-Phenolic*	7.8	3.3	4.0	0.0	32.0	33.5	4.1	10.0	5.13	8.4	10.1	5.92
Carbon-Phenolic	14.6	7.4	5.0	0.0	40.5	35.2	2.8	4.7	2.66	4.2	4.8	3.50
Nylon-Phenolic	8.0	4.5	4.0	0.0	55.5	33.5	6.9	7.4	6.04	13.9	7.4	7.02
Silica-Phenyl Silane + Buna "N"	26.5	7.4	5.0	0.0	31.5	36.5	1.2	4.9	2.64	1.5	4.9	3.59

*Predictions shown for these nozzles are based upon direct specification of either surface recession rate or surface temperature as established during arc-plasma firings (see Section 5.2 of text).

**These results taken directly from Figures 21a through 21f.

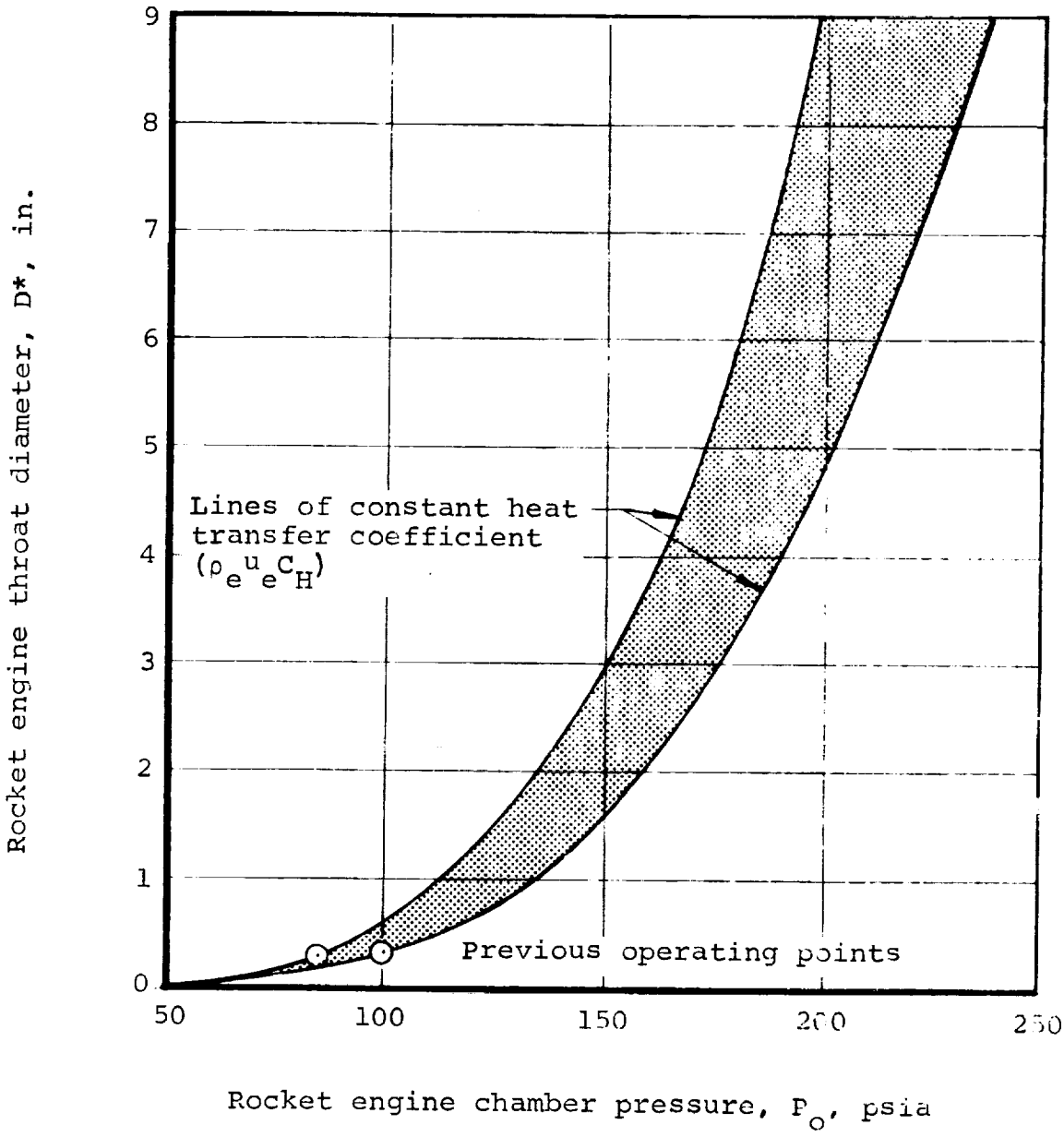

Figure 1. Range of Rocket Engine Operating Conditions for which Heat Transfer Coefficient is Simulated in Arc Plasma Device for N_2O_4-N_2H_4/UDMH Propellant

Preceding page blank

Note: Arrows indicate direction of increasing time

Rocket heat transfer coefficient corresponds to 100 psia chamber pressure and 1.2 inch throat diameter. Simulation test conditions correspond to initial and final chamber pressure of 100 psia and 50 psia respectively.

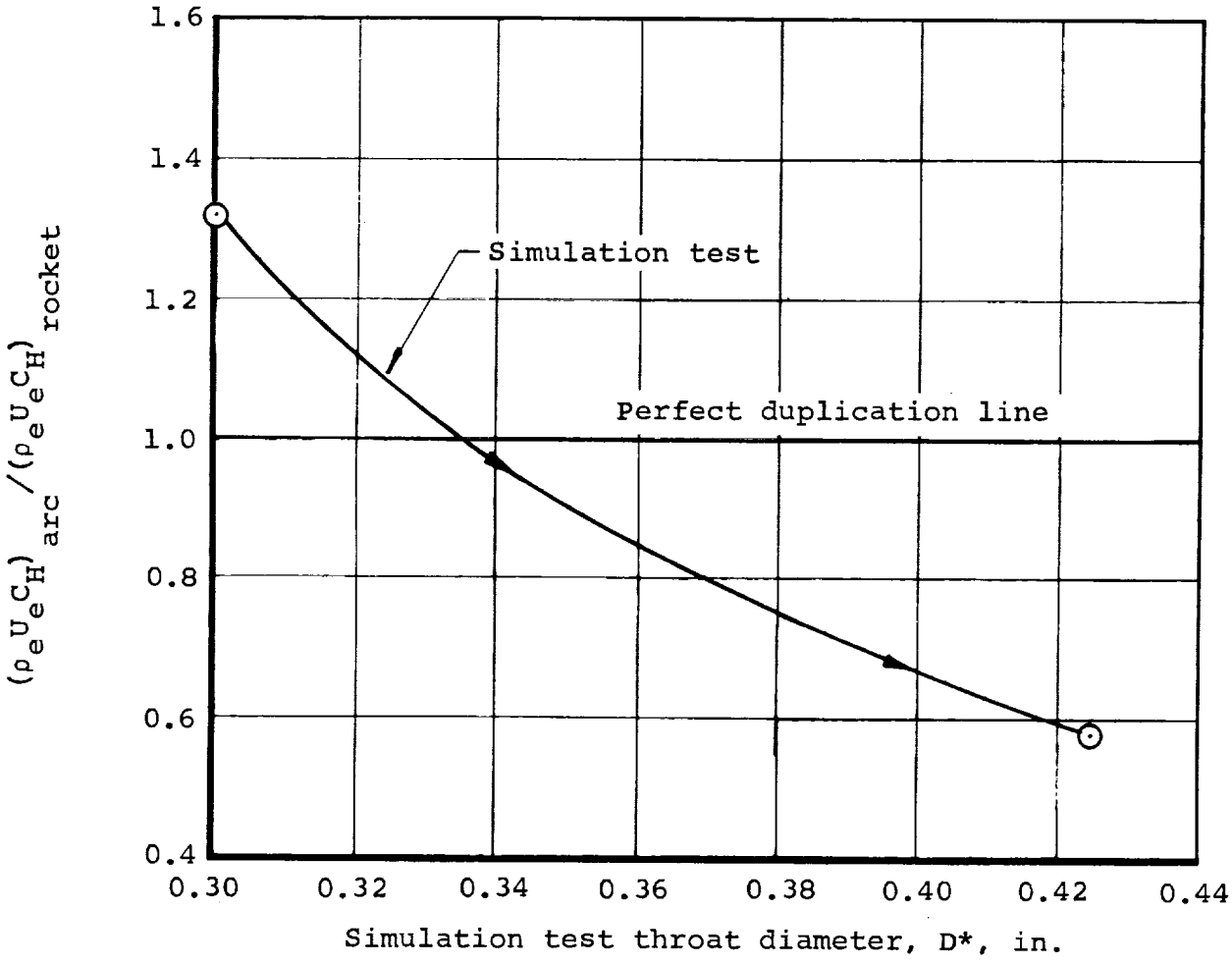

Figure 2. Ratio of Arc to Rocket Heat-Transfer Coefficient For Typical Simulation Test

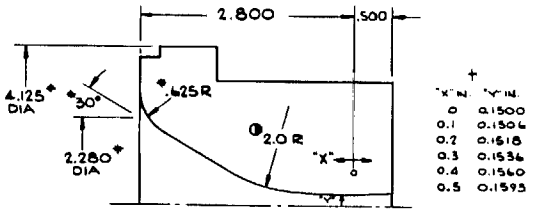

FIG. 3A

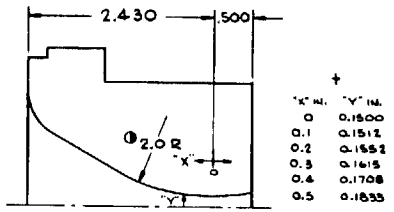

FIG. 3D

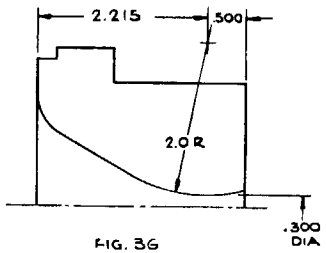

FIG. 3G

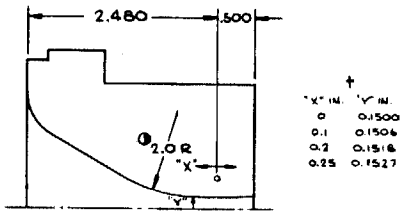

FIG. 3B

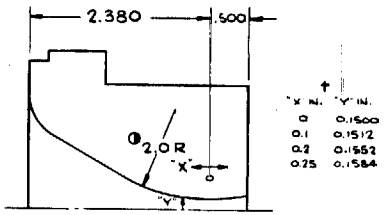

FIG. 3E

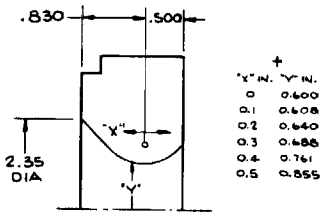

FIG. 3H

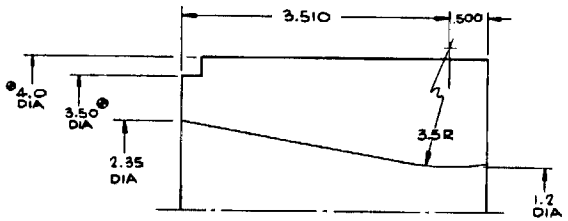

FIG. 3C

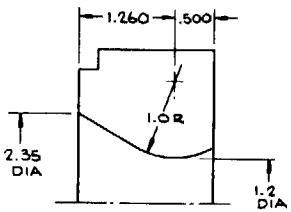

FIG. 3F

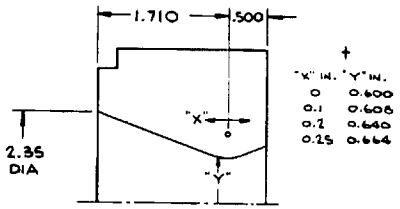

FIG. 3I

NOTES:

* INDICATES DIMENSIONS TYPICAL FOR ARC NOZZLES.

⊕ INDICATES DIMENSIONS TYPICAL FOR ROCKET NOZZLES.

◑ INDICATES BLEND RADIUS FROM FINAL TABULATED READING TO 30° ANGLE.

† TABULATED VALUES REPRESENT DISTANCE OVER WHICH A^*/A IS DUPLICATED.

FIG. 3 - VARIOUS ROCKET-ARC NOZZLE ABLATIVE MATERIAL TEST SPECIMEN CONFIGURATIONS FOR DUPLICATING A/A^* AS A FUNCTION OF AXIAL DISTANCE

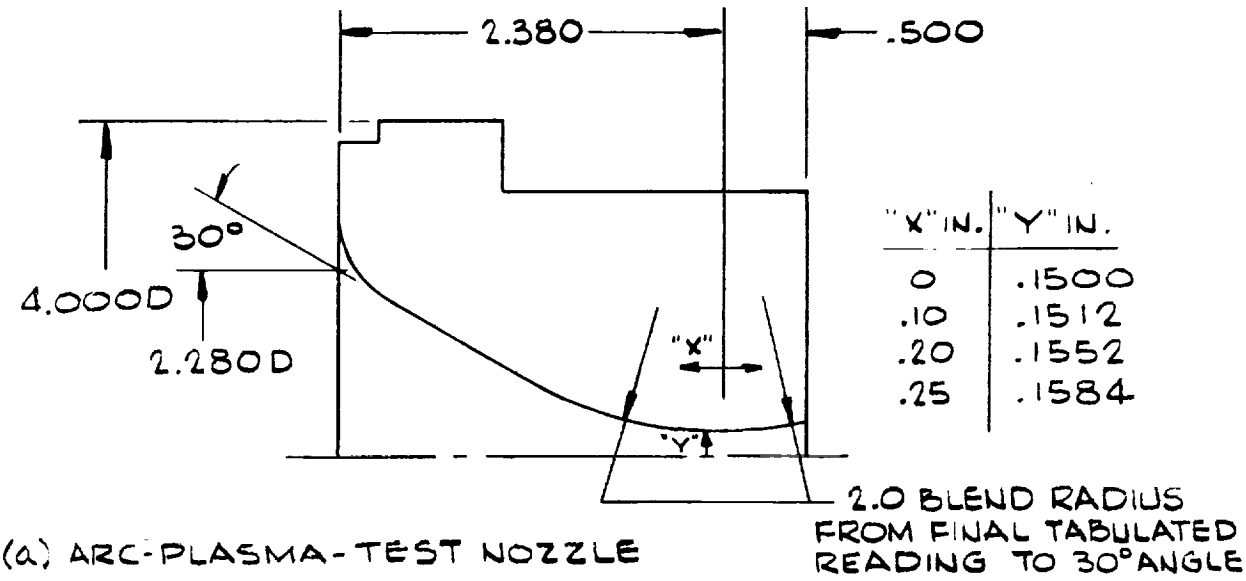

(a) ARC-PLASMA-TEST NOZZLE

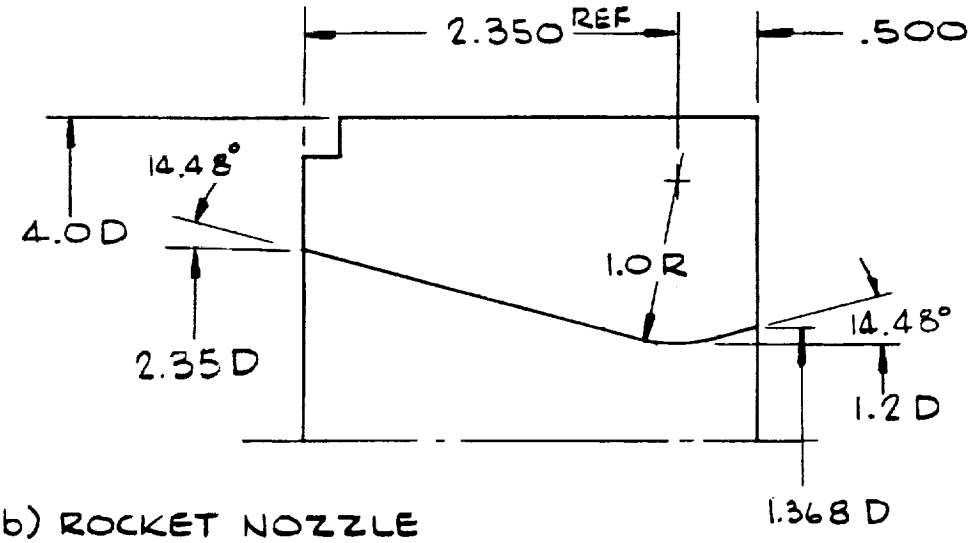

(b) ROCKET NOZZLE

FIG.4 - ROCKET NOZZLE & ARC-PLASMA-TEST NOZZLE DESIGNED TO DUPLICATE $A/A^* = f(x)$ FOR A DISTANCE OF 0.25 INCHES UP & DOWN STREAM OF THE THROAT

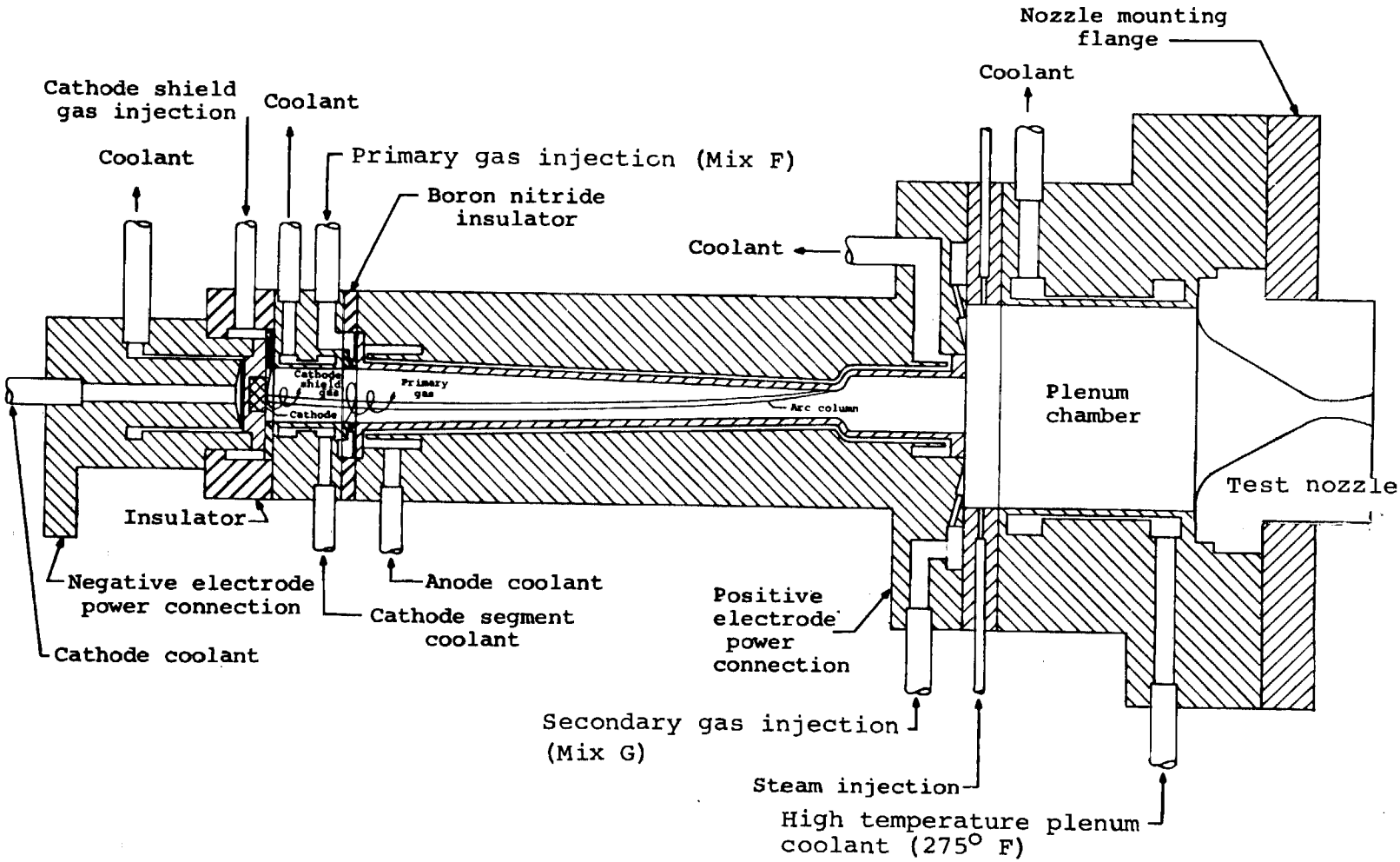

Figure 5. Constrictor Arc-Plasma Generator Rocket-Engine Environment Simulation Apparatus

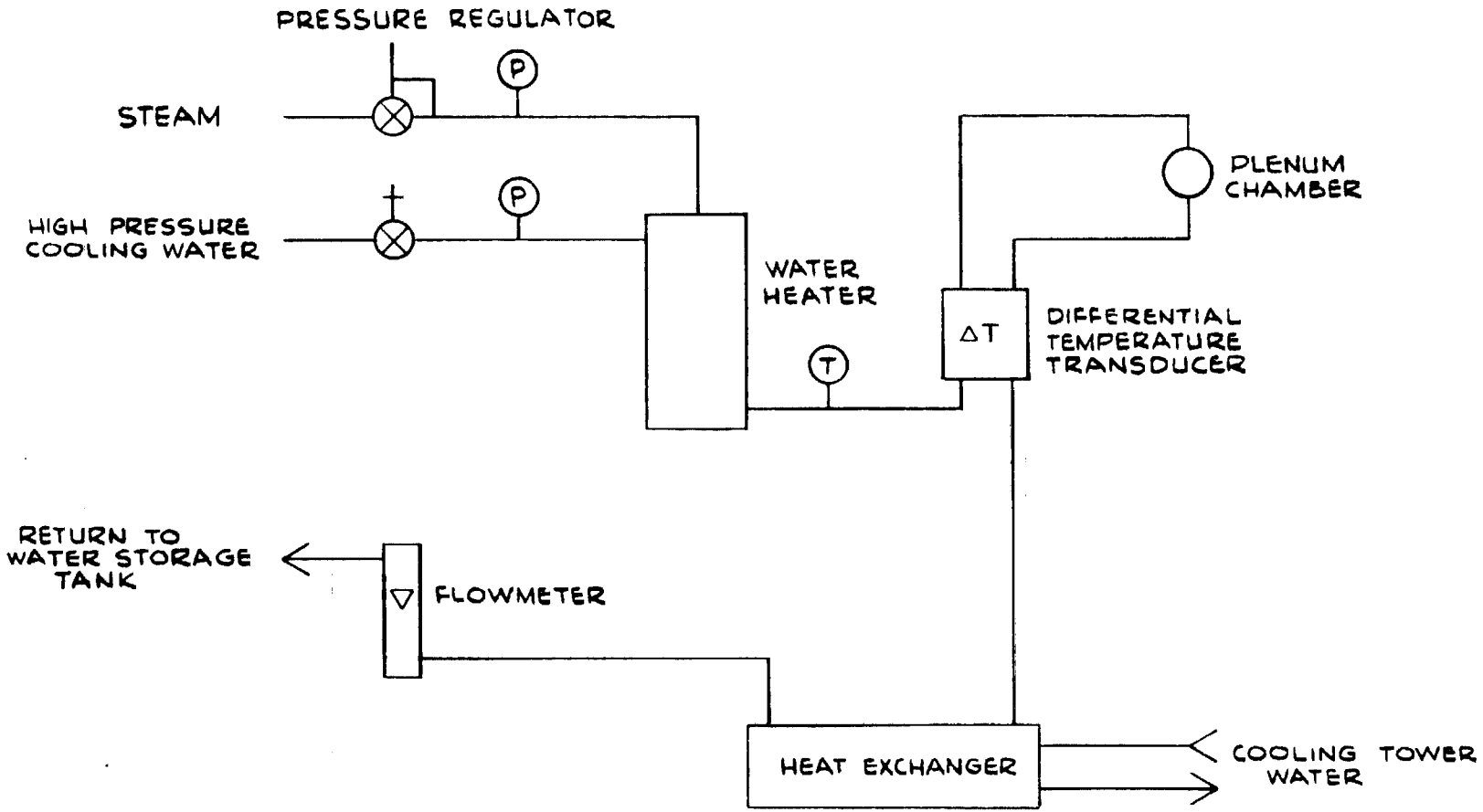

Figure 6. Schematic of Cooling Water Circuit for Mixing Plenum Chamber

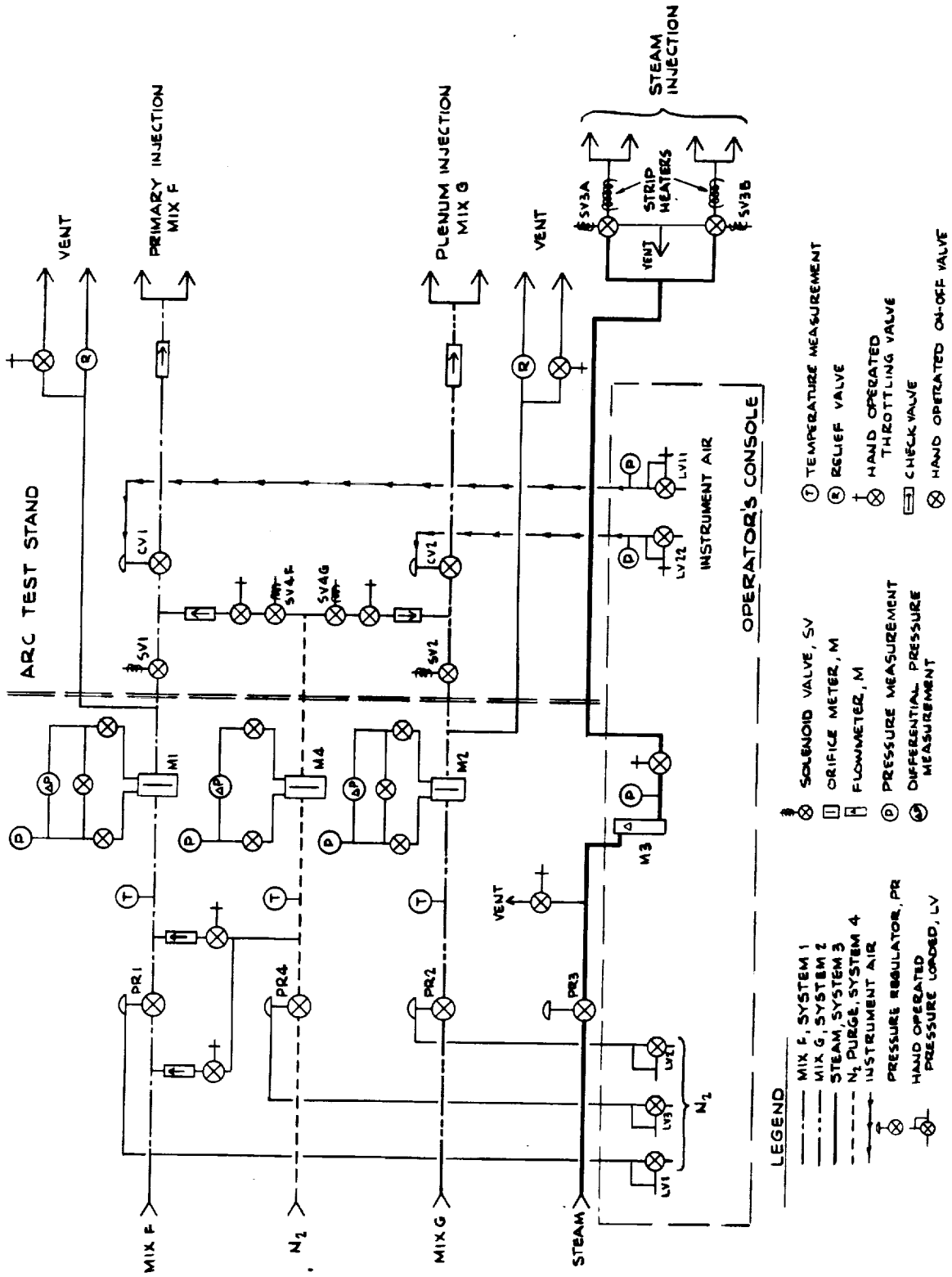

Figure 7. Schematic Representation of Gas Metering and Control System

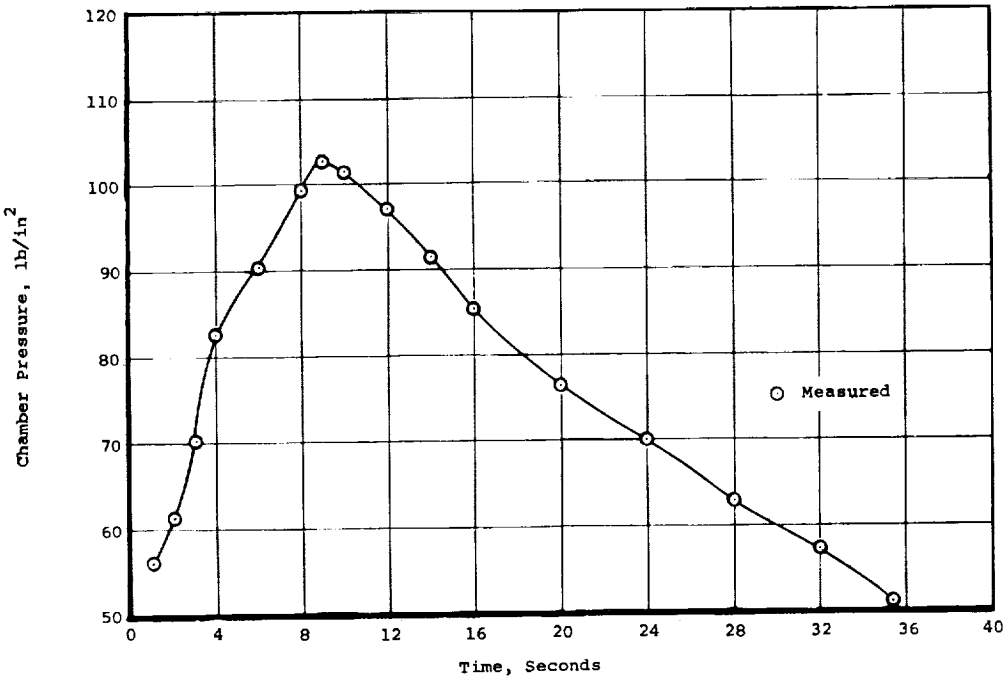

(a) Test 427, Nozzle NL-1, Silica-Phenolic

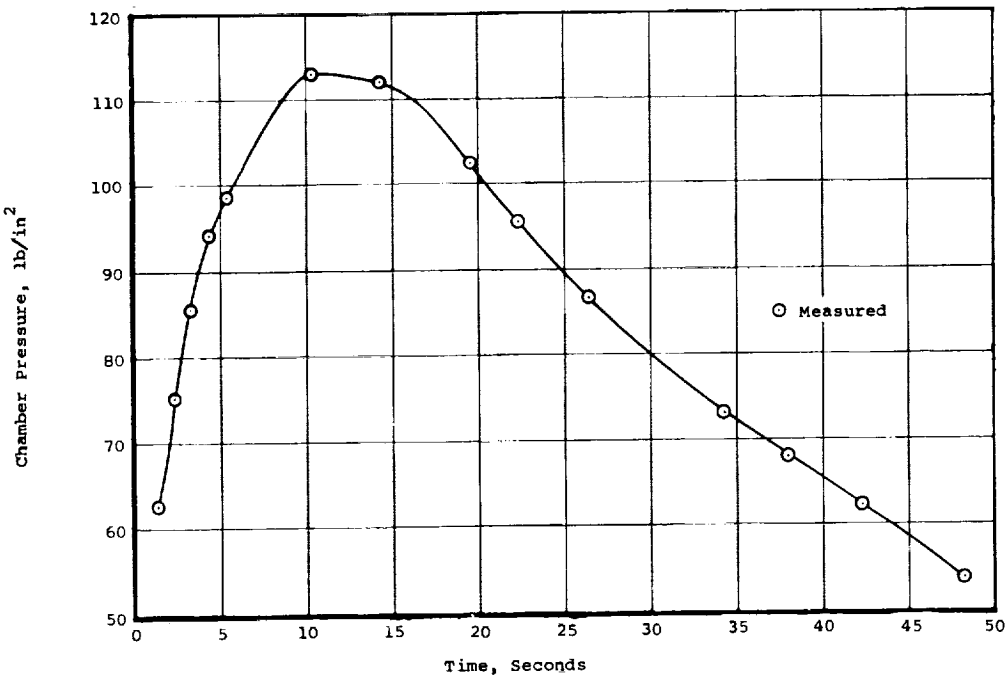

(b) Test 426, Nozzle NL-2, Graphite-Phenolic

Figure 8. Chamber Pressure History for Ablative Material Tests

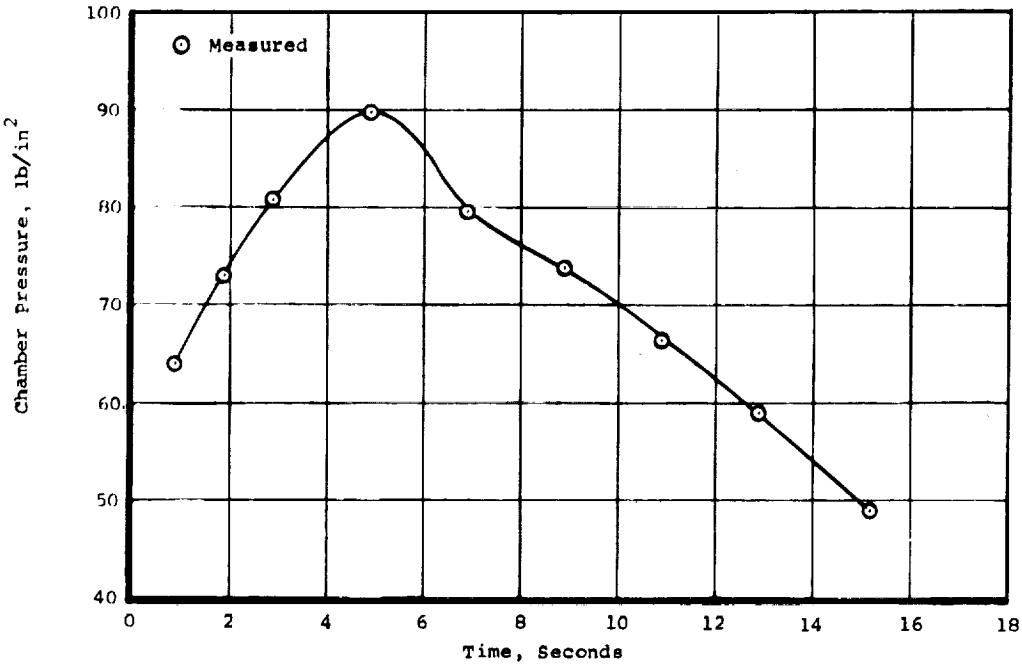

(c) Test 430, Nozzle NL-3, Asbestos-Phenolic

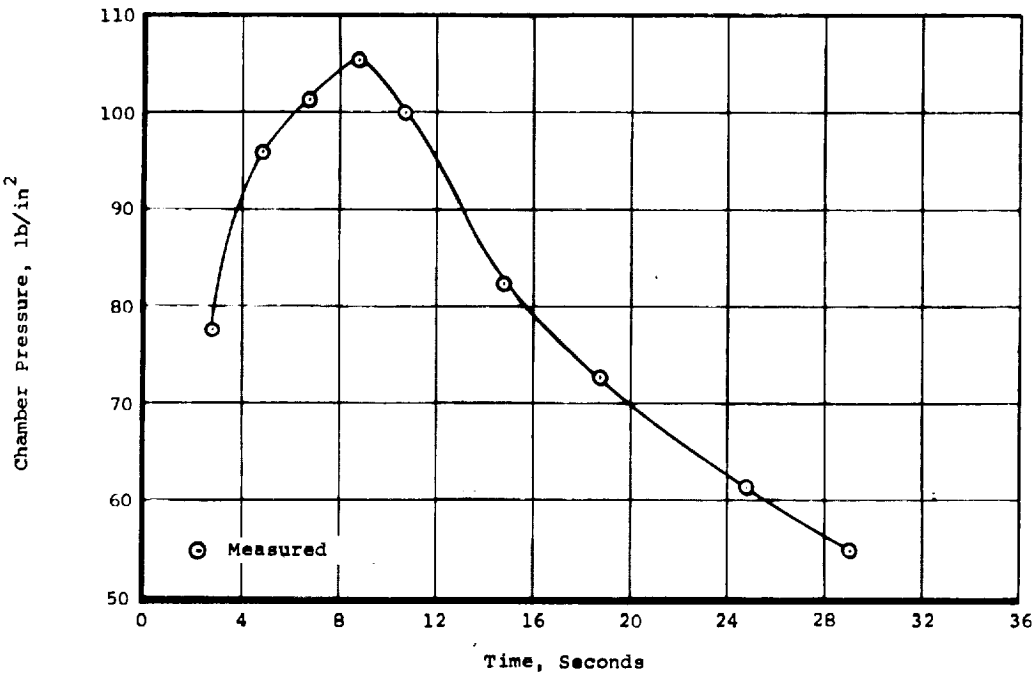

(d) Test 431, Nozzle NL-4, Carbon-Phenolic

Figure 8. (continued)

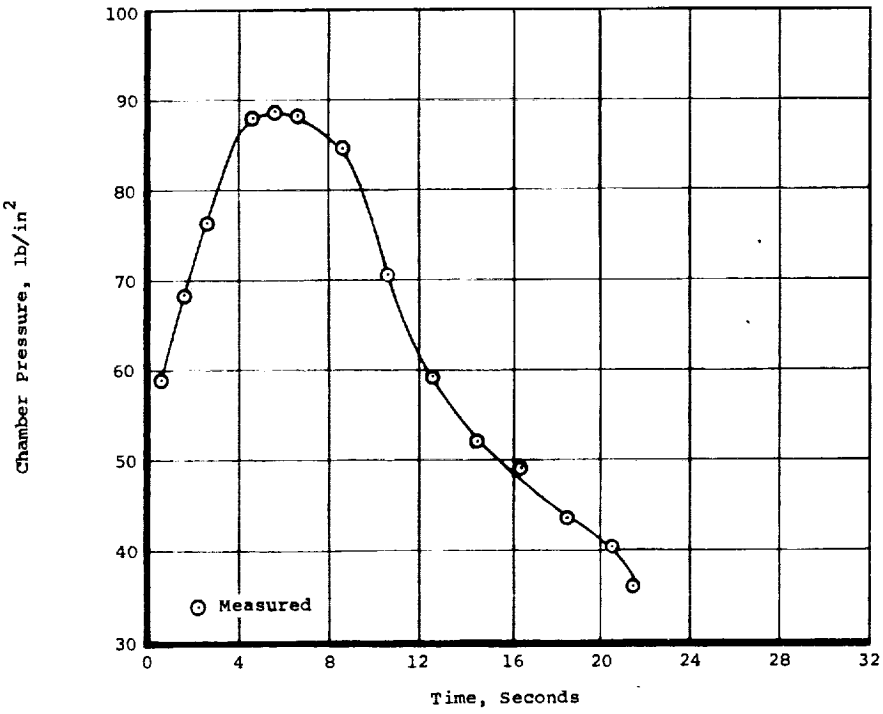

(e) Test 429, Nozzle NL-5, Nylon-Phenolic

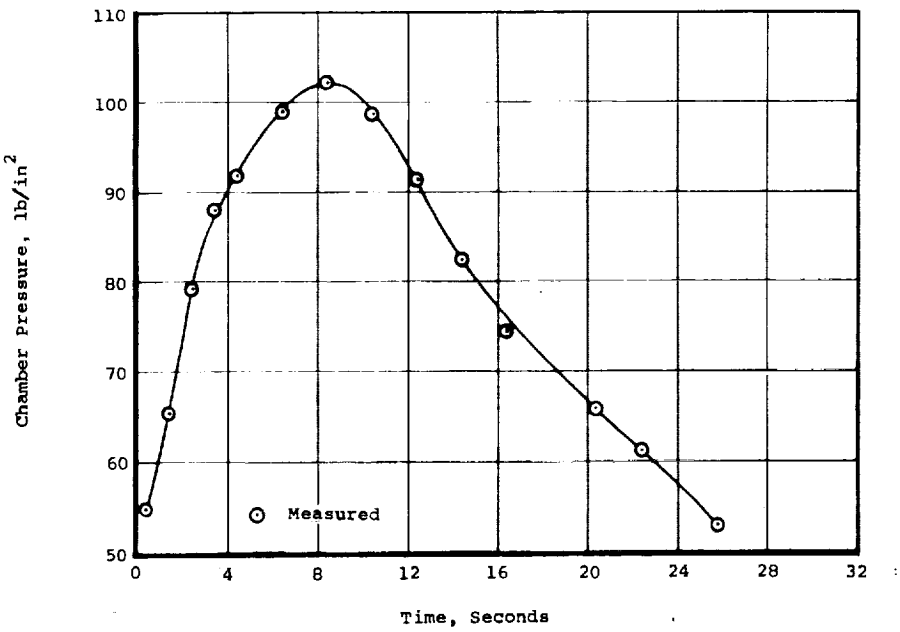

(f) Test 428, Nozzle NL-6, Silica-Phenyl Silane + Buna "N"

Figure 8. (concluded)

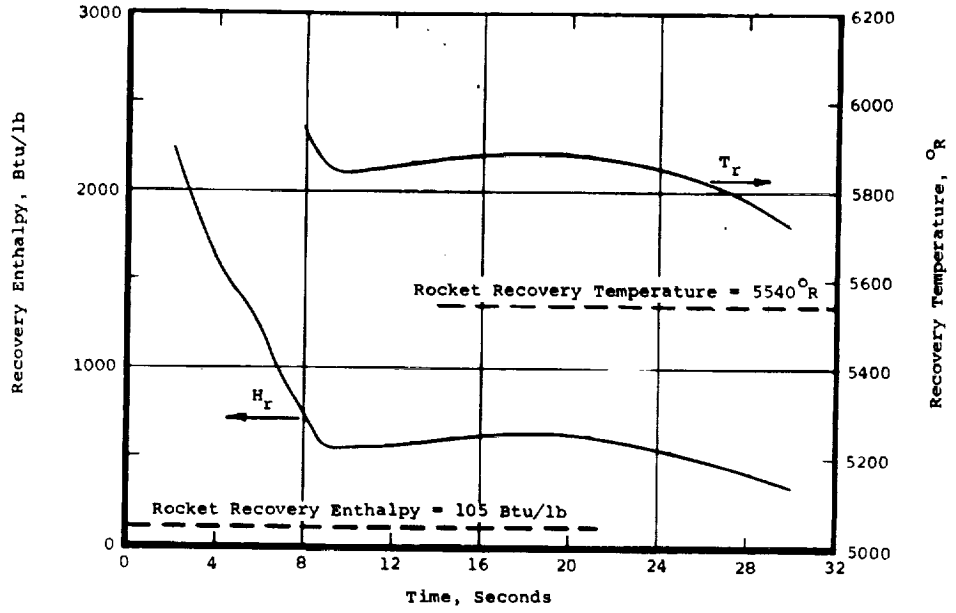

(a) Test 427, Nozzle NL-1, Silica-Phenolic

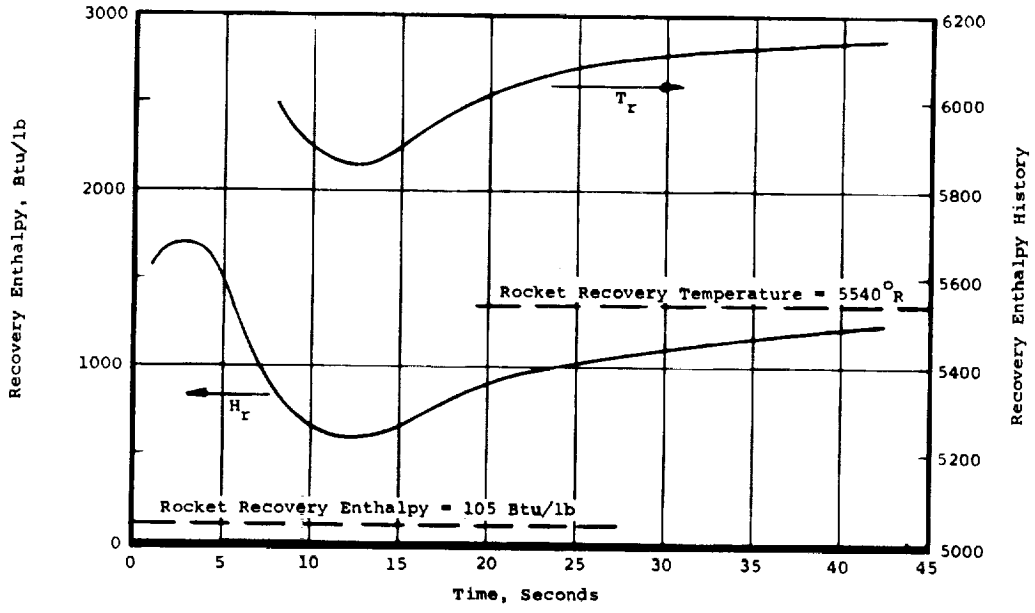

(b) Test 426, Nozzle NL-2, Graphite-Phenolic

Figure 9. Recovery Enthalpy and Temperature History for Ablative Material Tests

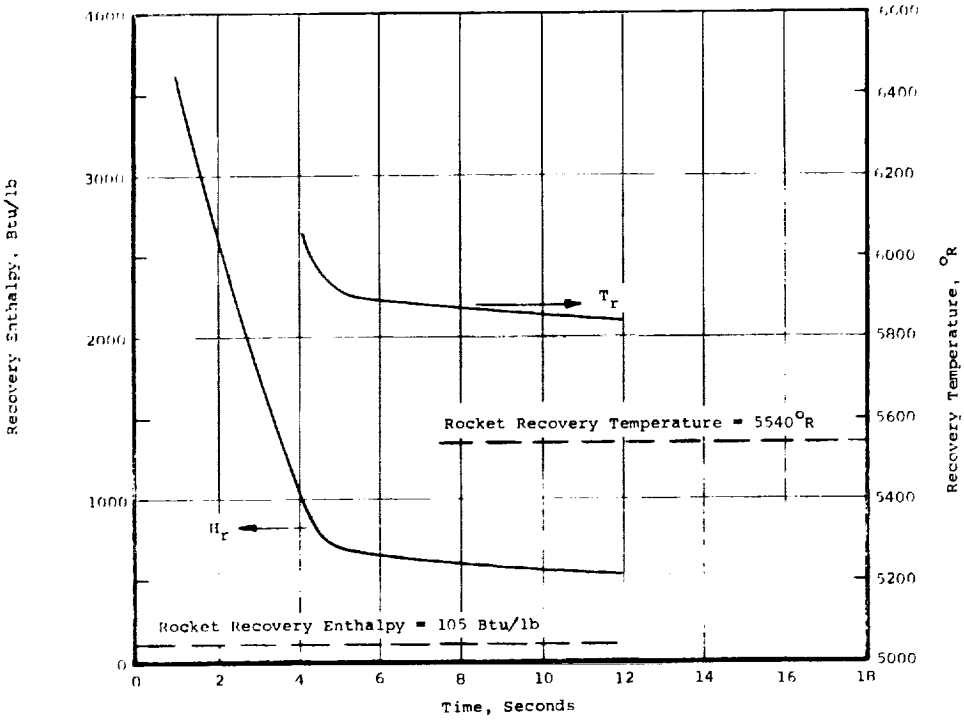

(c) Test 430, Nozzle NL-3, Asbestos-Phenolic

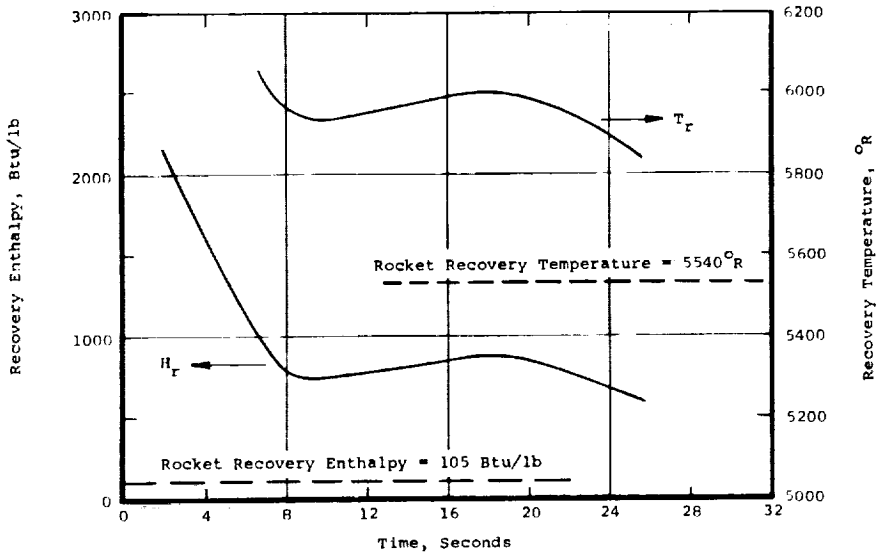

(d) Test 431, Nozzle NL-4, Carbon-Phenolic

Figure 9. (continued)

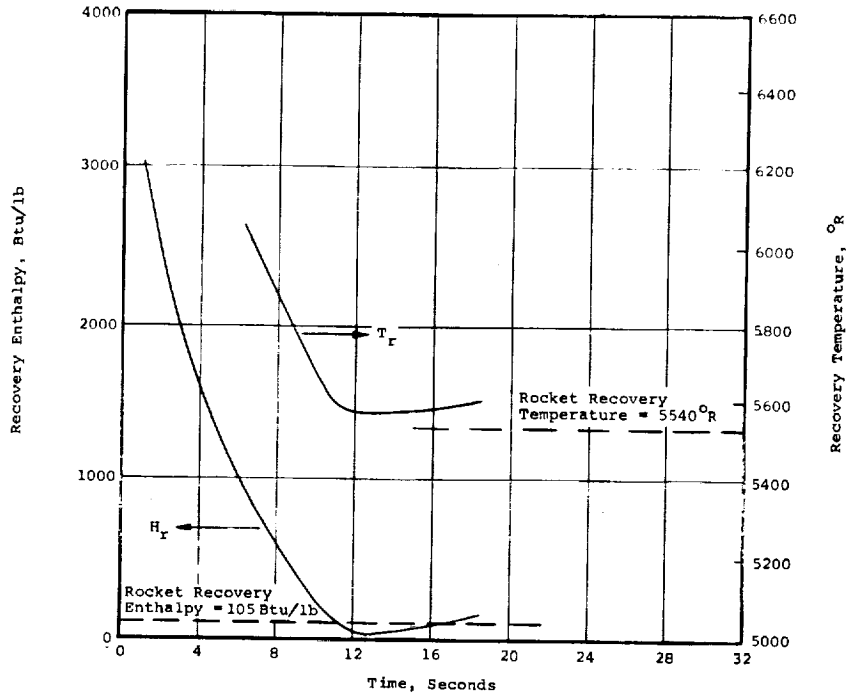

(e) Test 429, Nozzle NL-5, Nylon-Phenolic

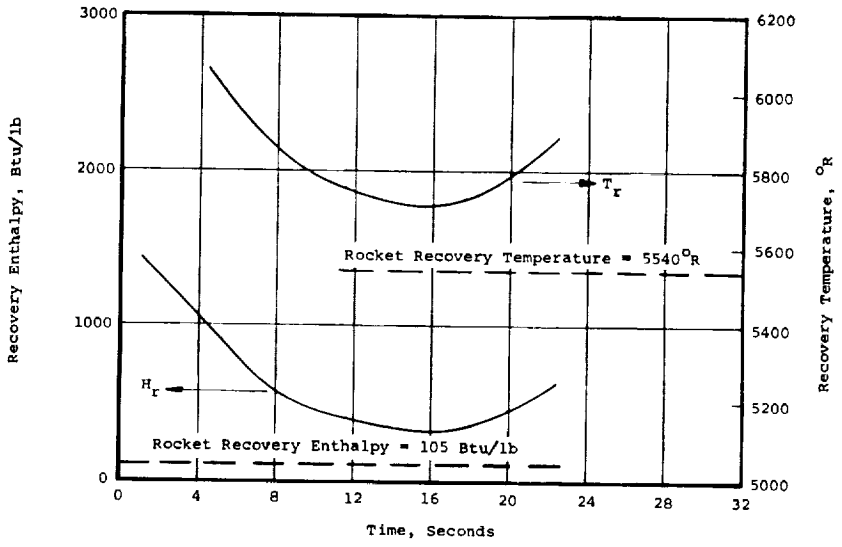

(f) Test 428, Nozzle NL-6, Silica-Phenyl Silane + Buna "N"

Figure 9. (concluded)

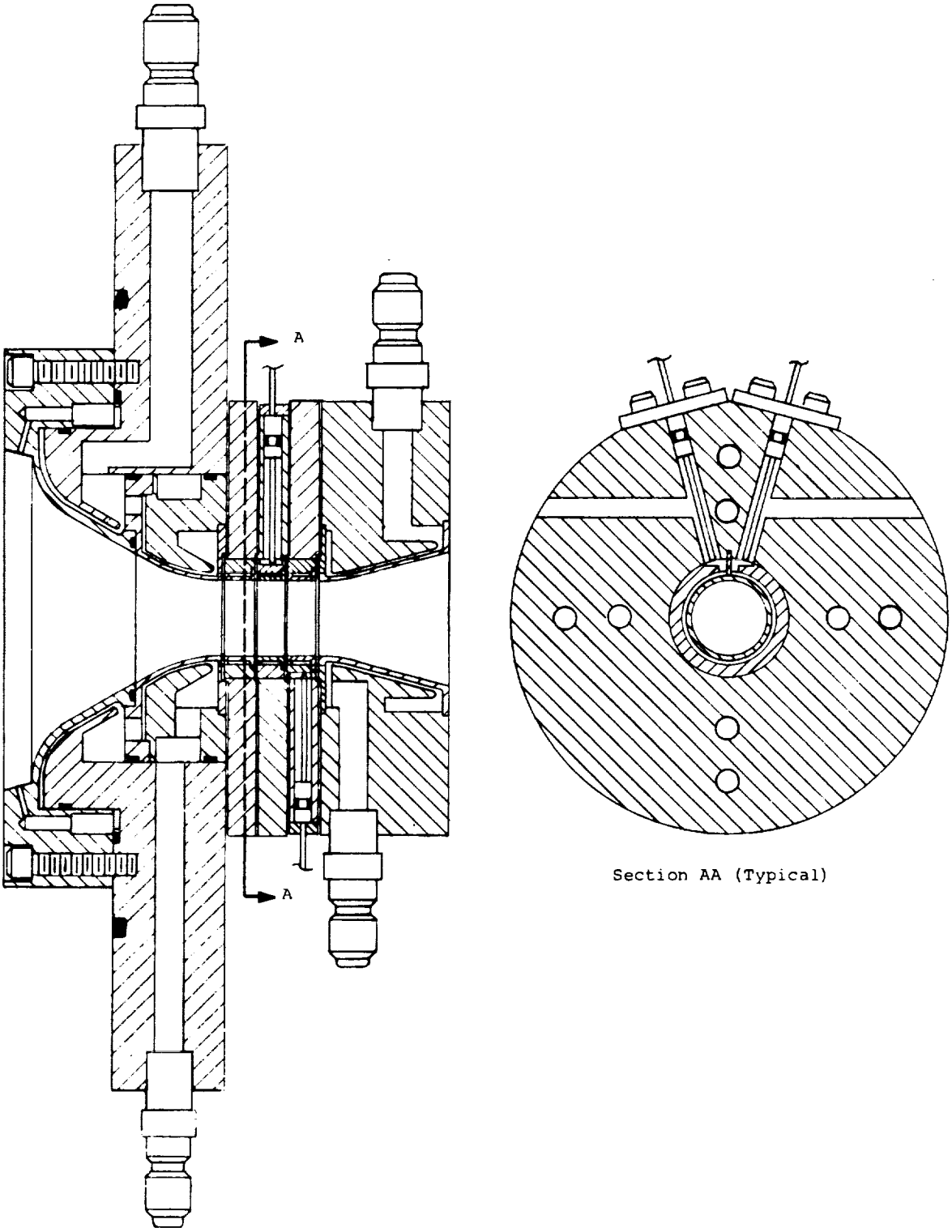

Figure 10. Schematic Drawing of Typical Heat-Transfer Calibration Nozzle

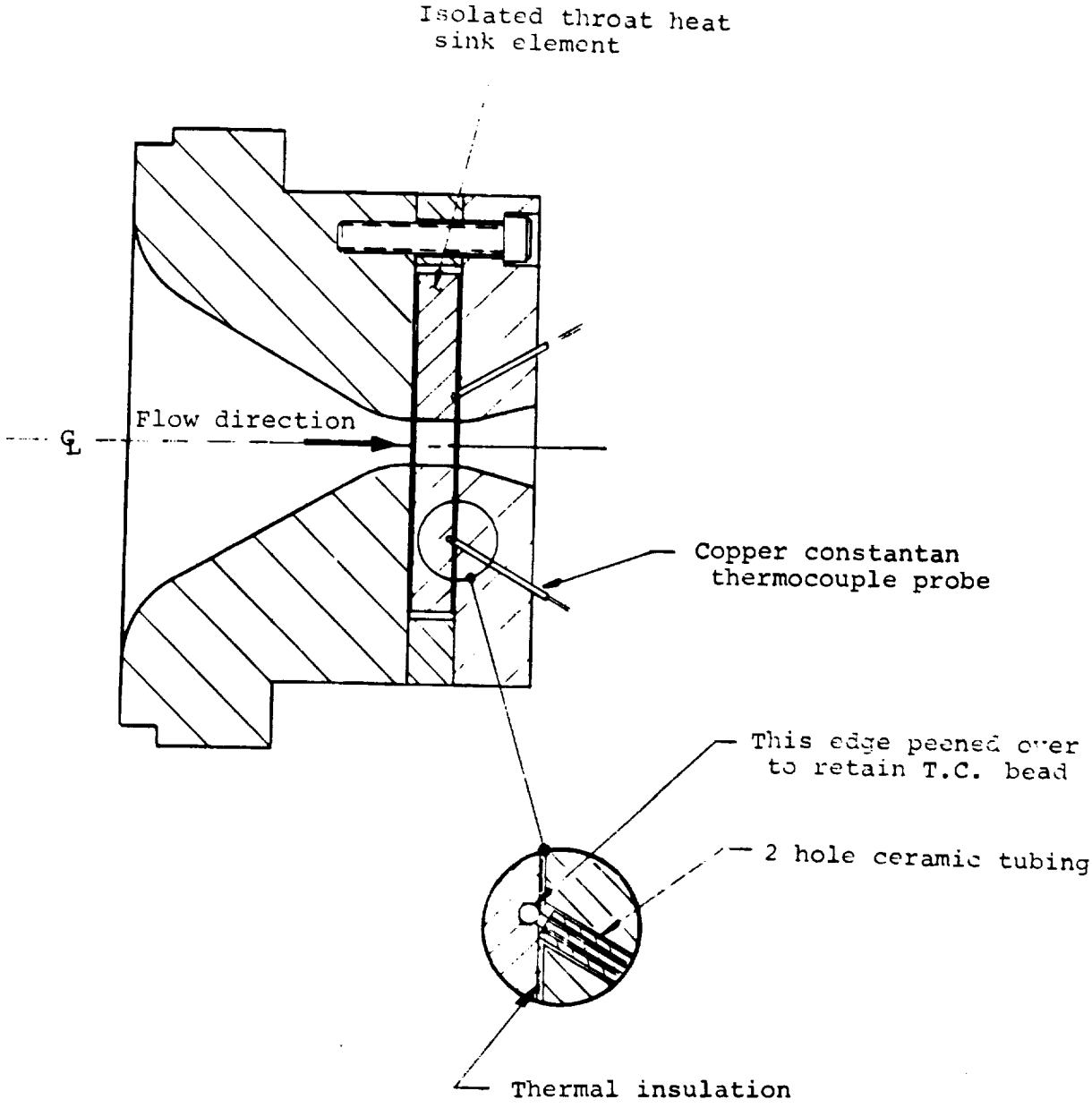

Figure 11. Section Representation of the Hot-Wall Calorimeter Model

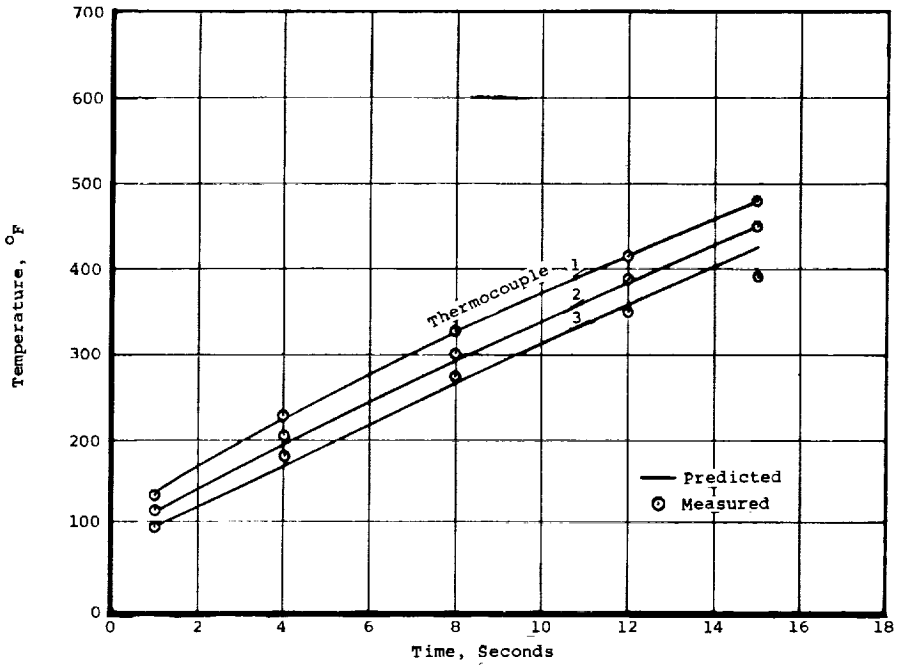

(a) Test 423, Hot-Wall Calorimeter

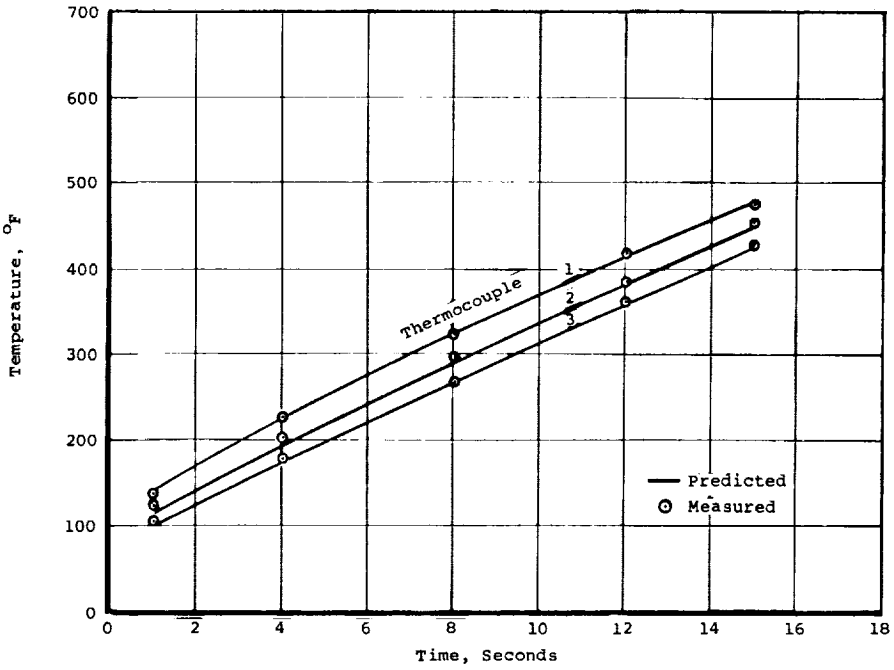

(b) Test 424, Hot-Wall Calorimeter

Figure 12. Thermocouple Tempterature Histories

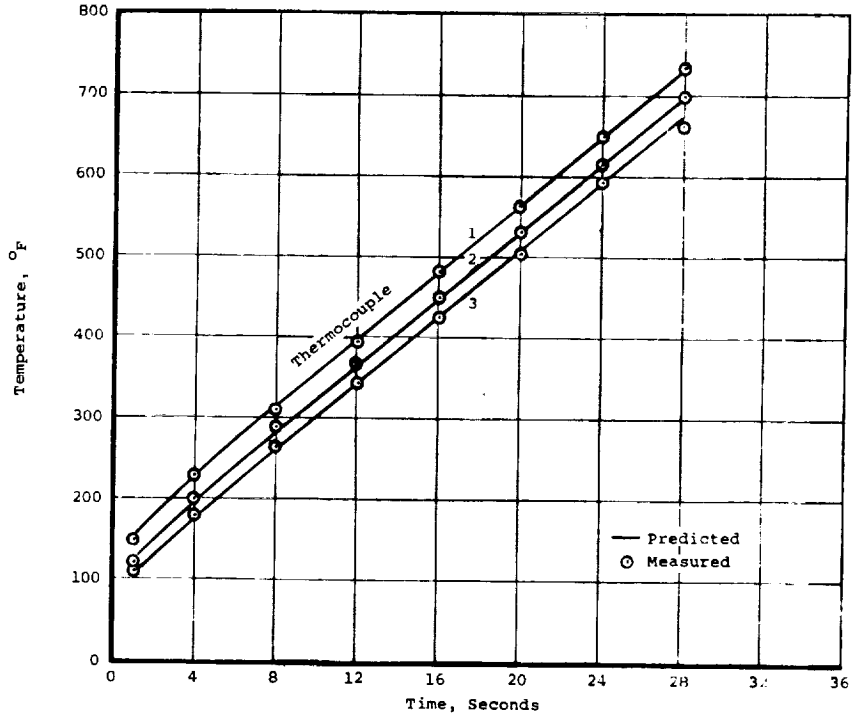

(c) Test 432, Hot-Wall Calorimeter

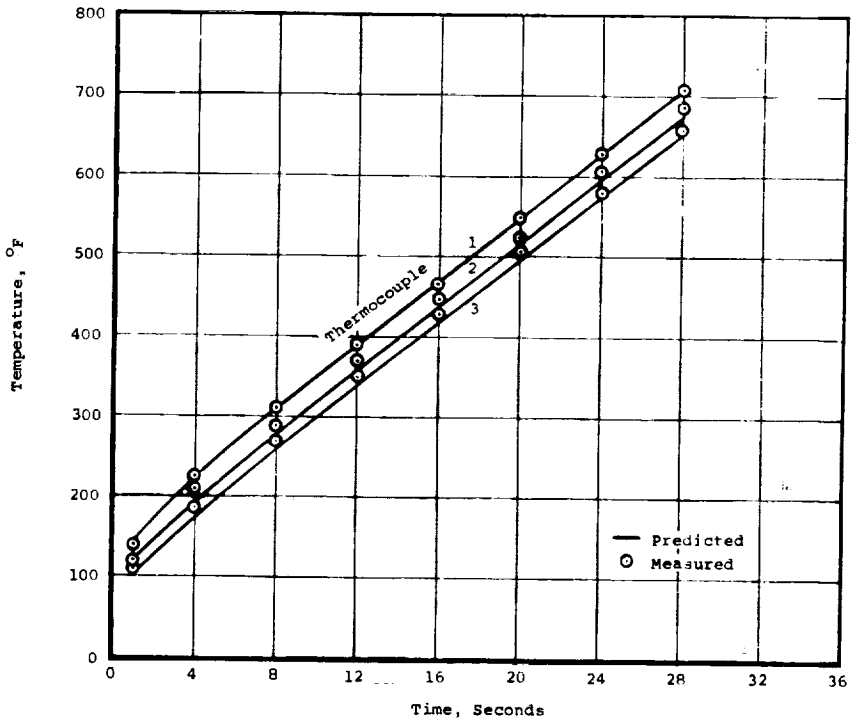

(d) Test 433, Hot-Wall Calorimeter

Figure 12. (concluded)

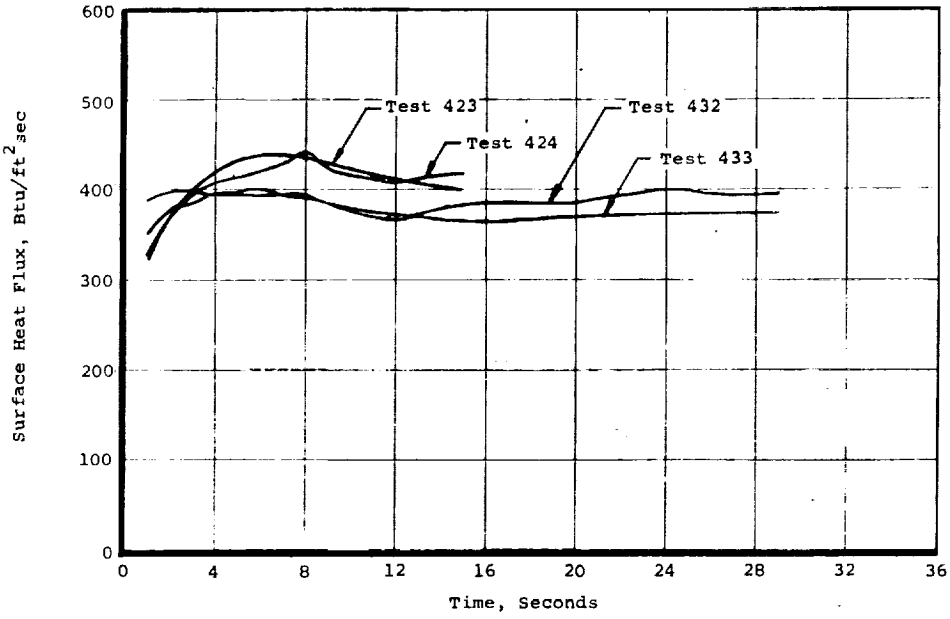

Figure 13. Surface Heat Flux Histories for Hot-Wall Calorimeter

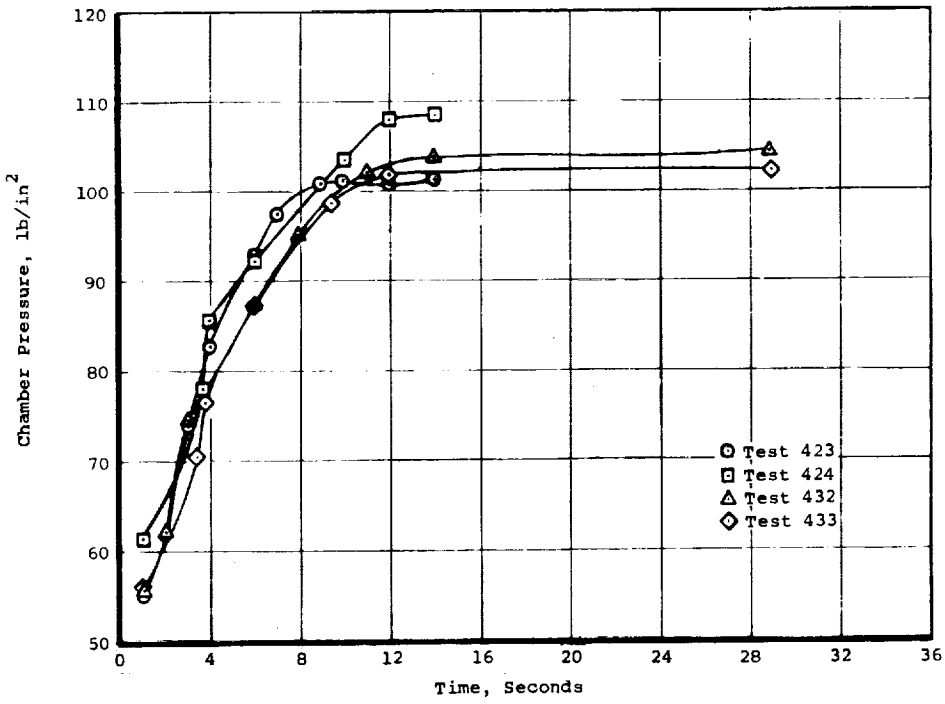

Figure 14. Chamber Pressure Histories for Hot-Wall Calorimeter

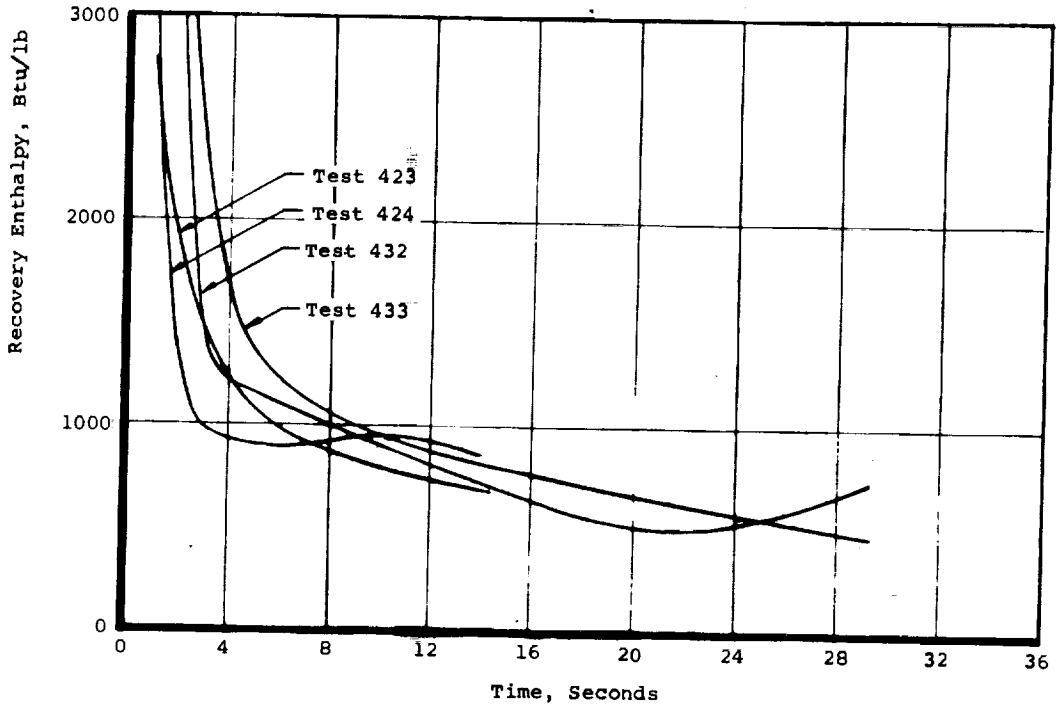

Figure 15. Recovery Enthalpy Histories for Hot-Wall Calorimeter

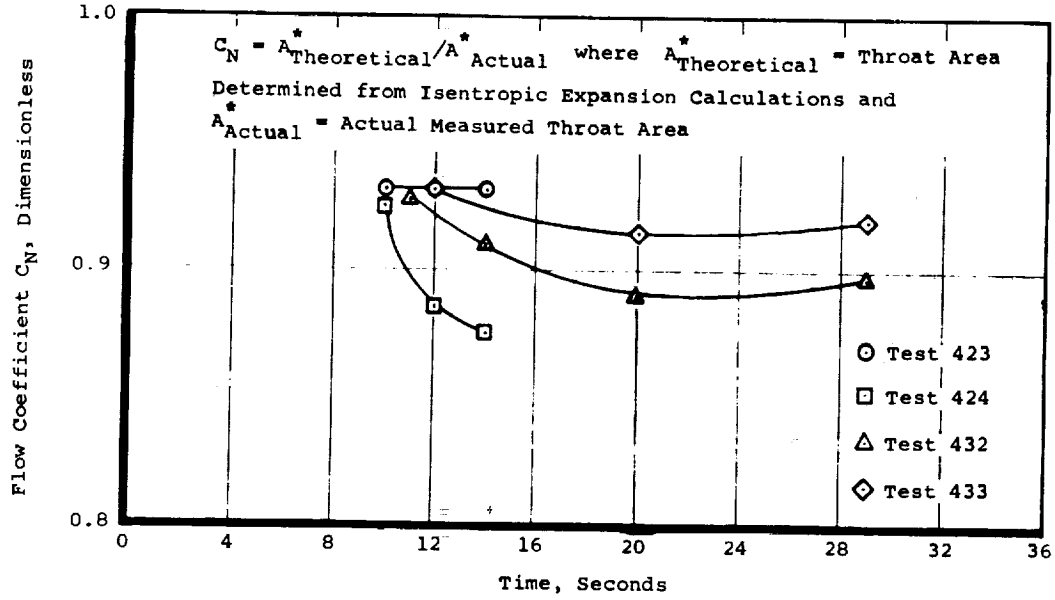

Figure 16. Flow Coefficient Variation for Hot-Wall Calorimeter

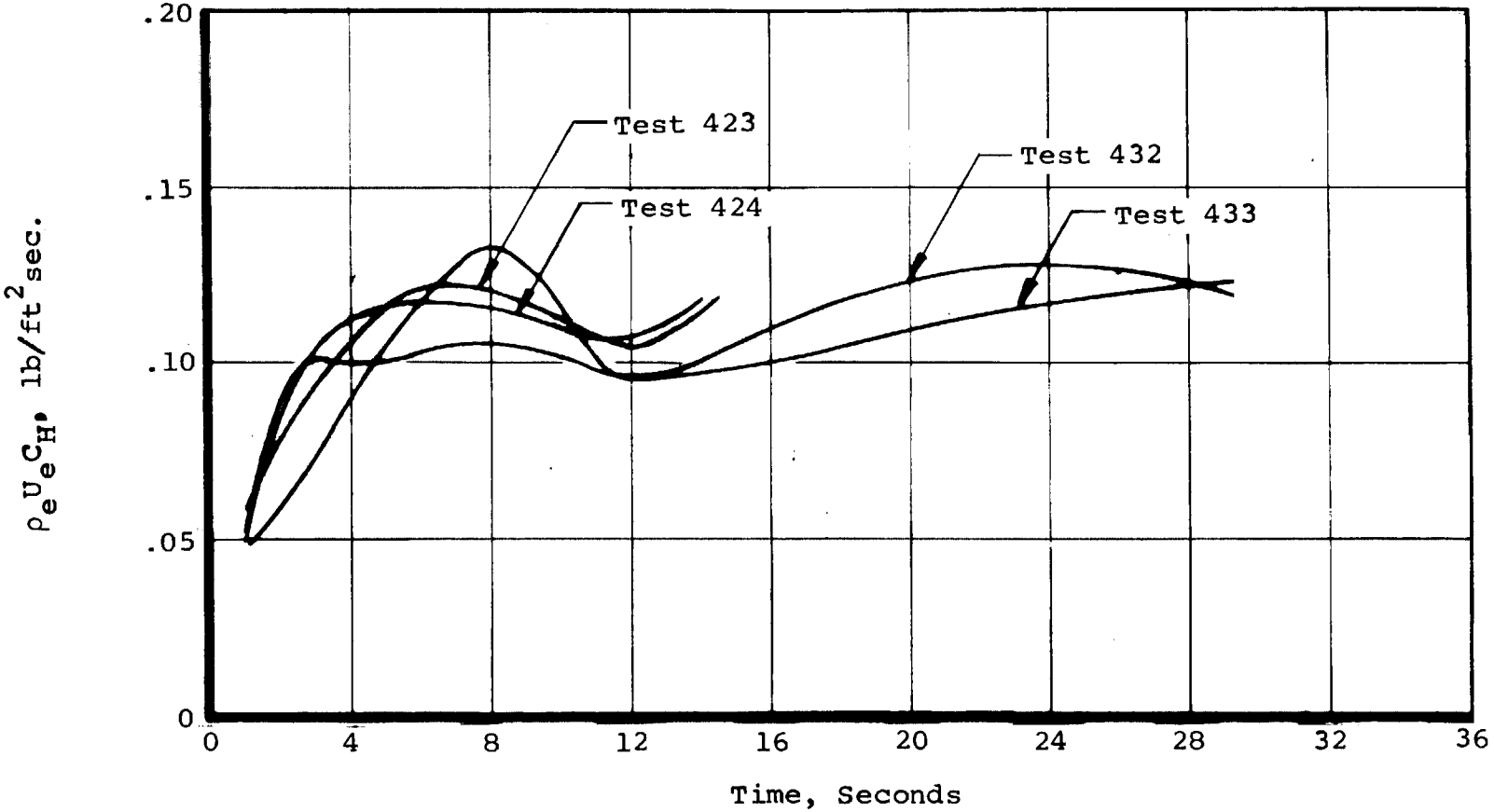

Figure 17. Heat Transfer Coefficient Histories for Hot-Wall Calorimeter

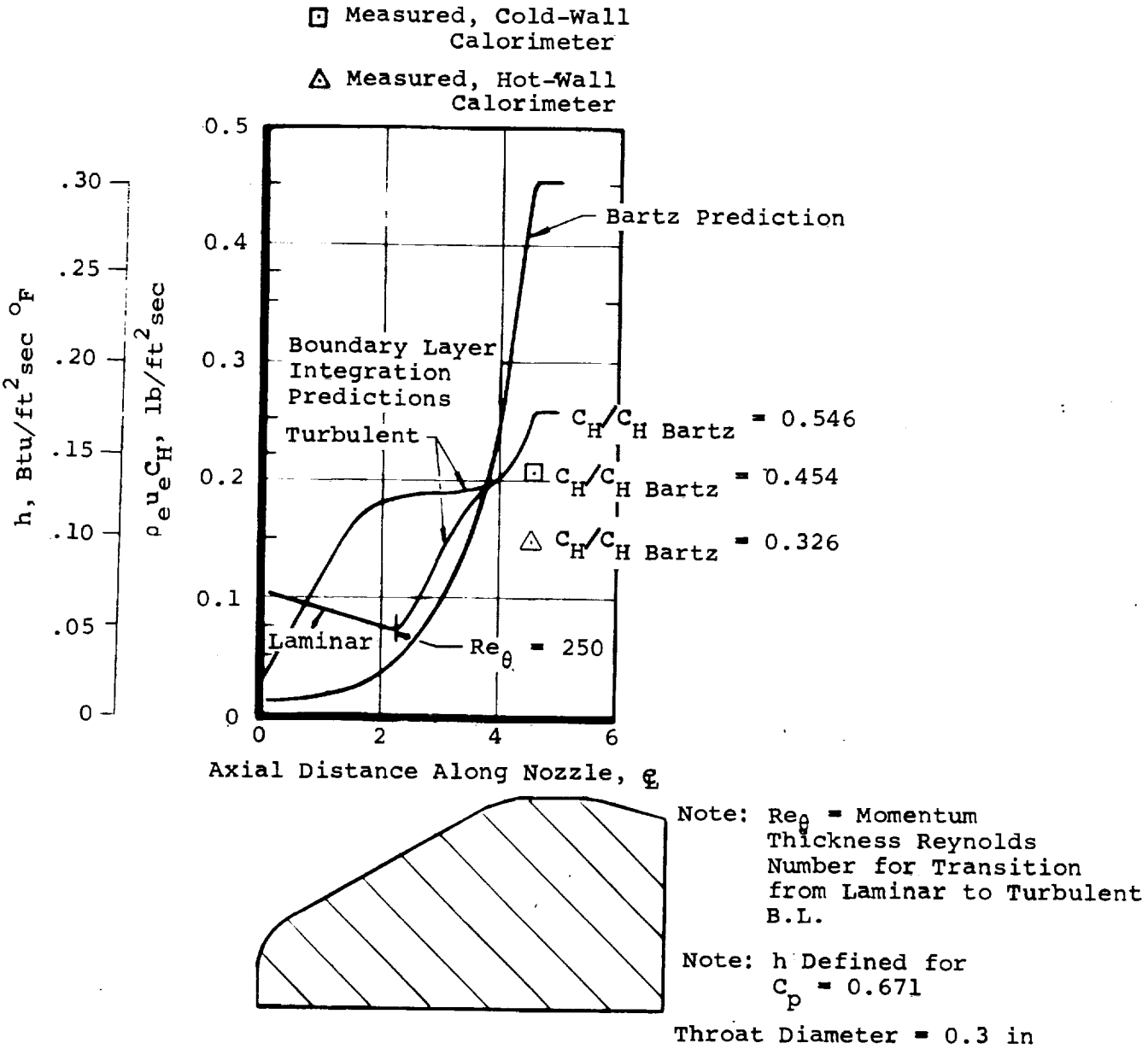

Figure 18. Comparison of Measured and Predicted Heat Transfer Coefficient

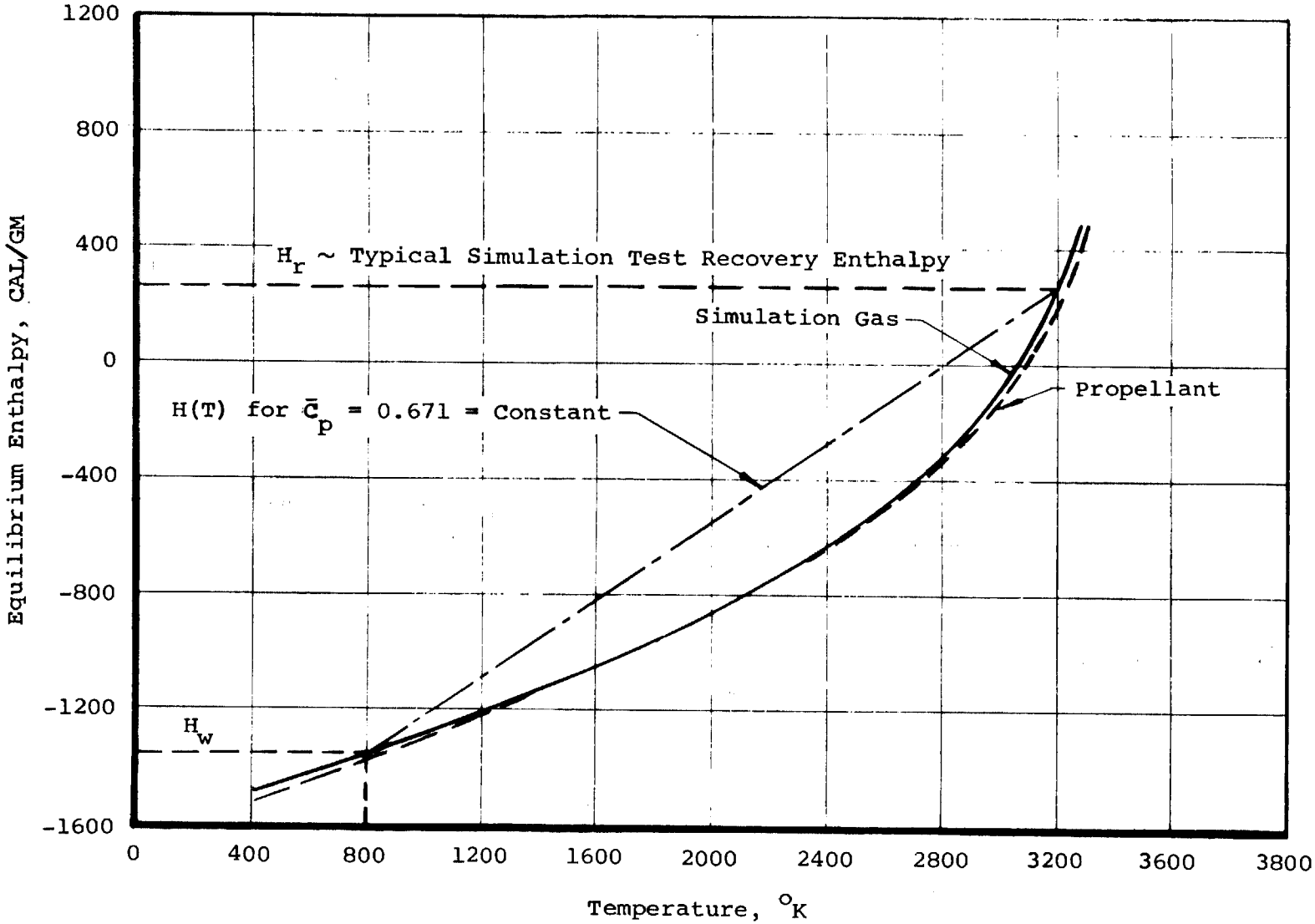

Figure 19. Enthalpy - Temperature Relation for the Simulation Gas and Rocket Exhaust Products.

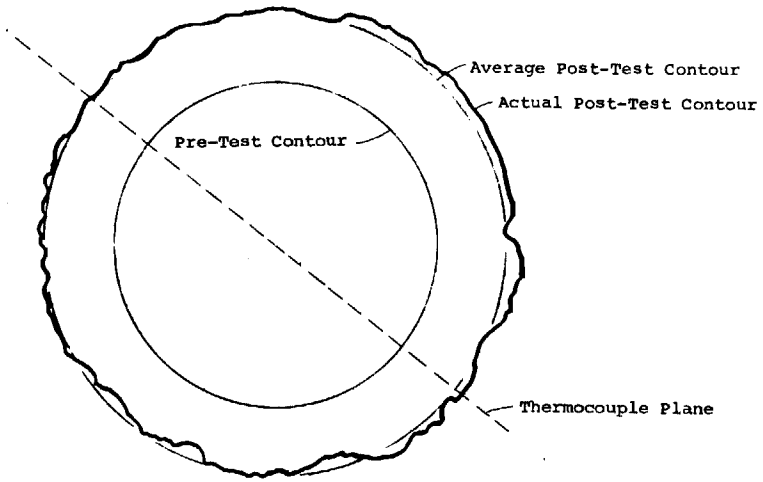

(a) Nozzle NL-1, MXS-89 Silica-Phenolic
Depth to First Thermocouple
from Eroded Surface = 0.070"

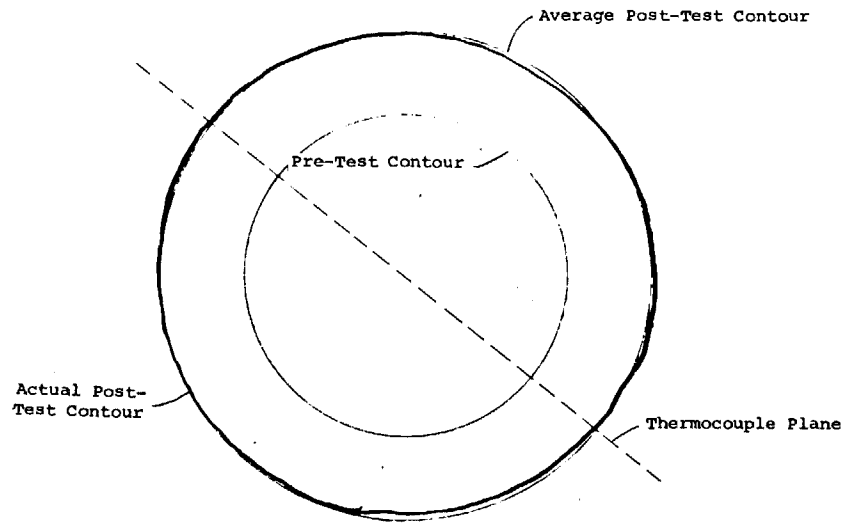

(b) Nozzle NL-2, MX4500 Graphite-Phenolic
Depth to First Thermocouple
from Eroded Surface = 0.015"

Figure 20. Post-Test Throat Contour Shadowgraph of Ablative Test Nozzles

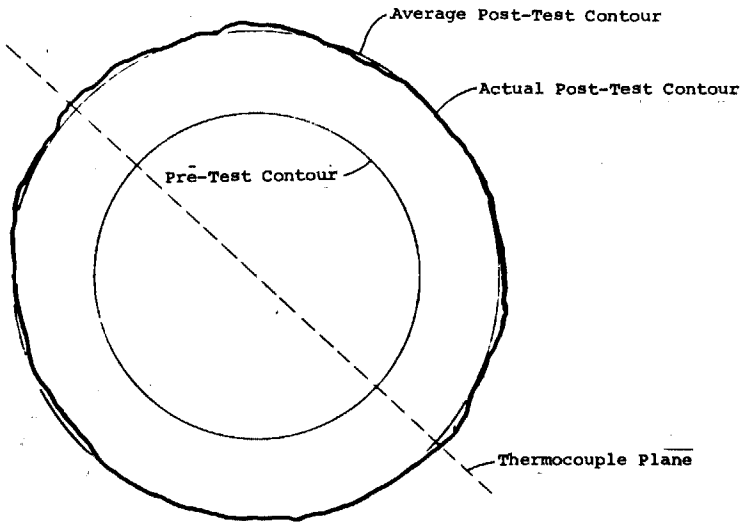

(c) Nozzle NL-3, MXA-11 Asbestos-Phenolic
Depth to First Thermocouple
from Eroded Surface - 0.050"

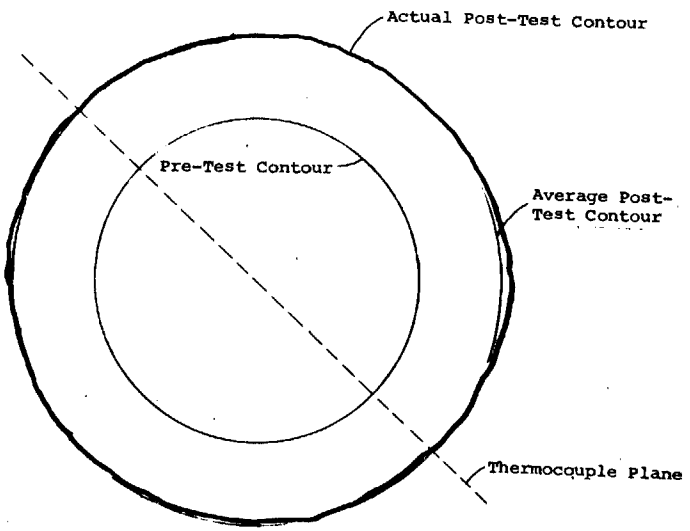

(d) Nozzle NL-4, MX4926 Carbon-Phenolic
Depth to First Thermocouple
from Eroded Surface - 0.030"

Figure 20. (continued)

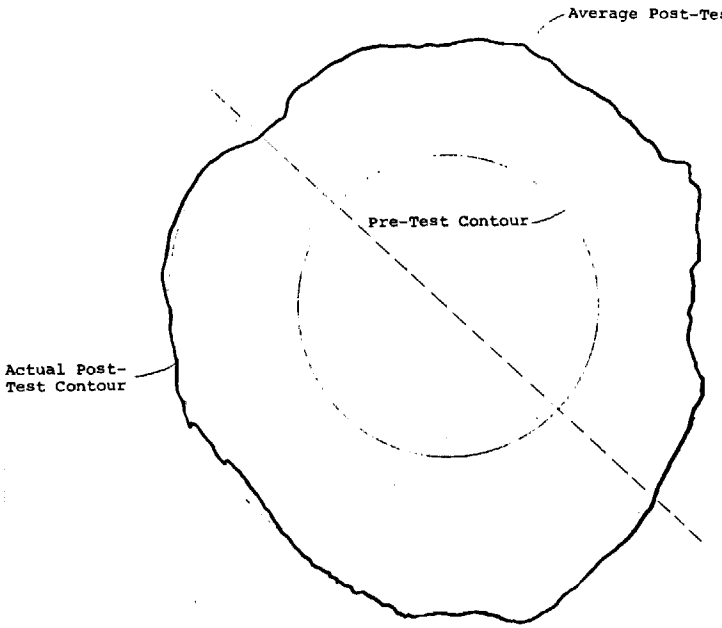

(e) Nozzle NL-5, FM5051 Nylon-Phenolic
Depth to First Thermocouple
from Eroded Surface = 0.040"

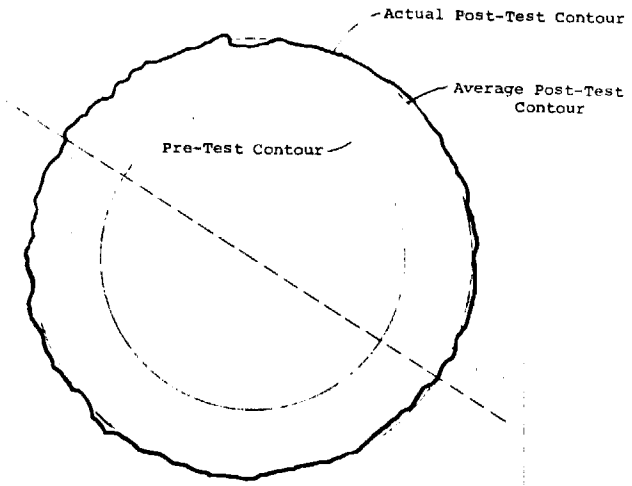

(f) Nozzle NL-6, XR2015 Silica-Phenyl Silane + Buna N
Depth to First Thermocouple
from Eroded Surface = 0.060"

Figure 20. (concluded)

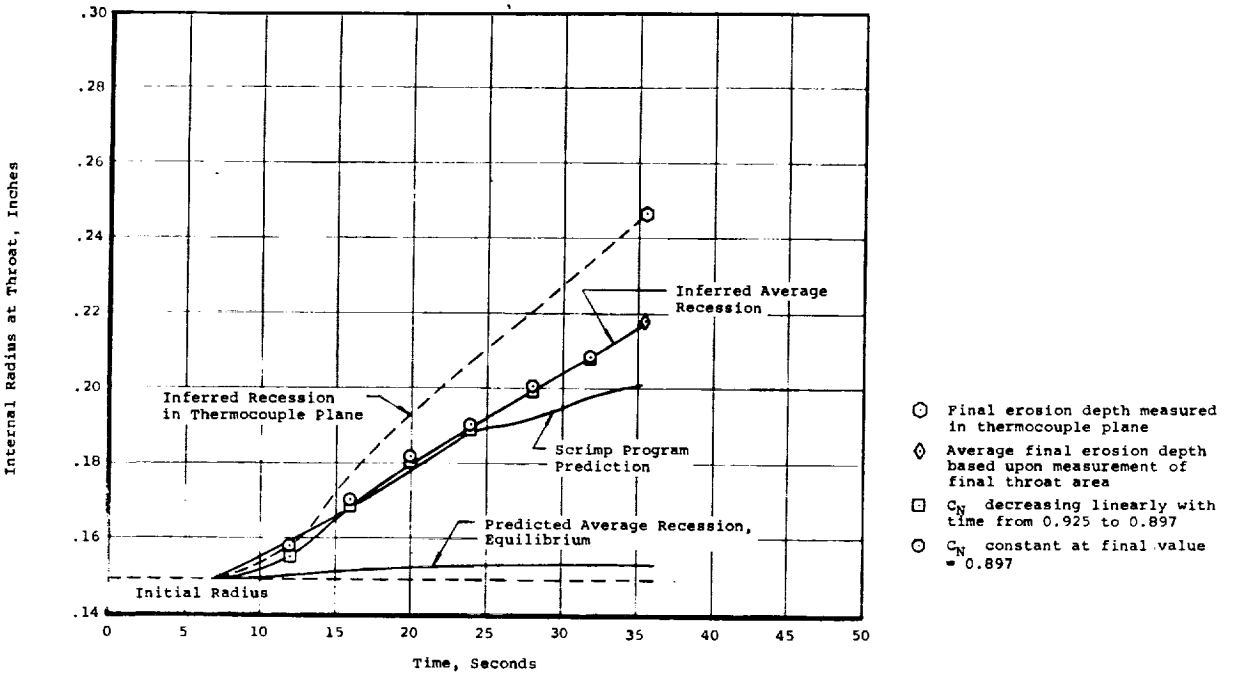

(a) Test 427, Nozzle NL-1, Silica Phenolic

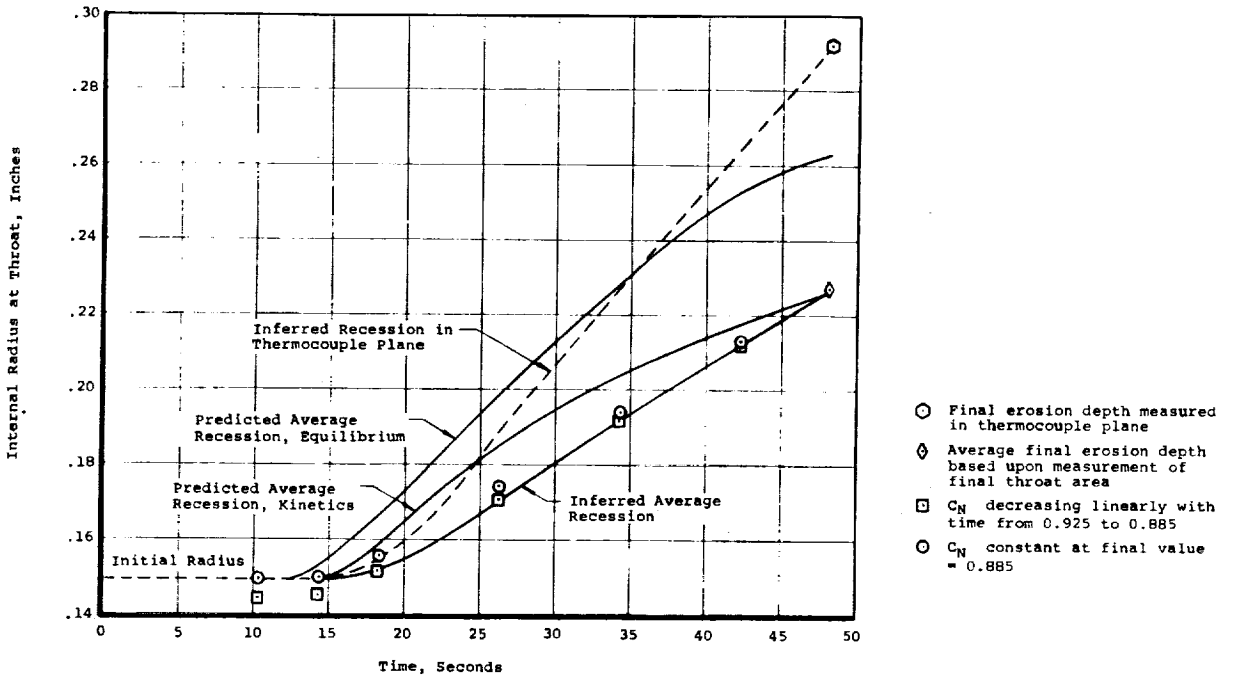

(b) Test 426, Nozzle NL-2, Graphite Phenolic

Figure 21. Predicted and measured surface recession history for ablative material simulation tests

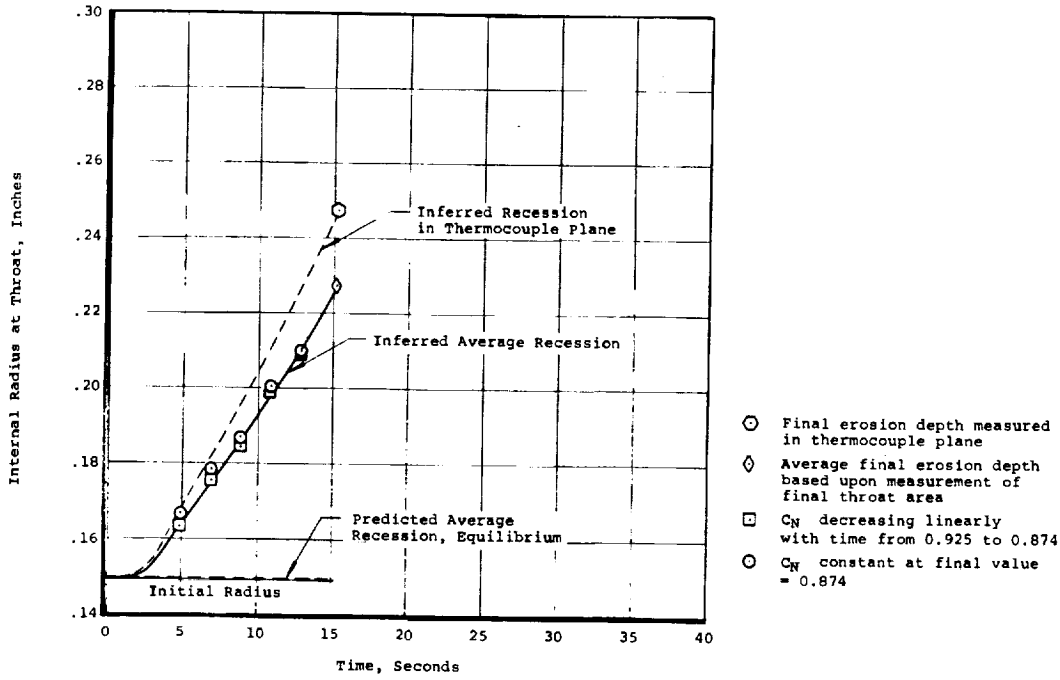

(c) Test 430, Nozzle NL-3, Asbestos Phenolic

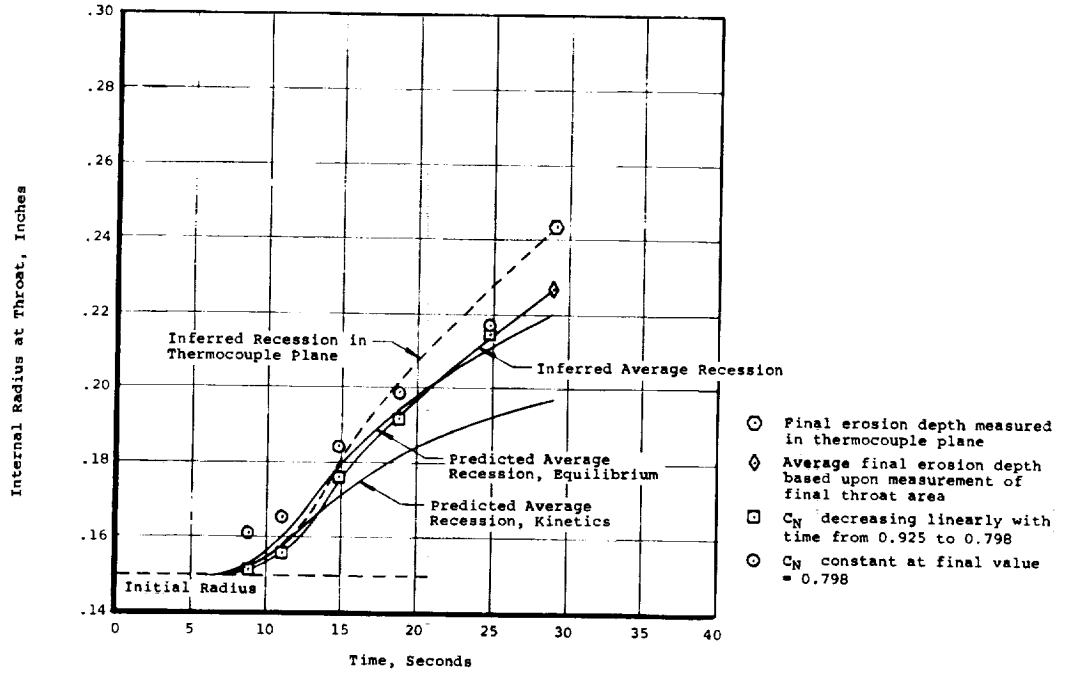

(d) Test 431, Nozzle NL-4, Carbon Phenolic

Figure 21. (continued)

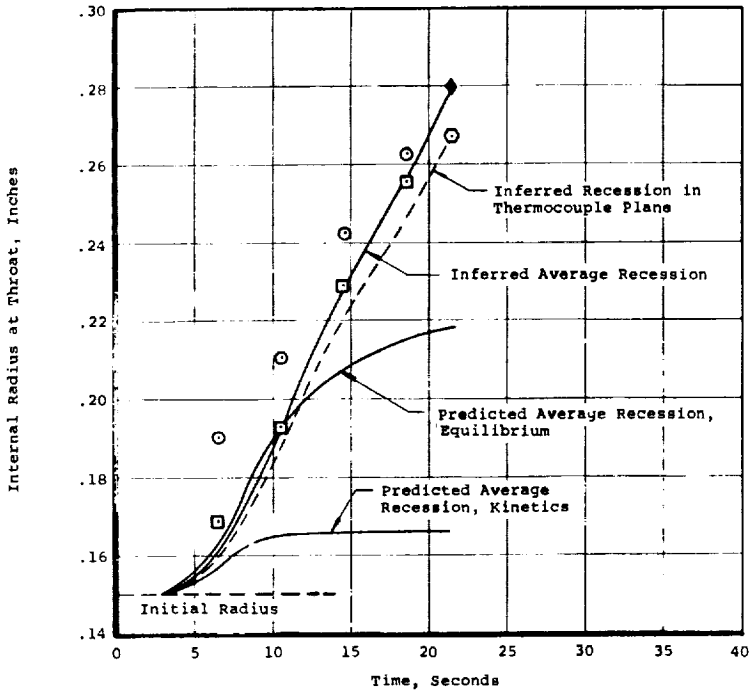

(e) Test 429, Nozzle NL-5, Nylon Phenolic

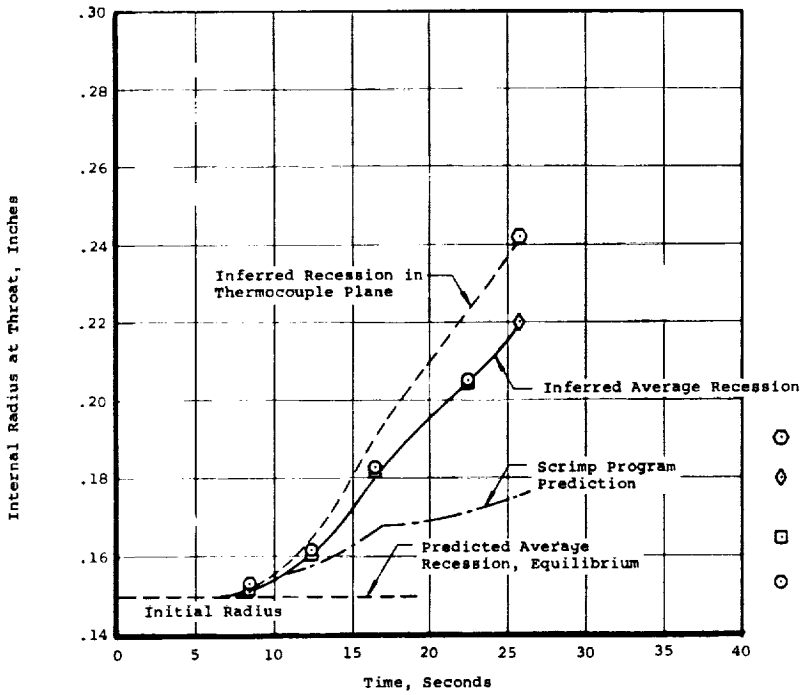

(f) Test 428, Nozzle NL-6, Silica Phenyl Silane + Buna N

Figure 21. (concluded)

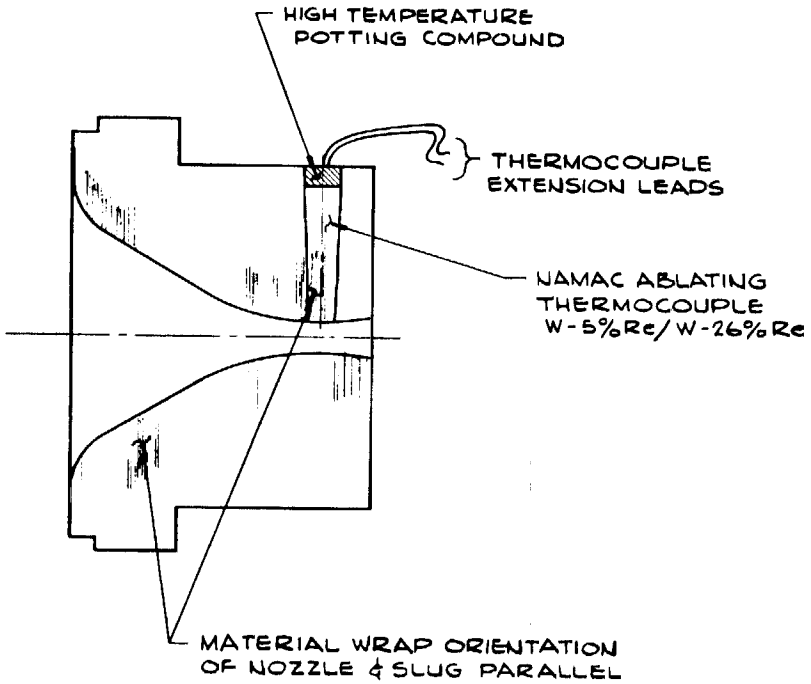

NOTE:
THERMOCOUPLE SLUG MADE FROM NOZZLE BODY RAW MATERIAL STOCK

Figure 22. Surface Temperature Sensor Installation Technique

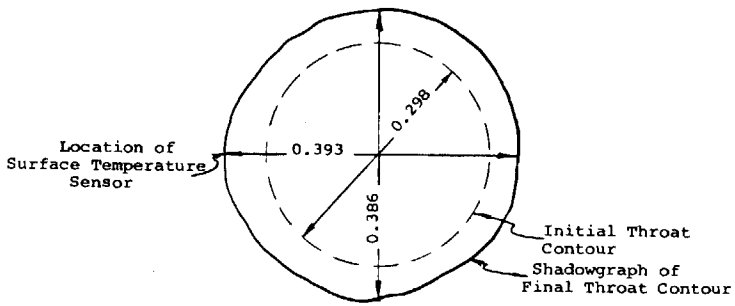

All dimensions in inches

Test Material	Graphite phenolic, MX4500
Chamber Pressure	210-150 psia
Test Gas	85% N_2 - 15% O_2
Total enthalpy	4700 BTU/Lb.
Thermocouple Material	W - 5% Re, W - 26% Re

Figure 23. Pre- and Post-Test Nozzle Contours and Test Conditions for Surface Temperature Sensor Verification Test

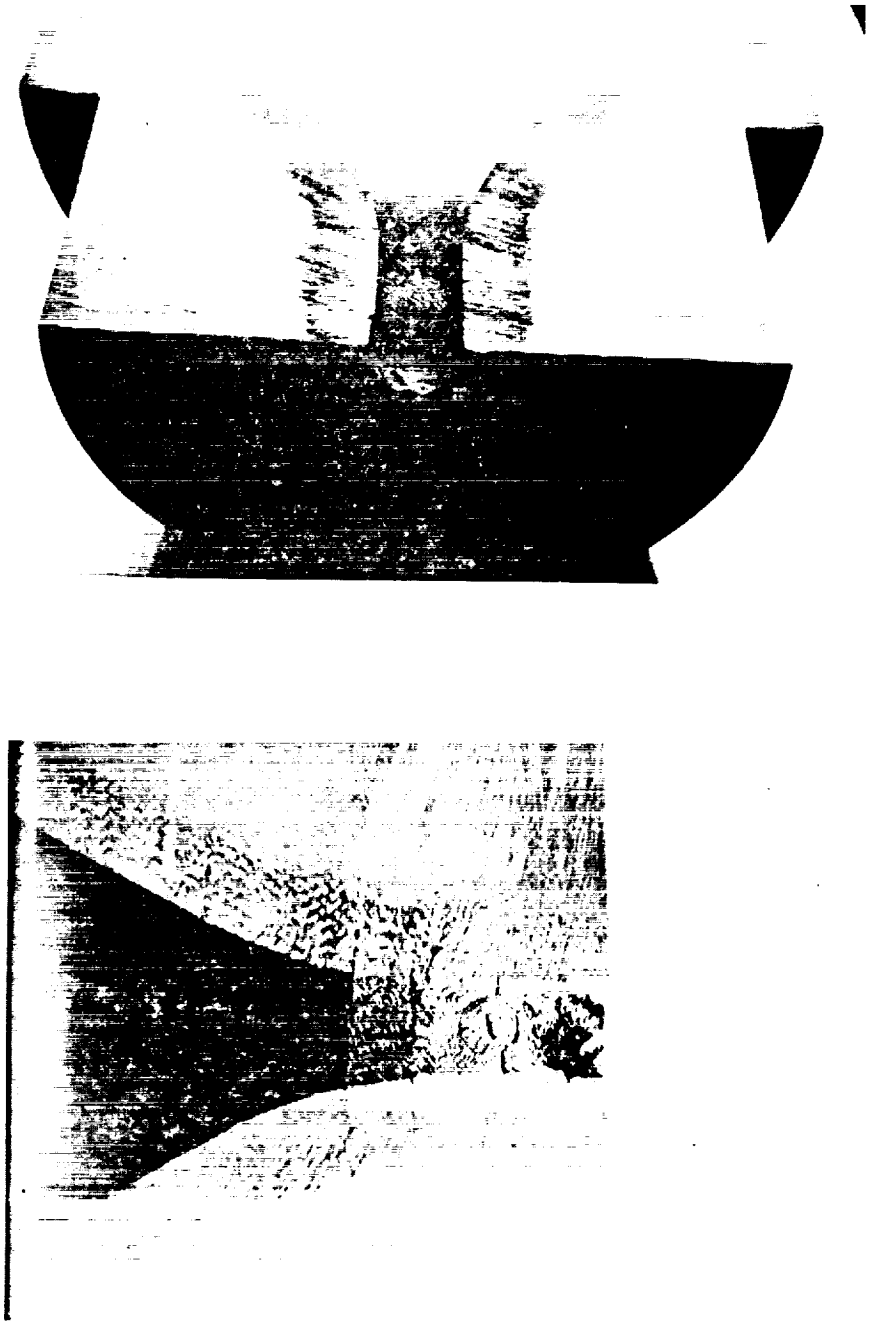

Figure 24. Post-Test Sectioned View of Graphite Phenolic Nozzle Instrumented with a NANMAC Surface Temperature Sensor

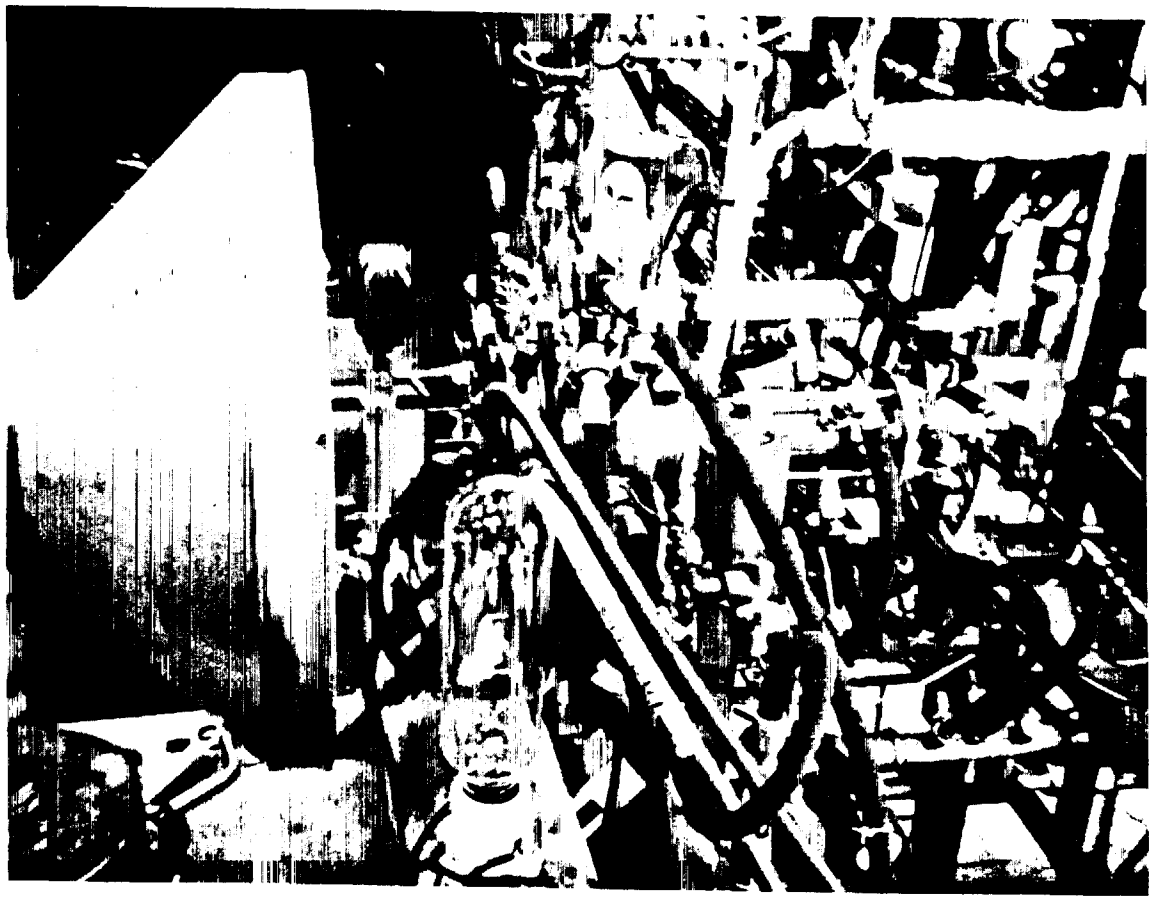

Figure 25. Optical Pyrometer Check-out Test Setup

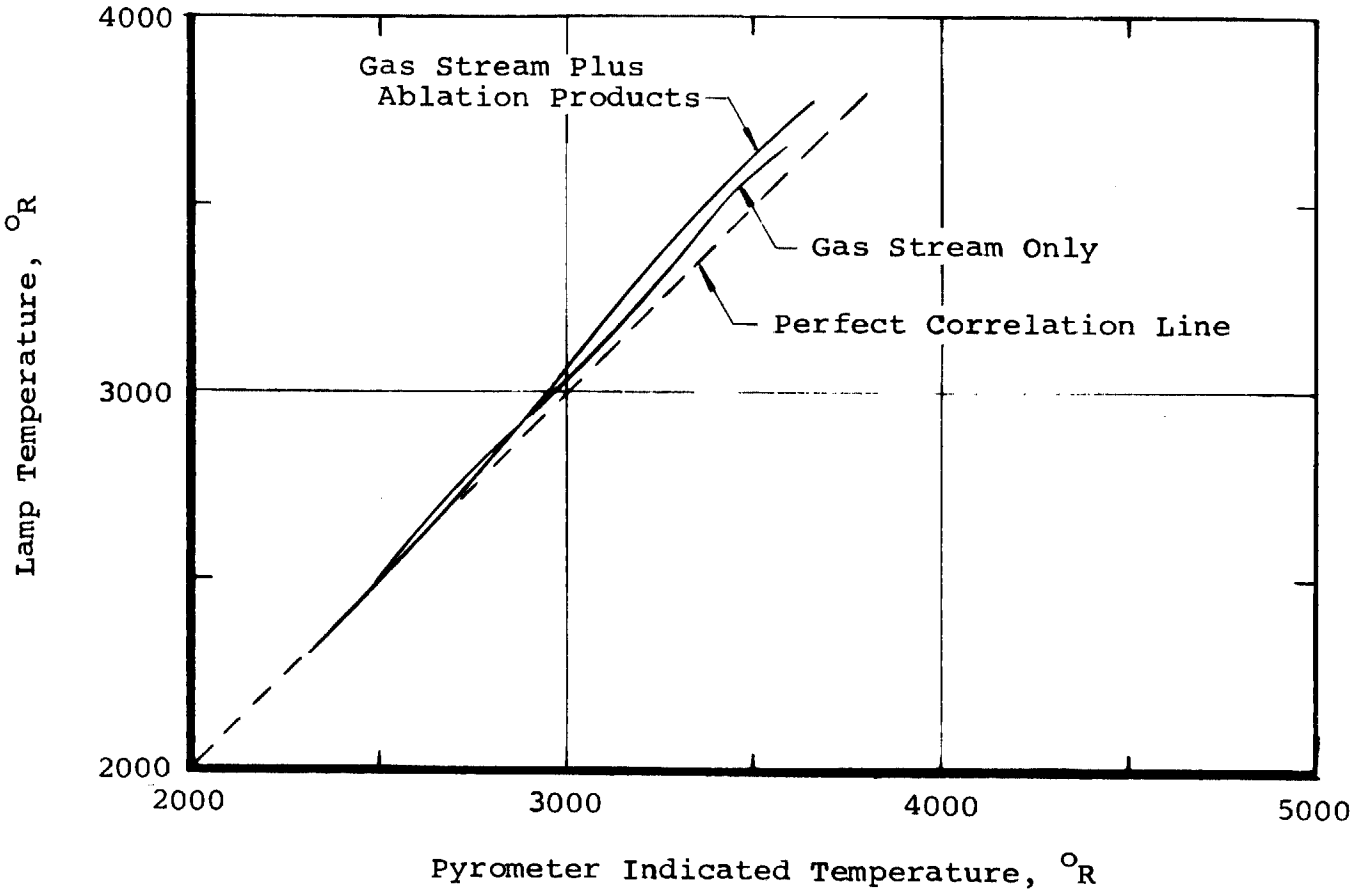

Figure 26. Effect of Gas Environment Interference Upon Lamp Temperature Sensed by Infrared Pyrometer.

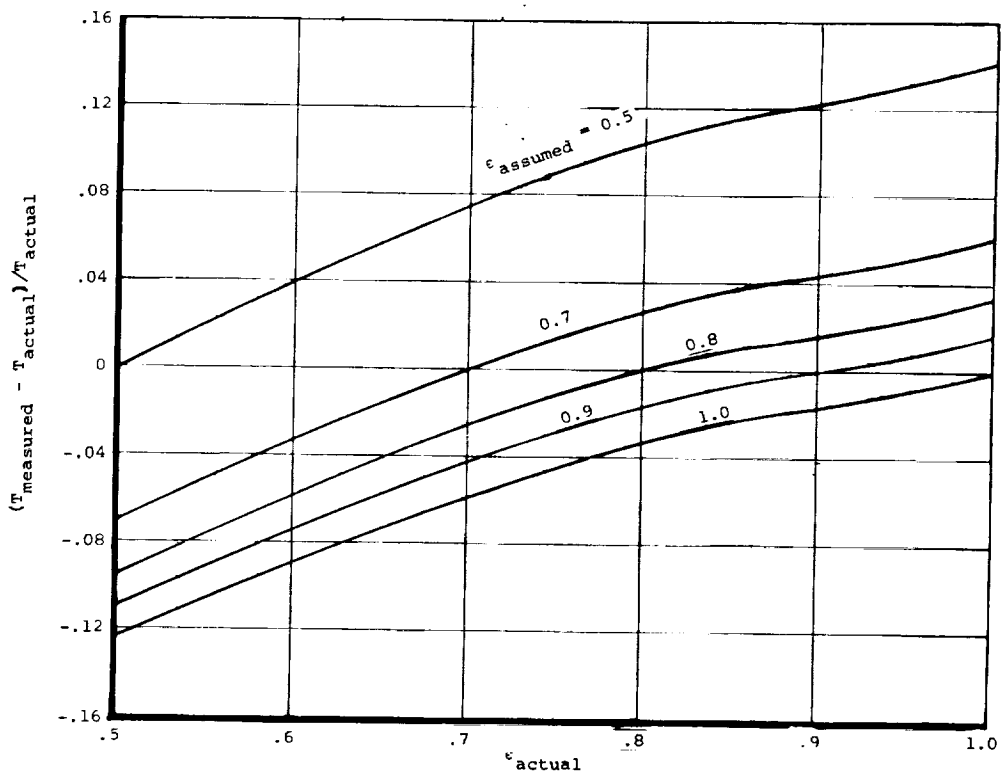

(a) $T_{indicated} = 5000^{\circ}R$

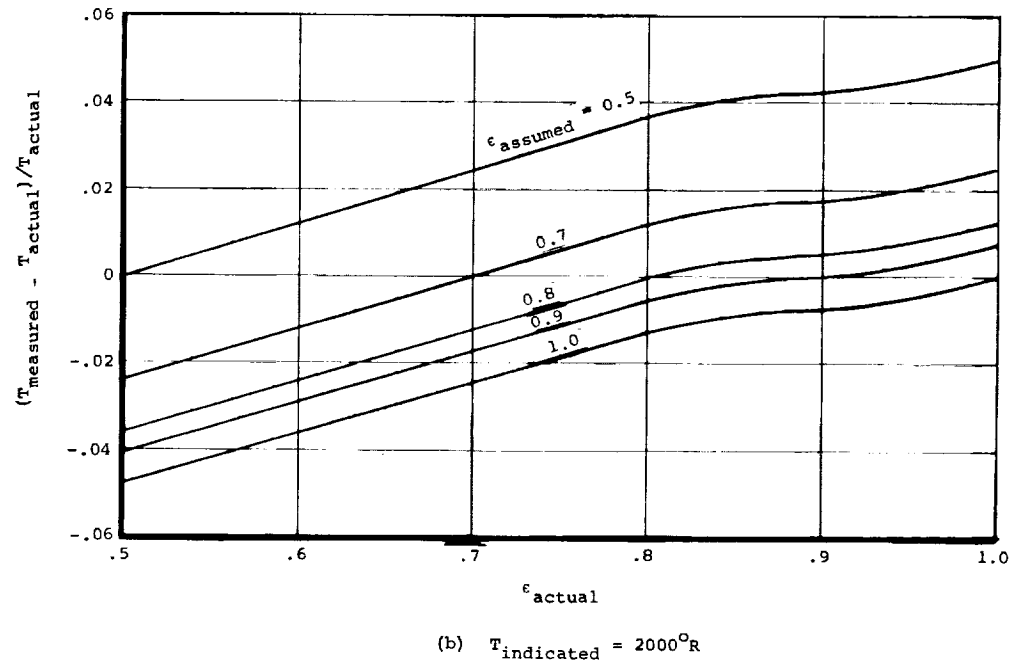

(b) $T_{indicated} = 2000^{\circ}R$

Figure 27. Percentage error in nozzle surface temperature determined from infrared pyrometer when the assumed value of surface emissivity differs from the actual value

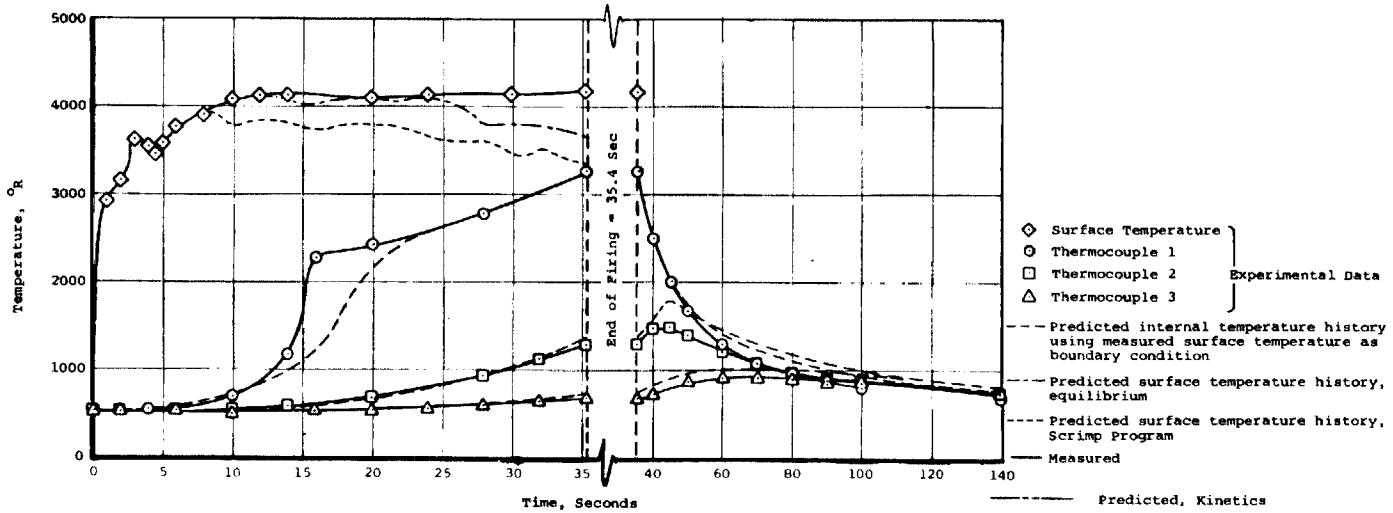

(a) Test 427, Nozzle NL-1, Silica Phenolic

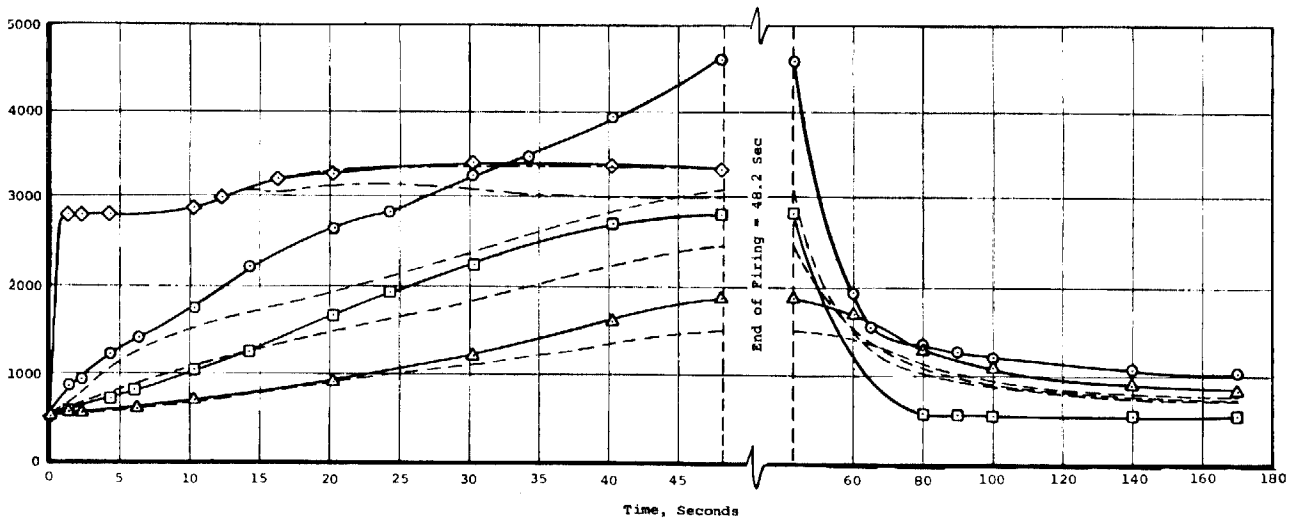

(b) Test 426, Nozzle NL-2, Graphite Phenolic

Figure 28. Measured and Predicted Surface and Subsurface Temperature Histories for Ablative Material Simulation Tests

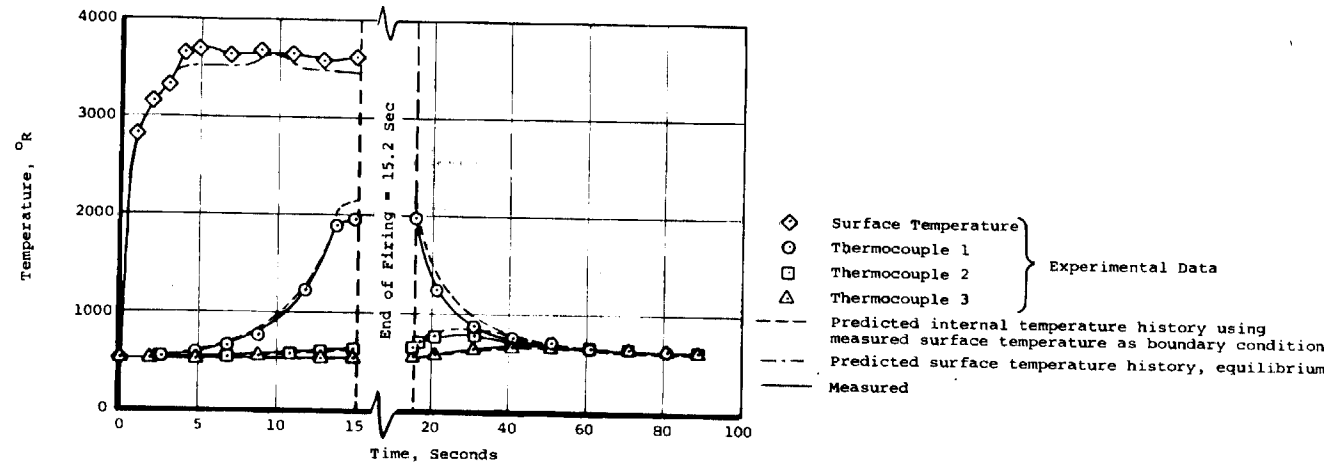

(c) Test 430, Nozzle NL-3, Asbestos Phenolic

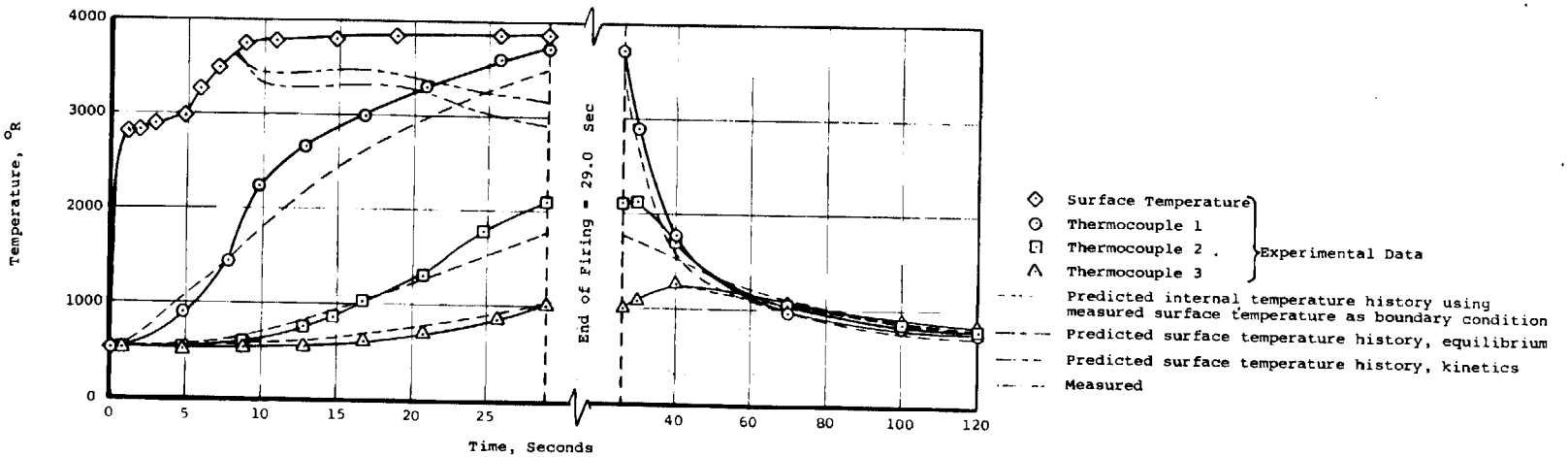

(d) Test 431, Nozzle NL-4, Carbon Phenolic

Figure 28. (continued)

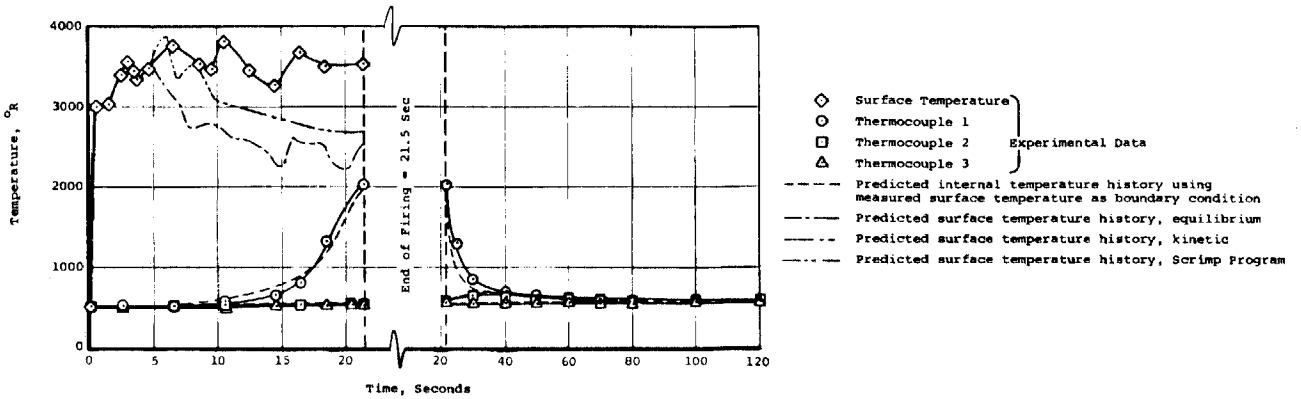

(e) Test 429, Nozzle NL-5, Nylon Phenolic

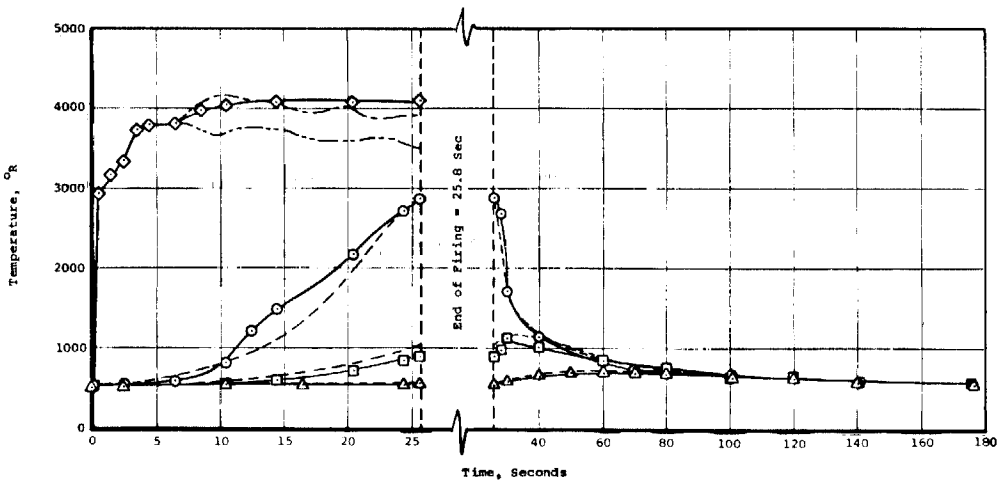

(f) Test 428, Nozzle NL-6, Silica Phenyl Silane + Buna N

Figure 28. (concluded)

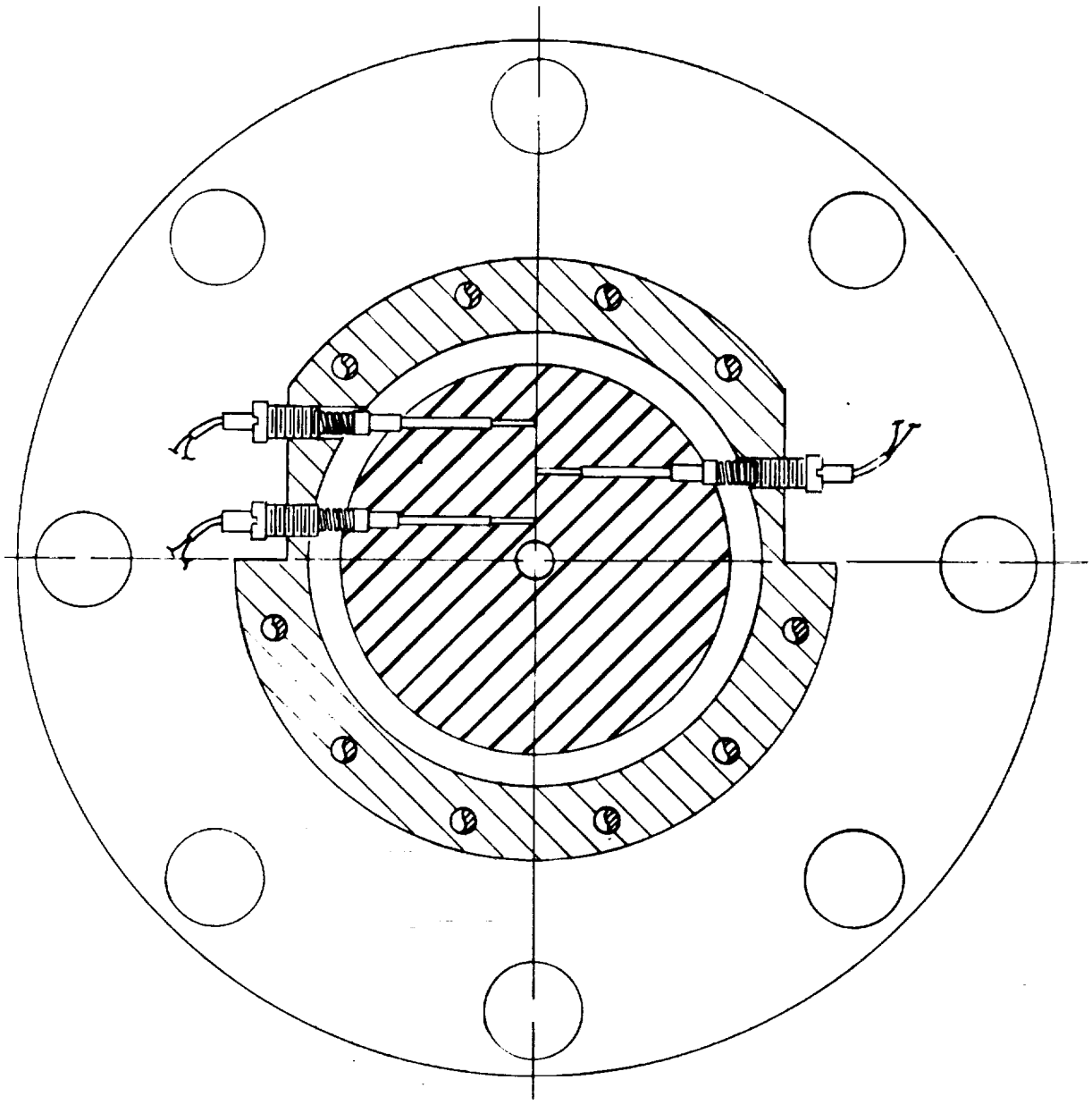

Figure 29. Thermocouple Installation in Test Nozzle

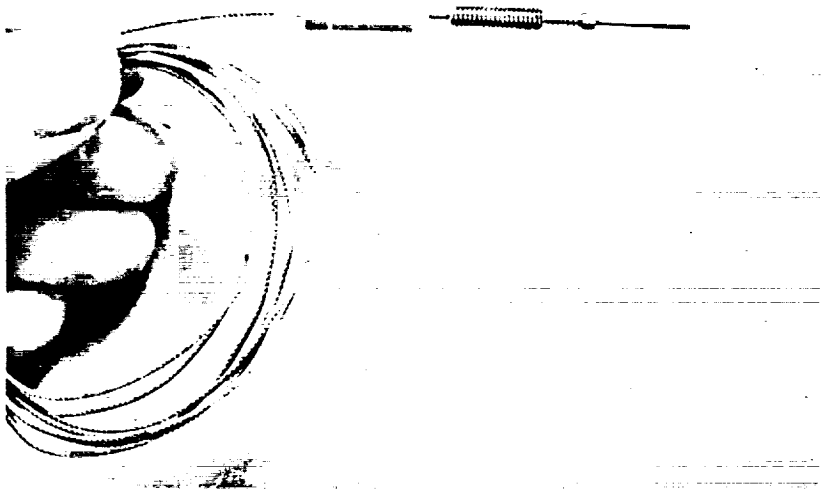

Figure 30. Thermocouple Probe

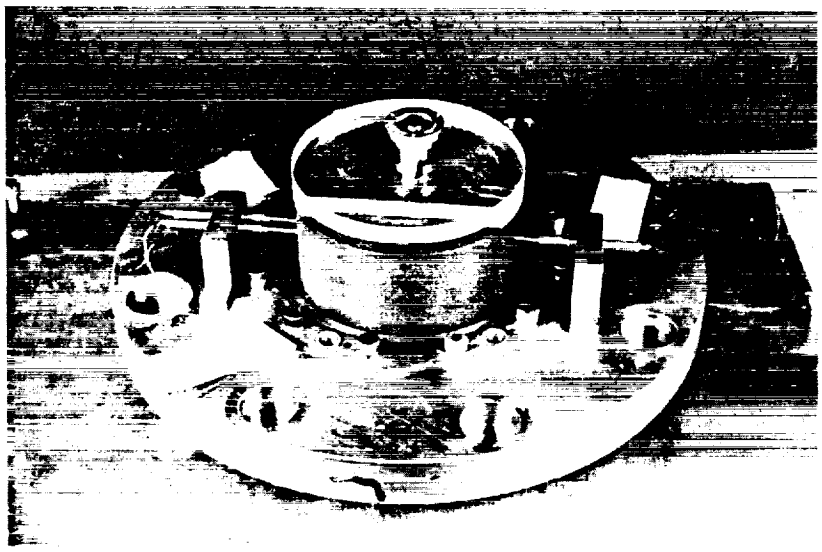

Figure 31. Instrumented Test Nozzle Set-Up for X-Ray Thermocouple Depth Evaluation

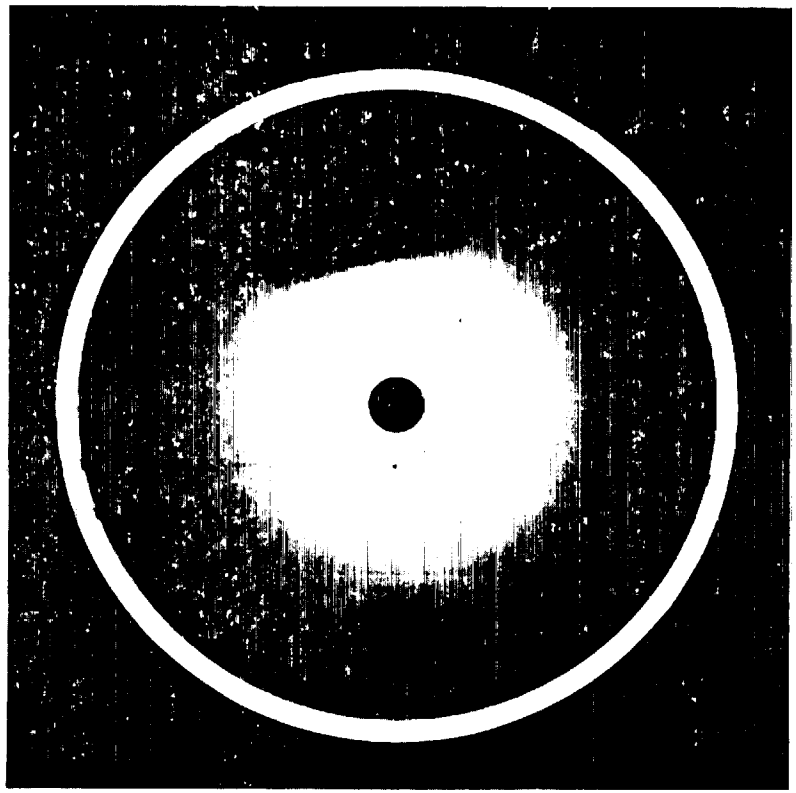

D* = 0.2980"

Thermocouple depths

δ_1 = 0.1680", δ_2 = 0.2850", δ_3 = 0.3775"

(a) NL-1, MXS-89 Silica Phenolic

D* = 0.2990"

Thermocouple depths

δ_1 = 0.1575", δ_2 = 0.2405", δ_3 = 0.4255"

(b) NL-2, MX-4500 Graphite Phenolic

Figure 32. X-Ray Photograph of Pre-Test Ablative Nozzle for Thermocouple Depth Specification

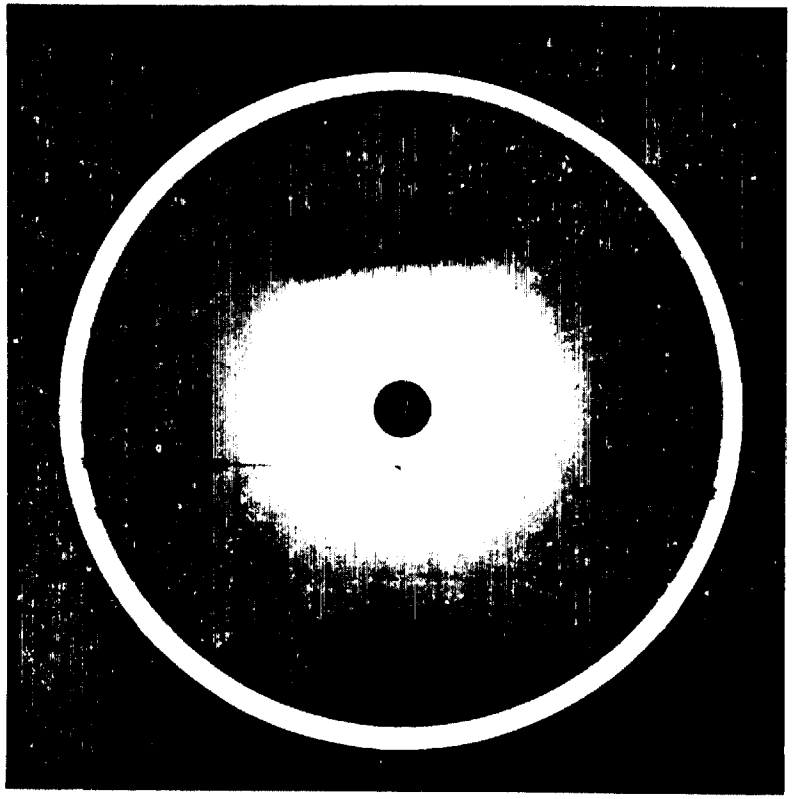

D* = 0.2990"

Thermocouple depths

δ_1 = 0.1480", δ_2 = 0.2600", δ_3 = 0.4015"

(c) NL-3, MXA-11 Asbestos Phenolic

D* = 0.2990"

Thermocouple depths

δ_1 = 0.1235", δ_2 = 0.2795", δ_3 = 0.3965"

(d) NL-4, MX4926 Carbon Phenolic

Figure 32. (continued)

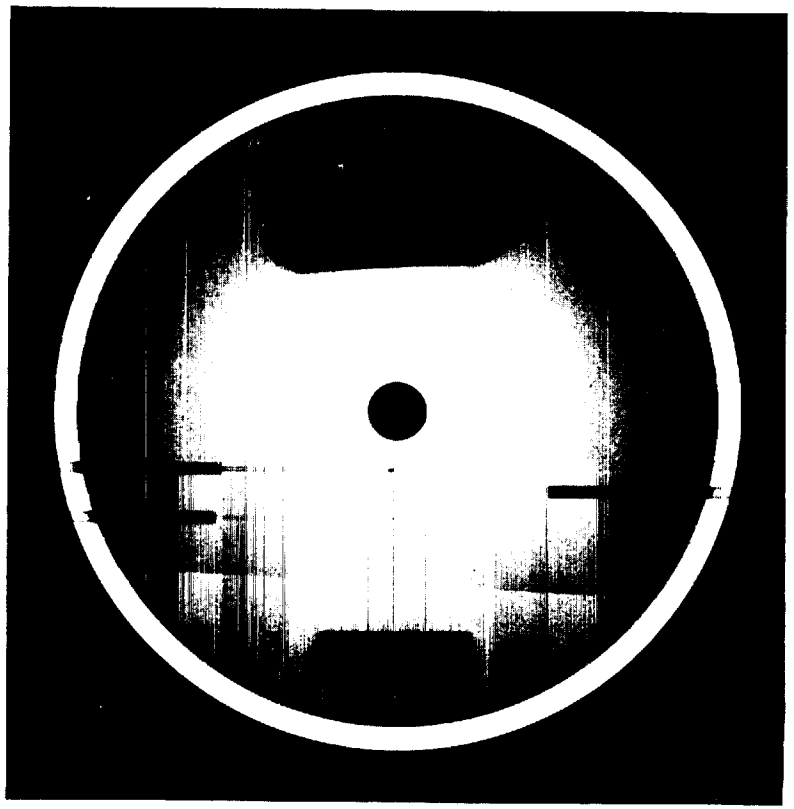

D* = 0.3000"

Thermocouple depths

δ_1 = 0.1570", δ_2 = 0.2595", δ_3 = 0.3960"

(e) NL-5, FM5051 Nylon Phenolic

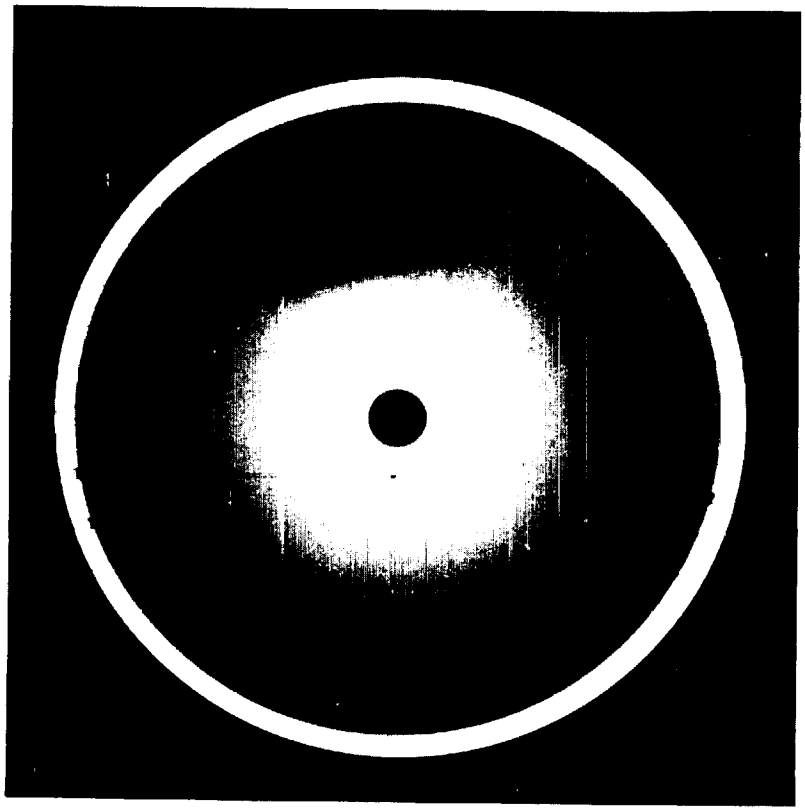

D* = 0.2990"

Thermocouple depths

δ_1 = 0.1530", δ_2 = 0.2355", δ_3 = 0.3915"

(f) NL-6, XR2015 Silica-Phenyl Silane + Buna N

Figure 32. (concluded)

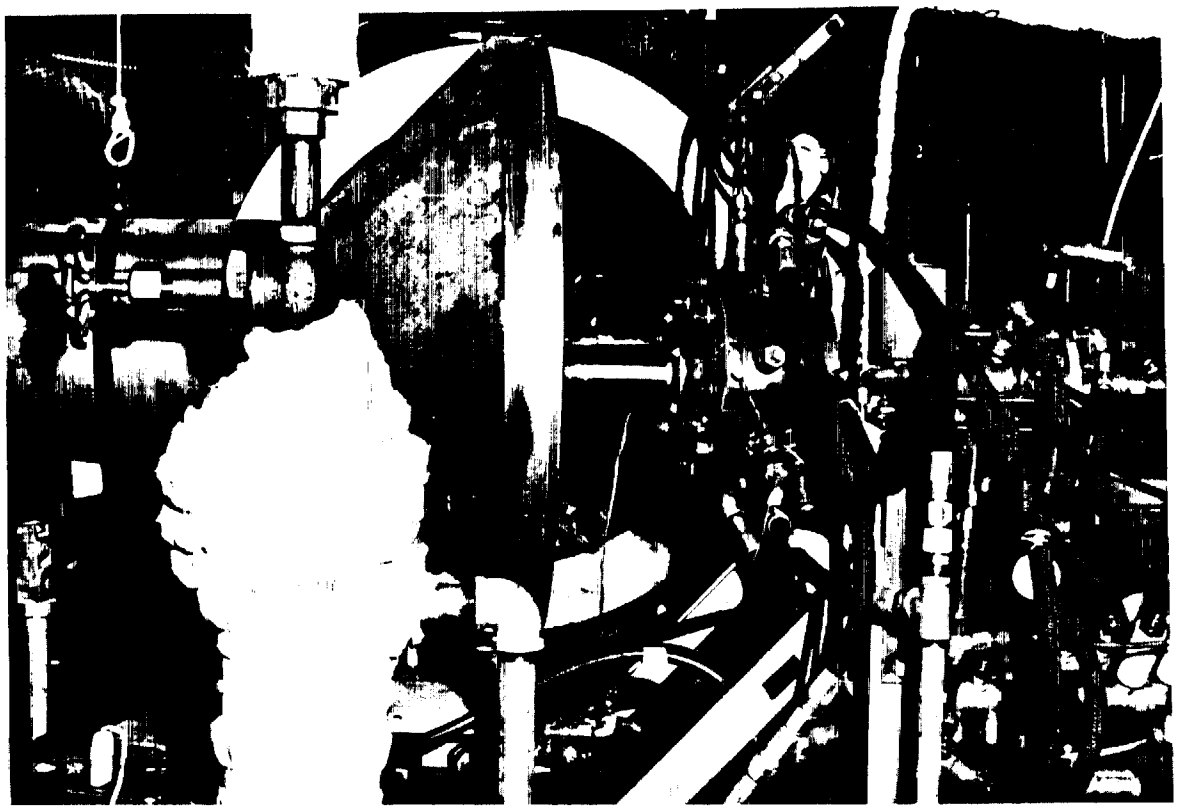

Figure 33. Ablative Material Rocket Environment Simulation Test

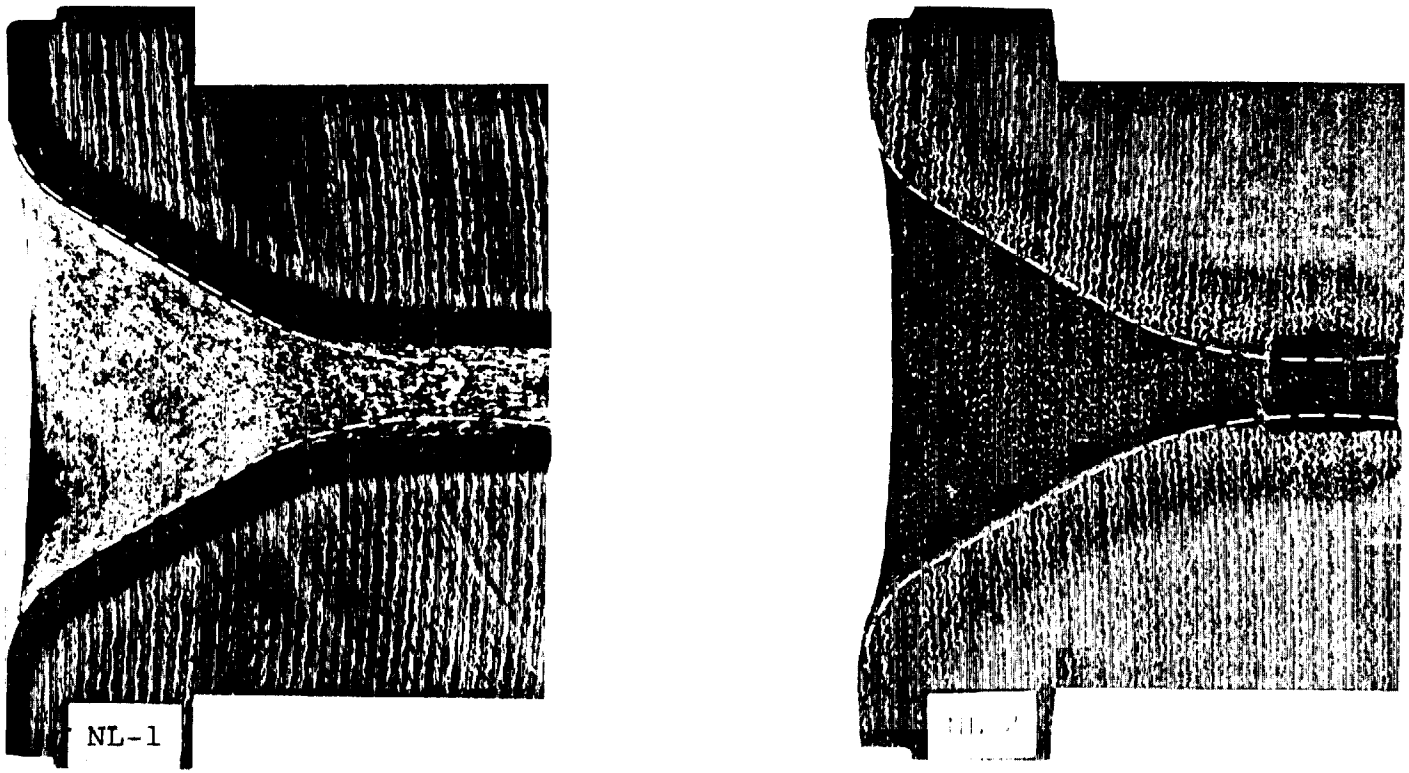

(a) NL-1, MXS-89 Silica Phenolic

(b) NL-2, MX4500 Graphite Phenolic

Figure 34. Post-Test Sectioned View of Ablative Material Test Nozzles

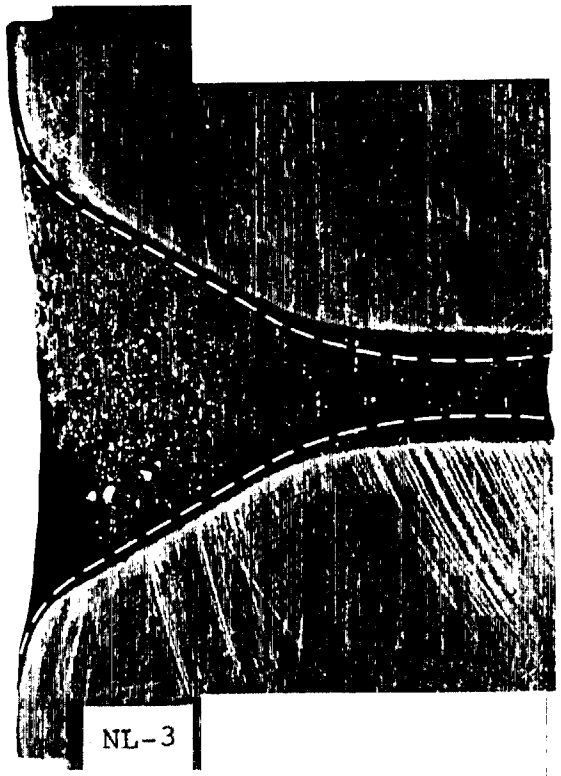

(c) NL-3, MXA-11 Asbestos Phenolic

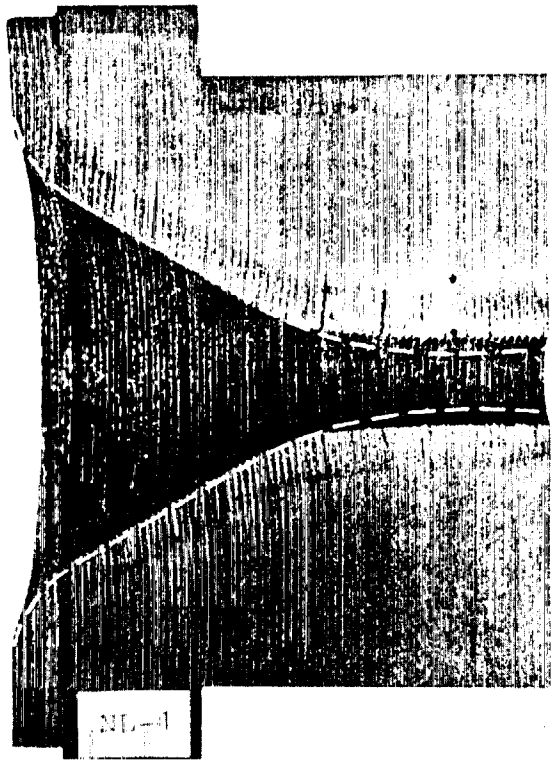

(d) NL-4, MX4926 Carbon Phenolic

Figure 34. (continued)

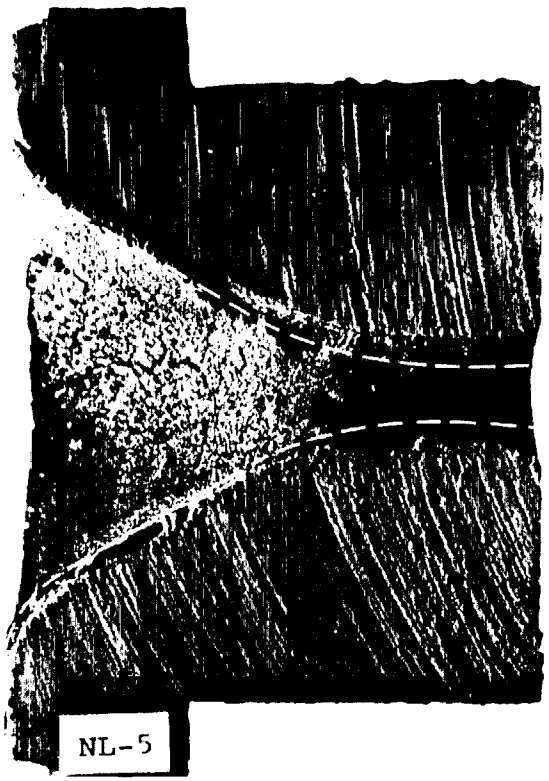

(e) NL-5, FM5051 Nylon Phenolic

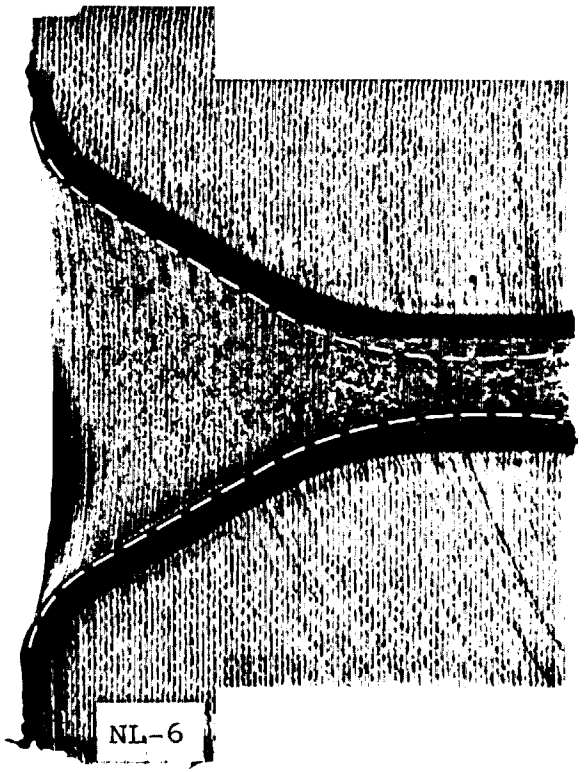

(f) NL-6, XR2015 Silica-Phenyl Silane + Buna N

Figure 34. (concluded)

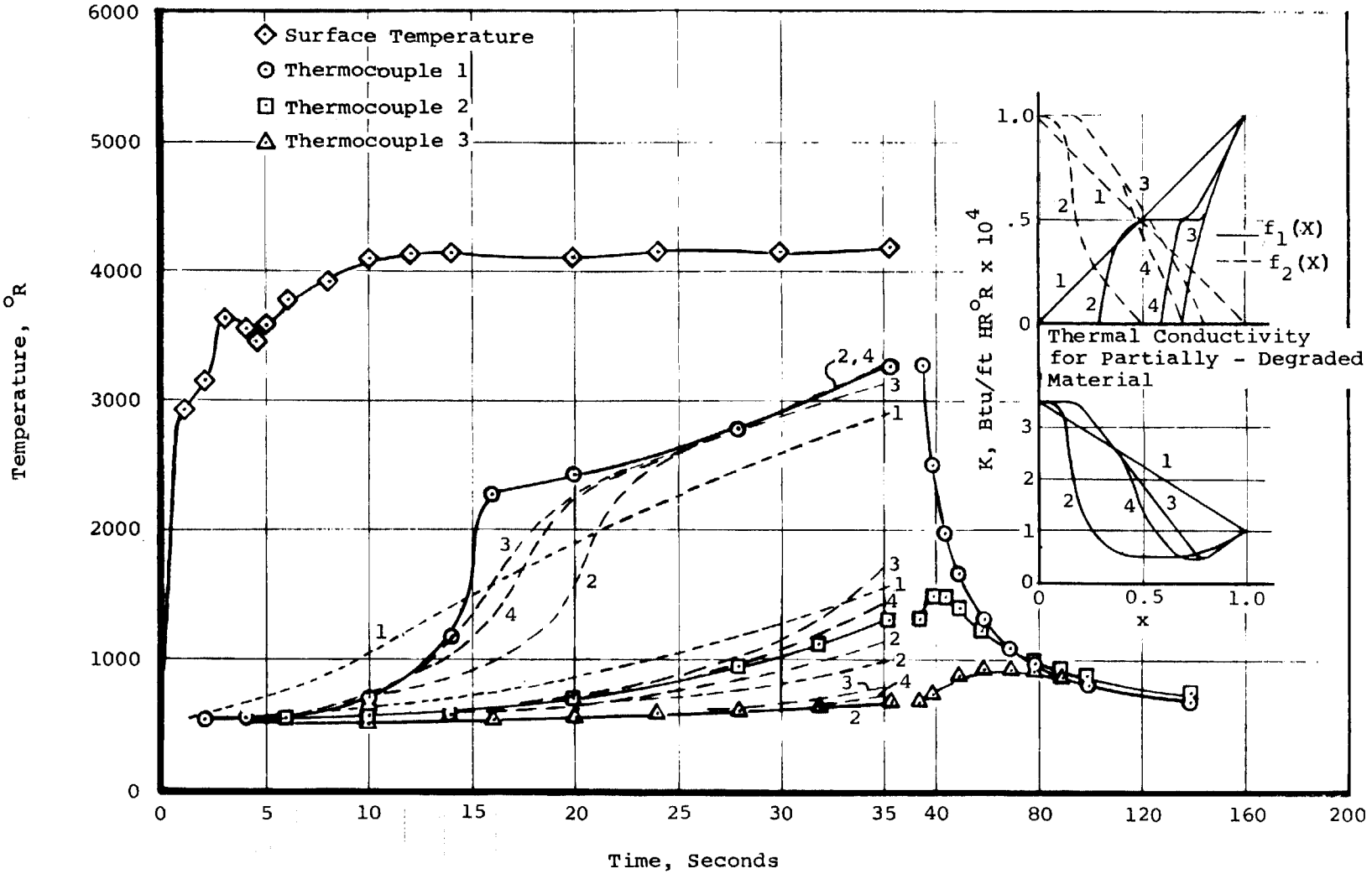

Figure 35. Series of Thermocouple Response Predictions (Dotted Lines) Compared to Experimental Data from Test (Solid Lines), Iterating on $f_1(X)$ and $f_2(X)$ where $K = K_p f_1(X) + K_c f_2(X)$ for the Partially Degraded Material

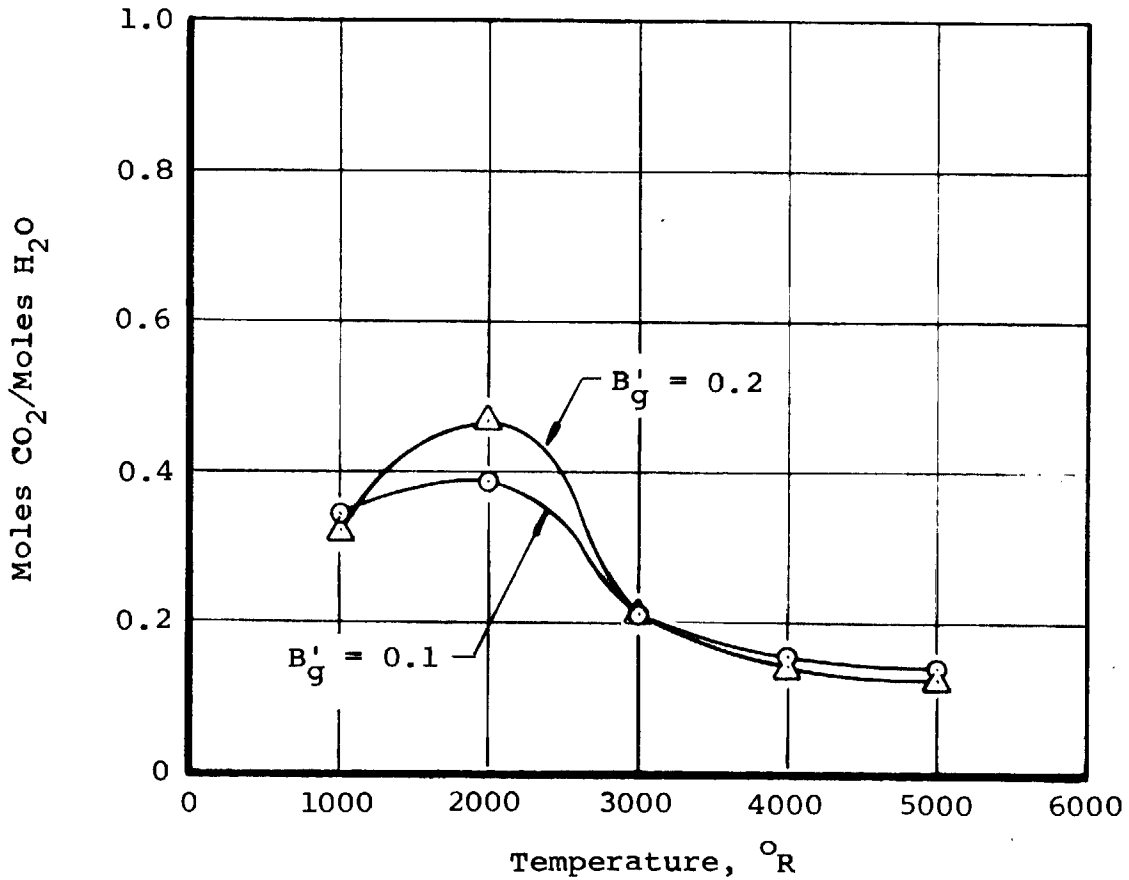

Reactions of Interest:

$CO_2 + C^* \rightarrow 2CO$

$H_2O + C^* \rightarrow CO + H_2$

Other Major Constituents are N_2 and CH_4

Figure. 36. Relative Reactant Concentration - CO_2 TO H_2O Produced by Mixture of Fuel and Pyrolysis Gases for Graphite Phenolic.

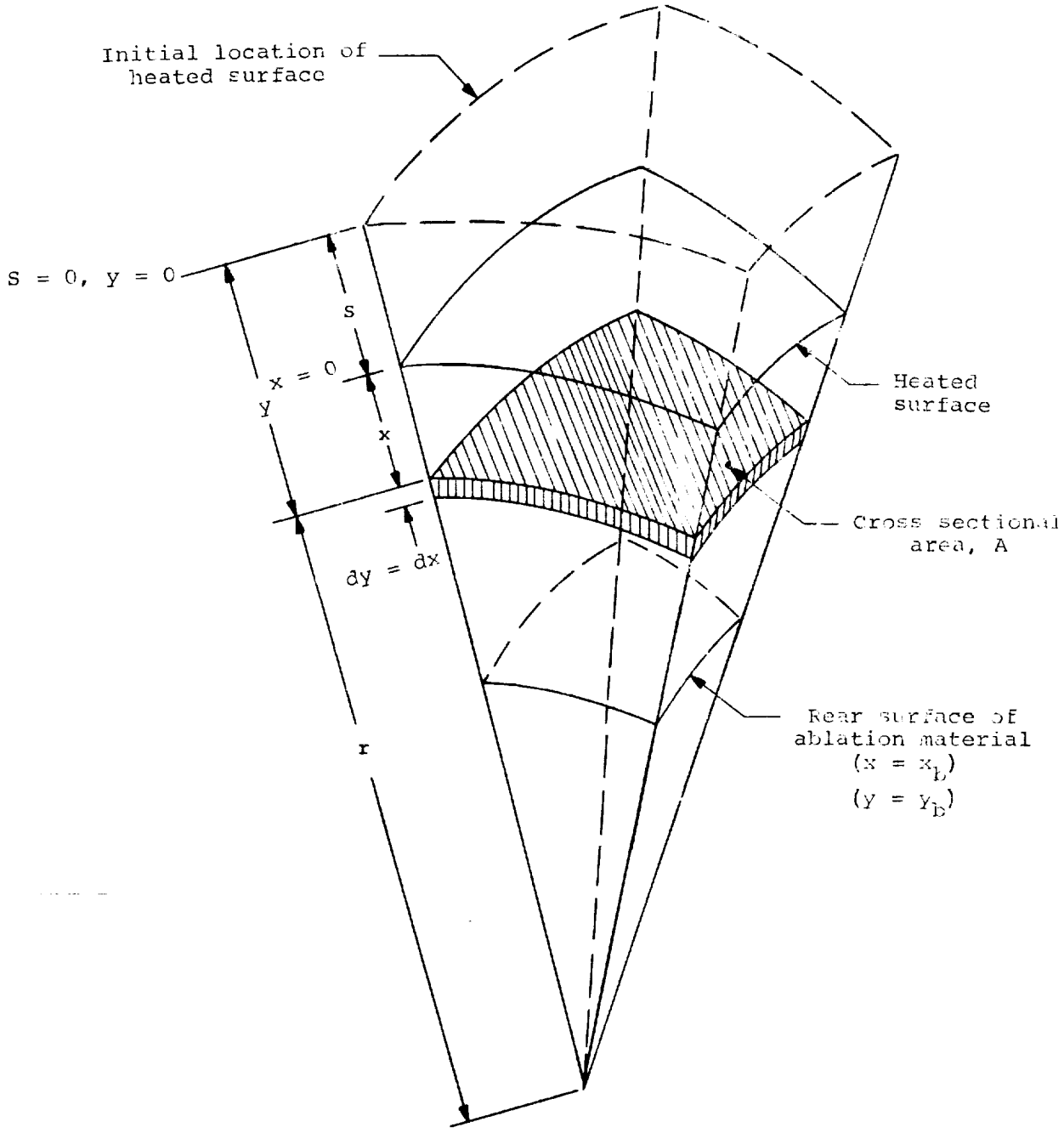

Figure 37. Geometrical Configuration and Coordinate System Illustration

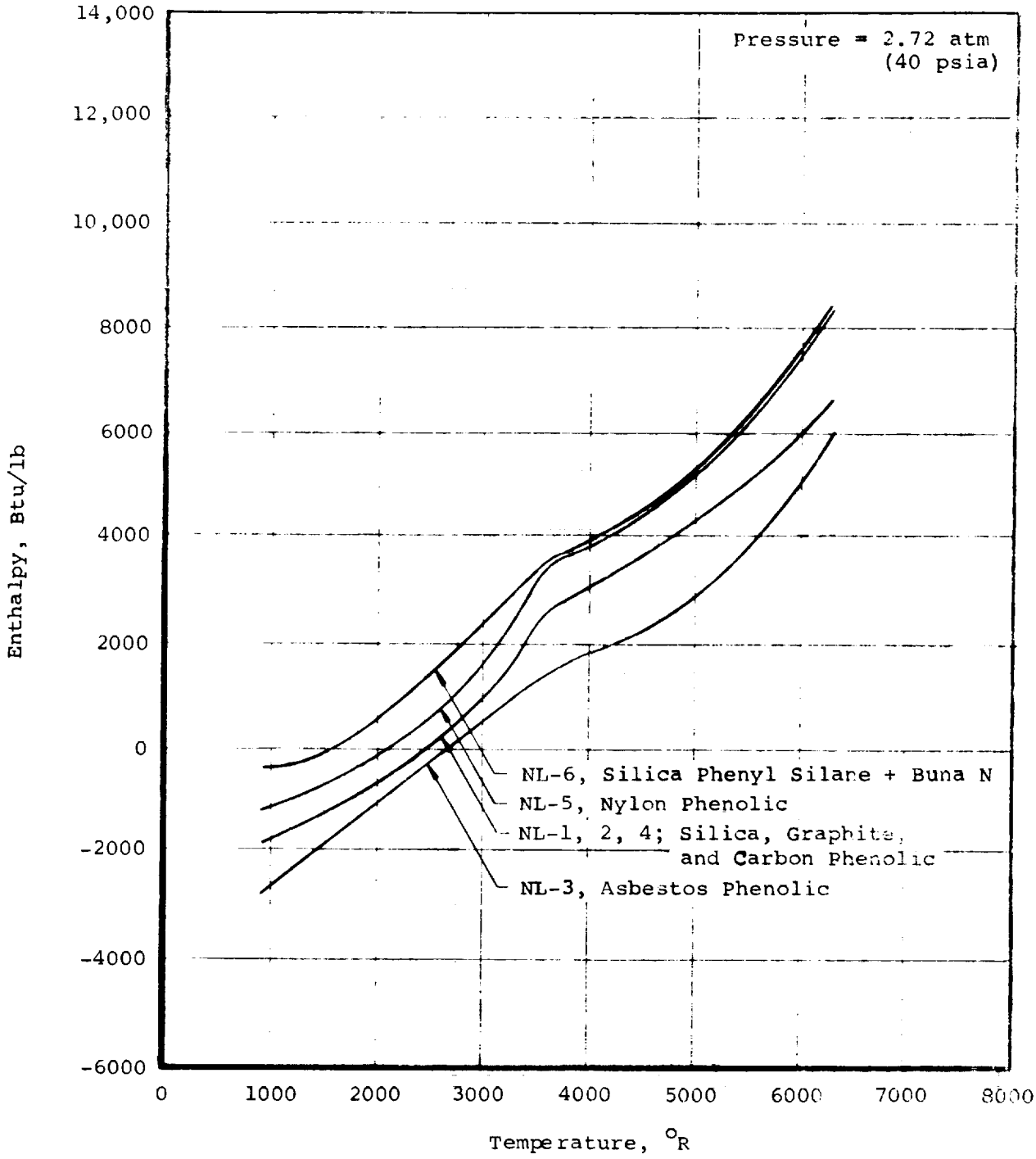

Figure 38. Resin Decomposition Gas Enthalpy.

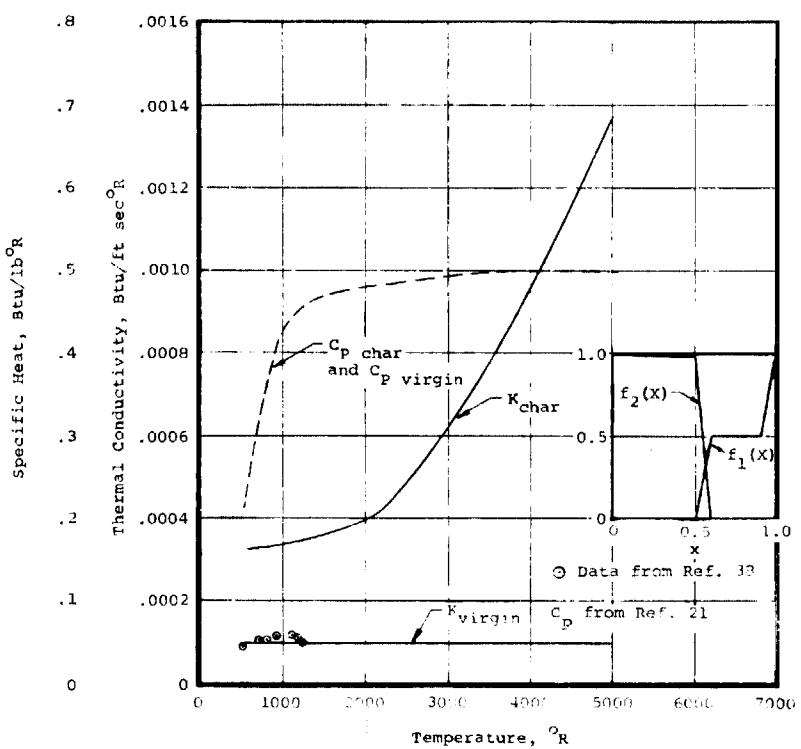

(a) MX5-89, Silica Phenolic Nozzle NL-1

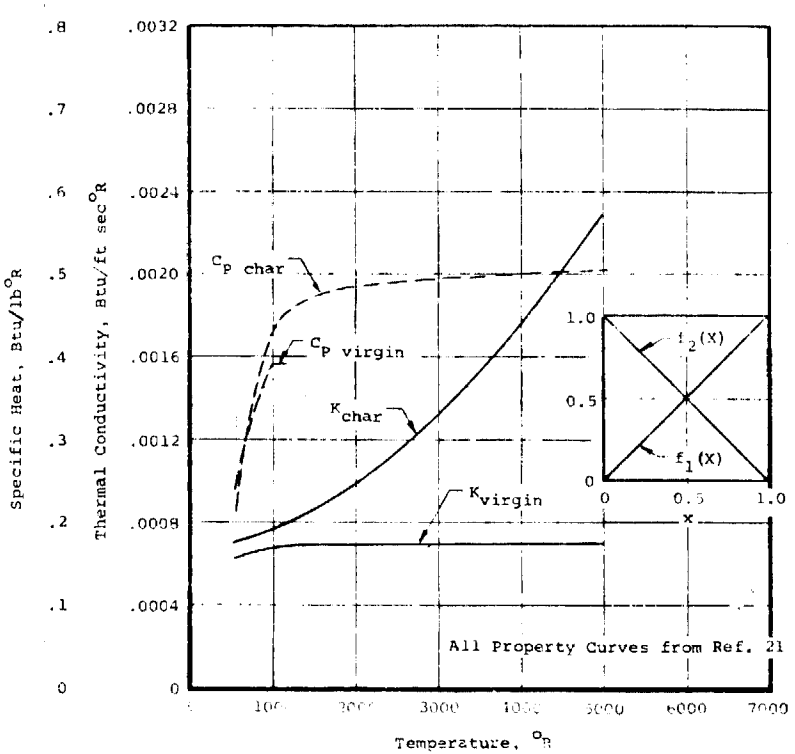

(b) MX4600, Graphite Phenolic Nozzle NL-2

Figure 39. Thermal Conductivity, f Functions, and Specific Heat

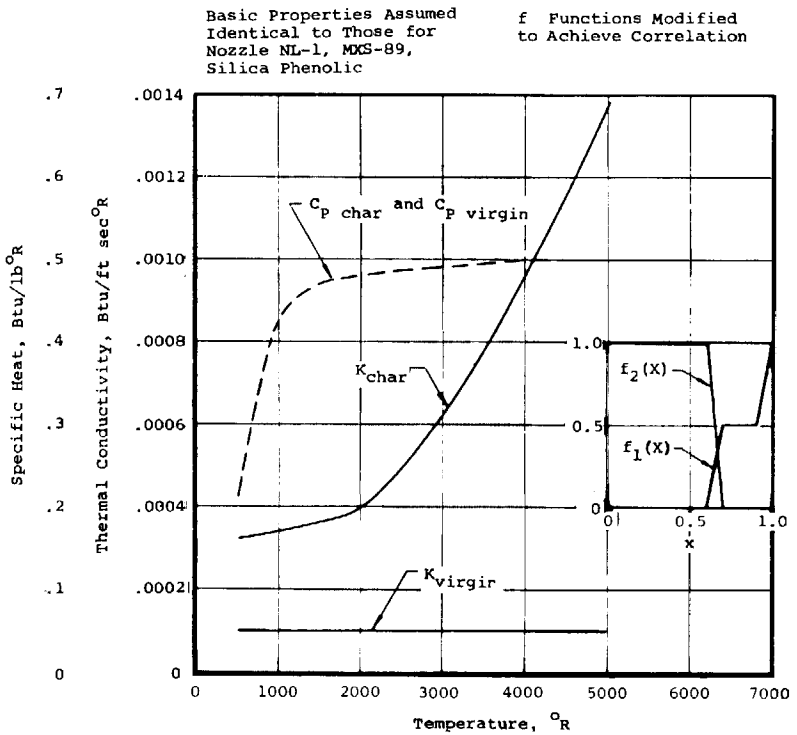

(c) MXA-11, Asbestos Phenolic Nozzle NL-3

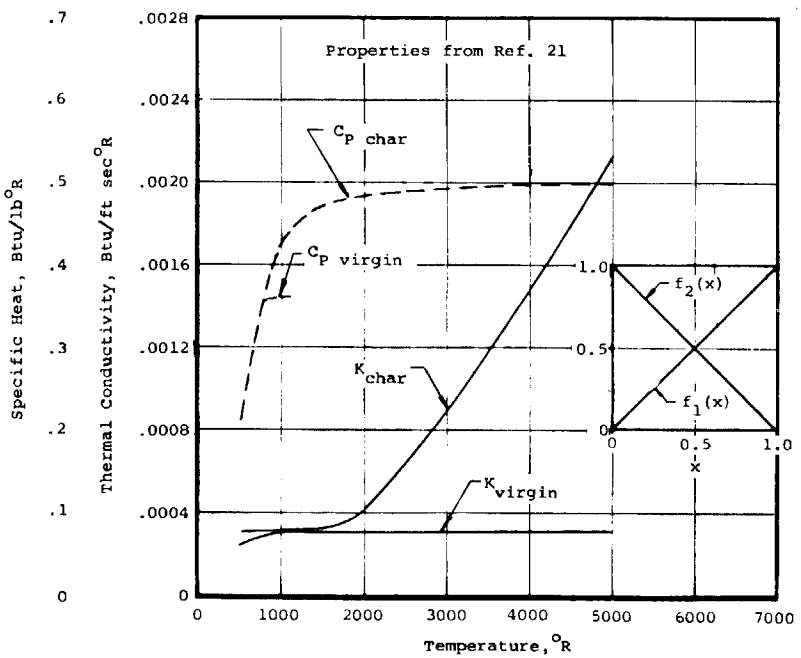

(d) MX4926, Carbon Phenolic Nozzle NL-4

Figure 39. (continued)

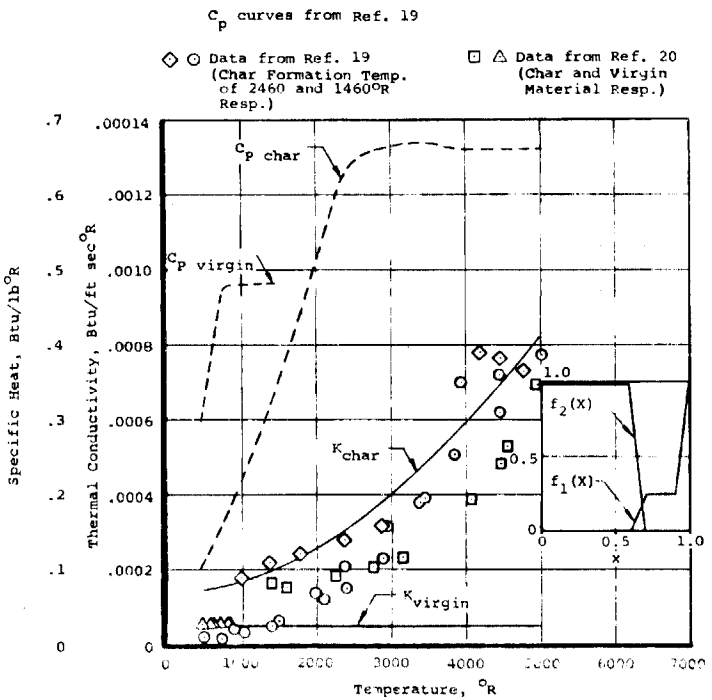

(e) FM-5051, Nylon Phenolic
Nozzle NL-5

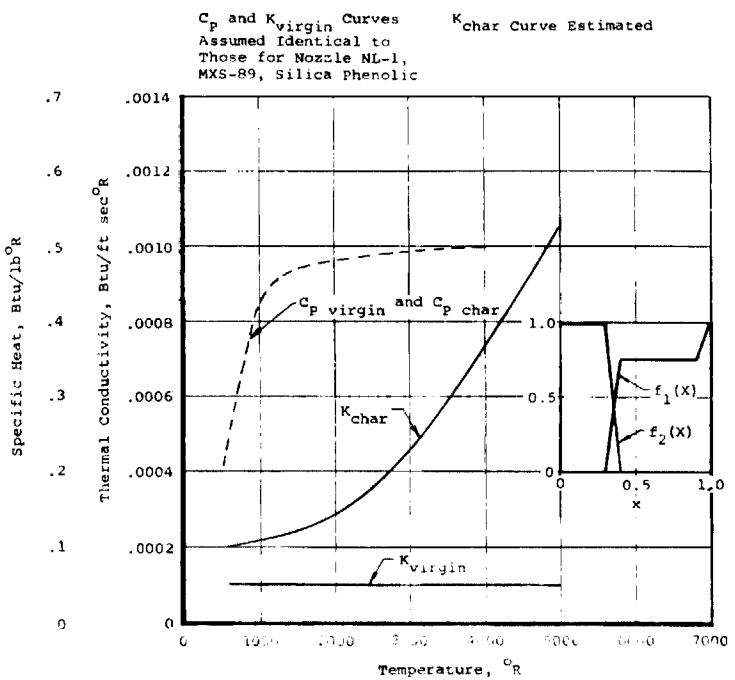

(f) XR2015 Silica-Phenyl Silane + Buna N
Nozzle NL-6

Figure 39. (concluded)

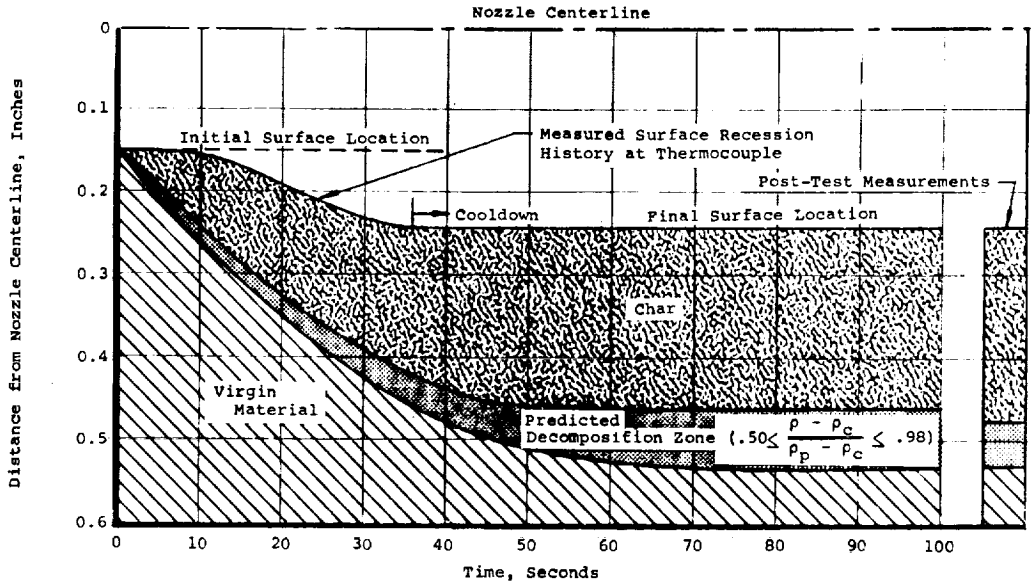

(a) Test 427, Nozzle NL-1, Silica Phenolic

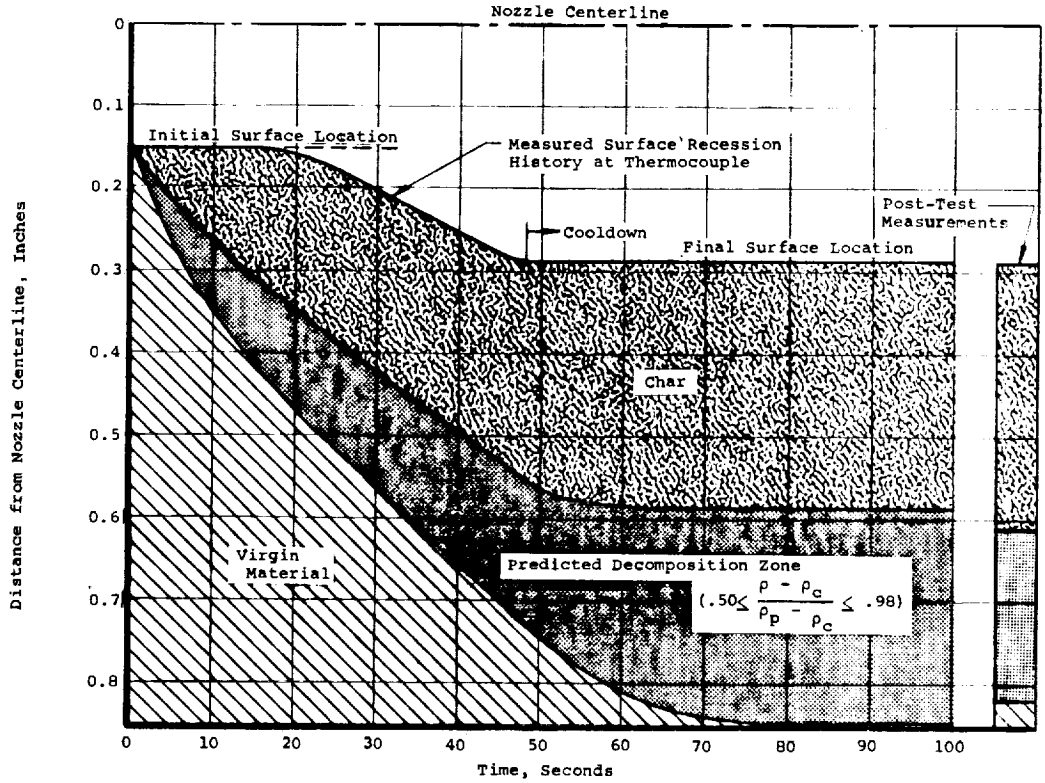

(b) Test 426, Nozzle NL-2, Graphite Phenolic

Figure 40. Comparison of Predicted and Measured Degradation Depth Specifying Measured Surface Temperature and Recession Histories as Boundary Conditions

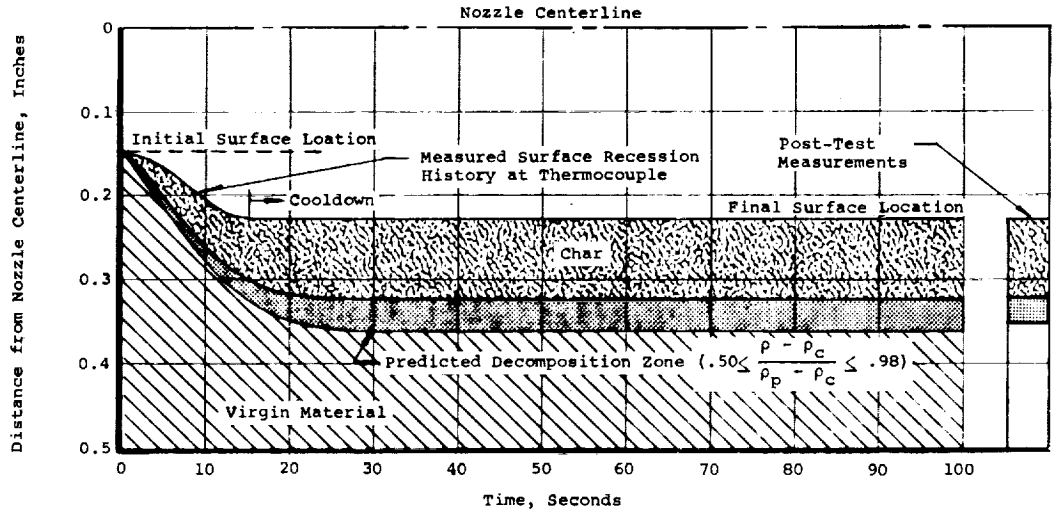

(c) Test 430, Nozzle NL-3, Asbestos Phenolic

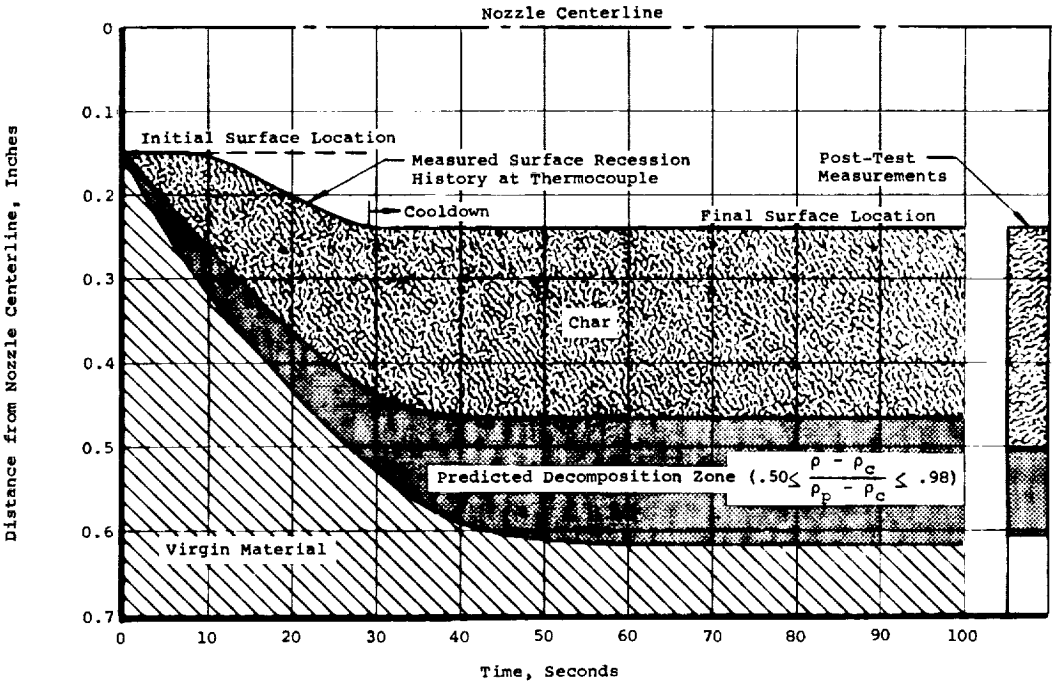

(d) Test 431, Nozzle NL-4, Carbon Phenolic

Figure 40. (continued)

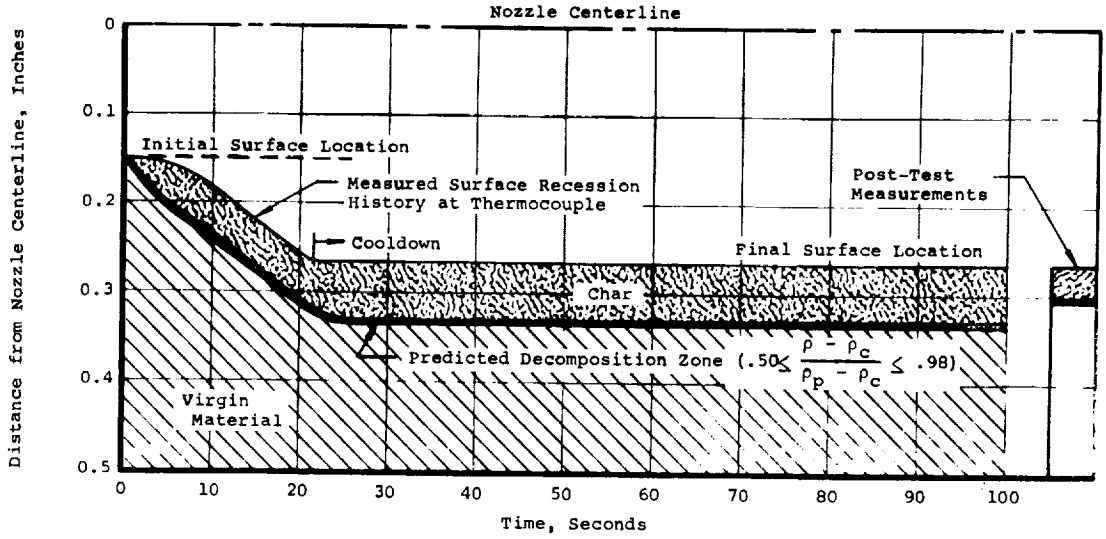

(e) Test 429, Nozzle NL-5, Nylon Phenolic

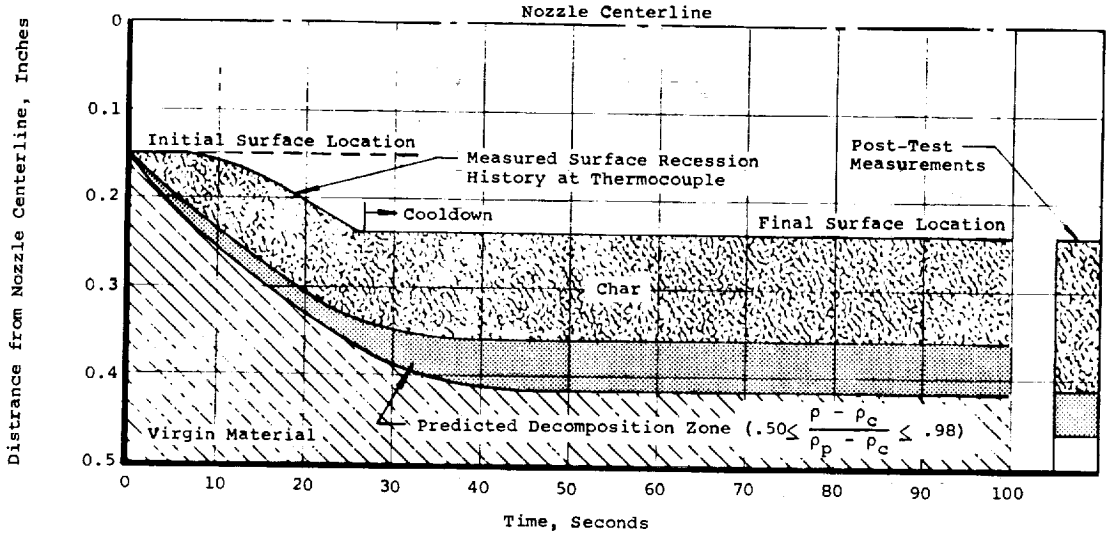

(f) Test 428, Nozzle NL-6, Silica Phenyl Silane + Buna N.

Figure 40. (concluded)

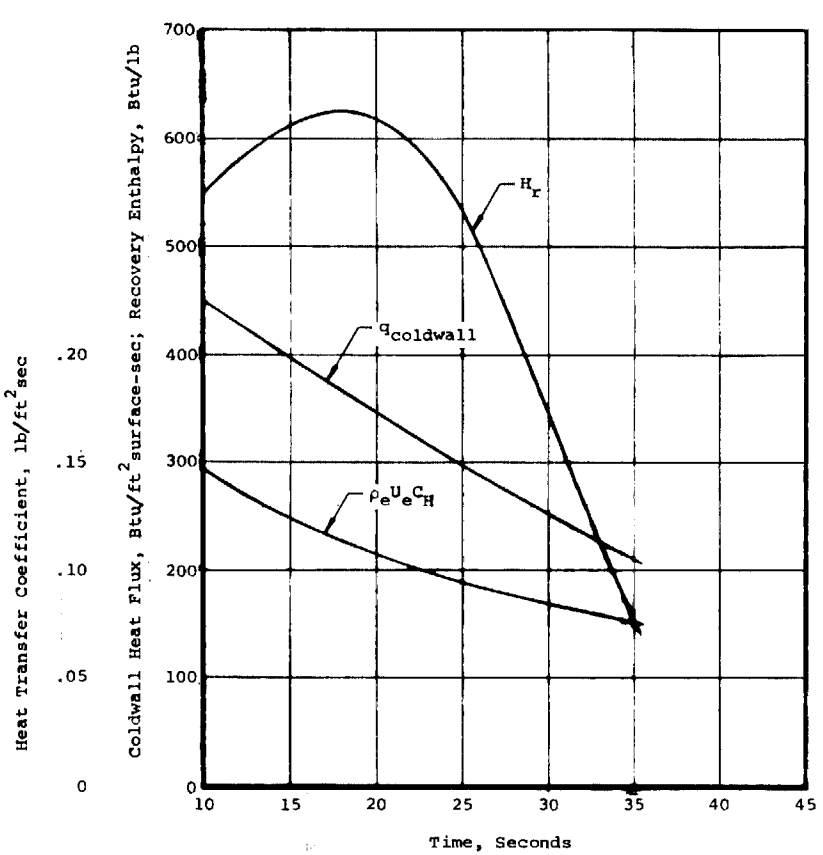

(a) Nozzle NL-1, MXS-89, Silica Phenolic

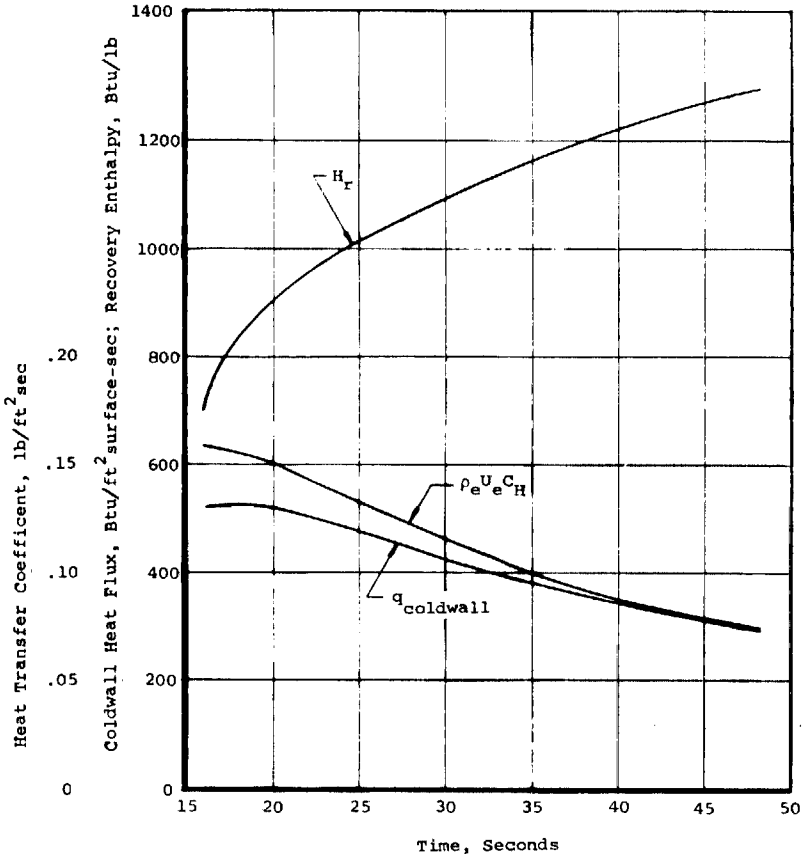

(b) Nozzle NL-2, MX4500, Graphite Phenolic

Figure 41. Heat Transfer Coefficient, Recovery Enthalpy, and Cold Wall Heat Flux Histories

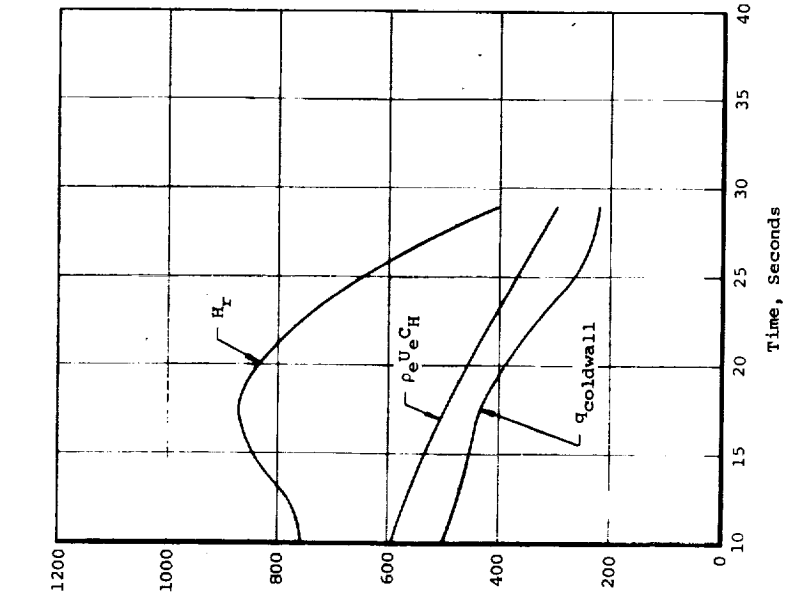

(d) Nozzle NL-4, MX4926, Carbon Phenolic

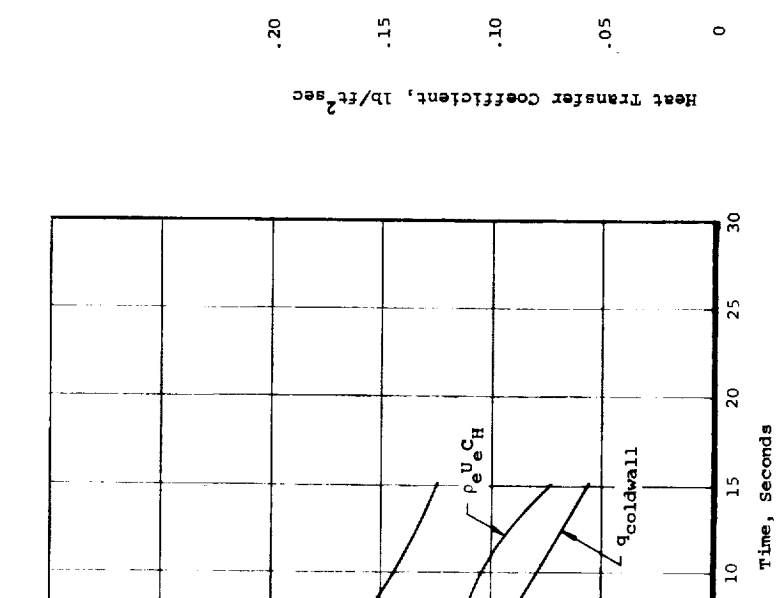

(c) Nozzle NL-3, MXA-11, Asbestos Phenolic

Figure 41. (continued)

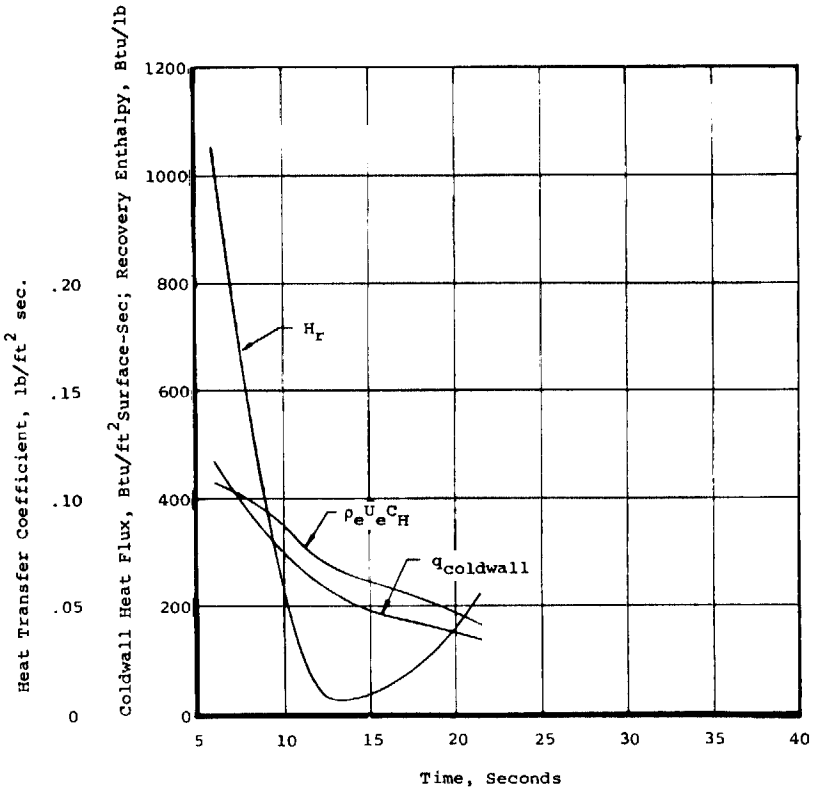

(e) Nozzle NL-5, FM5051, Nylon Phenolic

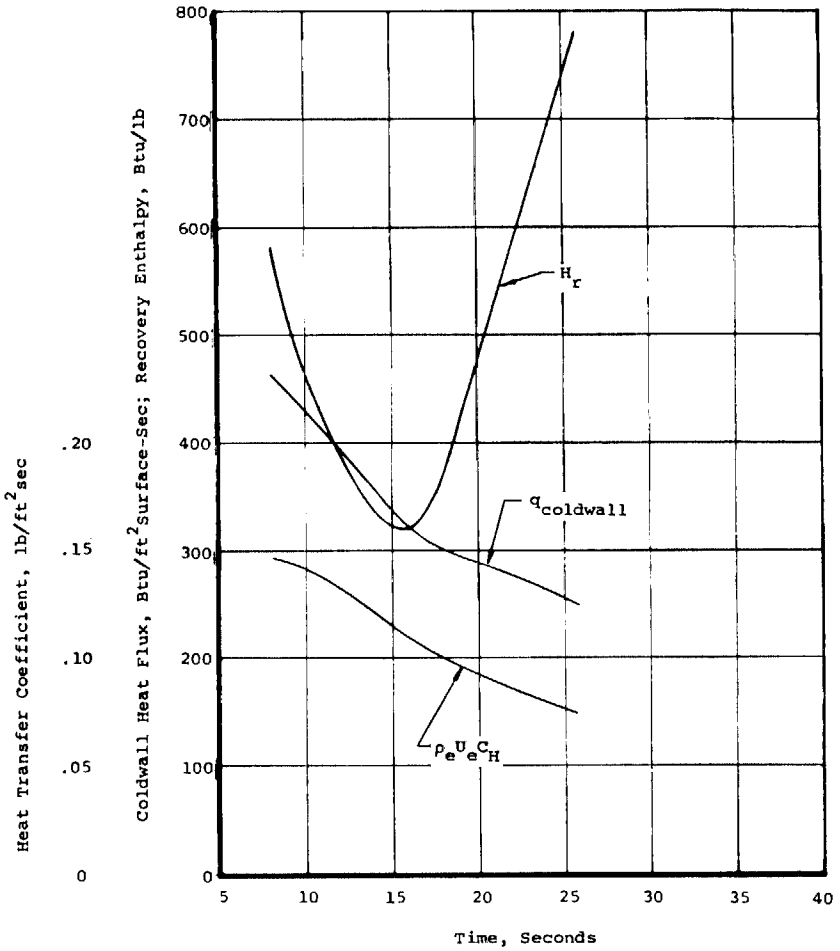

(f) Nozzle NL-6, XR2015, Silica-Phenyl Silane + Buna N.

Figure 41. (concluded)

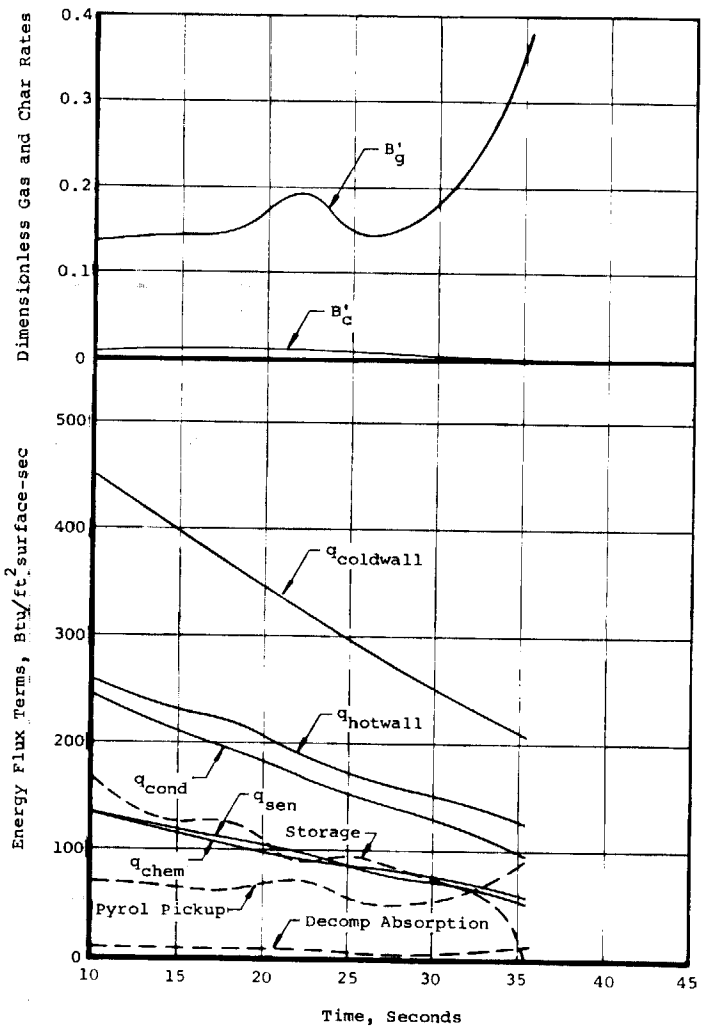

(a) Nozzle NL-1, MXS-89, Silica Phenolic.

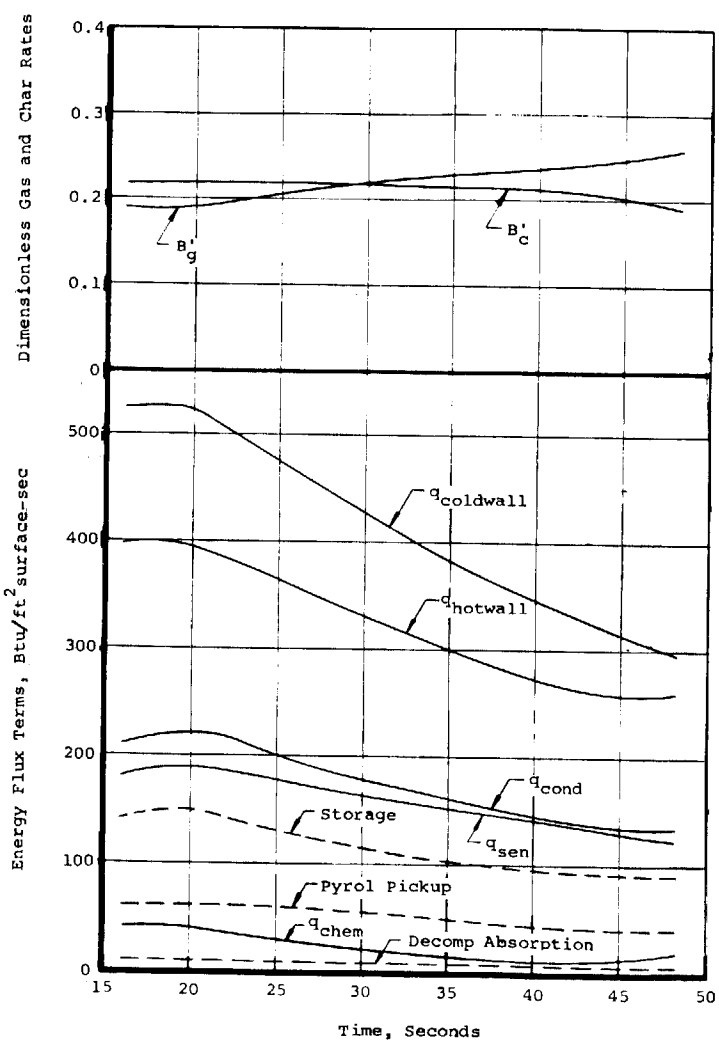

(b) Nozzle NL-2, MX4500, Graphite Phenolic

Figure 42. Surface Energy Flux and Interior Energy Terms

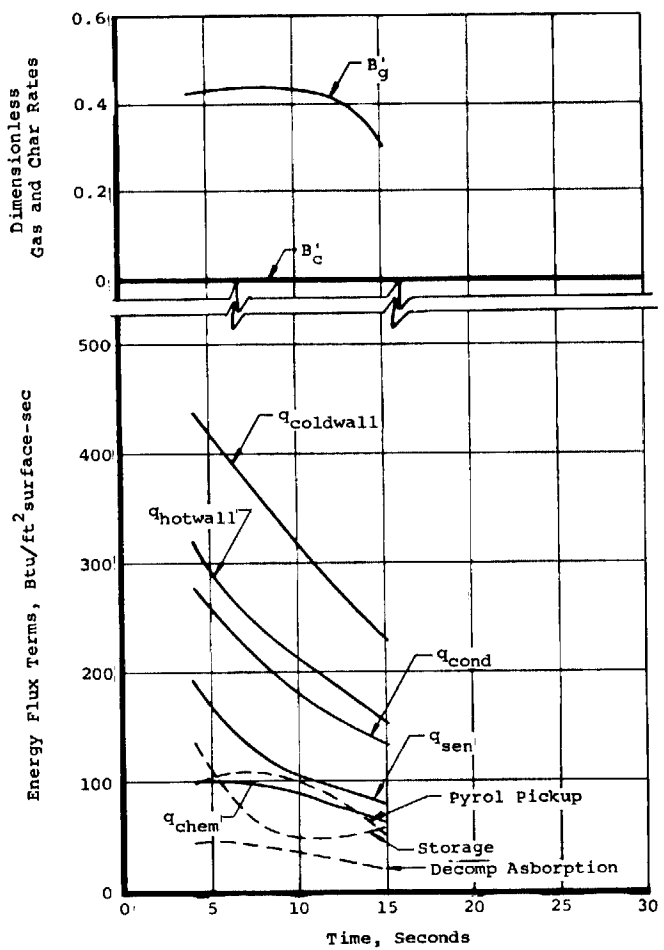

(c) Nozzle NL-3, MXA-11, Asbestos Phenolic

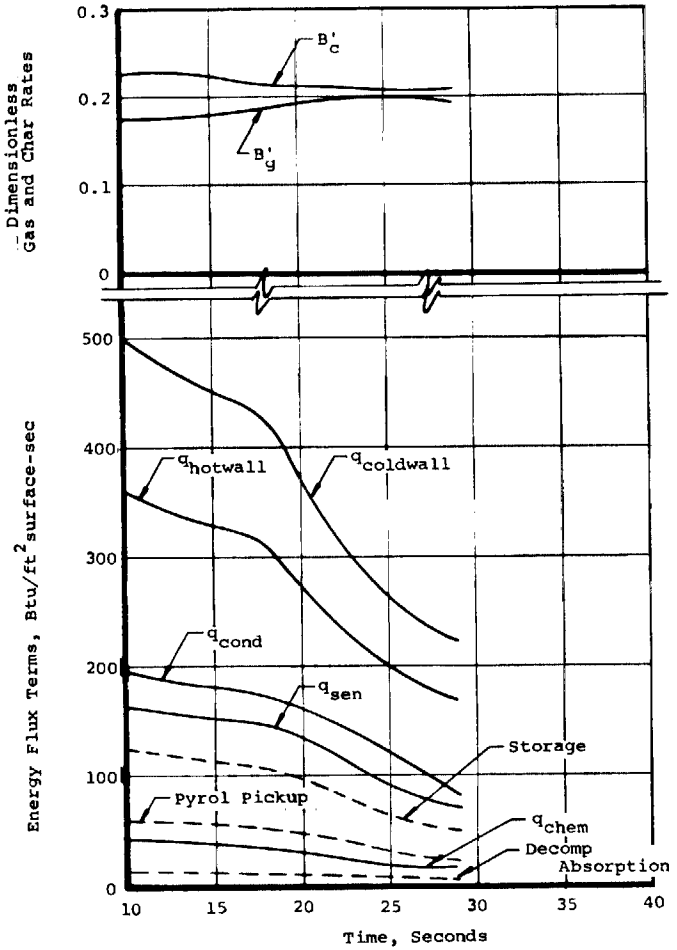

(d) Nozzle NL-4, MX4926, Carbon Phenolic

Figure 42. (continued)

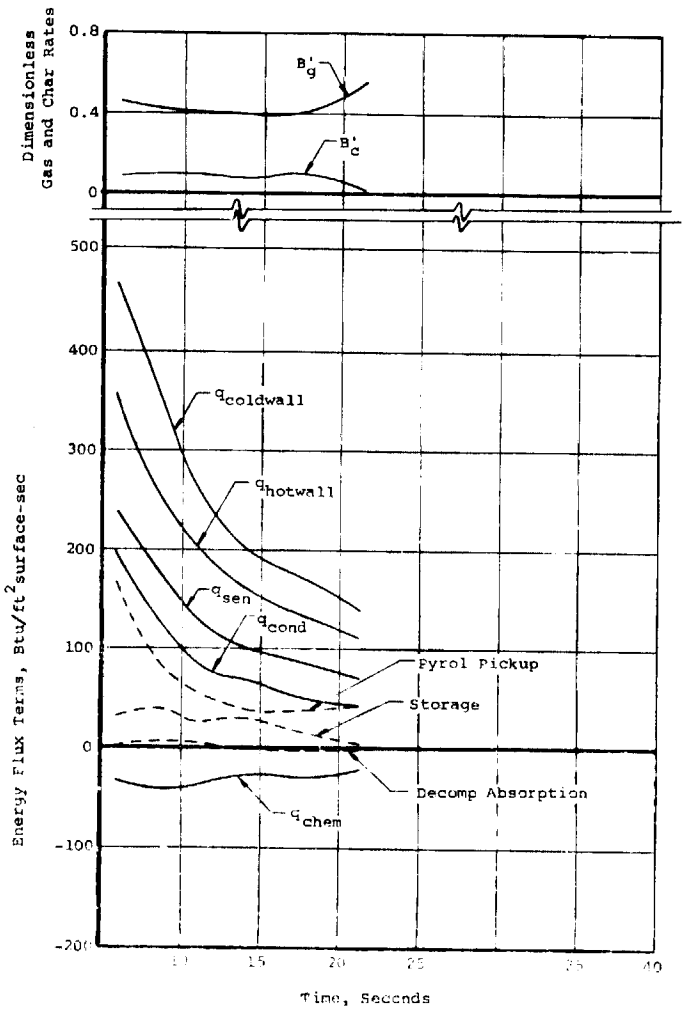

(e) Nozzle NL-5, FM5051, Nylon Phenolic

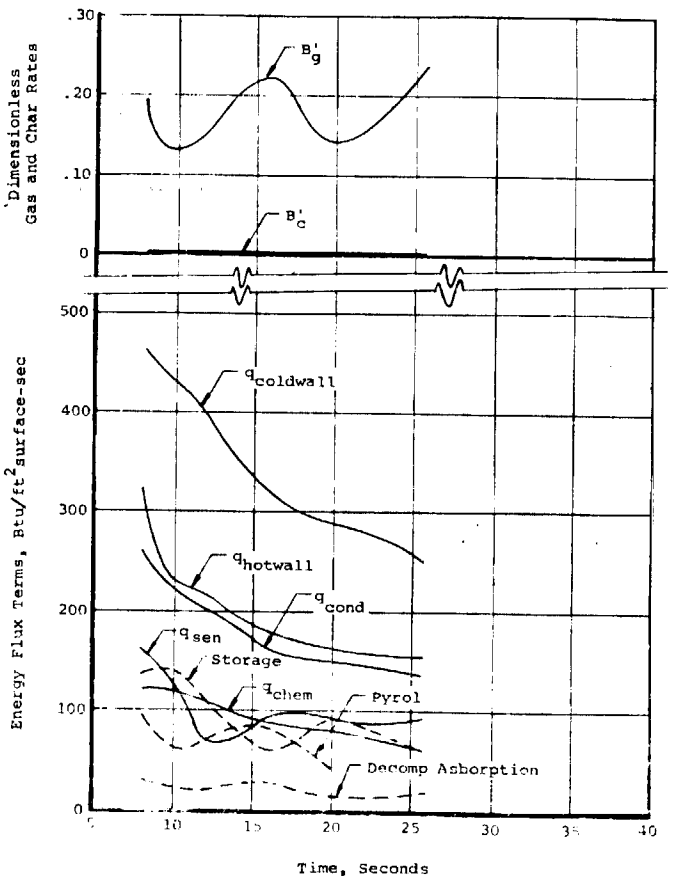

(f) Nozzle NL-6, XR2015, Silica-Phenyl Silane + Buna N

Figure 42. (concluded)

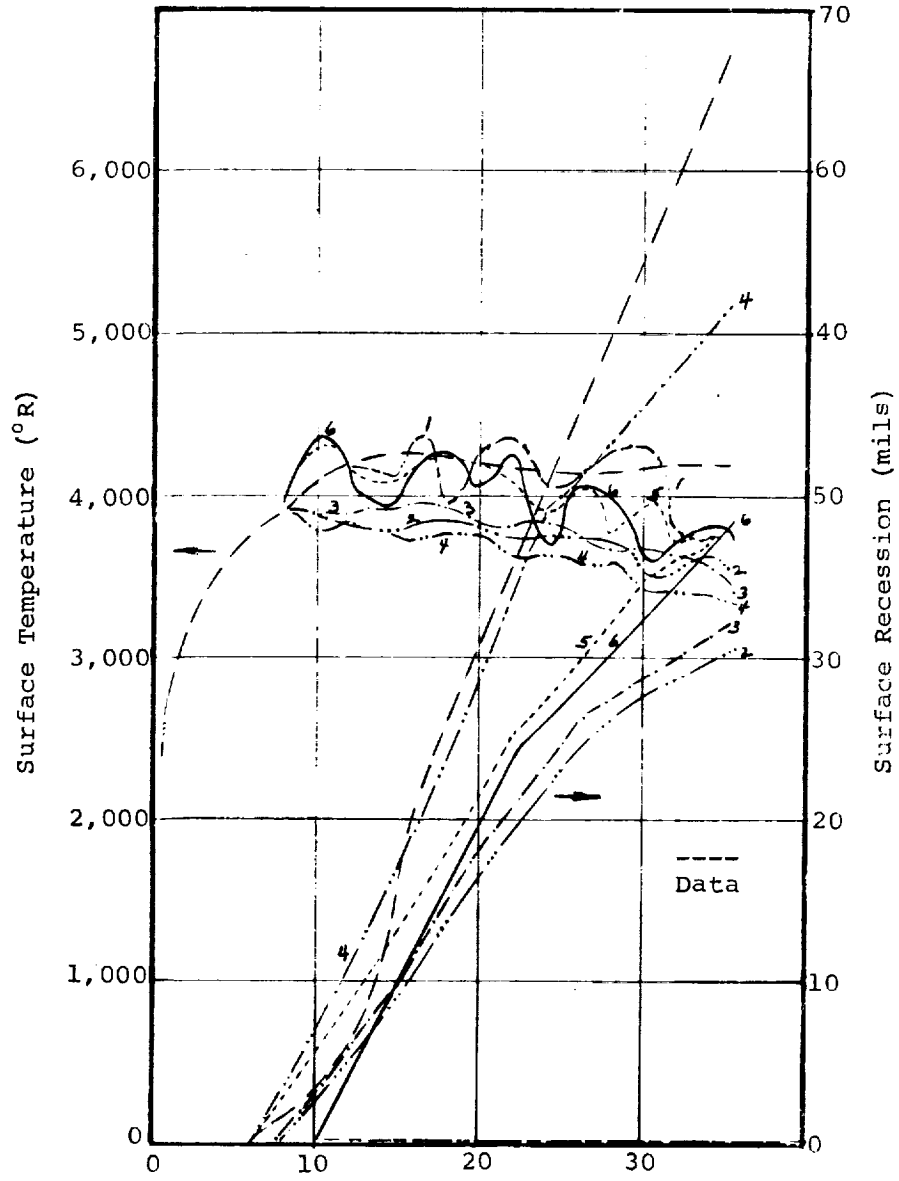

No.	Kinetics	Liquid Layer Carbon Criterion (lb/ft^3)	Max. Liq. Layer Thickness (mils)	Conductivity Parameter a
1	Nominal	∞	∞	1
2	"	5	2	1
3	"	5	1	0.5
4	"	7	2	0.5
5	"	7	2	0.1
6	10 x Nominal	7	4	0.1

Figure 43. Comparison of a Series of SCRIMP Program Predictions for Surface Temperature and Recession to Experimental Data, NL-1 Model

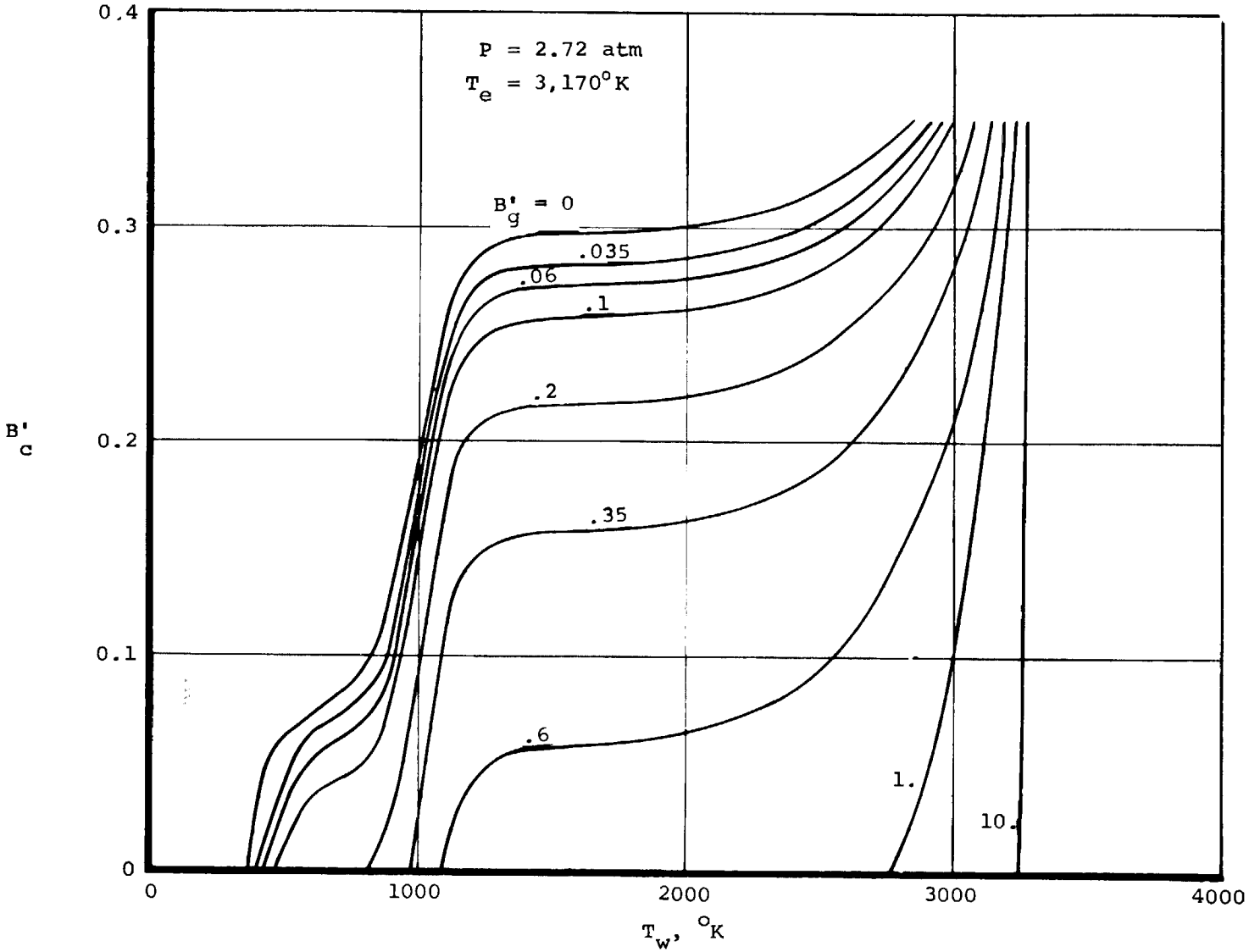

Figure 44. Equilibrium Surface Thermochemistry
Graphite Phenolic (NL-2) in N_2O_4-N_2H_4/UDMH

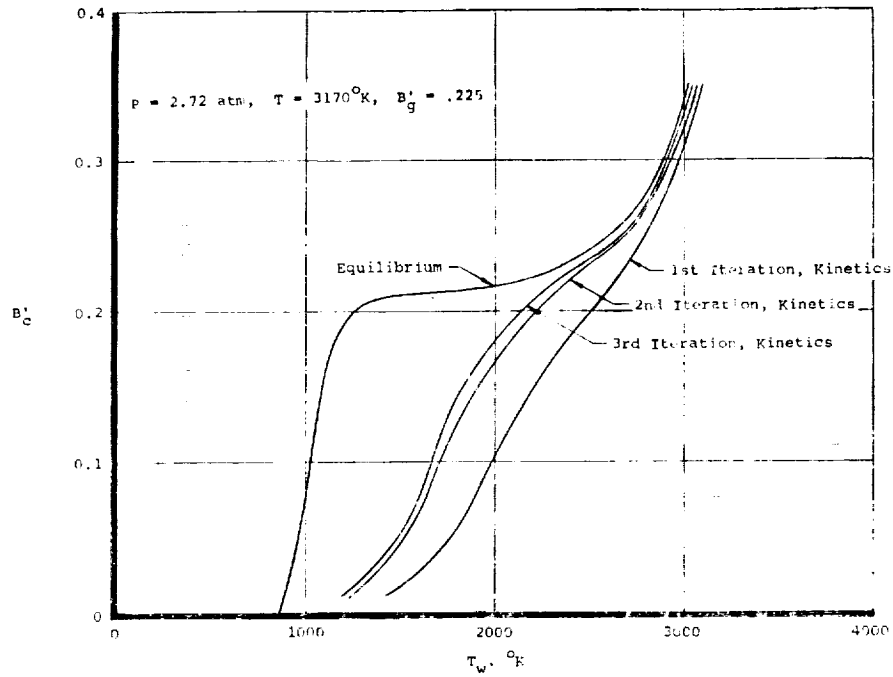

Figure 45. Comparison of Equilibrium and Kinetically-Controlled Surface Thermochemistry

Graphite Phenolic (NL-2) in N_2O_4 - N_2H_4/UDMH

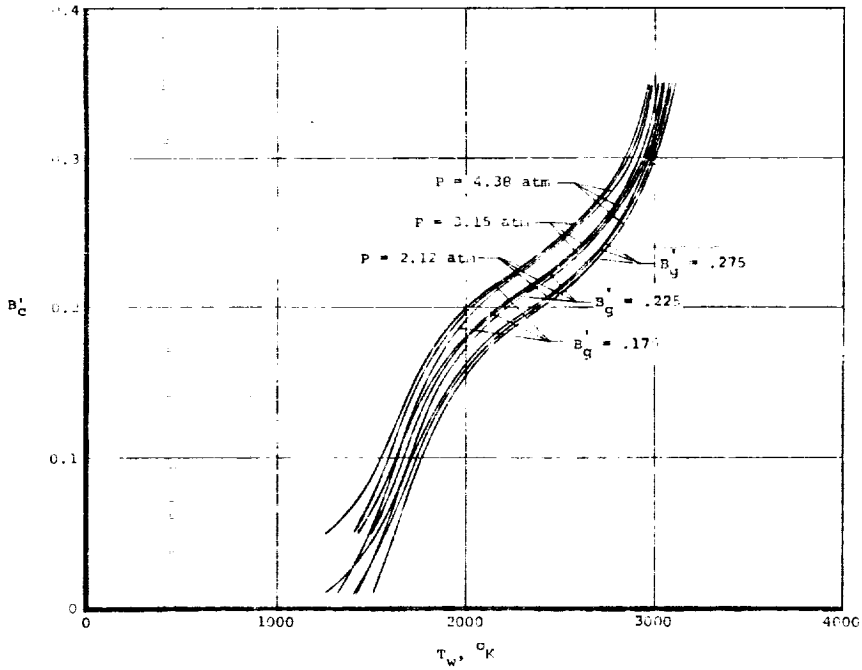

Figure 46. Kinetically-Controlled Surface Thermochemistry
Graphite Phenolic (NL-2) in N_2O_4 - N_2H_4/UDMH

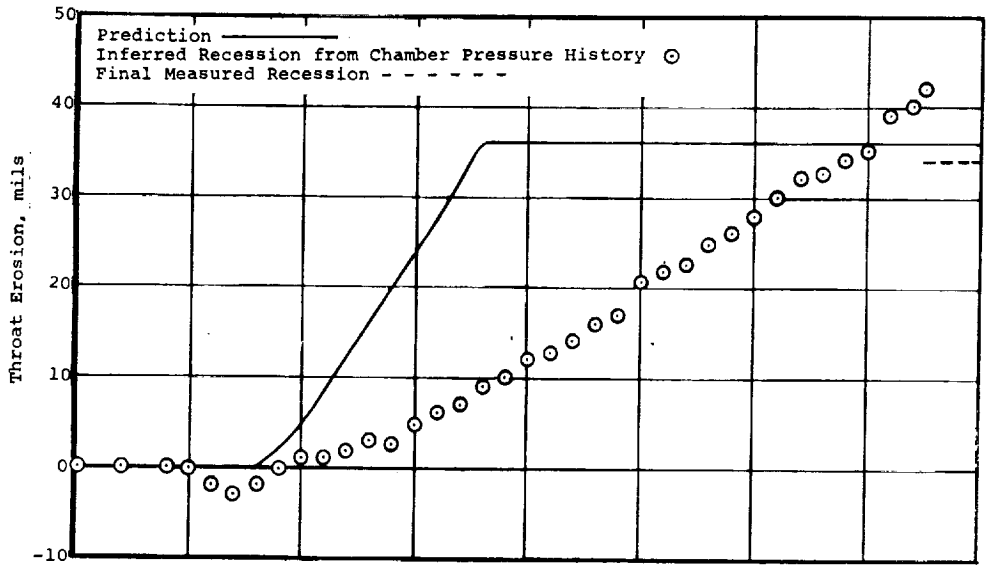

(a) Surface Recession Silica-Phenolic, MXS-89

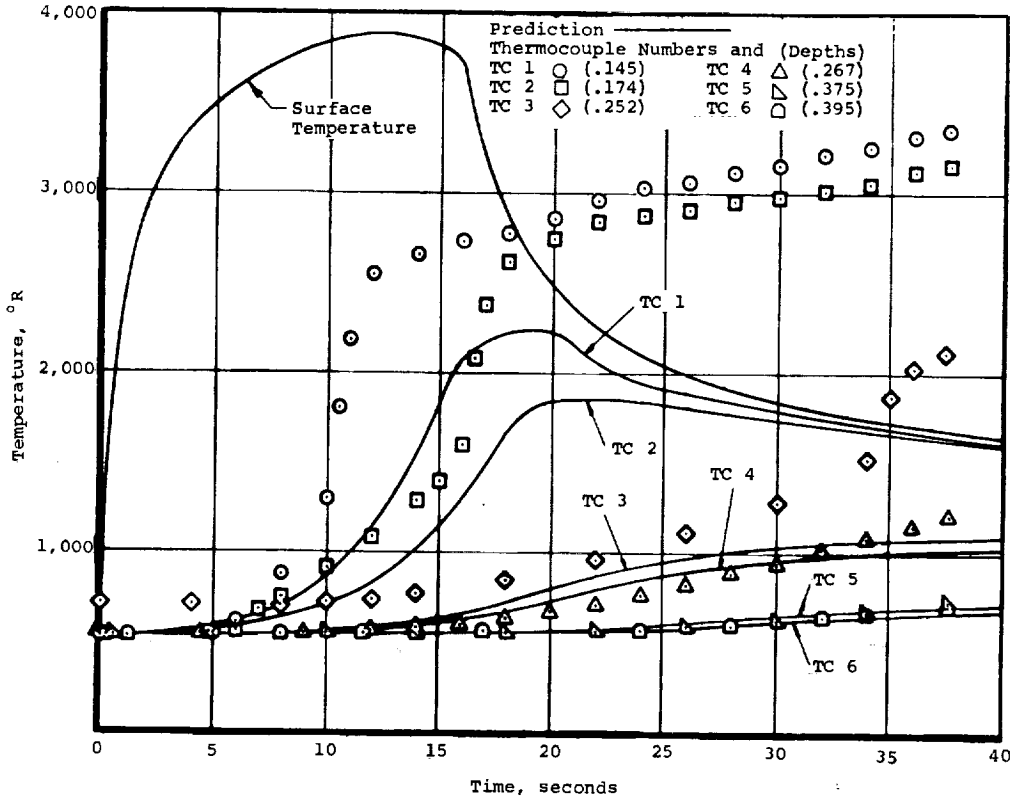

(b) Temperature Histories, Silica-Phenolic, MXS-89

Figure 47. Comparison of Measured and Predicted Ablative Material Response for Rocket Engine Throat (N_2O_4-N_2H_4/UDMH, O/F = 2.0, P_c = 100 psia, D* = 1.2 in)

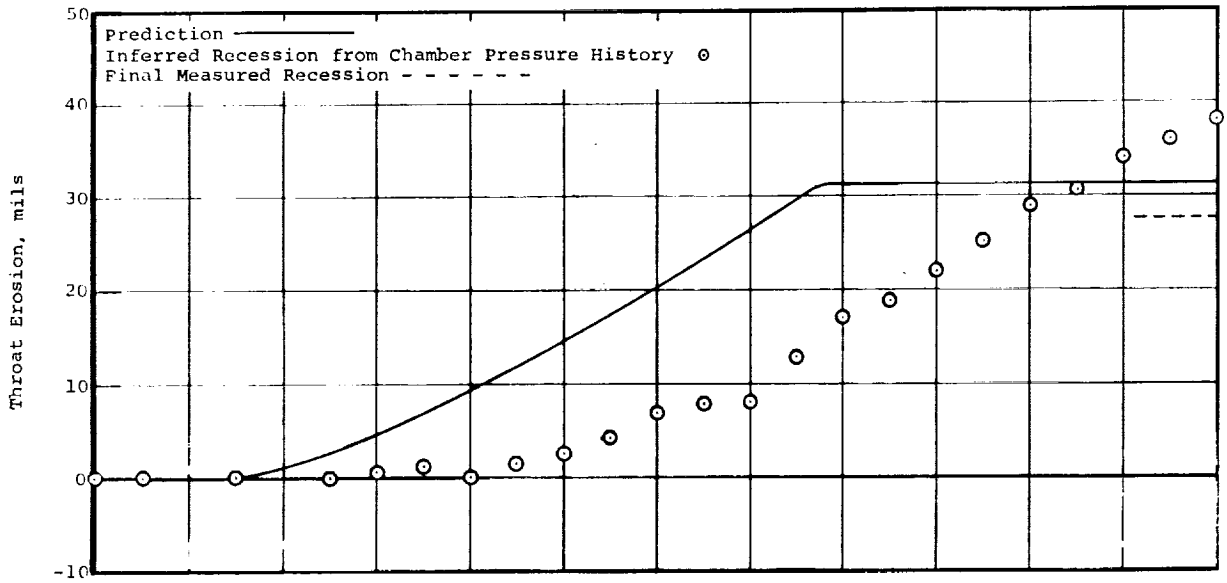

(c) Surface Recession, Graphite-Phenolic MX-4500

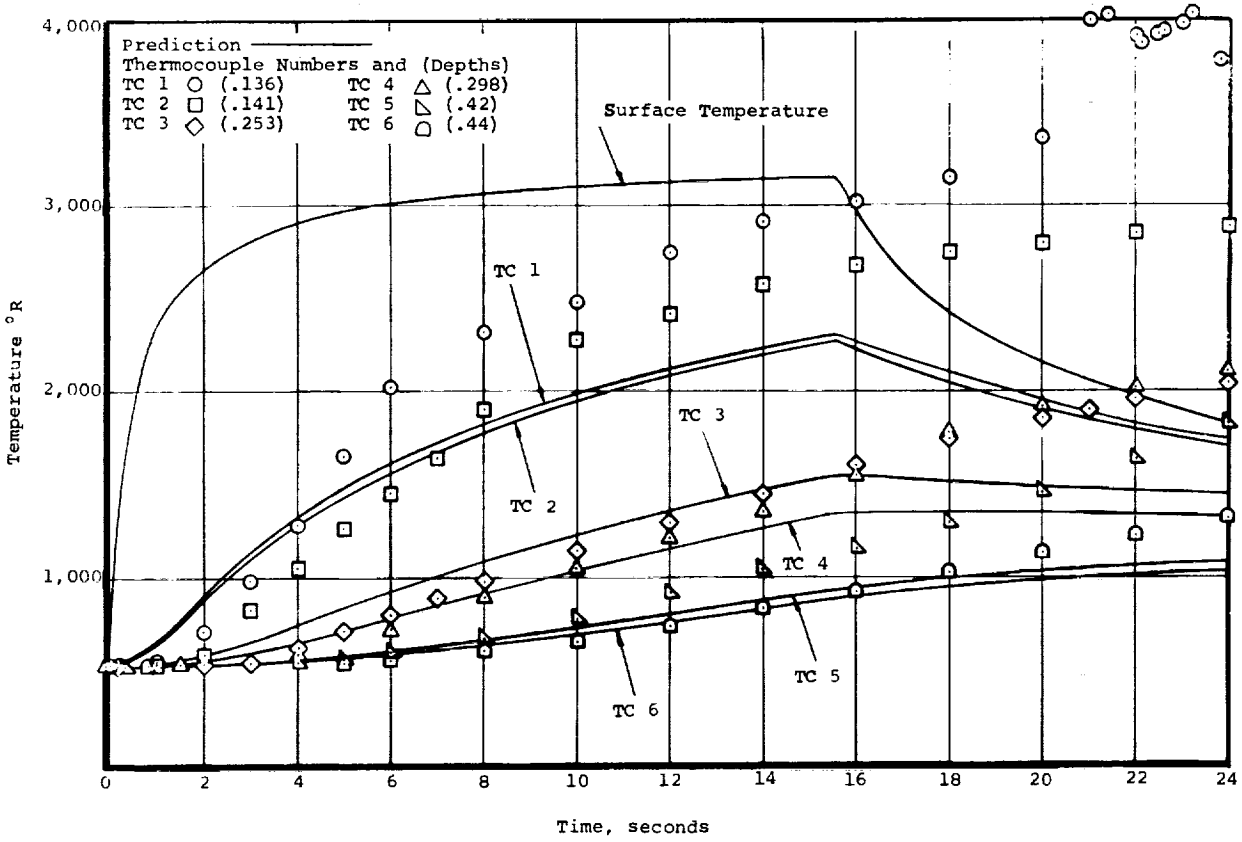

(d) Temperature Histories, Graphite-Phenolic MX-4500

Figure 47. (continued)

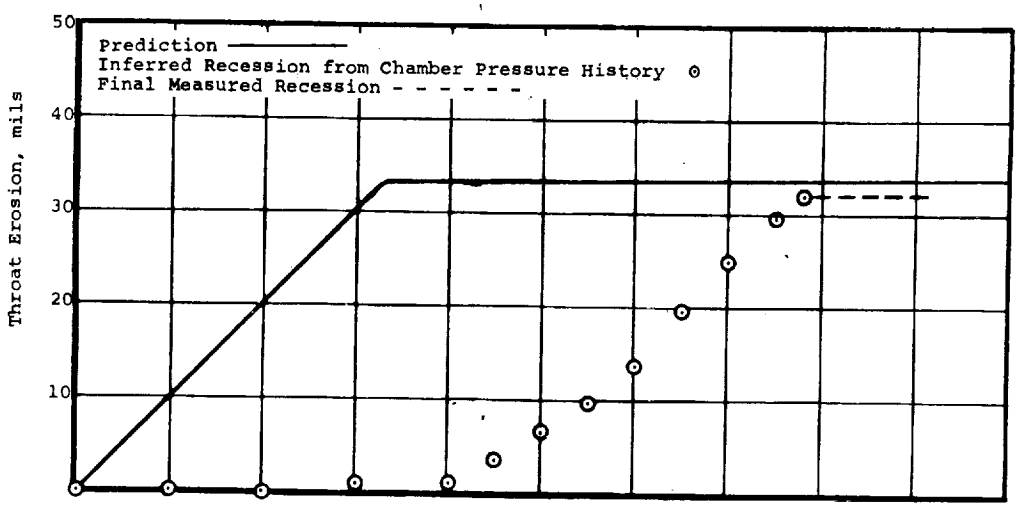

(e) Surface Recession, Asbestos-Phenolic, MXA-11

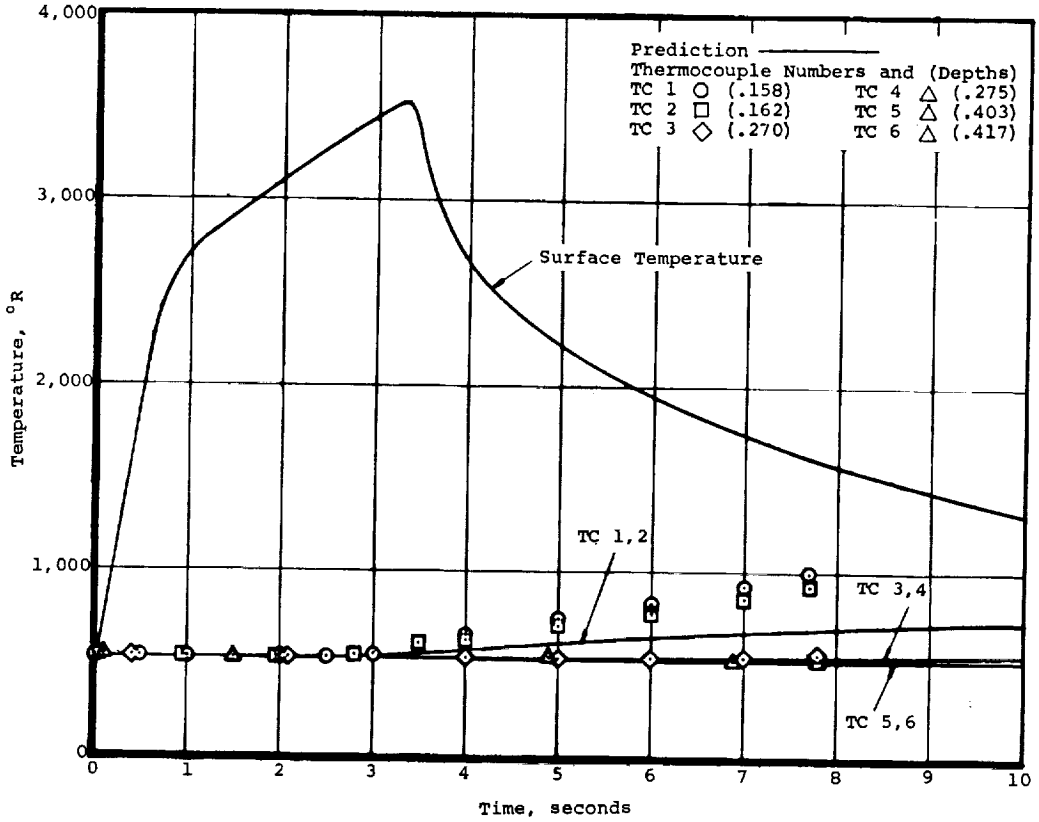

(f) Temperature Histories, Asbestos-Phenolic, MXA-11

Figure 47. (continued)

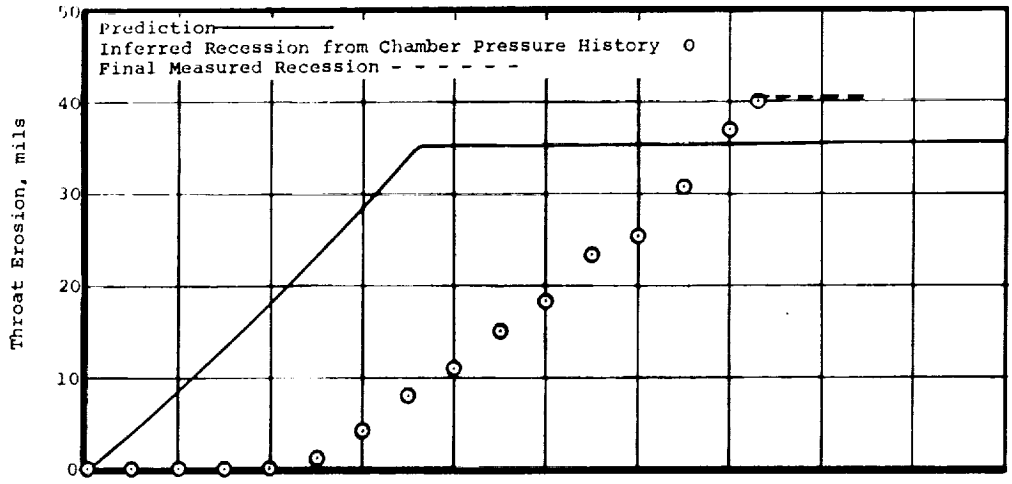

(g) Surface Recession, Carbon-Phenolic, MX-4926

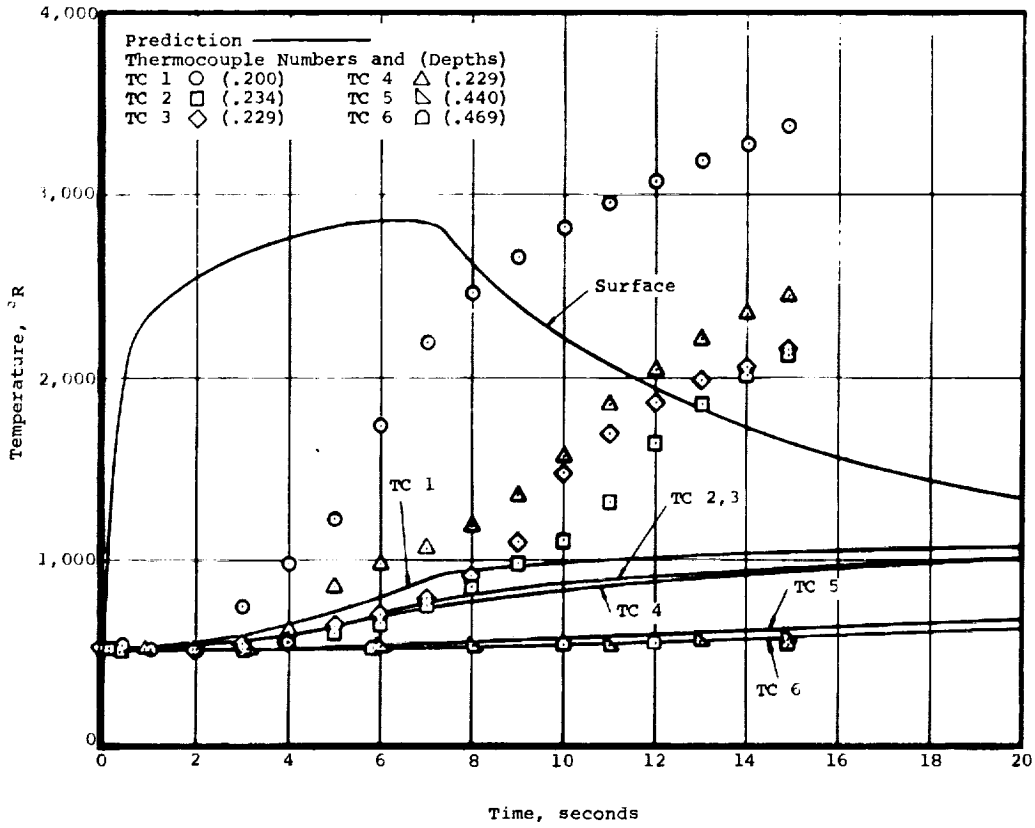

(h) Temperature Histories, Carbon-Phenolic, MX-4926

Figure 47. (continued)

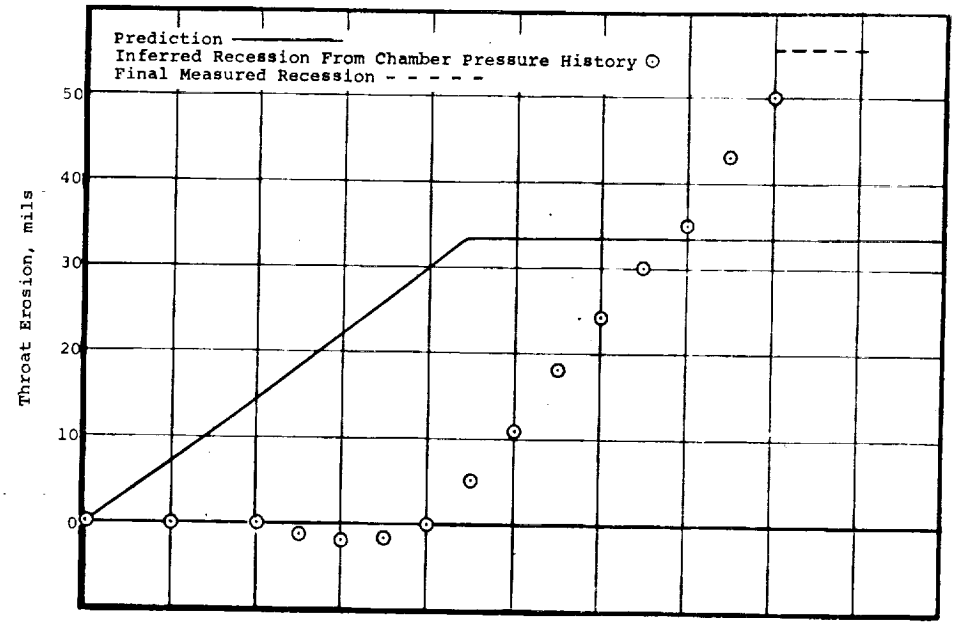

(i) Surface Recession, Nylon-Phenolic, FM-5051

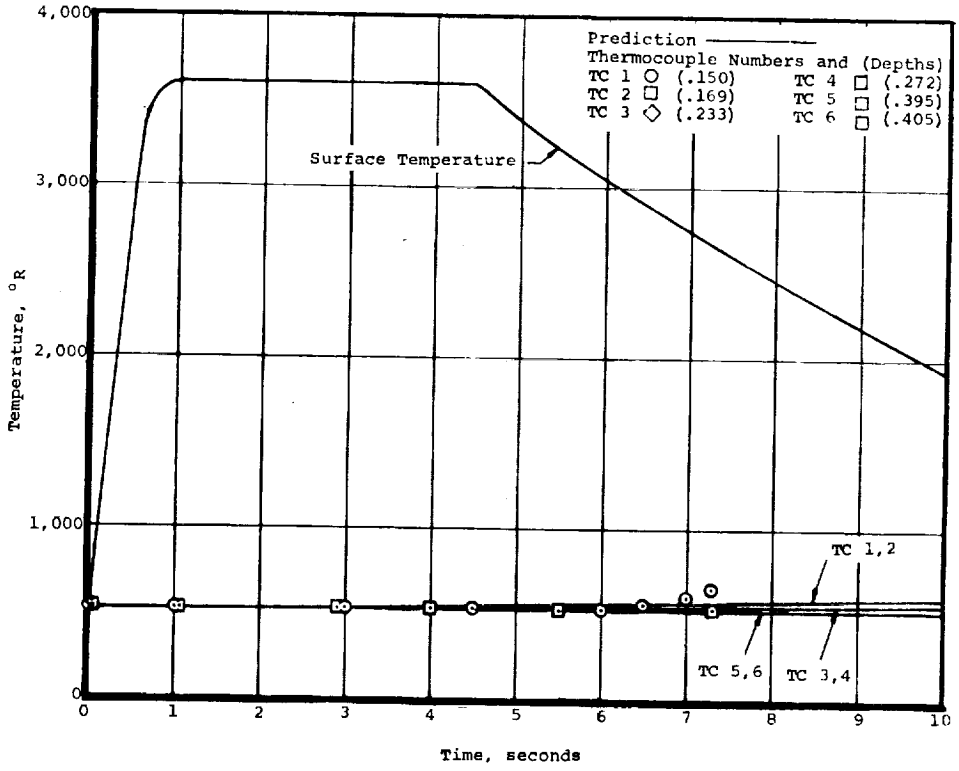

(j) Temperature Histories, Nylon-Phenolic, FM-5051

Figure 47. (continued)

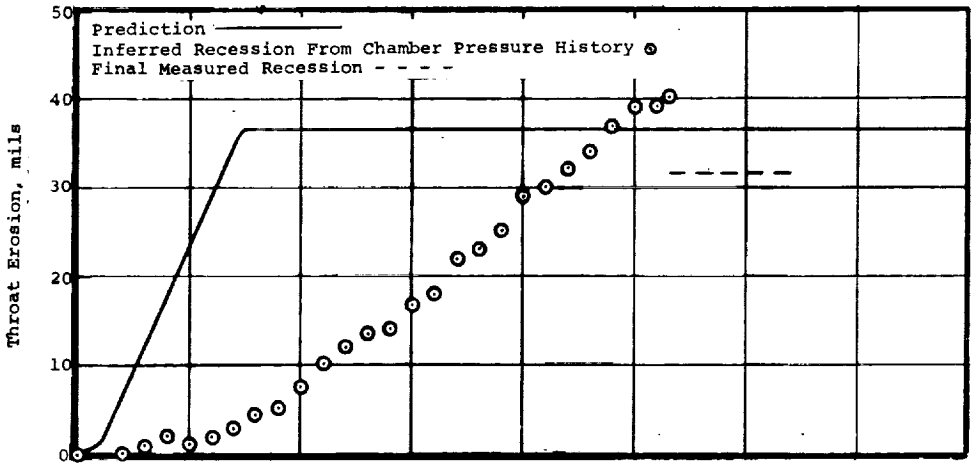

(k) Surface Recession, Silica-Phenyl Silane + Buna N, XR-2015

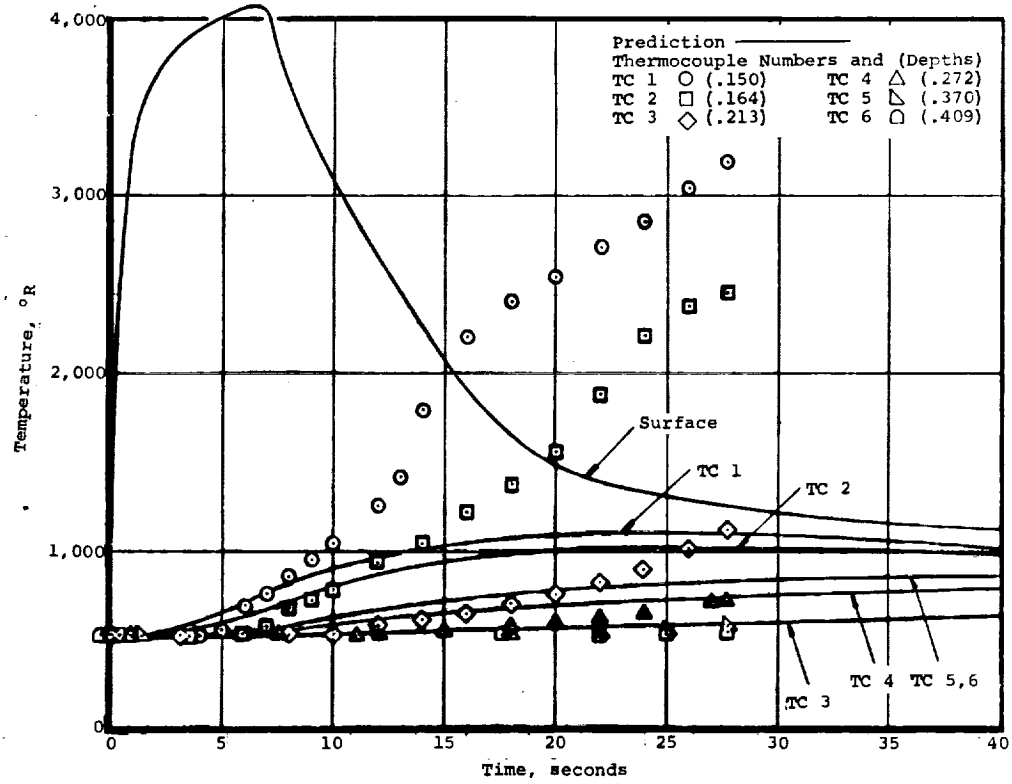

(l) Temperature Histories, Silica-Phenyl Silane + Buna N, XR-2015

Figure 47. (concluded)

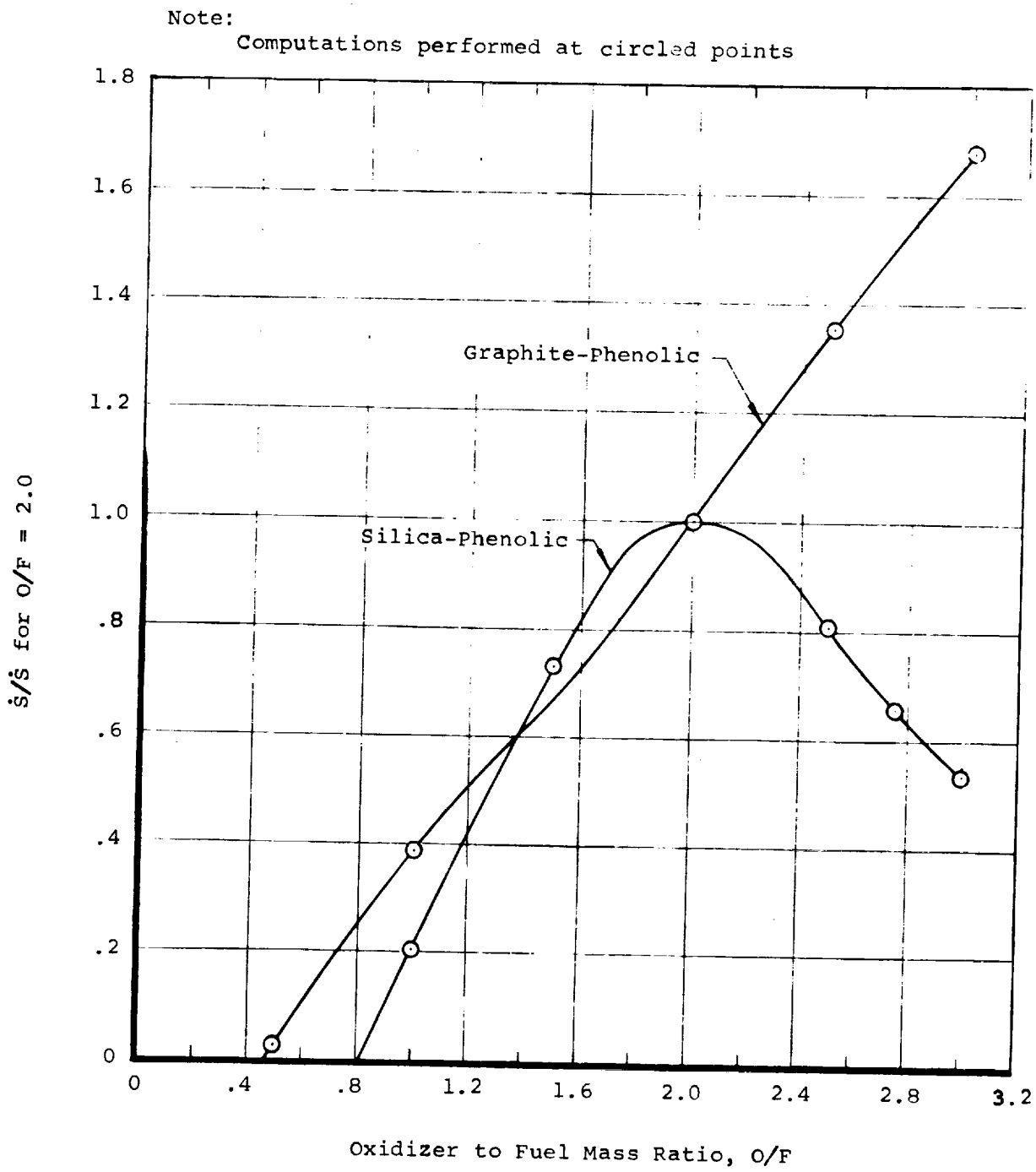

Figure 48. Variation of Steady State Surface Recession Rate for Different O/F Ratios - N_2O_4/Aerozine

APPENDIX A

AEROTHERM CHARRING MATERIAL ABLATIVE PROGRAM (CMA)

APPENDIX A

AEROTHERM CHARRING MATERIAL ABLATIVE PROGRAM (CMA)

General Description

The CMA program is a coded procedure for calculating the in depth thermal response of a charring, ablating material. The basic physics included correspond to simple charring. Initial versions of the program were described in Reference A-1, and subsequently a more complete description of the physics and mathematical treatment is given in Reference A-2. Reference A-3 is a program user's manual which describes input-output details.

The program is an implicit, finite-difference computational procedure for computing the one-dimensional transient transport of thermal energy in a three-dimensional isotropic material which can ablate from a front surface and which can decompose in depth. Decomposition (pyrolysis) reactions are based on a three-component model. The program permits up to eight different backup materials of arbitrary thickness. The back wall of the composite material may transfer energy by convection and radiation.

The ablating surface boundary condition may take one of three forms:

Option 1 - Film coefficient model convection-radiation heating with coupled mass transfer, including the effects of unequal heat and mass transfer coefficients (non-unity Lewis number) and unequal mass diffusion coefficients. Surface thermochemistry computations need not presume chemical equilibrium at the surface.

Option 2 - Specified surface temperature and surface recession rate.

Option 3 - Specified radiation view factor and incident radiation flux, as functions of time, for a stationary surface.

Any combination of the first three options may be used for a single computation. Option 3 is appropriate to cooldown after termination of convective heat input and is often useful in conjunction with Options 1 and 2.

The program permits the specification of a number of geometries, including plane, cylindrical or annular, and spherical. In the most general case, area may vary arbitrarily with depth.

The rear surface of the last node may be specified as insulated, or may experience convective and radiative heat transfer to a "reservoir" at a specified reservoir temperature if a rear surface convection coefficient and an emissivity are input.

Material properties such as thermal conductivity, specific heat, and emissivity are input as functions of temperature for virgin plastic and char.

For partially decomposed material, the program performs an appropriate averaging on density to determine effective material properties.

The basic solution procedure is by a finite difference approach. For each time step, the decomposition relations are solved and then the in-depth energy fluxes constructed in general terms. These are then harmonized with a surface energy balance (if a surface energy balance option is being used) and the in-depth temperatures determined. New material property values are set up and the solution is ready for the next time increment.

The CMA program outputs instantaneous mass ablation rates and blowing parameters for char and pyrolysis gas, total integrated mass ablation of char and pyrolysis gas, total recession and recession rates of surface, of the char line, and of the pyrolysis line. It also outputs the surface energy flux terms, namely, the energy convected in, energy radiated in, energy reradiated out, chemical generation, and conduction away (q_{cond}). Further, it describes how the input energy of q_{cond} is "accommodated" or "partitioned" in the solid material. Part of the energy is consumed in decomposing the plastic, part is consumed in sensible enthalpy changes of the solid, and part is "picked up" by the pyrolysis gases as they pass through the char. Thermocouple and isotherm output can also be called for.

Some Surface Energy Balance Details

In calculations under Option 1, the in-depth solution is coupled to a general film-coefficient boundary condition. This coupling could be accomplished through a direct calculation of the surface mass transfer, energy transfer, and chemical reaction events, but due to the non-linear aspect of the complicated surface events some complex iteration scheme would be required to accomplish this direct coupling. Instead of direct coupling, it has proved more expedient to prepare in advance a series of tables which include all the surface mass transfer and chemical relations. The in-depth solution may then be coupled to the surface events through a surface energy balance. For example when chemical equilibrium is achieved at the ablating surface and when no mechanical removal is occuring, the development presented in Reference A-4 describes the means for obtaining the thermodynamic state of the gas at the ablating surface in terms of the pressure, and char and pyrolysis off-gas rates.

$$\text{Thermodynamic state} = f(B'_g, B'_c, P)$$

where

$$B'_g = \frac{\dot{m}_g}{\rho_e u_e C_M} \qquad \text{(normalized pyrolysis off-gas rate)}$$

$$B'_c = \frac{\dot{m}_c}{\rho_e u_e C_M}$$ (normalized char recession rates)

P = boundary layer edge pressure

The thermodynamic state includes definition of surface temperature and gas molecular composition. This, in turn, enables evaluation of the various quantities appearing in the boundary layer driving potential for heat and mass transfer (Ref. A-4). Tables representing solutions to the functional relationship (A-1) are generated for a complete map covering the range of B'_g B'_c and P, of interest. These tables have, in the past, been generated with the Aerotherm EST program, Version 2 (Ref. A-5).

As an example of this procedure, suppose a table is prepared, which, for a parametric array of dimensionless char erosion rates (B'_c), dimensionless pyrolysis off-gas rates (B'_g), and pressure, presents the relevant ablating surface temperature and requisite boundary layer composition and enthalpy quantities. During each time step in the course of the in-depth solution the program generates a pyrolysis gas rate B'_g and computes the rate at which energy is conducted into the material from the surface. With B'_g and the pressure known, the input parametric tables then serve to define that B'_c which yields temperature and enthalpy quantities which provide a balanced, harmonized set of energy fluxes at the surface.

References to Appendix A

A-1 Rindal, R.A., Flood, D.T., and Kendall, R.M: Analytical and Experimental Study of Ablation Material for Rocket-Engine Application. Contract NAS 7-218, Vidya Report No. 201, NASA CR-54757, May 15, 1966.

A-2 Moyer, C.B. and Rindal, R. A.: Finite Difference Solution for the In-Depth Response of Charring Materials Considering Surface Chemical and Energy Balances. Aerotherm Corporation Final Report 66-7, Part II, March 14, 1967.

A-3 User's Manual, Charring Material Ablation Program (CMA) Version 2. Aerotherm Corporation, Palo Alto, California, June 1966.

A-4 Kendall, R.M., Rindal, R.A., and Bartlett, E.P.: A Multicomponent Boundary Layer Chemically Coupled to an Ablating Surface, AIAA Journal, Volume 5, No. 6, June 1967, pp. 1063-1071

A-5 User's Manual, Aerotherm Equilibrium Surface Thermochemistry Program (EST) Version 2, Aerotherm Corporation, Palo Alto, California, June 1966.

APPENDIX B

EXPERIMENTAL WORK ON CARBON-SILICA REACTIONS

APPENDIX B

EXPERIMENTAL WORK ON CARBON-SILICA REACTIONS

The importance of finite rate chemistry for the silica-carbon reaction in describing the ablation performance of silica reinforced plastics has been described by Beecher and Rosenweig, Reference B-1.

It was indicated that the three reactions most likely to occur under conditions of chemical equilibrium are:

$$SiO_2^* + C^* \rightarrow SiO + CO$$

$$SiO_2^* + 3C^* \rightarrow SiC^* + 2CO$$

$$SiO_2^* + 2C^* \rightarrow Si^* + 2CO$$

where the asterisk denotes condensed phases. Beecher and Rosenweig experimentally determined rate constants by reacting samples of pyrolyzed Fiberglas-reinforced phenolic resin in their reaction apparatus. Their rate constants were determined from recorder traces of the pressure rise of the collected volatiles which were identified as either CO or CO_2. Because of the strong equilibrium reaction potential they assumed that Reaction B-2 was controlling in causing depletion of carbon in their test sample. They further postulate that in a zone near the material surface the temperature may be sufficient to cause the silicon carbide formed to react via the following reaction.

$$SiC^* + 2SiO_2^* \rightarrow 3SiO + CO$$

Subsequent to the work of Beecher and Rosenweig a group at TRW performed similar experiments on a somewhat more elaborate scale (Ref. B-2). As a result of this work and the apparent disparity in specific rate constants, Beecher and Rosensweig re-evaluated their data and found that their original specific rate constant was four orders of magnitude too high (Reference B-3).

The TRW work by Blumenthal et al, (Reference B-2) provides the most extensive evaluation of the silica-carbon reaction made to date. In their work the reactions between carbon and silica were quantitatively investigated for four compressed powder systems and one charred, silica-reinforced, phenolic resin system, MX2600. Measurements were made in the temperature range 1300°C to 1600°C and at low pressures (10^{-3} to torr). Blumenthal et al proposed the same silica-carbon reaction scheme as did Beecher and Rosensweig (Reactions B-1 through B-3).

The reaction scheme which was controlling in the systems proposed was obtained by measuring the initial and final sample weights for each experiment and by X-ray diffraction analysis of the resulting solid products of reaction. A material balance was then performed assuming, in turn, that

Reactions B-1, B-2, and B-3 were taking place. With the assumption that the silicon carbide remained in the reaction tube and that the silicon monoxide and silicon evaporate and condense in a cooler part of the system, the weight losses calculated from Reactions B-1, (SiO formation) agreed closer with the measured weight losses than did reactions B-2 and B-3 (SiC and Si formation, respectively). The agreement, however, holds only for reaction temperatures of 1400°C and higher. At the 1300°C reaction temperature, the authors of Reference B-2 conclude that at least part of the silicon and silicon monoxide reaction products are not volatile and would remain in the reaction tube.

As a result of the overall material balance performed on the material samples it appears rather conclusive that reaction B-1 is sufficient to describe the kinetics of the silica-carbon reaction. Although silicon carbide may be formed as an intermediate product in a consecutive reaction mechanism which continues to silicon monoxide and carbon monoxide the rate controlling mechanism is formation of SiO and CO vapor products.

Blumenthal, et al then conclude that the most likely reaction sequence leading to the formation of SiO and CO products is the competing reactions of silica and carbon that take place initially, i.e.

$$SiO_2^* + C^* \rightarrow SiO + CO \qquad \text{(B-1)}$$

$$SiO_2^* + 3C^* \rightarrow SiC^* + 2CO \qquad \text{(B-2)}$$

followed consecutively by reaction of the silicon carbide with excess silica, i.e.,

$$SiC^* + 2SiO_2^* \rightarrow 3SiO + CO \qquad \text{(B-4)}$$

Therefore, the overall reaction of the reaction steps reflected by the above is the formation of silicon monoxide according to Reaction B-1.

$$SiO_2^* + C^* \rightarrow SiO + CO$$

Correlating the TRW rate data in terms of an Arrhenius equation leads to the following expression for the rate of carbon consumption in a carbon-silica mixture from MX2600.

$$\dot{m}_C = m_C A e^{-E/RT} \qquad \text{(B-5)}$$

where

$\dot{m}_C$ = carbon consumption rate, lb_C/sec

m_C = mass of carbon, lb

$A = 3.18 \times 10^6 \quad sec^{-1}$

$E = 70{,}000 \pm 10{,}000 \quad cal/mole$

The value of A cited here pertains to the B value of 70,000 cal/mole. If the 80,000 upper estimate for B is chosen, the appropriate value of A necessary to match the bulk of the data is 9×10^7 sec^{-1}.

REFERENCES TO APPENDIX B

B-1 Beecher, N., and Rosensweig, R. E.: Ablation Mechanisms in Plastics with Inorganic Reinforcement. ARS Journal, Vol. 31, No. 4, April, 1961, pp. 1802-1809.

B-2 Blumenthal, J. L., Santy, M. J. and Burns, E. A.: Kinetic Studies of High-Temperature Carbon-Silica Reactions in Charred Silica-Reinforced Phenolic Resins. Western States Section, The Combustion Institute, Fall Meeting, Santa Barbara, Calif., October 25-26, 1965. Paper No. WSCI 65-25; also AIAA Journal, Vol. 4, No. 6, June 1966, pp. 1053-1057.

B-3 Beecher, N. and Rosensweig, R. E.: Erratum: Ablative Mechanism in Plastics with Inorganic Reinforcement. AIAA Journal, Vol. 3, No. 8, August 1965.

APPENDIX C

MATERIAL PROPERTY EVALUATION

APPENDIX C
MATERIAL PROPERTY EVALUATION

Calculation of the ablative material response requires rather extensive, detailed information regarding the chemical and thermal properties of each material considered. The property data employed for each of the six ablative materials considered here has resulted from a combination of direct measurement and estimates based upon measurements for similar materials. In this appendix the chemical property values requiring definition are listed, and the values employed for the ablation material response calculations are given.

Ablative material chemical properties are defined here to include sufficient information to characterize the density and chemical elemental composition of the virgin material and char, and the elemental composition of the pyrolysis gas, in addition to a realistic kinetic equation for representing the rate of decomposition of the virgin material. Chemical elemental composition information is presented first, in Section C-1, ablation material density information is given in Section C-2, and in Section C-3 a description of the decomposition rate coefficients for each material is given, and finally, in Section C-4, heat of formation information is presented.

C-1 Chemical Composition

The chemical composition of the virgin material is based upon published data by pre-preg tape manufacturers regarding resin content in the uncured material. The char composition was estimated assuming nominal values for the residue fraction of decomposed organic constituents and assuming that such inorganic constituents as SiO_2 and graphite fibers retain their initial chemical identity in the char layer. The chemical elemental composition of the pyrolysis gas is then calculated by difference from the known virgin material and char compositions.

The quantity of chemical elements in the virgin material, char, and pyrolysis gas are related through an idealized irreversible reaction which is presumed to represent the ablative material decomposition process (after Ref. C-1)

$$n_r(\text{resin}) + (1-n_r)\ \text{reinforcement} \rightarrow \text{char} + \text{gas} \qquad (1)$$

where n_r represents that mole fraction of resin in one mole of virgin plastic. The means employed to evaluate the coefficients in Reaction (1) for each of the six ablative materials is described here.

(NL-1) Silica-Phenolic (MXS-89)

The resin solids and volitile content for the pre-preg tape are given in Reference C-2

	Min	Max	Mean
Resin Solids Content, %	27	33	30
Volitile Content, %	2	6	4

Assume 12 1/2 percent of the volatiles remain in the resin after curing.* Then the total organic content in the cured plastic becomes:

$$K_r = 0.30 + 0.125(.04) = 0.305 \frac{\text{Lb resin}}{\text{Lb virgin plastic}}$$

The remainder of the material in the virgin plastic consists of SiO_2 fibers and SiO_2 filler. The fibers and filler are treated as one, so:

$$K_{SiO_2} = 1.0 - 0.305 = 0.695 \frac{\text{Lb } SiO_2}{\text{Lb virgin plastic}}$$

The organic constituent consists of phenolic resin and is presumed to be represented chemically by C_6H_6O. The decomposition reaction then becomes:

$$n_r C_6H_6O + (1-n_r)SiO_2 \rightarrow \overbrace{n_c C + (1-n_r)SiO_2}^{\text{char}} + \overbrace{6\,n_r H + n_r O + (6\,n_r - n_c)C}^{\text{gas}} \qquad (2)$$

where: n_r is the number of moles of resin per mole of plastic

and n_c is the number of moles of carbon converted to char residue per mole of plastic decomposed

The resin mole fraction, n_r, is determined from the resin mass fraction, $K_r = 0.305$.

*As a rough rule of thumb it is assumed here that 7/8 ths of the volatiles will be driven off during the cure process.

$$\frac{n_r M_{C_6H_6O}}{n_r M_{C_6H_6O} + (1-n_r) M_{SiO_2}} \equiv K_r = 0.305$$

Rearranging yields

$$n_r = \frac{1}{\frac{M_{C_6H_6O}}{M_{SiO_2}} \left(\frac{1}{K_r} - 1\right) + 1} \qquad (3)$$

The effective molecular weights of resin and reinforcement are:

$$M_{C_6H_6O} = 94.1$$

$$M_{SiO_2} = 60.06$$

Substitution into the above yields the mole fraction of resin in the virgin material

$$n_r = 0.2185$$

The number of moles of carbon in the char results from considering the resin residue fraction remaining after complete decomposition. A variety of measurements have been reported for phenolic resin residue fraction ranging from 37 to 50 percent (Refs C-1 & C-3). A value of 40 percent is adopted for phenolic resin here, i.e.,

$$\frac{\text{mass of carbon residue}}{\text{initial phenolic resin mass}} = 0.4$$

Referring to Reaction (1) we may write

$$\frac{n_c M_c}{n_r M_{C_6H_6O}} = 0.4$$

from which, $n_c = 0.4\, n_r \frac{94.1}{12.011} = 0.684$. Substituting the above values for n_r (0.2185) and n_c (0.684) into Reaction (2) yields the effective decomposition reaction for the silica phenolic material (NL-1)

$$0.2185\ C_6H_6O + 0.7815\ SiO_2 \rightarrow 0.684\ C + 0.7815\ SiO_2$$

$$\overbrace{+\ 1.311\ H + 0.2185\ O + 0.627\ C}^{\text{gas}}$$

The above reaction should be considered as a balance on chemical elements and it is used to establish the relative amount of each chemical element in the char and pyrolysis gas. The elemental mass fractions ($\tilde{K}_k$) are derived from Reaction (4) as follows:

$$\tilde{K}_k = \frac{\tilde{\nu}_k M_k}{\sum_k \tilde{\nu}_k M_k} \qquad (5)$$

where $\tilde{K}_k$ is the mass fraction of element k, $\tilde{\nu}_k$ is the number of gram atoms of element k (e.g., for the char, $\tilde{\nu}_c = 0.684$) and M_k is the atomic weight of element k. Utilizing the coefficients in Reaction (4), and Equation (5) the elemental mass fractions in the char and pyrolysis gas may be evaluated.

Char

element	$\tilde{\nu}_{kc}$		M_k			$\tilde{K}_{kc}$ $\frac{\text{grams k}}{\text{gram char}}$
C	.684	x	12.011	=	8.23	.149
O	1.563	x	16.	=	25.00	.453
Si	.7815	x	28.06	=	21.95	.398
			$\sum_k \nu_{kc} M_k$	=	55.18	

Gas

element	$\tilde{\nu}_{kg}$		M_k			K_{kg} $\frac{\text{grams k}}{\text{gram gas}}$
H	1.311	x	1.008	=	1.322	.107
C	.627	x	12.011	=	7.53	.609
O	.2185	x	16.	=	3.5	.284
			$\sum_k \nu_{kg} M_k$	=	12.352	

The elemental composition of char and pyrolysis gas for the remaining 5 materials is presented in the following paragraphs.

(NL-2) Graphite-Phenolic (MX-4500)

The virgin material resin mass fraction for all 6 ablative materials was determined from pre-preg tape manufacturers data books (Refs. C-2 and C-4) as above for silica phenolic. The results for each material considered are shown in Table C-1. The effective decomposition reaction for the graphite phenolic material is

$$n_r\, C_6H_6O + (1 - n_r)C \rightarrow \overbrace{\left[(1 - n_r) + n_c\right] C}^{\text{char}} + \overbrace{(6n_r - n_c)C + 6n_rH + n_rO}^{\text{gas}} \qquad (6)$$

Rewriting Equation (3) for graphite fibers rather than SiO_2 fibers yields an expression for the number of moles of resin per mole of virgin material in terms of the resin mass fraction

$$n_r = \frac{1}{\frac{M_{C_6H_6O}}{M_C}\left(\frac{1}{K_r} - 1\right) + 1}$$

From Table C-1, $K_r = .326$, which yields $n_r = .0581$. As before we assume 40 percent of the phenolic remains behind as carbon after decomposition

$$n_c = .4\, n_r \left(\frac{M_{C_6H_6O}}{M_C}\right) = .182$$

Substituting the above into Reaction (6) yields the effective decomposition reaction for graphite-phenolic.

$$0.0581\, C_6H_6O + .9419\, C \rightarrow \overbrace{1.1239\, C}^{\text{Char}} + \overbrace{.1662\, C + .3482\, H + .0581\, O}^{\text{gas}} \qquad (7)$$

The elemental mass fractions are obtained as before.

Gas

element	$\tilde{\nu}_{kg}$		M_k			$\tilde{K}_{kg}$ $\frac{\text{grams k}}{\text{gram gas}}$
H	.3482	x	1.008	=	.3512	.107
C	.1662	x	12.011	=	1.9950	.609
O	.0581	x	16.	=	.930	.284
	$\sum_k \tilde{\nu}_{kg} M_k$			=	3.2762	

Since the char is all carbon, $\tilde{K}_{kc} = 1.0$ for k = C, and $K_{kc} = 0$ for all other k.

(NL-3) Asbestos Phenolic (MXA-11)

The chemical composition of asbestos phenolic is based on the assumption that the reinforcing fibers have the crystaline configuration of chrysotile asbestos $(M_gO)_3 \cdot (SiO_2)_2 \cdot (H_2O)_2$ (Ref. C-5). The effective decomposition reaction is then written as

$$n_r\, C_6H_6O + (1 - n_r)(M_gO)_3\,(SiO_2)_2\,(H_2O)_2 \rightarrow \overbrace{n_c\, C + (1 - n_r)\left[3M_gO + 2SiO_2\right]}^{\text{char}} \overbrace{+ (6n_r - n_c)C + (2n_r + 4)H + (2 - n_r)O}^{\text{gas}} \qquad (8)$$

The above reaction is written assuming the water of hydration in the asbestos fibers is driven off during the char formation reaction. This would normally be expected to occur in the temperature range 800°F - 1100°F (Ref. C-5). As noted from Reaction (8) all of the metal oxides are presumed to remain inert during the char formation reaction. Rewriting Equation (3) for asbestos phenolic yields:

$$n_r = \frac{1}{\frac{M_{C_6H_6O}}{3M_{MgO}+2M_{SiO_2}+2M_{H_2O}}\left(\frac{1}{K_r} - 1\right) + 1}$$

From Table C-1 $K_r = 0.435$, which results in $n_r = 0.694$. As for silica- and graphite-phenolic 40 percent of the resin mass is assumed to remain as carbon residue after decomposition

$$n_c = .4n_r\left(\frac{M_{C_6H_6O}}{M_C}\right) = 2.175$$

Substituting the above values into Reaction (8) yields the effective decomposition reaction for asbestos phenolic

$$.694\, C_6H_6O + .306\, (M_gO)_3 \cdot (SiO_2)_2 \cdot (H_2O)_2 \rightarrow \overbrace{2.175\, C + .918\, M_g + .612\, Si + 2.142\, O}^{\text{char}} \overbrace{+ 1.985\, C + 5.384\, H + 1.306\, O}^{\text{gas}} \qquad (9)$$

The elemental mass fractions in the char and gas are obtained from Reaction (9) as before.

Char

element	$\tilde{\nu}_{kc}$		M_k			$\tilde{K}_{kc}$
C	2.175	x	12.011	=	26.15	.2616
O	2.142	x	16.	=	34.30	.3432
Mg	.918	x	24.32	=	22.32	.2233
Si	.612	x	28.06	=	17.18	.1719
			$\sum_k \tilde{\nu}_{kc} M_k$	=	99.95	

Gas

element	$\tilde{\nu}_{kg}$		M_k			$\tilde{K}_{kg}$
H	5.384	x	1.008	=	5.42	.108
C	1.985	x	12.011	=	23.85	.476
O	1.306	x	16.	=	20.90	.416
					50.17	

(NL-4) Carbon-Phenolic (MX 4926)

The effective decomposition reaction for carbon-phenolic is taken to be identical to that for graphite-phenolic (NL-2) since the same resin is employed and the resin mass fraction in the virgin materials is the same.

(NL-5) Nylon-Phenolic (FM-5051)

The effective decomposition reaction for nylon phenolic is

$$n_r\, C_6H_6O + (1 - n_r)\, C_6H_{11}ON \rightarrow \overbrace{n_c\, C}^{\text{char}}$$

$$+ \overbrace{(6 - n_c)\, C + (11 - 5n_r)\, H + O + (1 - n_r)\, N}^{\text{gas}}$$

All of the carbon in the char is presumed to come from the decomposition of phenolic resin since all of the nylon will be driven off in the gas form. From Table C-1, the resin mass fraction is $K_r = 0.326$. Then

$$n_r = \frac{1}{\frac{M_{C_6H_6O}}{M_c}\left(\frac{1}{K_r} - 1\right) + 1} = 0.546$$

and again assuming a 40-percent resin residual,

$$n_c = .4n_r\left(\frac{M_{C_6H_6O}}{M_c}\right) = 1.712$$

The decomposition reaction becomes

$$.546\ C_6H_6O + .454\ C_6H_{11}ON \rightarrow \overbrace{1.712\ C}^{\text{char}}$$

$$\overbrace{+\ 4.288\ C + 8.27\ H + .454\ N + O}^{\text{gas}} \qquad (10)$$

Since the char is all carbon, $\tilde{K}_{kc} = 1.0$ for $k = C$.

			Gas			
element	$\tilde{\nu}_{kg}$		M_k			$\tilde{K}_{kg}$
H	8.27	x	1.008	=	8.34	.1016
C	4.288	x	12.011	=	51.40	.6260
N	.454	x	14.008	=	6.35	.0774
O	1.	x	16.	=	16.00	.1950
			$\sum_k \tilde{\nu}_{kg}M_k$	=	82.09	

(NL-6) Silica-Phenyl Silane + Buna N (XR-2015)

Of the six materials considered the chemical composition of silica-phenyl silane + Buna N is the most uncertain. The model employed here results from a quantitative chemical elemental analysis on the virgin material and a rather crude model to characterize the basic organic resin structure.

It is first assumed that the phenyl silane effective composition may be represented as follows:

$$C_{6-n}\ H_6\ O\ Si_n$$

where $0 \leq n \leq 6$

This arrangement assumes that the phenyl silane is formed from a phenolic resin chain (C_6H_6O) by replacing some carbon atoms with silicon atoms. The other constituents presumed to be present in the virgin material are SiO_2 reinforcement and Buna N rubber. The Buna N rubber is presumed to contain 1/3 mole fraction of acrila nitrile (C_3H_3N) and 2/3 mole fraction butadiene (C_4H_6) which results in an effective molecule for Buna N of $C_{11}H_{15}N$. The virgin material composition may then be written as

$$n_{r_1}\ C_{6-n}\ H_6\ O\ Si_n + n_{r_2}\ C_{11}\ H_{15}\ N + (1 - n_{r_1} - n_{r_2})\ SiO_2 \qquad (11)$$

Some limits on the value of the unknown, n, may be established from the results of a quantitative elemental analysis on the virgin material (Ref. 6)

element	K $\frac{\text{mass observed}}{\text{mass virgin material}}$
H	0.0288
C	.2538
N	.018
ash (SiO_2)	.6457
	.9463

It may be noted that the material was not analyzed for oxygen content so the missing material is presumed to be oxygen. Since the ash must be all SiO_2 it may be concluded that there was sufficient oxygen in the phenyl silane resin to oxidize all of the Si atoms in the resin plus an oxygen excess equal to 5.37 mass percent of the virgin plastic mass. We may consider the decomposition of the phenyl silane resin in the light of the above conclusion.

$$C_{6-n}\ H_6\ O\ Si_n \rightarrow C_{6-n}\ H_6 + n\ SiO_2 + (1 - 2n)\ O \qquad (12)$$

Since excess oxygen was given off $(1-2n) > 0$, or $0 \leq n \leq .5$. It is possible to gain a better feeling for the value of n by introducing some additional information based upon estimates made during personnel communications with

several pre-preg tape manufacturers. It was estimated that the mass ratio of phenyl silane to Buna N is about 1:1. Further, it is noted that the silica fiber reinforcement mass fraction is about $K_{SiO_2} \tilde{=} .6$. A rough estimate on the over-all mass fractions in the virgin material then becomes $K_{SiO_2} = 0.6$, $K_{\text{Phenyl Silane}} = 0.2$, $K_{\text{Buna N}} = 0.2$. We note from the above considerations that an amount of excess oxygen equal to 5.37 percent of the virgin material mass was driven off during decomposition

$$\frac{\text{mass excess oxygen}}{\text{mass virgin material}} = .0537$$

Referring to Reaction (12) and noting that phenyl silane is the only possible source of excess oxygen we may write:

$$(1 - 2n) \frac{M_O}{M_{C_{6-n}H_6 O Si_n}} K_{\text{phenyl silane}} = .0537 \frac{\text{grams O}}{\text{gram virgin matl.}} \qquad (13)$$

where

$$M_O = 16.$$

$$M_{C_{6-n}H_6 O Si_n} = (6 - n)(12.011) + 6(1.008) + 16 + n(28.06)$$

$$K_{\text{phenyl silane}} = 0.2 \frac{\text{gram phenyl silane}}{\text{gram virgin matl.}}$$

Solving for n yields $n = -.256$. This is not possible so we conclude that the mass fraction of phenyl silane must be greater than 0.2 ($K_{\text{Phenyl Silane}} > 0.2$). In effect, more excess oxygen was given off than the total oxygen content in the virgin material if $K_{\text{Phenyl Silane}} = 0.2$. In order to obtain a lower limit for the mass fraction of phenyl silane in the virgin material which must exist to produce the observed excess oxygen content set $n = 0$ and solve for $K_{\text{Phenyl Silane}}$ in Equation (13), which yields:

$$K_{\text{Phenyl Silane}} = .3125$$

If $n = 0$, the only silicon in the virgin material is that contained in the silica reinforcement in which case the mass fraction of ash corresponds identically to the mass fraction of SiO_2 in the virgin material. $K_{SiO_2} = .6457$, but $K_{\text{Phenyl Silane}} = .3125$ so $K_{\text{Buna N}} = .0418$. At this point it is

informative to deduce what the effective molecular configuration of the organic components would be based on the above speculation. Referring to Reaction (11) and noting that $n = 0$ we may write

$$\frac{n_{r_1} M_{C_6H_6O}}{n_{r_2} M_{C_{11}H_{15}N}} = \frac{.3125}{.0418}$$

Solving for the resin mole ratio yields:

$$\frac{n_{r_1}}{n_{r_2}} = 12.81$$

which yields an effective molecular configuration as follows:

$$12.81\ C_6H_6O + C_{11}H_{15}N \rightarrow C_{87.9}H_{91.9}O_{12.81}N$$

normalizing on carbon the postulated molecular composition may be written as:

$$C_6H_{6.27}O_{.875}N_{.0682}$$

We may compare this with the effective molecular composition for the organic constituents deduced from the quantitative elemental analysis (assuming no silicon atoms in the resin).

$$C_6H_{8.14}O_{.955}N_{.366}$$

The measured and postulated compositions do not differ too markedly considering the magnitude of speculation contained in the postulated composition. It is, therefore, concluded that the quantity of silicon atoms in the phenyl silane resin is not very significant, and for purposes of this investigation the resin may be assumed to contain no silicon. As such, the molecular composition of the resin will be taken as shown above and the effective decomposition reaction for the virgin plastic becomes:

$$n_r\ (C_6H_{8.14}O_{.955}N_{.366}) + (1 - n_r)\ SiO_2 \rightarrow \overbrace{n_cC + (1 - n_r)\ SiO_2}^{\text{char}}$$

$$+ \overbrace{(6n_r - n_c)\ C + 8.14n_r\ H + .955n_r\ O + .366n_r\ N}^{\text{gas}} \qquad (14)$$

As established above, the SiO_2 mass fraction is 0.6457, so $K_r = 0.3543$. The number of moles of resin is then given by

$$n_r = \frac{1}{\frac{M_{C_6H_{8.14}O_{.955}N_{.366}}}{M_{SiO_2}}\left(\frac{1}{K_r} - 1\right) + 1} = .2475$$

Because the resin is basically different from phenolic resin it does not appear advisable to assume that 40 percent of the resin remains behind as char In order to better establish the resin residual fraction several samples of the virgin material were decomposed in an inert environment at $2000^{\circ}R$. The results indicate

$$\frac{m_{char}}{m_{virgin}} = .717 = \frac{n_c M_c + (1 - .2475) M_{SiO_2}}{.2475\ M_{C_6H_{8.14}O_{.955}N_{.366}} + (1 - .2475) M_{SiO_2}}$$

which yields

$$n_c = .422$$

It is interesting to note that the mass of resin converted to carbonaceous residue is only 20 percent compared to 40 percent for phenolic resin. Substituting the above values into Reaction 14 yields the effective decomposition reaction for silica-phenyl silane + Buna N

$$.2475\ C_6H_{8.14}O_{.955}N_{.366} + .7525\ SiO_2 \rightarrow$$

$$\overbrace{.422\ C + .7525\ SiO_2}^{\text{char}} + \overbrace{1.063\ C + 2.015\ H + .2362\ O + .0905\ N}^{\text{gas}} \qquad (15)$$

The elemental composition of char and gas become

Char

element	$\tilde{\nu}_{kc}$		M_k			$\tilde{K}_{kc}$
C	.422	x	12.011	=	5.07	.1009
O	1.505	x	16.	=	24.10	.4791
Si	.7525	x	28.06	=	21.10	.4200
			$\sum_k \tilde{\nu}_k M_k$	=	50.27	

Gas

element	$\tilde{\nu}_{kg}$		M_k			$\tilde{K}_{kg}$
H	2.015	x	1.008	=	2.03	.1025
C	1.063	x	12.011	=	12.78	.6460
N	.0905	x	14.008	=	1.27	.0641
O	.2362	x	16.	=	3.71	.1874
					19.79	

The elemental mass fractions for the char and gas of all six ablative materials were presented above and are summarized in Table C-1. In the following ing section, the virgin material and char densities are established.

C-2 Virgin Material and Char Density

The density of the plastic at any point in the degradation process is taken to be represented by an equation of the form (after Ref. C-1)

$$\rho = \Gamma (\rho_A + \rho_B) + (1 - \Gamma) \rho_C \qquad (16)$$

where ρ_A and ρ_B represent the density of two constituents in the resin, ρ_C represents the density of the fabric reinforcement (which is presumed here to include both fibers and filler), and Γ is the resin volume fraction in the virgin plastic. Equation 16 relates the density of the composite to the density of its constituents and the relative quantity of each in the composite. In this section the densities of each constituent in the virgin material and the char are evaluated.

If, for example, Equation 16 is utilized to calculate silica-phenolic density, ρ, from published values of the phenolic resin density $(\rho_A + \rho_B)$, the density of silica, ρ_C, and the resin mass fraction, K_r; a value of the virgin material density is computed which exceeds that measured by about 7 percent. It is rationalized that some voids exist in the material and that they are most probably in between adjacent strands in the reinforcement fibers Based on this reasoning the reinforcement density is reduced by an amount necessary to satisfy Equation (16) with the measured virgin material density and the known values of resin density and resin mass fraction. This is accomplished by solving Equation (16) for the reinforcement density and expressing the resin volume fraction, Γ, in terms of the reported resin mass fraction. For purposes of simplifying the algebra it is convenient to combine the two resin densities $\rho_A + \rho_B = \rho_r$. Introduce the definition of the resin mass fraction

$$K_r = \frac{m_r}{m_r + m_C} \left(\frac{\text{mass resin}}{\text{mass resin + mass constituent C}} \right)_{\substack{\text{in virgin} \\ \text{plastic}}}$$

Expressing the above in terms of densities and volumes yields

$$K_r = \frac{\rho_r V_r}{\rho_r V_r + \rho_C V_C} = \frac{\rho_r}{\rho_r + \rho_C \left(\frac{V_C}{V_r}\right)} \tag{17}$$

Introduce the definition of resin volume fraction

$$\Gamma = \frac{V_r}{V_r + V_C} = \left(\frac{\text{Volume resin}}{\text{Volume resin + Volume constitutent C}}\right)_{\substack{\text{in virgin} \\ \text{plastic}}} \tag{18}$$

Combining Equations (17) and (18) results in an expression for the volume fraction in terms of densities and mass fractions

$$\Gamma = \frac{1}{1 + \frac{\rho_r}{\rho_C}\left(\frac{1}{K_r} - 1\right)} \tag{19}$$

Substituting in Equation (16) and solving for the reinforcement density (constituent C) yields:

$$\rho_C = \frac{\rho\ \rho_r\left(\frac{1}{K_r} - 1\right)}{\frac{\rho_r}{K_r} - \rho} \tag{20}$$

Equation (20) is employed to calculate the reinforcement fiber density in the virgin material ρ_{C_1}*. The measured virgin material density, ρ_1, of all six ablative materials, the resin density, ρ_{r_1}, the resin mass fraction, K_{r_1}, and the computed reinforcement density, ρ_{C_1}, are shown in Table C-1. All materials but one contain phenolic resin for which the density is pretty well known, $\rho_{r_1} = (\rho_{A_1} + \rho_{B_1}) = 81$ lb/ft^3 from Reference C-1 For the last

*Subscript 1 refers to virgin material, subscript 2 to char.

material, however (silica-phenyl silane + Buna N), the resin density was not known so in this case the resin density was computed from Equation (20) employing a value for the silica reinforcement density, ρ_{C_1}, as obtained for silica-phenolic. In effect, we are assuming that the same silica fibers are used in both materials and that the same void fractions exist between adjacent strands in the fibers. The density computed in this manner is 76.9 lb/ft^3. It is not apparent whether it makes sense to divide the phenyl silane + Buna N resin into two parts as is done for phenolic resin ($\rho_r = \rho_A + \rho_B$). As will be indicated later, however, the same decomposition kinetic coefficients are employed in this analysis for both resin systems, so, with this in mind, it seems appropriate to divide the phenyl silane + Buna N resin into two parts. It is assumed that the same relative amounts of constituents A and B exist in both resin systems

$$\left(\frac{\rho_A}{\rho_B}\right)_{\text{phenyl silane + Buna N}} = \left(\frac{\rho_A}{\rho_B}\right)_{\text{phenolic resin}} = 3$$

then

$$\rho_{A1} = \frac{\rho_{A_1} + \rho_{B_1}}{1.33} = \frac{76.9}{1.33} = 57.8 \frac{Lb}{ft^3} \text{ and } \rho_{B_1} = 76.9 - 57.8 = 19.1 \frac{Lb}{ft^3}$$

The density of each constituent in the char is obtained assuming that the materials retain dimensional stability during the decomposition process. The char constituent densities must be consistent with the decomposition reactions derived above in Section C-1.

(NL-1) Silica-Phenolic (MXS-89)

The silica reinforcement is presumed to not enter into the decomposition reaction (Reaction 4), so its density remains unchanged, $\rho_{C_1} = \rho_{C_2}$. To be consistent with Reaction 4 the residual density of the phenolic must be 40 percent of the virgin material value

$$\rho_{r_2} = 0.4\ \rho_{r_1} = 32.4$$

But from Reference C-1, $\rho_{r_1} = \rho_{A_1} + \rho_{B_1}$ and $\rho_{B_2} = 0$. So $\rho_{A_2} = \rho_{r_2}$. The char density is then evaluated from Equation (16) utilizing $\rho_{A_2} = 32.4$, $\rho_{B_2} = 0$, $\rho_{C_2} = 120.3$ and evaluating the initial resin volume fraction, Γ, from Equation (19). The resin volume fraction has been evaluated for all six materials and is shown in Table C-1. For silica phenolic, $\Gamma = 0.395$ ft^3 resin/ft^3 virgin material and the char density is 85.6 lb/ft^3.

(NL-2) Graphite Phenolic (MX-4500)

As for silica phenolic $\rho_{C_2} = \rho_{C_1}$, $\rho_{A_2} = 32.4$, and $\rho_{B_2} = 0$. The resulting char density is shown in Table C-1.

(NL-3) Asbestos Phenolic (MXA-11)

The asbestos fiber does lose some water so its density in the char must be reduced an appropriate amount. The fiber volume is assumed to remain constant as the water is driven off so the fiber density is reduced in proportion to the mass loss associated with dehydration

$$\rho_{C_2} = \rho_{C_1} \frac{M_{(M_gO)_3\cdot(SiO_2)_2}}{M_{(M_gO)_3\cdot(SiO_2)_2\cdot(H_2O)_2}} = 128.3(.87) = 111.7 \frac{Lb}{ft^3}$$

The initial and final densities of the phenolic resin constituents is the same as above. The resulting density information is summarized in Table C-1.

(NL-4) Carbon Phenolic (MX4926)

Again, $\rho_{C_2} = \rho_{C_1}$ and the resin constituents are the same as above.

(NL-5) Nylon Phenolic (FM-5051)

The reinforcement fiber (constituent C) is nylon which is completely vaporized during the char formation reaction (Ref. C-1) so $\rho_{C_2} = 0$, and the phenolic constituent densities are the same as for the other materials.

(NL-6) Silica-Phenyl Silane + Buna N (XR-2015)

The reinforcement fibers (constituent C) are silica and are presumed not to enter into decomposition reactions below the surface, so $\rho_{C_2} = \rho_{C_1}$. The resin residual fraction is obtained from the char density measurement for this material. As described above (Section C-1) the fraction of resin remaining as carbonaceous residue is 20.4 percent, or $\rho_{r_2} = .2\ \rho_{r_1}$. As indicated earlier the phenyl silane + Buna N is presumed to be divided into two constituents ($\rho_r = \rho_A + \rho_B$). As for phenolic resin we assume $\rho_{B_2} = 0$, so

$\rho_{A_2} = \rho_{r_2} = 15.4\ lb/ft^3$.

C-3 Decomposition Kinetics

The total decomposition rate for the composite is given by differentiating Equation (16) with respect to time

$$\frac{\partial \rho}{\partial \theta} = \Gamma \left(\frac{\partial \rho_A}{\partial \theta} + \frac{\partial \rho_B}{\partial \theta} \right) + (1 - \Gamma) \frac{\partial \rho_C}{\partial \theta}$$

Where the decomposition rate of each constituent is presumed to be represented by a rate equation of the Arrhenius form

$$\frac{\partial \rho_i}{\partial \theta} = -k_i e^{-E_i/RT} \rho_{i_1} \left(\frac{\rho_i - \rho_{i_2}}{\rho_{i_1}} \right)^{n_i}, \quad i = A, B, \text{ and } C$$

The kinetic coefficients for each material are shown in Table C-1. For all six materials the kinetic coefficients for constituents A and B are taken to be the same as for phenolic resin as reported in Reference C-1. The reinforcement fibers for only 2 of the six materials decompose to a significant extent, nylon fabric and asbestos fabric. The rate coefficients for nylon are taken from Reference C-1 and the rate coefficients for asbestos fiber decomposition were derived giving consideration to the temperature at which the fibers would lose their water of hydration. According to Reference C-5, chrysotile asbestos fibers lose their water of hydration over the temperature range 1210°R to 1570°R. The kinetic coefficients employed for these fibers were derived by simply requiring a gradual loss of the water over this temperature range.

C-4 Heat of Formation Data

The heat of formation of the virgin plastic and char is required to properly characterize the energy associated with the material decomposition reaction. The chemical energy base state is taken to correspond to that utilized in the JANAF Thermochemical Tables (Ref. C-7), that is, the elements in their normal state are presumed to have no chemical energy. All heats of formation are taken at 298°K. The method employed to evaluate the heat of formation for each material is described here.

(NL-1) Silica-Phenolic (MX5-89)

The heat of formation for silica is taken from Reference C-7

$$\Delta H_{f_{SiO_2}} = -6510 \text{ Btu/lb}$$

The heat of formation for phenolic resin is (after Ref. C-1)

$$\Delta H_{f_{C_6H_6O}} = -1100 \text{ Btu/lb}$$

The virgin material heat of formation then becomes

$$\Delta H_{f_{virgin}} = K_r \left(\Delta H_{f_{C_6H_6O}}\right) + (1 - K_r)\left(\Delta H_{f_{SiO_2}}\right)$$

The char heat of formation is obtained assuming that the carbonaceous residue is of the same crystalline form as the carbon base state

$$\Delta H_{f_{carbon}} = 0$$

The char heat of formation then becomes

$$\Delta H_{f_{char}} = \Delta H_{f_{SiO_2}} (1 - K_r) \frac{\rho_{virgin}}{\rho_{char}} \frac{\text{Btu}}{\text{Lb char}}$$

The resin mass fraction and densities in the above expression were derived previously and are shown in Table C-1 along with the heat of formation data.

(NL-2) Graphite-Phenolic (MX-4500)

Both the graphite fibers and the carbonaceous residue are presumed to have the same heat of formation as the carbon base state ($\Delta H_f = 0$). The virgin material heat of formation becomes:

$$\Delta H_{f_{virgin}} = K_r \Delta H_{f_{C_6H_6O}}$$

and, for the char

$$\Delta H_{f_{char}} = 0$$

(NL-3) Asbestos-Phenolic (MXA-11)

The heat of formation of the asbestos fibers is taken as the weighted average of the heat of formation of each constituent in the fibers. The effective molecular configuration is:

$$(MgO)_3 \cdot (SiO_2)_2 \cdot (H_2O)_2$$

The heat of formation of the metal oxides is taken for their crystal forms and for H_2O as liquid. The values, taken from Reference C-7 are:

$$\Delta H_{f\ MgO} = -143.7 \times 10^3 \text{ cal/mole MgO}$$
$$\Delta H_{f\ SiO_2} = -217.5 \times 10^3 \text{ cal/mole } SiO_2$$
$$\Delta H_{f\ H_2O} = -67.8 \times 10^3 \text{ cal/mole } H_2O$$

then

$$\Delta H_{f\ \text{asbestos}} = \frac{3(\Delta H_{f\ MgO}) + 2(\Delta H_{f\ SiO_2}) + 2(\Delta H_{f\ H_2O})}{M_{(MgO)_3 \cdot (SiO_2)_2 \cdot (H_2O)_2}}$$

$$\Delta H_{f\ \text{asbestos}} = -3620 \text{ Cal/gr} = -6510 \text{ Btu/lb}$$

and the asbestos-phenolic heat of formation is

$$\Delta H_{f\ \text{asbestos-phenolic}} = K_r(\Delta H_{f\ \text{phenolic}}) + (1-K_r)\Delta H_{f\ \text{asbestos}}$$
$$= -4151 \text{ Btu/lb}$$

The char heat of formation is obtained considering the energy associated with the dehydrated fibers and resin residue. From Table C-1 the density of the dehydrated asbestos fibers is, $\rho_{C_2} = 111.7 \text{ lb/ft}^3$. The corresponding heat of formation for the dry fibers becomes

$$\Delta H_{f\ \text{dry asbestos}} = \frac{3(\Delta H_{f\ MgO}) + 2(\Delta H_{f\ SiO_2})}{M_{(MgO)_3 \cdot (SiO_2)_2}} = -3590 \frac{\text{Cal}}{\text{gr}}$$
$$= -6460 \frac{\text{Btu}}{\text{lb}}$$

The resin residue heat of formation is taken as zero so the char heat of formation includes only the energy of the dry asbestos fibers.

$$\Delta H_{f\ char} = \Delta H_{f\ dry\ asbestos} \frac{\rho_{C_2}}{\rho_{C_1}} (1-K_r) \frac{\rho_{virgin}}{\rho_{char}} = -4780 \frac{Btu}{lb\ char}$$

(NL-4) Carbon-Phenolic (MX-4926)

The virgin material and char heat of formation are evaluated in the same manner as for graphite-phenolic (NL-2).

(NL-5) Nylon-Phenolic (FM-5051)

The heat of formation of nylon and phenolic are taken from Reference 1.

$$\Delta H_{f\ phenolic} = -1100\ Btu/lb,\ \Delta H_{f\ nylon} = -1520 \frac{Btu}{lb}$$

$$\Delta H_{f\ virgin} = K_r\ \Delta H_{f\ phenolic} + (1-K_r) \Delta H_{f\ nylon} = -1311 \frac{Btu}{lb}$$

The carbonaceous residue is taken to be at the carbon reference state, so,

$$\Delta H_{f\ char} = 0$$

(NL-6) Silica-Phenyl Silane + Buna N (XR-2015)

Information on the heat of formation of phenyl silane + Buna N is lacking so it is assumed here to be the same as the heat of formation of phenolic resin. The heat of formation of the virgin material and char are evaluated in the same manner as for silica-phenolic.

REFERENCE TO APPENDIX C

C-1 Kratsch, K. M., Hearne, L. F., and McChesney, H. R.: Thermal Performance of Heat Shield Composites During Planetary Entry. Presented at AIAA-NASA National Meeting, Palo Alto, California, Sept. 30, 1963.

C-2 The Ablative Thermal Insulation Handbook, Fiberite Corporation, Winona, Minnesota.

C-3 McCuen, P. A., Schaefer, J. W., Lundberg, R. E., and Kendall, R. M.: A Study of Solid-Propellant Rocket-Motor Exposed Materials Behavior. Final Report, Contract No. AF 04(611)-9073, Vidya Project No. 9061, Feb. 26, 1965.

C-4 Ablative Materials Handbook, U.S. Polymeric Materials, Incorporated, Santa Ana, California.

C-5 Handbook of Asbestos Textiles, Asbestos Textile Institute, Philadelphia Pennsylvania, Second Edition, 1961.

C-6 Laboratory Report, Truesdail Laboratories, Incorporated, Los Angeles, California. Aerotherm P.O. No. 01159, July 14, 1966.

C-7 JANAF Thermochemical Tables, The Dow Company, Midland, Michigan, August, 1965.

TABLE C-1

ABLATION MATERIAL CHEMICAL PROPERTIES

Nozzle Number		NL-1	NL-2	NL-3	NL-4	NL-5	NL-6
Material		Silica Phenolic (MXS 89)	Graphite-Phenolic (MX 4500)	Asbestos-Phenolic (MXA 11)	Carbon-Phenolic (MX 4926)	Nylon-Phenolic (FM 5051)	Silica-Phenyl Silane + Buna N (XR-2015)
ρ_{virgin}	Lb virgin/ft^3 virgin	104.8	87.9	102.3	91.3	75.3	98.8
ρ_{char}	Lb char/ft^3 char	85.6	70.7	68.1	73.2	15.1	70.8
Effective resin molecule		C_6H_6O	C_6H_6O	C_6H_6O	C_6H_6O	C_6H_6O	$C_6H_{8.14}O_{.955}N_{.366}$
Effective reinforcement molecule		SiO_2	C	$(M_gO)_3 \cdot (SiO_2)_2 \cdot (H_2O)_2$	C	$C_6H_{11}ON$	SiO_2
ρ_{A1}	Lb initial A/ft^3 resin	60.75	60.75	60.75	60.75	60.75	57.8
ρ_{A2}	Lb final A/ft^3 resin	32.4	32.4	32.4	32.4	32.4	15.4
ρ_{B1}	Lb initial B/ft^3 resin	20.24	20.25	20.25	20.25	20.25	19.1
ρ_{B2}	Lb final B/ft^3 resin	0	0	0	0	0	0
ρ_{C1}	Lb initial C/ft^3 resin	120.3	91.7	128.3	97.4	70.4	117.0
ρ_{C2}	Lb final C/ft	120.3	91.7	111.7	97.4	0	117.0
K_r	Lb resin/lb virgin	0.305	0.326	0.435	0.330	0.500	0.354
Γ	ft^3 resin/ft^3 virgin	0.395	0.354	0.549	0.372	0.465	0.455
k_A	Sec^{-1}	4.48×10^9	4.48×10^9	4.48×10^9	4.48×10^9	4.48×10^9	4.48×10^9
k_B	Sec^{-1}	1.40×10^4	1.40×10^4	1.4×10^4	1.4×10^4	1.4×10^4	1.4×10^4
k_C	Sec^{-1}	--	--	5.27×10^6	--	$1.85 \times 10^{1.3}$	--
$-E_A/R$	(^oR)	3.68×10^4	3.68×10^4	3.68×10^4	3.68×10^4	3.68×10^4	3.68×10^4
$-E_B/R$	(^oR)	1.54×10^4	1.54×10^4	1.54×10^4	1.54×10^4	1.54×10^4	1.54×10^4
$-E_C/R$	(^oR)	--	--	5.8×10^4	--	4.71×10^4	-
n_A		3	3	3	3	3	3
n_B		3	3	3	3	3	3
n_C		--	--	1	--	1	--
$\tilde{K}$	Lb Hydrogen/Lb gas	0.107	0.107	0.108	0.107	0.102	0.103
$\tilde{K}_{Cg}$	Lb Carbon/Lb gas	0.609	0.609	0.476	0.609	0.626	0.646
$\tilde{K}_{Ng}$	Lb Nigrogen/Lb gas	0	0	0	0	0.077	0.064
$\tilde{K}_{Og}$	Lb Oxygen/Lb gas	0.284	0.284	0.416	0.284	0.195	0.187
$\tilde{K}_{Cc}$	Lb Carbon/Lb char	0.149	1.000	0.262	1.000	1.000	0.101
$\tilde{K}_{Oc}$	Lb Oxygen/Lb char	0.453	0	0.343	0	0	0.479
$\tilde{K}_{Mgc}$	Lb Magnesium/Lb char	0	0	0.223	0	0	0
$\tilde{K}_{Sic}$	Lb Silicon/Lb char	0.398	0	0.172	0	0	0.420
ΔH_{fv}	Btu/Lb virgin Matl.	-4856	-358.6	-4151	-363.0	-1311	-4590
ΔH_{fc}	Btu/Lb char	-5540	0	-4780	0	0	-5850

APPENDIX D

MODEL FOR THERMAL CONDUCTIVITY IN THE SILICA CARBON REACTION ZONE

APPENDIX D

MODEL FOR THERMAL CONDUCTIVITY IN THE SILICA CARBON REACTION ZONE

In Section 4.3.2.1.2 in the main text, it was suggested that it would be adequate to give conductivity data for the carbon-silica reacting mixture as a function of density, temperature and an empirical porosity factor. In the model, the thermal conductivity will be "tied to" certain states of known temperature-dependent conductivities. At the deepest part of the reaction zone, the material is pure char and has the pure char thermal conductivity. On the other hand, it may safely be presumed that at the liquid-layer boundary, the carbon structure has broken up. The residual isolated lumps of carbon are adjacent to voids formed during the generation of reaction gas and, therefore, presumably no longer play much of a role as a thermal conductor. Therefore, at this density it seems reasonable to switch over to a pure silica conductivity as the basic conductivity, rather than the experimental char conductivity used for the original silica-carbon char. Between these two states (the char state and the liquid-layer edge state), the basic conductivity may be varied linearly with density between char conductivity and silica conductivity (both of which are of course temperature dependent). The basic conductivity must then itself be corrected for density and porosity effects. This density correction factor should be unity at the char density and ρ/ρ_{SiO_2} at the liquid-layer edge density (which numerical experimentation, as described below, seems to indicate is about 50 lb/ft^3, corresponding to a carbon density of 7 lb/ft^3). In addition, there must be a porosity correction of some sort, since a porous material of a given density may exhibit a wide range of conductivities depending on the size and orientation of the holes. Since the porosity effect is not known in advance, it is desirable to leave it as a free parameter. Denoting this parameter a, we have the correction $a\rho_{liq}/\rho_{SiO_2}$ at the liquid-layer edge density.

Thus, the proposed relationship is

$$k(\rho,T) = k_o(\rho,T)\,f(a,\rho)$$

where

$$k_o(\rho,T) = k_{SiO_2}(T) + (k_{char}(T) - k_{SiO_2}(T))\ \frac{(\rho - \rho_{liq})}{(\rho_{char} - \rho_{liq})}$$

and

$$f(a,\rho) = \frac{a\rho_{liq}}{\rho_{SiO_2}} + \frac{(\rho_{SiO_2} - a\rho_{liq})}{\rho_{SiO_2}}\ \frac{(\rho - \rho_{liq})}{(\rho_{char} - \rho_{liq})}$$

$$\rho_{liq} \le \rho \le \rho_{char}$$

and

$$\rho_{liq} = 50 \text{ lb/ft}^3$$
$$\rho_{char} = 85.6 \text{ lb/ft}^3$$
$$\rho_{SiO_2} = 130 \text{ lb/ft}^3$$

This scheme is utilized for densities below the char density but not below $\rho_{liq} = 50$ lb/ft^3. Below 50 lb/ft^3 the silica conductivity is presumed to dominate, so that

$$\left.\begin{aligned} k_o &= k_o(T) = k_{SiO_2}(T) \\ f(a,\rho) &= \frac{a\rho}{\rho_{SiO_2}} \end{aligned}\right\} \qquad 22 \leq \rho \leq 50$$

The lower limit of 22 lb/ft^3 allowed for this relationship may be explained as follows. As a final complexity, a specimen silica foam from a rocket motor of the same material as considered here showed a minimum density of 22 lb/ft^3 rather than the "naive" minimum of 8.95 lb/ft^3 computed for complete carbon consumption and no shrinkage. Thus, there appears to be some shrinkage near the surface and the density correction should be frozen at

$$f(a,\rho) = \frac{a\ 22}{\rho_{SiO_2}}$$

However, since the SCRIMP computer program does not allow for shrinkage, the thermal conductivity should be further modified to compensate for the shrinkage effect, which reduces the thickness of the material. This shrinkage may be simulated by multiplying the conductivity by $22/\rho$, since the material is compacted from a computed density of ρ to a density of 22 lb/ft^3. Thus, for $\rho < 22$ we have

$$\left.\begin{aligned} k &= k_o(T)\ f(a,\rho) \\ k_o(T) &= k_{SiO_2}(T) \\ f(a,\rho) &= a\ \frac{22}{\rho_{SiO_2}}\ \frac{22}{\rho} \end{aligned}\right\} \qquad \rho \leq 22 \text{ lb/ft}^3$$

Here, the ρ is, of course, a "naive" computed density not allowing for the shrinkage which actually occurs.

The thermal conductivity model presented here has the virtues that

1. it could be incorporated into the program with minimal programming effort,
2. it provides for the appropriate transition between a char conductivity and the silica conductivity,
3. it provides a plausible density dependence, and
4. the adjustable parameter, a , provides a convenient mechanism for computational experimentation.

The model has the obvious defects that

1. it does not account for radiation contributions to the conductivity except through the basic k_{SiO_2} temperature function, which may not be at all adequate for the increasingly porous material near the surface,
2. the requisite basic SiO_2 conductivity data are not too well known.

Unfortunately, the thermal conductivity has a very important effect both on the transient surface response (as is typical for all ablation problems) and on the steady-state recession rate (typical only of liquid-layer problems). As noted in the main text, the choice of k for the reaction layer has a dominating influence on the predictions.